Thèse

présentée pour obtenir le grade de Docteur
de l'École Nationale Supérieure des Télécommunications

Spécialité : **Électronique et Communications**

DAMIEN KUBRAK

Etude de l'hybridation d'un récepteur GPS avec des capteurs bas coûts pour la navigation personnelle en milieu urbain

Soutenue le 24 mai 2007 devant le jury composé de

Gérard Maral	Président
Gérard Lachapelle	Rapporteur
Günter Hein	Rapporteur
Michel Monnerat	Examinateur
Christophe Macabiau	Co-directeur de thèse
Marie-Laure Boucheret	Co-directeur de thèse
Marc Pontif	Invité

Remerciements

Cette thèse est le fruit de trois années de travail passées principalement au sein du Laboratoire de Traitement du Signal et de Télécommunication (LTST) de l'ENAC, ainsi que sur le site d'Alcatel Alenia Space, maintenant devenu Thales Alenia Space. Elle m'a permis d'acquérir une connaissance théorique approfondie des techniques de traitement du signal GPS et de navigation inertielle, tout en ayant la possibilité de tester les algorithmes étudiés en conditions réelles. Il est pour moi évident que les moyens mis à ma disposition m'ont largement aidé dans mes recherches.

J'ai par ailleurs bénéficié d'un environnement de travail très favorable. En ce sens, je voudrais particulièrement remercier Christophe Macabiau, responsable du laboratoire LTST de l'ENAC, et Michel Monnerat, ingénieur dans le service Location Based Services de Thales Alenia Space, pour m'avoir permis de réaliser cette thèse. Ces deux personnes ont été déterminantes pour moi tout au long de ces trois années, et je leur en suis reconnaissant.

Je dois à Christophe une grande partie de ces travaux. Je le remercie pour le temps qu'il m'a consacré, la motivation qu'il a su me procurer, les connaissances qu'il m'a transmises… et au-delà pour sa légendaire bonne humeur se traduisant généralement par de belles chansonnettes d'époque, ainsi que des rires particulièrement retentissants.

Bien que souvent occupé par les affaires courantes du département Location Based Services, Michel a toujours su trouver le temps pour discuter des grandes orientations de cette thèse, reflechir aux problèmes techniques posés et a toujours facilité mon travail. Il m'a par ailleurs laissé une grande liberté dans mes activités de recherche.

J'aimerais aussi remercier Anne-Christine Escher pour son implication et l'aide qu'elle m'a apportée dans le domaine de la navigation inertielle. Cet aspect très technique était relativement neuf pour moi au début de cette thèse.

Je profite de cette occasion pour remercier Stéphane Corazza, Florian Dargeou et Antonio Dias pour m'avoir aidé dans l'utilisation du serveur AGPS pour mes diverses experiences en conditions réelles.

Un grand merci à mes deux 'co-bureau', Emilie et Hanaa, sans qui je n'aurais jamais pu mourir de chaud l'été. Je leur reconnais néanmoins un sens de l'organisation très développé qui m'a souvent été salvateur, aussi bien au laboratoire que lors de nos voyages. Evidemment, je n'oublie pas Benjamin, Mathieu et Olivier qui ont pu admirer ma défense de fer au football et ma ponctualité au De Danu, Anaïs qui restera pour moi ce qui se fait de mieux en matière de curiosité, Christophe, Philippe, Audrey, Na, Marie-Laure, Antoine…

Enfin, je tiens à souligner la patience de Claire tout au long de ces trois années, et je finirai par ces quelques nano-encouragements à Julien : « le bout du tunnel n'est peut-être pas si loin ».

Résumé

A l'origine, les services basés sur la localisation trouvaient la justification de leur développement dans les nouvelles directives sur les appels d'urgence émises d'abord aux Etats-Unis avec le E-911. Mais aujourd'hui, ils prennent de plus en plus d'importance dans la vie de tous les jours. Plusieurs technologies de positionnement peuvent répondre au besoin de localisation d'un individu, qu'il soit à l'intérieur ou à l'extérieur d'un bâtiment. Parmi ces techniques, le système GPS, et plus généralement GNSS, est particulièrement adapté aux applications nécessitant un positionnement précis dans tous types d'environnements. Il ne requiert aucune infrastructure, si ce n'est une antenne de réception et une puce pour décoder et traiter les messages transmis au travers des signaux. Aussi, ce moyen de localisation est à même de répondre aux besoins de positionnement d'applications comme les services d'urgence, la navigation en voiture, l'e-tourisme…

Le positionnement par GPS a néanmoins des limites liées aux phénomènes affectant les signaux lors de leur propagation. Dans la mesure où les services liés à la localisation des personnes sont déployés dans des zones urbaines, la solution de position peut être entachée d'erreurs dues aux multitrajets qui se combinent au trajet direct des signaux reçus. Par ailleurs, il est probable que les signaux GPS puissent être bloqués ou fortement atténués par les bâtiments, contribuant de fait à une augmentation de la sensibilité aux intercorrelations et donc une dégradation de la précision et de la disponibilité du service de positionnement. Les récentes évolutions des récepteurs GPS dites « haute sensibilité » (HSGPS) ou « assistées » (AGPS) peuvent partiellement surmonter les difficultés de fournir une position à l'intérieur d'un bâtiment. Néanmoins, les améliorations apportées par ces nouvelles architectures restent limitées lorsque des signaux à très faible puissance doivent être traités. En conséquence, des techniques complémentaires doivent être utilisées pour aider, voire remplacer le cas échéant, les systèmes basés sur le traitement des signaux GPS.

Parmi les systèmes candidats, ceux basés sur des capteurs inertiels bas coûts sont prometteurs. En effet, ils sont susceptibles d'améliorer les performances globales du système de navigation intégré tout en minimisant son surcoût, et ce, malgré la faible qualité des capteurs utilisés. Cette thèse est dédiée à l'utilisation de tels senseurs comme moyen complémentaire de navigation. Plusieurs objectifs sont fixés parmi lesquels l'amélioration de la précision et de la disponibilité de la solution de position, mais aussi l'étude de la réduction de la charge de calcul des récepteurs HSGPS et AGPS tout en conservant les performances des systèmes actuels.

Les techniques avancées de traitement du signal (modes « haute sensibilité » et « assisté ») sont dans un premier temps étudiées à la fois théoriquement et sur la base d'analyses de performance en conditions réelles. Les résultats obtenus lors de tests montrent que le positionnement urbain est rendu possible grâce à ces techniques, même si les effets des multitrajets et des intercorrelations dégradent sensiblement la précision. L'AGPS fournit des solutions de position plus précises que l'HSGPS, ce qui privilégie son utilisation dans un système intégré de navigation. Néanmoins, il est clairement démontré que même avec ces techniques avancées de traitement du signal, le positionnement à l'intérieur d'un bâtiment reste très difficile, voire impossible pour une grande majorité des cas.

Les algorithmes alternatifs de navigation basés sur l'utilisation de capteurs tels que des accéléromètres, des gyroscopes, mais aussi des magnétomètres ou encore un capteur de pression sont étudiés dans un second temps. Différentes architectures sont détaillées et optimisées pour

compenser les dérives introduites par les erreurs de mesure intrinsèques aux senseurs. Un filtre permettant l'estimation dynamique des biais affectant les mesures des gyroscopes est dans ce contexte proposé à la fois pour la navigation pédestre et la navigation en voiture.

La possibilité de réduire la complexité du traitement effectué par les récepteurs AGPS et HSGPS est également abordée dans cette thèse. Plus particulièrement, une technique permettant d'estimer la contribution utilisateur sur le Doppler total affectant la porteuse du signal reçu est proposée. Ses performances sont testées sur des données réelles collectées en environnement urbain. Il est démontré que cette contribution peut être estimée dans la plupart des cas avec précision quelle que soit la dynamique de l'utilisateur, réduisant de fait la complexité de l'étage d'acquisition des signaux GPS. De meilleures performances sont néanmoins atteintes dans le cas particulier de la navigation pédestre.

Enfin, l'amélioration de la disponibilité et de la précision de la solution de position en environnement urbain et à l'intérieur de bâtiments est étudiée. Plusieurs schémas d'hybridation ayant pour but de combiner les différents modules GPS (AGPS, HSGPS) et les systèmes de navigation inertielle basés sur les capteurs bas coûts sont analysés. Une approche différente de celle traditionnellement suivie est proposée dans le cadre de la navigation en voiture pour coupler de façon serrée les modules GPS et le système de navigation inertielle. Ce schéma d'hybridation permet de corriger les erreurs des capteurs bas coûts dès lors que deux mesures de pseudodistance et de Doppler sont disponibles, même si cette technique est sensible à la géométrie des satellites utilisés par rapport au cap du véhicule. Dans le cadre de la navigation pédestre, une hybridation lâche en temps réel est proposée et implantée. La performance du système intégré de positionnement à l'intérieur des bâtiments a été testée en conditions réelles, montrant une précision de 10 mètres par rapport à la trajectoire de référence, y compris lors d'interruptions complètes du service GPS (2 min dans les tests effectués).

Mots clés : HSGPS, AGPS, acquisition, MEMS, INS, hybridation, Kalman

Hybridisation of a GPS Receiver with Low-Cost Sensors for Personal Positioning in Urban Environment

Abstract

First driven by the regulation on emergency calls in the United States (E-911), Location Based Services (LBS) are currently gaining more and more importance in everyday life. Numerous positioning technologies are foreseen to allow the location of one user whether he is indoors or outdoors. Among these techniques, GPS and even more GNSS are well adapted to applications requiring accurate positioning whatever the environment (urban or rural). Such a positioning technique requires no extra infrastructure but a chipset to decode and process GPS signals. As a consequence, this makes it very suitable to fulfil the location requirements of applications such as emergency services (US E911), guidance of rescue teams, in-vehicle navigation, e-tourism… The technique has nevertheless limitations due to errors that affect the incoming signals. Because Location Based Services are likely to be deployed in urban areas, strong multipath may affect the signals, contributing to a high position bias. GPS signals may also be blocked or faded by buildings, which may expose the receiver to cross-correlation distortions in case of large difference between the Signal-to-Noise Ratios (SNRs), decreasing in the same time the accuracy and the availability of the positioning service.

The ability of providing a position solution especially indoors is then a great challenge that can be partially handled with High Sensitivity GPS or Assisted GPS solutions. However, such processing improvements still encounter big issues in the aforementioned harsh environments because of the weak power of the signals to acquire and process. As a consequence, complementary techniques shall be used to support or replace GPS-based positioning systems. Among the possible augmentations, inertial sensor-based techniques are promising ones since they may offer a cost-effective means of improving the overall performance despite the intrinsic low accuracy and stability of the sensors output.

The purpose of this thesis is to investigate the use of such low-cost sensors as a self-contained augmentation of a GPS-based positioning system. More specifically, this study addresses the improvement of the position solution availability and accuracy, as well as the decrease of the processing load of HSGPS/AGPS receivers thanks to information provided by the set of sensors.

In the first place, the performance of the new GPS processing techniques (HSGPS and AGPS) is analysed based on theoretical simulations and field test trials. Results from these test campaigns show that a good accuracy is achievable in urban areas, even if multipath and cross-correlations degrade the overall performance. AGPS is shown to give better measurements than HSGPS, which makes it more suitable for hybridisation purposes. However, there is an unavoidable lack of availability indoors where GPS signals are too weak to be processed.

The augmentation of the aforementioned GPS-based navigation solutions is then addressed through the use of low-cost sensors (typically accelerometers, gyroscopes, magnetometers and a pressure sensor). Different pure inertial navigation algorithms are detailed and optimised mechanisations designed to compensate for the low performance of the low-cost sensors used throughout this thesis are proposed. In particular, an attitude filter capable of dynamically estimating the gyroscope biases is developed and tested in actual conditions.

The improvement of the acquisition stage of AGPS and HSGPS receivers is investigated based on the self-contained augmentations previously described. The reduction of the Doppler uncertainty due to user's motion is more specifically addressed. Tests on data collected during

urban vehicle trials are used to assess the performance of the proposed technique. It is shown that the user's Doppler contribution can be well estimated whatever the dynamic experienced by the receiver, which contributes to the decrease of the acquisition stage complexity. However it should be pointed out that better performances are obtained in the pedestrian navigation case than in the land vehicle navigation case.

The position solution availability and accuracy in urban canyons and indoor environments is finally addressed through several hybridisation schemes aimed at fusing the different GPS modules (HSGPS or AGPS) and the low-cost inertial sensors. A non-standard tight coupling scheme is proposed in the frame of land vehicle navigation. Results show that urban navigation using only 2 pseudorange and Doppler measurements is possible, even if the accuracy of the integrated navigation system is sensitive to the geometry of the satellite used for hybridisation. A real time loose coupling prototype is implemented and tested for the specific pedestrian navigation case. The accuracy of the integrated navigation system is shown to stay within 10 metres from the reference trajectory even during complete GPS outages of about 2 minutes according to the trials exercised.

Key words: HSGPS, AGPS, Acquisition, MEMS, INS, Hybridisation, Kalman filter.

Table of Contents

REMERCIEMENTS ..... **I**

RESUME ..... **III**

ABSTRACT ..... **VII**

TABLE OF CONTENTS ..... **IX**

LIST OF FIGURES ..... **XIII**

LIST OF TABLES ..... **XIX**

ABBREVIATIONS ..... **XXI**

CHAPTER 1: INTRODUCTION **1**

1.1 BACKGROUND 1
1.2 MOTIVATIONS AND OBJECTIVES 2
1.3 CONTRIBUTIONS 3
1.4 THESIS OUTLINE 5

CHAPTER 2: GPS-BASED POSITIONING **7**

2.1 THE GLOBAL POSITIONING SYSTEM 8
2.1.1 Fundamentals *8*
2.1.1.1 Space Segment 8
2.1.1.2 Control Segment 10
2.1.1.3 User Segment 11
2.1.2 GPS Signal Processing *12*
2.1.2.1 GPS Signal Acquisition 13
2.1.2.2 GPS Signal Tracking 17
2.1.3 GPS Measurements *22*
2.1.3.1 Pseudorange Measurement 22
2.1.3.2 Doppler Measurement 23
2.1.3.3 Carrier Phase Measurement 24
2.1.4 Measurement Errors *24*
2.1.4.1 Satellite Orbital Error ΔD 24
2.1.4.2 Ionospheric Error ΔI 24
2.1.4.3 Tropospheric Error ΔT 25
2.1.4.4 Multipath μ 25
2.1.4.5 Time Synchronisation Δb 25
2.1.4.6 Tracking Loops Jitter 25
2.2 GPS PROCESSING ENHANCEMENT 26
2.2.1 Positioning Technologies and Issues *26*
2.2.2 High Sensitivity GPS *27*
2.2.2.1 Principle 27
2.2.2.2 Performance Overview 29
2.2.3 Assisted GPS *30*
2.2.3.1 Principle 30
2.2.3.2 Enhanced AGPS 32
2.2.3.3 Acquisition Performance 33
2.3 HS-GPS / AGPS PERFORMANCE ANALYSIS 35
2.3.1 HSGPS / AGPS Modules *35*
2.3.2 Performance Assessment *36*
2.3.2.1 Accuracy 36
2.3.2.2 Time-To-First-Fix 37
2.3.2.3 Availability 37
2.3.3 Comparative Test Results *37*
2.3.3.1 Light Indoor Environment 37
2.3.3.2 Urban Street Environment 39
2.3.3.3 Kinematic Urban Test 40
2.3.3.4 Indoor Test 41
2.4 CONCLUSION 41

CHAPTER 3: INERTIAL NAVIGATION SYSTEMS 44

3.1 INERTIAL NAVIGATION OVERVIEW 45
3.1.1 Basic principle 45
3.1.2 Frames and Coordinates 45
3.1.3 Sensors 46
3.1.3.1 Accelerometer 46
3.1.3.2 Gyroscope 47
3.1.3.3 Measurements Errors 48
3.2 STRAP DOWN ATTITUDE COMPUTATION 48
3.2.1 Attitude Algorithm 49
3.2.2 Attitude Initialisation 51
3.2.3 Euler's Angles Singularity Issue 52
3.3 MEMS SENSOR UNIT PERFORMANCE OVERVIEW 54
3.3.1 Xsens Motion Tracker 54
3.3.1.1 Accelerometer 54
3.3.1.2 Gyroscopes 55
3.3.2 Gyroscope Output Approximation 56
3.4 CLASSICAL INERTIAL NAVIGATION SYSTEM 58
3.4.1 Fundamental Inertial Differential Equation 58
3.4.2 INS Mechanisation in the Navigation Frame 60
3.4.3 Expected Accuracy 61
3.5 THE PARTICULAR CASE OF THE PEDESTRIAN NAVIGATION 62
3.5.1 Mechanisation in the Navigation Frame 63
3.5.2 Travelled Distance Estimation 65
3.5.2.1 Parameters 65
3.5.2.2 Velocity Models 68
3.5.2.3 Regression Coefficients 69
3.5.3 Displacement Direction Estimation 73
3.5.4 Unconstrained Navigation Issue 74
3.5.5 PNS Mechanisation 76
3.5.6 Expected Accuracy 76
3.6 CONCLUSION 79

CHAPTER 4: SENSOR-BASED AUGMENTATIONS 80

4.1 PRESSURE SENSOR 81
4.1.1 Principle and Output Model 81
4.1.2 Performance assessment 82
4.1.3 Improvement of the Position Solution 83
4.2 MAGNETIC FIELD SENSOR 85
4.2.1 Earth Magnetic Field 85
4.2.2 Sensor Output Model 86
4.2.3 Magnetic Heading 86
4.2.4 Calibration Procedures and Magnetic Interferences 87
4.3 DRIFT-FREE ATTITUDE FILTER 89
4.3.1 Inclination Filter 90
4.3.1.1 State Transition Models 90
4.3.1.2 Measurement Models 94
4.3.1.3 Inclination Filter Summary 95
4.3.2 Heading Filter 95
4.3.2.1 State Transition Models 95
4.3.2.2 Measurements Models 97
4.3.2.3 Heading Filer Summary 98
4.3.3 Optimised Drift-Free Attitude Filter 99
4.3.4 Drift-Free Attitude Filter 100
4.3.4.1 Design n°1: Attitude Filter using all the Sensors 100
4.3.4.2 Design n°2: Attitude Filter using only 1 Gyroscope 100
4.3.5 Test Results 101
4.3.5.1 The Pedestrian Navigation Case 102
4.3.5.2 The Land Vehicle Navigation 106
4.4 OTHER AUGMENTATION TECHNIQUES 109
4.4.1 Zero velocity UPdaTe (ZUPT) 109
4.4.2 Velocity and Height Constraints 110

4.5 CONCLUSION 110

CHAPTER 5: SENSORS AIDING FOR GPS ACQUISITION 112

5.1 INTRODUCTION 113
5.2 RECEIVER DOPPLER UNCERTAINTY 115
5.2.1 Satellite Contribution 115
5.2.2 Local Oscillator Contribution 118
5.2.3 User Contribution 119
5.3 SENSORS AIDING FOR DOPPLER UNCERTAINTY REDUCTION 120
5.3.1 Motion Recognition 120
5.3.2 Sensor Fusion & Integration Scheme 121
5.3.3 Satellite Geometry Issue 123
5.3.4 On-Demand Doppler Estimation 125
5.3.5 Doppler Reduction Procedure 126
5.4 TEST RESULTS 127
5.4.1 The Pedestrian Navigation Case 127
5.4.2 The Land Vehicle Navigation Case 129
5.5 CONCLUSIONS 131

CHAPTER 6: GPS/IMU HYBRIDISATION FOR PERSONAL NAVIGATION 134

6.1 INTEGRATION STRATEGIES & ARCHITECTURES 135
6.1.1 Loose Coupling 135
6.1.2 Tight Coupling 136
6.1.3 Sensors Augmentation 137
6.1.4 Practical Use Cases 138
6.2 LAND VEHICLE NAVIGATION CASE 138
6.2.1 Introduction 138
6.2.2 Integrated Navigation System 140
6.2.2.1 INS Mechanisation 140
6.2.2.2 Measurement Equations 143
6.2.2.3 Coupling Methodology 144
6.2.3 Test Results 148
6.2.4 Conclusion 156
6.3 PEDESTRIAN NAVIGATION CASE 157
6.3.1 Introduction 157
6.3.2 PNS Mechanisation Performance 158
6.3.2.1 Static Performance 158
6.3.2.2 Constrained Navigation 159
6.3.2.3 Unconstrained Navigation 162
6.3.2.4 Conclusion 163
6.3.3 Integrated Navigation System 164
6.3.3.1 Introduction 164
6.3.3.2 Coupling Methodology 165
6.3.3.3 Test Results 171
6.3.4 Conclusion 176
6.4 CONCLUSION 177

CHAPTER 7: CONCLUSIONS AND FUTURE WORK 178

7.1 CONCLUSIONS 178
7.2 FUTURE WORK 180

APPENDIX A: DOPPLER EFFECT 182

APPENDIX B: QUATERNION-BASED ATTITUDE COMPUTATION 186

APPENDIX C: LEAST SQUARES AND KALMAN FILTERING 190

APPENDIX D: FREQUENCY ESTIMATION TECHNIQUES 194

BIBLIOGRAPHY 200

List of Figures

Figure 2.1: GPS L1 signal generation architecture. 9
Figure 2.2: Baseband C/A PSD. 10
Figure 2.3: Structure of a GPS frame. 10
Figure 2.4: General GPS receiver architecture. 12
Figure 2.5: Single dwell serial search acquisition structure. 14
Figure 2.6: Probability of detection for a constant dwell time of 20ms. 17
Figure 2.7: Single dwell serial search mean acquisition time for a constant dwell time of 20ms 17
Figure 2.8: Generic Phase Lock Loop architecture [3]. 17
Figure 2.9: Performance of several Costas PLL discriminators. 19
Figure 2.10: Generic Delay Lock Loop architecture [3]. 20
Figure 2.11: Single dwell serial search probability of detection for a constant dwell time of 500ms. 27
Figure 2.12: Single dwell serial search mean acquisition time for a constant dwell time of 500ms 27
Figure 2.13: FFT-based acquisition scheme. 28
Figure 2.14: Costas Phase Lock Loop tracking performance. 29
Figure 2.15: Probability of no error (BER of 0) in the demodulation of the ephemeris/clock block (White Gaussian Noise Channel). 29
Figure 2.16: Comparative navigation test in urban environment. 30
Figure 2.17: Assisted-GPS basic principle. 31
Figure 2.18: AGPS acquisition enhancement. 31
Figure 2.19: EGNOS coverage. 33
Figure 2.20: Positioning server accuracy. 33
Figure 2.21: Mean signal duration required for a successful acquisition. Pfa = 1e-5, no frequency error. 34
Figure 2.22: Mean acquisition time for a successful acquisition. Pfa=1e-5, no frequency error. 35
Figure 2.23: Light indoor environment. 38
Figure 2.24: 2D plot of BT-338 (standalone) in light indoor environment. 38
Figure 2.25: 2D plot of BT-338 (MS-based) in light indoor environment 38
Figure 2.26: Urban street environment (heading north). 39
Figure 2.27: Urban street environment (heading south). 39
Figure 2.28: 2D plot of BT-338 (standalone) in urban street environment. 40
Figure 2.29: 2D plot of BT-338 (MS-based) in urban street environment. 40
Figure 2.30: 2D plot of BT-338 (standalone) in urban dynamic test. 40
Figure 2.31: 2D plot of BT-338 (MS-based) in urban dynamic test. 40
Figure 2.32: AGPS tracking result of a pedestrian going outside / inside buildings. 41
Figure 2.33: HSGPS tracking result of a pedestrian going outside / inside buildings. 41
Figure 3.1: Inertial *(I)*, ECEF *(e)* and navigation *(n)* frames. 46
Figure 3.2: Navigation *(n)* frame. 46
Figure 3.3: Euler's angles definiton. 49
Figure 3.4: Estimated inclination angle error as a function of several accelerometer biases. 52
Figure 3.5: Accelerometer inclination measurement scheme. 52
Figure 3.6: Euler's angles singularity issue. 53
Figure 3.7: Euler's angles singularity resolution. 53
Figure 3.8: Xsens motion tracker and sensors performance. 54
Figure 3.9: Accelerometers turn-on bias. 55
Figure 3.10: Accelerometer turn-on scale factor. 55

Figure 3.11: Gyroscopes turn-on bias. 56
Figure 3.12: Gyroscope triad static outputs. 56
Figure 3.13: Rotation rate of *(e)* with respect to *(I)* expressed in *(n)*. v_N=v_E=140 km/h, h=0. 58
Figure 3.14: Rotation rate of *(e)* with respect to *(I)* expressed in *(n)*. 58
Figure 3.15: Inertial Navigation System (INS) mechanisation. 60
Figure 3.16: Predicted and actual INS horizontal RMS error. 62
Figure 3.17: Biases and scale factor impact on INS horizontal accuracy. 62
Figure 3.18: DGPS velocity of reference. Walk n°1 66
Figure 3.19: DGPS velocity of reference. Walk n°2 66
Figure 3.20: Best parameters computed every 2 steps. Walk n°1. 67
Figure 3.21: Best parameters computed every 2 steps. Walk n°2. 67
Figure 3.22: Best parameters computed over 2s. Walk n°1 68
Figure 3.23: Best parameters computed over 2s. Walk n°2 68
Figure 3.24: Regression coefficients. Non-linear model. 70
Figure 3.25: Regression coefficients. Non-linear model (close-up). 70
Figure 3.26: Regression coefficients. Linear model. 1st method. 70
Figure 3.27: Regression coefficients. Linear model. 2nd method 70
Figure 3.28: Mean DGPS velocity profile of the eleven reference tests 71
Figure 3.29: Curvilinear distance estimation error with respect to DGPS measurements 71
Figure 3.30: Mean DGPS velocity profile of the eight reference tests. 72
Figure 3.31: Regression coefficients. Linear velocity model. 2nd method 72
Figure 3.32: Reference velocity used for regression 73
Figure 3.33: DGPS velocity profile (up) and distance estimation error (down). 73
Figure 3.34: Regression coefficients. Linear model. 2nd method 73
Figure 3.35: Parameters of the velocity model (unit m/s). IMU is moved while walking. 75
Figure 3.36: Relationship between the acceleration magnitude and the parameters (unit m/s^2). 75
Figure 3.37: Pedestrian Navigation System (PNS) mechanisation. 76
Figure 3.38: Error of a pedestrian walking a straight path assuming constant velocity and heading rate biases. 77
Figure 3.39: Trajectory error of a pedestrian walking a straight path assuming constant velocity and heading biases. 77
Figure 3.40: 2D upper bound position error assuming a constant velocity bias. 78
Figure 3.41: Detail of the contributions of each 2D upper bound position error. 78
Figure 4.1: Pressure measurement principle. 81
Figure 4.2: Altitude-to-pressure relationship. 81
Figure 4.3: Required pressure resolution to enable a 1m vertical resolution. 82
Figure 4.4: Impact of the pressure variation on the computed altitude 82
Figure 4.5: Altitude and temperature variations recorded over 13 hours in a closed room. 83
Figure 4.6: Vertical velocity computed with the pressure sensor measurements. 83
Figure 4.7: 3D RMS position error using pressure measurements with three different computations methods. 84
Figure 4.8: DOPs improvement due to the processing of the pressure measurements. 84
Figure 4.9: Earth's magnetic field intensity [22]. 85
Figure 4.10: Earth's magnetic field declination [22]. 85
Figure 4.11: Earth magnetic field [25]. 87
Figure 4.12: Magnetic heading error with respect to inclination error. 87
Figure 4.13: Calibration test diagram in a non perturbed magnetic environment. 88
Figure 4.14: Magnetic field magnitude variation during the different vehicle engine start. 89
Figure 4.15: Magnetic interferences due to the dashboard equipments of a vehicle. 89

Figure 4.16: Typical rotation rate patterns for pedestrian navigation (upper part) and land vehicle navigation (lower part). 92
Figure 4.17: PSD of the three rotation rate components in the mobile frame *(m)*, 1st order GM and 2nd order band-pass filter. 92
Figure 4.18: Typical acceleration magnitude patterns for pedestrian navigation (upper part) and land vehicle navigation (lower part). 93
Figure 4.19: PSD of the three acceleration components in the mobile frame *(m)*, 1st order GM and 2nd order band-pass filter. 93
Figure 4.20: Inclination filter principle. 95
Figure 4.21: Heading filter principle. 98
Figure 4.22: Attitude filter algorithm using all the sensors. 100
Figure 4.23: Attitude filter algorithm with only 1 gyroscope in the sensors unit. 101
Figure 4.24: Attitude filter heading solution. 102
Figure 4.25: Normalised magnetic field magnitude. 102
Figure 4.26: Attitude filter and gyro-based heading errors. All sensors are used. 103
Figure 4.27: Attitude filter heading error. All sensors used. 103
Figure 4.28: Trajectories using different heading sources. Pedestrian case with the triad of gyroscopes. 104
Figure 4.29: Attitude filter and gyro-based heading errors. Only one gyroscope is used. 105
Figure 4.30: Y axis gyro bias estimate of the Inclination Kalman Filter (IKF). 105
Figure 4.31: Trajectories using Different Heading Sources. Pedestrian Case with only one Gyroscope. 106
Figure 4.32: Heading errors with respect to the DGPS reference. All the sensors are used. 107
Figure 4.33: Trajectories using different heading sources. Land vehicle case with three gyroscopes. 107
Figure 4.34: Trajectories using different heading sources. Land vehicle case with only one gyroscope. 108
Figure 4.35: ZUPT. Theoretical velocity error profiles. 110
Figure 4.36: ZUPT. Theoretical position error profiles. 110
Figure 5.1: Navigation systems integration principle. 113
Figure 5.2: Satellite position definition with respect to the user's position. 116
Figure 5.3: Satellite Doppler uncertainty. GPS time known at ±2s. 117
Figure 5.4: Satellite Doppler uncertainty. User's position uncertainty of ±15km. 117
Figure 5.5: Satellite Doppler uncertainty. GPS time known at ±2s. User's position uncertainty of ±15km. 117
Figure 5.6: Satellite Doppler uncertainty. GPS time known at ±2s. Results with real GPS ephemeris. 117
Figure 5.7: Local Oscillator drift (ProPak GL2plus, static test case). 118
Figure 5.8: Frequency bins and number of frequency bins to explore with respect to a user Doppler uncertainty of +/- 250 Hz. 119
Figure 5.9: Sliding window variances computed from three different acceleration magnitude sources. 121
Figure 5.10: Illustration of elevation (left) and azimuth (right) errors for a user's position uncertainty of ±15km and a GPS time of ±2s. 122
Figure 5.11: Bad satellite geometry configuration with respect to the user's heading. 124
Figure 5.12: Typical issue of the user's velocity estimation. Land vehicle case. 124
Figure 5.13: Drift-free attitude filter with in motion alignment aiding. 125
Figure 5.14: Attitude angles error with respect to the estimated angles with a static initialisation of the filter. 126

Figure 5.15: Close-up on the first epochs. The convergence of the filter is shown here and lasts about 10 seconds. 126
Figure 5.16: User's Doppler uncertainty reduction procedure. 126
Figure 5.17: User's Doppler prediction accuracy using filtered (a) and gyro-based (b) attitude as well as the modelled pedestrian velocity. The reference user's Doppler is taken from GPS measurements. 128
Figure 5.18: User's Doppler prediction accuracy using filtered and gyro-based attitude and the Doppler model of equation (5.7). The reference user's Doppler is taken from GPS measurements. 128
Figure 5.19: Reduction of the number of user's Doppler bins with respect to different coherent integration times for an initial uncertainty of ±250 Hz using data provided by MEMS senors. 129
Figure 5.20: User's velocity estimation using all possible combinations of measurements from two GPS satellites. 130
Figure 5.21: User's Doppler prediction accuracy using the filtered attitude. 130
Figure 5.22: Improvement of the combination of MEMS. 131
Figure 6.1: Loose coupling integration scheme. Open-loop architecture. 136
Figure 6.2: Loose coupling integration scheme. Closed-loop architecture. 136
Figure 6.3: Tight coupling integration scheme. Open-loop architecture. 137
Figure 6.4: Tight coupling integration scheme. Closed-loop architecture. 137
Figure 6.5: Hybridisation architecture using external measurements for correction purposes. 138
Figure 6.6: IMU placement with respect to the vehicle. 141
Figure 6.7: Simplified INS mechanisation for land vehicle navigation. 142
Figure 6.8: Integrated Navigation System mechanisation as designed for land vehicle navigation. Closed-loop architecture. 148
Figure 6.9: Reference trajectory (red) and OEM4 position solution (blue). Urban trial. 149
Figure 6.10: Different heading estimates as computed during the urban trial. 150
Figure 6.11: Standalone Inertial Navigation System position solutions using different heading sources. 150
Figure 6.12: INS/GPS position solution using filtered and non-filtered heading. Two Doppler measurements used for hybridisation when available. 151
Figure 6.13: Integrated Navigation System trajectory. 2 Doppler and 2 pseudorange measurements used when available. 152
Figure 6.14: Biased (red) and unbiased (blue) along track velocity profile. 153
Figure 6.15: Two particular velocity profile discontinuities. 153
Figure 6.16: Satellite geometry issue. 154
Figure 6.17: Along track velocity profile corrected by the Inertial Navigation System when bad satellites configurations are detected. 154
Figure 6.18: Corrected and non-corrected Integrated Navigation System trajectories. 2 Doppler measurements used for hybridisation when available. 155
Figure 6.19: Vertical performance of the Integrated Navigation System (upper plot). Vertical profile of the exercised trial (lower plot). 156
Figure 6.20: Static errors of three different inertial navigation algorithms using low-cost sensors. 159
Figure 6.21: Position solutions as provided by three different navigation systems. Short dynamic test. 160
Figure 6.22: PNS position solutions using 100% of GPS data for velocity model calibration. Long dynamic test. 160
Figure 6.23: PNS horizontal RMS error. Long dynamic test. 161
Figure 6.24: PNS position solutions using the first 10% of GPS data for velocity model calibration. Long dynamic test. 161

Figure 6.25: Unconstrained navigation solutions. 162
Figure 6.26: Displacement direction detection result. 163
Figure 6.27: Possible measurement configurations. 169
Figure 6.28: Real time sensor fusion architecture (closed-loop loose coupling architecture). 169
Figure 6.29: Data synchronisation principle. 170
Figure 6.30: Integrated Pedestrian Navigation System. 171
Figure 6.31: Real time Pedestrian Navigation System interface [53]. 171
Figure 6.32: HSGPS tracking performance in urban and indoor environments. 172
Figure 6.33: AGPS tracking performance in urban and indoor environments. 172
Figure 6.34: HSGPS/IMU hybridisation results. 172
Figure 6.35: AGPS/IMU hybridisation results. 172
Figure 6.36: Pedestrian trial inside and outside buildings. AGPS single point position solution (blue) and reference trajectory (yellow outdoors, orange indoors). 173
Figure 6.37: AGPS/IMU hybridisation. Long test. 174
Figure 6.38: GPS measurements availability and regression coefficients (unitless) without variability detection (real time results). 175
Figure 6.39: GPS measurements availability and corrected regression coefficients (unitless) after variability detection (post processing results). 175
Figure 6.40: AGPS/IMU hybridisation results. Long test with corrected regression coefficients (post processing results). 176

List of Tables

Table 1.1 – Applications of MEMS Accelerometers and Gyroscopes in Consumer Products [54]. ... 2
Table 2.1: Light indoor cold start test results. ... 38
Table 2.2: Light indoor tracking test results. ... 38
Table 2.3: Urban street cold start test results ... 39
Table 2.4: Urban street tracking test results. ... 39
Table 3.1: Accelerometer triad turn-on biases and scale factors. ... 55
Table 3.2: Gyroscope triad turn-on biases. ... 56
Table 3.3: Candidate parameters to the pedestrian velocity model. ... 65
Table 3.4: Correlation results. Parameters computed each step. ... 67
Table 3.5: Correlation results. Parameters computed every 2 steps. ... 67
Table 3.6: Cross-correlation coefficients (1 step). ... 68
Table 3.7: Cross-correlation coefficients (2 steps). ... 68
Table 3.8: Distance estimation accuracy – Method 2. ... 71
Table 3.9: Pedestrian mechanisation simulation parameters. ... 78
Table 4.1: Toulouse Earth's magnetic field characteristics (year 2005) [22]. ... 85
Table 4.2: Measurement unit configuration given typical test cases. ... 102
Table 5.1: Number of frequency bins to explore given an initial user's Doppler uncertainty of ±250Hz. Pedestrian navigation case. ... 129
Table 5.2: Number of frequency bins to explore given an initial user's Doppler uncertainty of ±250Hz. Land vehicle navigation case. ... 131
Table 6.1: Typical Allan constants for different types of oscillators (units of seconds) [44]. ... 146
Table 6.2: OEM4 tracking performance in urban environment. ... 149

Abbreviations

AGPS ..... Assisted Global Positioning System
AOA ..... Angle of Arrival
BER ..... Bit Error Rate
BTS ..... Base Transceiver Station
C/A ..... Coarse/Acquisition
CDF ..... Cumulative Density Function
CGI ..... Cell Global Identity
COO ..... Cell of Origin
DCO ..... Digitally Controlled Oscillator
DFT ..... Discrete Fourier Transform
DLL ..... Delay Lock Loop
DoF ..... Degree of Freedom
DOP ..... Dilution of Precision
DSP ..... Digital Signal Processor
EARS ..... Euler's Angles Singularity Resolution
ECEF ..... Earth-Centred Earth-Fixed
ECEF ..... Earth-Centred Earth-Fixed
EKF ..... Extended Kalman Filter
E-OTD ..... Enhanced Observed Time Difference
FFT ..... Fast Fourier Transform
FLL ..... Frequency Lock Loop
GNSS ..... Global Navigation Satellite System
GPS ..... Global Positioning System
GSM ..... Global System for Mobile communications
HDOP ..... Horizontal Dilution of Precision
HSGPS ..... High-Sensitivity Global Positioning System
IF ..... Intermediate Frequency
ILSQ ..... Iterative Least SQuare
IMU ..... Inertial Measurement Unit
INS ..... Inertial Navigation System
ISA ..... Inertial Sensor Assembly
LBS ..... Location Based Services
LMU ..... Location Measurement Unit
LO ..... Local Oscillator
LoS ..... Line of Sight
LSQ ..... Least Square
MEMS ..... Micro Electro Mechanical System
MIM ..... Magnetic Interference Mitigation
MSL ..... Mean Sea Level
OTD .....Observed Time Difference
PDA .....Personal Digital Assistant
PDF .....Probability Density Function
PDR.....Pedestrian Dead-Reckoning
PLL .....Phase Lock Loop
PND .....Personal Navigation Device
PNS .....Personal Navigation System
PPM .....Parts Per Million
PPS.....Precise Positioning Service
PRN.....Pseudo Random Noise
PSD .....Power Spectral Density
RAIM .....Receiver Autonomous Integrity Monitoring
RTD .....Relative Time Difference
SIS.....Signal in Space
SMLC.....Service Mobile Location Center
SNR.....Signal to Noise Ratio
SPS.....Standard Positioning Service
TOA .....Time of Arrival
TTFF .....Time to First Fix
UMTS .....Universal Mobile Telecommunication System
VDOP.....Vertical Dilution of Precision

Chapter 1: Introduction

1.1 Background

Service sets around the location of a mobile, often referred as Location Based Services (LBS), are currently gaining more and more importance in the all day life. First driven by regulation issues under the E911 law dedicated to provide a location mean to the emergency call, many commercial applications or services are available today. Some are aimed at reaching a large public with mass-market perspectives such as in-vehicle or personal navigation, the others focus on specific applications such as fleet management, e-tourism, and location of workers…

Several techniques can be used to enable the location of one user in many environments. Among them, GPS-based techniques are today very attractive due to the great effort made by the industry to miniaturise front-ends and processing cores into one single chipset while increasing both acquisition and tracking sensitivity and availability of the position solution especially in urban environments. Software-based solutions are also taking more and more importance since they offer more flexibility and cost effective means to enable GPS in handsets, even if they require today non negligible computational load. The recent convergence of wireless communication providers and cell-phone industry roadmaps also tremendously accelerate the use of the GPS-based positioning techniques and more specifically Assisted GPS (AGPS). For all these reasons, it seems obvious that satellite-based techniques will become an essential part of seamless positioning systems.

However, GPS-based positioning techniques still encounter issues in indoor areas where users are very likely to go in. The processing of GPS signals is indeed very challenging as the chipsets have to deal with signals of very weak power. Receivers have to use long coherent integration time to reduce the effect of noise and increase the probability of detecting a specific satellite signal, but it makes them very sensitive to local oscillator stability, user's Doppler contribution as well as cross-correlation peaks that might be wrongly considered as a true correlation one (often referred as near far effect). Strong multipath may also affect incoming signals, reducing at the same time the accuracy of the position solution.

As a consequence, even if GPS is a good mean to fulfil the needs of most of location applications, it still encounters big issues in harsh environments. It is therefore very likely in many indoor cases to have a complete interruption of the positioning service. In order to get the position a user whatever his location, alternative systems shall be coupled with GPS. Many exist based on the processing of WIFI, UWB, pseudolites, TV or mobile phone signals, with all different accuracies. However, all the previously mentioned augmentations require infrastructure that can largely be found in urban environments but certainly not in rural areas making indoor location still an issue.

Self-contained augmentations have the advantage of being available wherever the user is. Inertial sensors, and more generally small sensors, are the typical example of self-contained augmentation that does not require any extra infrastructure to give information about the motion experienced by a mobile. As they are currently gaining more and more importance in many products, their use to support or replace GPS inside buildings can be a great opportunity to improve the performance of the positioning system, even if their respective intrinsic performance is somewhat too poor to allow traditional inertial navigation.

1.2 Motivations and Objectives

The efforts of the semiconductor industry to produce small, low consumption and powerful chipsets are bearing fruit for now a couple of years. Today, many portable devices such as PDA or cell phones are now equipped with small GPS chipsets that includes both the RF front-end and the base-band signal processor. This trend is all the more stressed in the sensor industry as the demand is far more important [54]. Automotive industry is currently the leading sector that drives the design and the performance of the mass market sensors, but applications at consumer level are taking more and more importance. Table 1.1 illustrates the recent needs for accelerometer and gyroscope sensors in consumer products according to [54].

Consumer product	Function	Examples of products	MEMS inertial device(s)	Status of commercialisation
Cell phones	Pedometer, image rotation, menu scroll, gaming, free-fall detection (HDD protection), navigation	NTT DoCoMo pedometer (2003) Vodafone image rotation (2004) Samsung SGH E760, Nokia 3230 (navigation and gaming)	2- or 3-axis accelerometer, 1- or 2-axis gyroscope	Accelerometer in cell phone since 2003 Gyroscope expected in 2007–2008
PDA	Navigation IMU, Web content navigation	Toshiba PocketPC e740	2- or 3-axis accelerometer 2-axis gyroscope	Demonstrator in 2002 at Paris PDA show
Digital Still Cameras (DSC)	Image stabilisation	All Panasonic DSCs, e.g. Lumix ($200), Pentax Optio A10 ($350) Canon, Sony DSCs	Two 1-axis gyroscopes or one 2-axis gyroscope Two 2-axis accelerometers	Gyroscope established since late 1990s Accelerometer emerging
Camcorders	Image stabilisation, free-fall detection (HDD protection)	Upper end: Panasonic (over $1500) High end: JVC 30Gb, Toshiba 60Gb	Two 1-axis gyroscopes or one 2-axis gyroscope	Gyroscope established since late 1990s
Laptops	Free fall detection (HDD protection), GPS dead-reckoning assist (anti-theft)	IBM, Toshiba, Apple laptops	2- or 3-axis accelerometer	Free-fall detection established Other applications emerging
MP3 players	Free fall (HDD protection)	iPod with hard disc drive	3-axis accelerometer	Established
Others: toys, games, personal transporter, robots	Realistic motion	Nintendo's Kirby "Tilt-n-Tumble" GameBoy, Microsoft gamepad "Sidewinder Freestyle Pro", Segway, Sony Aibo robot, Sony PS3	2- or 3-axis accelerometers, 1- or 2-axis gyroscopes	Established

Table 1.1 – Applications of MEMS Accelerometers and Gyroscopes in Consumer Products [54].

The use of such sensors is all the more interesting as the sensor industry is constantly improving their integration in small packages while lowering their power consumption. Three-axis accelerometers are now widely available, as for instance [56], as well as three-axis magnetometers [57]. Gyroscopes are more difficult to integrate in a single chip due to the more complex measurement procedure. However, a major integration step has been reached with the recent announcement of mass production of a two-axis low cost gyroscope [55] in a single small die.

At the time this thesis started, the market perspectives of MEMS inertial sensors were obviously not known but somewhat expected due to the increase of their use in consumer products. Furthermore, the packaging of these low-cost sensors was already small enough to make them easily incorporable in Personal Navigation Devices (PND) such as cell phones, PDA even GPS for cars. Studying the pertinence of their use to supply GPS in order to meet LBS requirement was therefore already motivated.

All along the three years this Ph.D. lasted, the MEMS performance and market perspective

evolutions has strengthened the idea that they could represent a cost effective augmentation system. The use of such small sensors in combination with hardware-based or software-based GPS receivers is very likely to become a real low-cost possibility in a quite near future. As a result of these motivations, several objectives were set along this thesis with respect to typical navigation use cases. They all can be summarised in three main categories.

Given a set of low-cost sensors, a first objective was to determine what improvement could be brought in the different inertial navigation algorithms used for land vehicle or pedestrian navigation in order to enhance the navigation systems performance. Several points were of particular interest, and more specifically those listed below:

- The effectiveness of using a pressure sensor.
- The effectiveness of using a triad of magnetometers.
- The possibility of reducing the impact of the typical errors that dramatically affect the inertial navigation systems (gyroscope biases, accelerometer biases).
- The performance of self-contained augmentations based on the set of low-cost sensors.

A second objective was to analyse the feasibility of combining information from the set of low-cost sensors to reduce the HSGPS/AGPS processing core complexity or equivalently computational load when dealing with weak signals. The following points were consequently investigated:

- Improvement of the acquisition stage (especially in cold start mode) within the scope of a software-based receiver.
- Decrease of the Time to First Fix using the external set of low-cost sensors.
- Decrease of the computational load / increase of sensitivity.

Finally, the last objective was to get insights of several hybridisation schemes. The main goal was to improve the position solution availability and accuracy in harsh environments where GPS modules (either HSGPS or AGPS) can not provide accurate and reliable position solutions. The following points were thus addressed:

- Investigation of the feasibility of integrating the set of sensors in handheld devices.
- Improvement of both availability and reliability of the position solution as provided by the integrated navigation system.
- Use of very few GPS measurements to enable the correction of the error affecting the low-cost sensors output.
- Research of criteria to monitor the quality of GPS measurements in the perspective of GPS/INS hybridisation for Pedestrian Navigation System.

1.3 Contributions

The different topics studied in this thesis are detailed throughout the report. Here are summarised the main subjects that were investigated. Some of these points have been published in conferences (papers published are mentioned in the different chapters of this report – see the bibliography for details).

- **Simulation of the performance of a software-based AGPS acquisition stage**. The main goal of this simulation methodology is to assess the performance that can be expected from a software-based AGPS in order to estimate the computational load for a given use case and consequently the acquisition time performance of such a receiver in typical urban / indoor environments.

- **Analysis of the performance of both HSGPS and AGPS in typical urban environments**. This analysis is done through field test trials in real conditions in order to analyse the performance of the Assisted solution with respect to the High Sensitivity one in terms of time to fix and accuracy. In the same time, the position solutions quality is compared to determine which module is more suited to hybridisation with the low-cost sensors.

- **Optimisation of INS algorithms for both land vehicle and pedestrian navigation**. An exhaustive analysis of the mechanisations is provided with a particular focus on the Pedestrian Navigation System (PNS). A detailed analysis of the relationship between parameters computed from the acceleration magnitude and the velocity of the pedestrian is done, aiming at elaborating a simple but reliable model that is used to compensate for accelerometer biases.

- **Euler's angle singularity resolution algorithm**. Within the scope of this thesis and in the particular case of the pedestrian navigation, the possibility of combining a GPS chipset with low-cost sensors in a handheld device is investigated. As a consequence, the Portable Navigation Device (PND) may experience all possible attitudes including those introducing singularity in the computation of the Euler's angles (and so the heading). A specific compensation algorithm is described in the thesis that prevent from using an unreliable heading information caused by pitch angle values of +/-90°, allowing the tracking of the heading of a PND while moved during the walk.

- **Improvement of the heading accuracy**. An attitude filter capable of estimating the gyroscope biases as they occur during the motion is provided in this thesis. The capability of estimating these biases while the unit is in motion is especially addressed and discussed. This filter includes the Euler's angles singularity resolution algorithm mentioned above. It also includes a magnetic mitigation technique that prevents magnetic interferences from dramatically degrading the heading accuracy, especially when the user is nearby iron objects.

- **Tracking of the pedestrian heading with respect to a moving handheld device**. If the PND contains the low-cost sensors that shall be combined with GPS data to provide an integrated navigation system, and because the PND may be handheld while the user is requesting its location, the heading of the PND may differ from that of the user. An algorithm dedicated to keep track of the true pedestrian heading is proposed for medium handset motions.

- **Analysis of the improvement brought by the use of a barometer**. The possibility of using a pressure sensor in order to get absolute or differential altitude measurements is studied to enhance the position solution using less than four GPS measurements. Discussion of the methodology used to incorporate the altitude measurements is also done.

- **Improvement of the GPS acquisition stage**. The processing of attitude and velocity information provided by the sensors assembly is used to estimate the user's Doppler, which consequently allow a reduction of the number of Doppler bins to explore and therefore reduces the acquisition complexity. The capability of the attitude filter to provide sable attitude measurements is tested within this contribution for "on-demand" user's Doppler estimation.

- **Tight integration architecture taking advantage of very few GPS measurements**. Designed for land vehicle application, the proposed tight integration architecture is demonstrated to allow the navigation using only 2 Doppler measurements, but accumulating errors. As soon as 2 pseudoranges are added, the integrated navigation system does not accumulate errors anymore and accuracy within 40m from the reference trajectory is shown possible with low-cost sensors. However, the proposed hybridisation architecture is very sensitive to geometry of the satellite used in the integration filter.

- **Real time low-cost sensors/AGPS (or HSGPS) integrated pedestrian navigation system**. A real time integrated navigation system prototype that fuses MEMS sensors with AGPS (or HSGPS) is developed to ease the characterisation of such a seamless positioning system especially in outdoor to indoor and indoor to outdoor transition phases. Several GPS quality monitoring criteria are proposed and their pertinence is tested on actual data, which demonstrated a 2D error within 10 metres from the reference trajectory even during GPS outage of about 2 minutes.

1.4 Thesis Outline

This thesis report is organised as follows:

Chapter 2 recalls the basics of the GPS positioning techniques and gives insights of current enhancements in the processing core of mass-market receivers such as HSGPS and AGPS. Simulations are done to estimate signal processing performance such as time to fix with respect to typical satellite configurations. Both types of low-cost receivers are tested in urban and indoor environment to assess their respective performances and find the module that gives the best ones.

Chapter 3 introduces the alternative navigation systems based on inertia principles. First the classical Inertial Navigation System (INS) mechanisation is derived in details and its performance relative to the quality of the sensors used within the scope of this thesis is discussed. The particular case of the pedestrian navigation is then addressed in great details and the mechanisation chosen in the thesis is justified. The performance of such a mechanisation is simulated according to several error models and compared to what can be obtained using the classical INS.

Chapter 4 deals with the possible self-contained augmentations that can be implemented in order to improve the performance of the algorithms described in chapter 3. In particular, the addition of a pressure sensor and magnetometers are discussed. Several well-known error limitation principles are recalled. This chapter focuses also on the dynamic estimation of gyroscope drifts and an attitude filter capable of providing stable heading information is proposed. The possibility of mitigating magnetic interferences is also addressed.

Chapter 5 focuses on the improvement of the HSGPS/AGPS processing stage and more specifically on the acquisition stage. The different Doppler contributions affecting the incoming signal are analysed, with more attention paid to that of the user. The possibility of estimating the user's Doppler prior to engage the acquisition process and assuming the unit containing both the GPS chipset and the sensors assembly in motion is then investigated. The sensors fusion algorithm is tested for pedestrian and land vehicle navigations. Both static and dynamic cases are studied.

Chapter 6 addresses more specifically the improvement of the position solution via the

hybridisation of the different navigation systems described in chapter 2 and chapter 3. The land vehicle navigation case is studied through a tight integration scheme which differs from the standard one usually used to fuse GPS and INS. The pedestrian navigation case is addressed through a loose coupling scheme. A real time pedestrian navigation system is developed for that purpose. These different hybridisation algorithms are tested in typical urban conditions and respective performance results are detailed.

Chapter 2: GPS-Based Positioning

This chapter is dedicated to the presentation of the GPS-based positioning technique for personal positioning. In a first part, the GPS fundamentals are recalled and a focus is put on the measurements available at the output of a GPS receiver for further integration with another navigation system and more specifically with an Inertial Navigation System (INS). The main processing stages of a standard GPS receiver are then briefly presented. In a third time, new architectures such as HSGPS and AGPS are discussed. The weakest points of the standard GPS processing are highlighted and solutions implemented in the new processing architectures are described. The performance of each type of positioning method is finally discussed in terms of time to acquire, time to fix and position accuracy. A comparative test between HSGPS and AGPS is also presented in typical indoor environments and the need for augmentations in harsh environment is demonstrated.

2.1 The Global Positioning System

2.1.1 Fundamentals

The Global Positioning System (GPS) is a satellite radionavigation system that can provide any user on Earth at any time with the signals necessary for an accurate determination of its position, velocity as well as the bias of its own clock, independently of weather conditions.

The basic principle of getting its position using GPS relies on range measurement. A user equipped with a receiver computes its location by measuring the delay of propagation of the signals coming from several transmitting satellites. These satellites have a known position, so that once the clock bias of the local receiver oscillator with respect to the satellite transmitter has been solved, these propagation delays can be converted into geometric distance, allowing the resolution of the 2D / 3D user's position. The velocity of the user can also be computed using the rate of change of these propagation delays.

In such a positioning system, timing is a very critical point. Indeed, the satellites are transmitting permanently continuous waveforms (the GPS signal) that are designed to be easily related with a time scale. Transmitters and receivers are aware of the signal characteristics and properties, so that the demodulation of the GPS navigation message is done trough a processing designed to take advantage of the GPS signal modulation. The propagation delay is thus measured by comparing the received signal to a locally generated copy of that signal. However, as the receiver clock is not synchronised with the satellites clocks, the time delay measurement is biased by the clock bias between the receiver and the satellite. Thus, in order to determined that bias, GPS satellites broadcast in their navigation message satellite clocks biases with respect to that reference time. As a consequence, the propagation measurements can be considered to be only biased by the receiver clock bias so that this remaining unknown is just simply added to the three basic unknown user's coordinates. Four satellites are thus at least needed to compute the user's location.

GPS is composed of three segments defined as space, control and user. They all are described in the following subsections.

2.1.1.1 Space Segment

The space segment is the satellite part of the positioning system. It is composed of 24 satellites orbiting in 6 different orbit planes inclined at about 55°, with a radius of about 26600km [1]. The period of revolution of a GPS satellite is 12 sidereal hours, so that the ground track of each satellites is repeated every 24 sidereal hours, that is 23h56min. The satellite payload contains four atomic clocks, two based on Rubidium and two on Caesium, for a precise signal generation. The satellites are currently emitting a signal propagated on two carriers (L1, L2) with the following properties:

- L1 at 1575.42MHz with a QPSK modulation. The in-phase channel is modulated by a known Gold code of length 1023, the C/A code, with a rate of 1.023MHz. The quadrature channel is modulated by a known P code or unknown encrypted version Y code, both clocked at 10.23MHz.
- L2 at 1227.6MHz, with a BPSK modulation of the carrier by the P(Y) code.

C/A codes are widely known so that the service provided through the L1 C/A carrier called Standard Positioning Service (SPS) is accessible by everybody. Opposite, the Precise Positioning Service (PPS) supported by L2 and the quadrature channel at L1 is reserved to US military and their allies since they are the only ones capable of decoding the Y code. The service provided on L2 and L1 with the P(Y) code is not within the scope of this thesis. Consequently, the following will focus on the L1 C/A carrier.

All the satellites use the same frequencies to transmit the GPS navigation message. The generation of the L1 signal is as described below in Figure 2.1. The transmitted signal is the result of the 2-modulo sum of the spreading codes *c* and *p* (or *y*) and the navigation message *d*, which are then QPSK modulated. The spreading code *c* used on GPS modulation is a Gold code, with length N=1023 bits. Its rhythm is larger than the data rate, so that the modulation is a spread spectrum modulation.

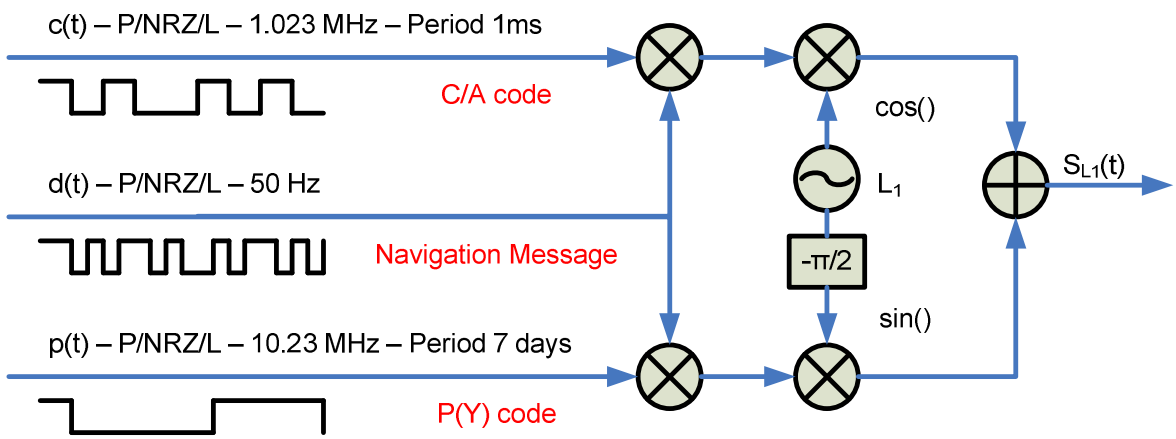

Figure 2.1: GPS L1 signal generation architecture.

The signal transmitted on L1 by the GPS satellite *i* is a combination of the C/A and P(Y) codes, which is 3dBW lower than the C/A component. Omitting the P(Y) component, the GPS L1 signal transmitted by satellite *i* is then as written in equation (2.1):

$$s^i(t) = A \cdot d^i(t) c^i(t) \cos(2\pi L_1 t) \tag{2.1}$$

where:

- d^i is the P/NRZ/L materialisation of the satellite i navigation message at 50 Hz.
- c^i is the P/NRZ/L materialisation of satellite i C/A code at 1,023 MHz.
- m is the P/NRZ/L materialisation waveform.
- A is the amplitude of the C/A component.

It is then straightforward to compute the Power Spectral Density (PSD) of the signal transmitted on L1, according to equation 2.1. The L1 PSD is thus as follows [3]:

$$S_{s^i}(f) = A^2 \cdot S_d(f) \otimes S_c(f) \otimes \left(\frac{\delta(f - L_1) + \delta(f + L_1)}{4} \right) \tag{2.2}$$

where:

- T_c is the spreading code chip period.

- $S_d(f)$ is the PSD of the GPS navigation data.
- $S_c(f)$ is the PSD of the C/A code.
- f_R is the repetition frequency of the spreading code c.

The PSD of the base band C/A component $S_{dc}(f) = S_d(f) \otimes S_c(f)$ is plotted in Figure 2.2. The total bandwidth of the transmitted GPS signal on L1 is larger than 20 MHz. Due to the spreading code properties, the spectrum lies below the noise spectrum.

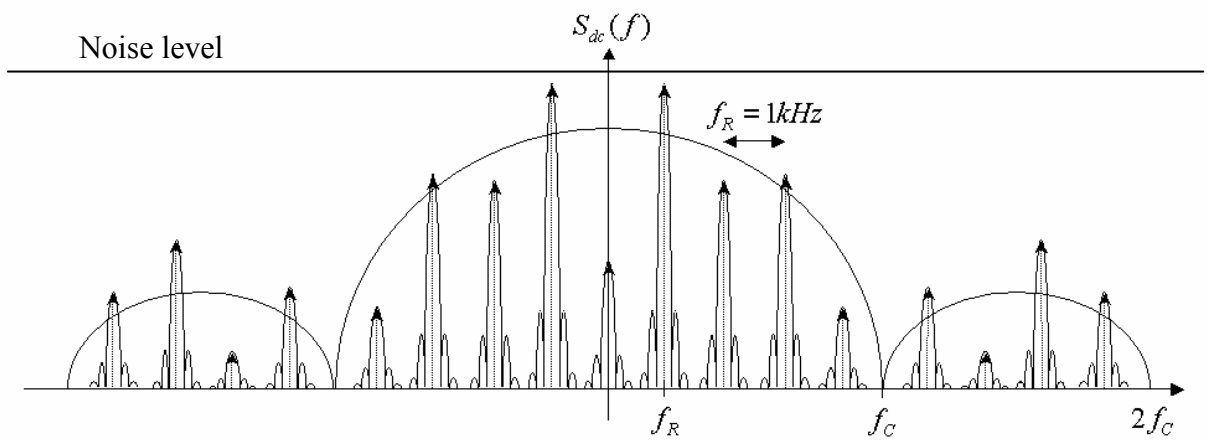

Figure 2.2: Baseband C/A PSD.

2.1.1.2 Control Segment

The role of the control segment is to ensure the surveillance of the received signal characteristics, to compute the ephemeris data and the satellites clock corrections, and to download the navigation message into the satellites payload. The control segment is composed of 5 surveillance stations scattered around the globe, 1 main control station called the Master Control Station (MCS) located in Colorado, 4 download stations. These stations perform normally 1 download per day per satellite, with the possibility to do 3 downloads per day per satellite.

Subframe 1	TLM	HOW	GPS Week Number - Space Vehicle Accuracy and Health - Satellite Clock Correction Terms
Subframe 2	TLM	HOW	Ephemeris Parameters
Subframe 3	TLM	HOW	Ephemeris Parameters
Subframe 4	TLM	HOW	Almanac and Health Data for Satellites 25-32, Special Messages, Satellite Configuration Flags, and Ionospheric and UTC Data
Subframe 5	TLM	HOW	Almanac and Health Data for Satellites 1-24 and Almanac Reference / Time and Week Number

30 bits

300 bits

Figure 2.3: Structure of a GPS frame.

The navigation message generated for each satellite is necessary for the receivers to compute

the position and the velocity of the user. This 50 bits per second data stream is synchronous with the 1 kHz C/A spreading code epochs. The navigation message is periodic. It contains 37500 bits, and thus, lasts 12,5 min. The data is formatted into 30-bits word, and words are grouped into subframes of 10 words. A subframe is then composed of 300 bits, and lasts 6 seconds. Five subframes form a frame. Therefore, a frame is composed of 1500 bits, and lasts 30 seconds. Frames are grouped together, and the 25 frames of 37500 bits compose the navigation message. Figure 2.3 illustrates the navigation message structure.

In the message, much of the data is repeated every frame, and some every subframe. The navigation dataframes are periodically updated, approximately every 2 hours, and are valid for 4 hours. According to the above description, it is clear that without any external aid, the minimum time required for a receiver to incorporate the pseudorange measurements made on a new specific satellite in the position solution is then 30 seconds because satellite clock correction and ephemeris data are repeated in each frame. Details about the messages can be found in [1].

2.1.1.3 User Segment

That segment is composed of the authorised users (military) and non-authorised users (civilians). The receivers can be static on Earth, or mobile in a vehicle on Earth, in an aircraft or a spacecraft. They permanently collect GPS signals and process them to compute the position and velocity of the user. At the input of the receiver's antenna and compared to what is transmitted by the different satellites, the GPS signals are affected by delays accumulated during the different phases of the propagation. At the output of the receiver's antenna, the signal is as follows:

$$r(t) = g(t) \otimes s(t) + w(t) + j(t) \tag{2.3}$$

where:
- g is the pulse response of the propagation channel.
- w is an additive white noise.
- j is the sum of the jammer signals.

Assuming that the propagation channel modifies the received signal such as g is a pure delay ($g(t) = \delta(t-\tau)$), at the output of the receiver's antenna, the complete expression of the continuous signal is then given by equation (2.4):

$$r(t) = \left\{ \sum_{i=1}^{N} \sum_{k=0}^{M^i-1} A_k^i \cdot d^i(t-\tau_k^i) \cdot c^i(t-\tau_k^i) \cdot \cos\left(2\pi L_1 t - \theta_k^i\right) \right\} + j(t) + w(t) \tag{2.4}$$

where:
- A_k^i is the amplitude of the received signal at epoch k. It is time dependent.
- τ_k^i is the propagation delay affecting the received signal at epoch k. It is time dependent.
- θ_k^i is the carrier phase shift, including Doppler effect at first order at epoch k.
- N is the number of received satellite signals.
- M^i is the number of satellite i signal replica due to multipath.

2.1.2 GPS Signal Processing

The main elements of a GPS receiver are illustrated in Figure 2.4. The purpose of the receiver is to make the pseudorange measurements and demodulate the navigation message in order to compute the position of the receiver's antenna. After being digitised, the signal is processed to enable the data demodulation. It first goes through the detection process, i.e. the acquisition stage. Once the signal has been acquired on a specific receiver channel, the tracking of the signal is engaged. DLL are used to track the spreading code phase, whereas PLL (or FLL) are used to track the phase (frequency) of the carrier. Finally, the SIS data are demodulated and processed with the pseudorange measurements to compute the user's location. All these stages are described in the next subsections.

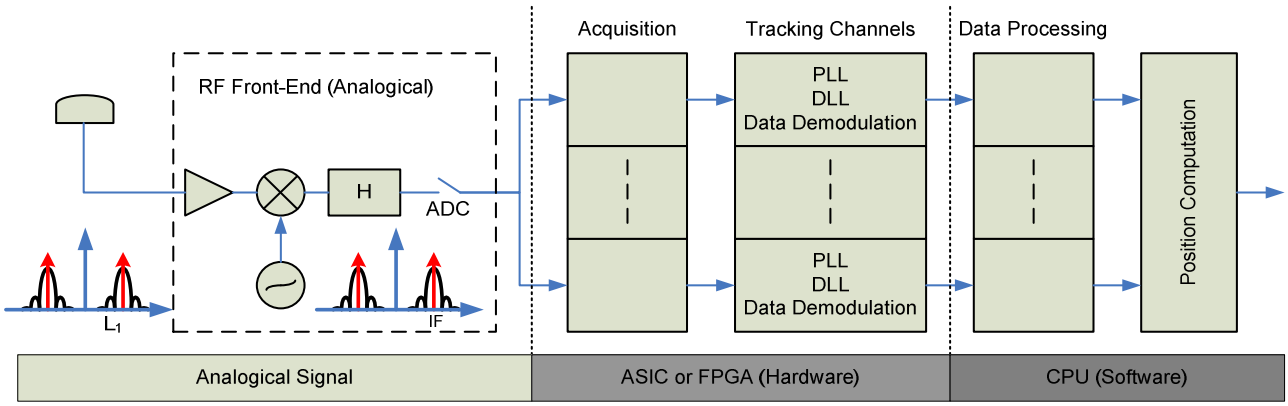

Figure 2.4: General GPS receiver architecture.

As a first approximation and neglecting multipath, interference, and the other GPS satellite signals, the received signal is amplified, filtered and the frequency of modulation L1 reduced to an Intermediate Frequency (IF), as illustrated in Figure 2.4. The digitised received signal at the output of the RF Front-End can thus be modelled as written in equation (2.5).

$$r_f(k) = r_f(kT_e) = Ad(kT_e - \tau_k)c_f(kT_e - \tau_k)\cos\left(\underbrace{2\pi f_I kT_e - \theta(kT_e)}_{\varphi:\ phase\ of\ the\ received\ signal}\right) + n(kT_e) \tag{2.5}$$

where:

- c_f is the result of the filtering of the code modulation of the signal sensed by the user's antenna by the selection filter H.
- f_I is the IF.
- n is a white Gaussian thermal noise with PSD $N_0/2$ dBW.Hz^{-1}.
- θ is the random phase offset affecting the received signal.

Details about the relationship of the phase of the received signal and the Doppler frequency can be found in appendix A. It is just recalled here to clearly show that the GPS processing stages can be based on the processing of the phase θ or the Doppler frequency f_d.

$$\frac{1}{2\pi}\frac{d\varphi}{dt}\bigg|_{t=kT_e} = f_I + f_d(kT_e) \tag{2.6}$$

where:

– f_d is the Doppler frequency affecting the received signal at epoch k.

2.1.2.1 GPS Signal Acquisition

2.1.2.1.1 Principle and General Architecture

The GPS signal acquisition is an energy search process that requires the replication of both code and carrier of the transmitted signal to acquire. Because of the propagation of the emitted signal and the velocity of the satellites relative to the user, the received signal at the input of a GPS receiver is delayed and attenuated. Free space losses, user's antenna pattern and the user's environment (whether he is indoors, in urban canyons or outdoors…) are the main factors responsible for delays and attenuations. In order for the tracking process to be properly initialised, the initial estimates of the code delay τ and the carrier phase shift θ must have a low uncertainty. The goal of the acquisition process is then do determine such values.

This rough estimation is done while the acquisition process tries to detect a GPS signal, i.e. while the acquisition process is searching for the right PRN code used for transmission and needed to demodulate the navigation message. This PRN search is done by exploring all possible PRN codes as well as all possible code and phase shifts by performing correlations with a local generated spreading code replica. Since C/A code are characterised by a high correlation value and low cross-correlation values, the PRN is declared detected once the output of the correlator is higher than a predetermined threshold.

The length of a C/A-code is of 1023 chips so that all the 1023 C/A-code phase bins have to be explored. To be initiated properly, the code tracking loop (DLL) needs roughly a precision of half a chip on the code delay. Thus, the acquisition process explores the code with a half chip step, which is $2\times1023 = 2046$ C/A-code bins.

The phase or Doppler research depends directly on the dynamic of the satellite relative to the user's antenna. According to satellite and user velocities, the Doppler variation lies in the range of ±5 kHz (see appendix A fore more details). This range can be increased to ±6kHz because of the drift of the receiver local oscillator. The true Doppler affecting the received signal is then to be found in that range. The Doppler bin size is directly related to the coherent integration time used in the acquisition process, as demonstrated in [4]. It is equal to half the inverse of the coherent integration time T_p.

The coherent integration time T_p can vary from 1 ms up to the duration of a GPS data bit, that is 20 ms. We define the dwell time τ_d as the product of the coherent integration time T_p by the number of non-coherent integrations M, as given in equation (2.7).

$$\tau_d = MT_p \tag{2.7}$$

The most classical acquisition structure is shown below in Figure 2.5. The output T is used as a test statistic to detect whether the estimated code delay $\hat{\tau}$ and the Doppler shift $\hat{f}_d$ (or the phase shift $\hat{\theta}$) match the true ones or not.

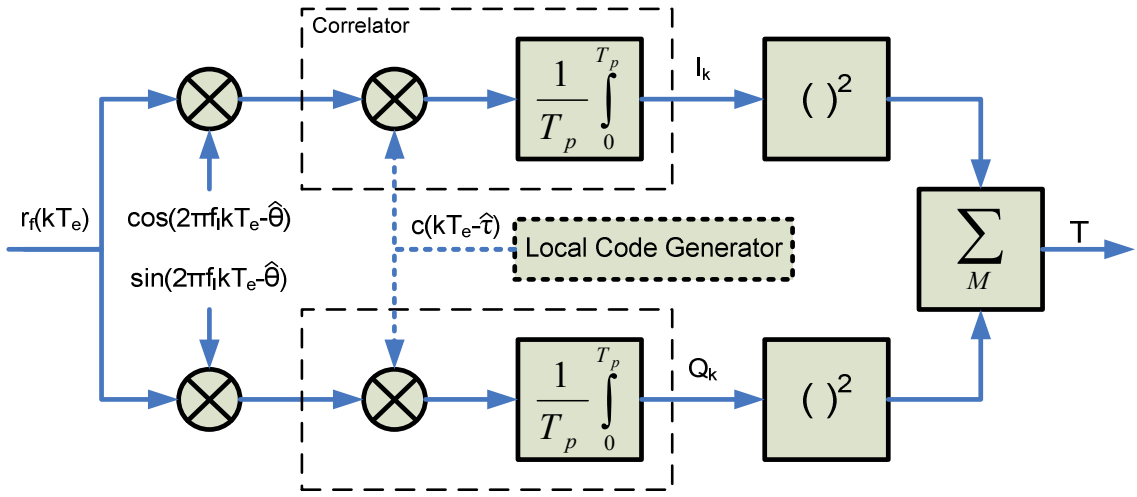

Figure 2.5: Single dwell serial search acquisition structure.

This classical acquisition scheme is called the single dwell serial search acquisition scheme. It is one out of several techniques that can be used to acquire GPS signals, whose basic principle is to perform coherent and non-coherent integrations for a given Doppler/Phase bin and code bin. The signal is first correlated over the coherent integration time T_p, then squared and the process is repeated M times. After a given dwell time τ_d, the output signal T is compared to a decision threshold. If higher, the tracking mode is engaged for certain amount of seconds. If during this period the tracking loops fail to compute an estimation of the code delay and the Doppler/Phase shift yielding a high energy, the search process continues from where it had stopped to switch into tracking mode, incrementing the bins according to the search strategy. If no signal has been detected after exploring the whole uncertainty region, the search process restarts from the beginning, or searches another GPS PRN code.

Assuming some Doppler affects the received signal making the signal phase time dependent, assuming also that no data bit transition while correlating the signal, equations (2.8) and (2.9) give the expressions of the outputs of the correlators for both in-phase and quadrature channels [3]:

$$I_k = \frac{A}{2}\cdot d_k \cdot \left(\frac{\sin(\pi\Delta f T_p)}{\pi\Delta f T_p}\right)\cdot R_{c_f c}(\tau_k-\hat{\tau}_k)\cdot\cos(\theta_k-\hat{\theta}_k)+n_I(k) \tag{2.8}$$

$$Q_k = \frac{A}{2}\cdot d_k \cdot \left(\frac{\sin(\pi\Delta f T_p)}{\pi\Delta f T_p}\right)\cdot R_{c_f c}(\tau_k-\hat{\tau}_k)\cdot\cos(\theta_k-\hat{\theta}_k)+n_Q(k) \tag{2.9}$$

where:

- n_I, n_Q are centred Gaussian noises with power $\sigma^2_{n_I}$ and $\sigma^2_{n_Q}$ respectively. $\sigma^2_{n_I}=\sigma^2_{n_Q}=N_0 f_p/4$
- $R_{c_f c}$ is the cross-correlation between the received filtered spreading code (which has been filtered by the RF front-end filter) and the local replica code.
- $\hat{\tau}$ is the estimation of the group propagation delay.
- $\hat{\theta}$ is the estimation of the received phase shift.
- Δf is the Doppler uncertainty. $\Delta f = f_d - \hat{f}_d$.

2.1.2.1.2 Statistical Hypothesis Test

The detection process of a GPS signal, and thus the rough estimation of the code delay and carrier shift, is based on a statistical hypothesis test. Two basic assumptions can be made on the acquisition status, either the GPS signal to acquire is present at the input of the acquisition channel or not. According to the acquisition structure of Figure 2.5, the output of the acquisition stage T can be written as given follows:

$$T = \sum_{k=1}^{M} \left[I_k^2 + Q_k^2 \right] \tag{2.10}$$

In the absence of the GPS signal to acquire, the test statistic T is equal to T_0:

$$T_0 = \sum_{k=1}^{M} \left[n_I^2(k) + n_Q^2(k) \right] \tag{2.11}$$

Because both n_I and n_Q follow a normal distribution with zero mean and a variance of σ_n^2, they can be re-written as $\sigma_n n'_I$ and $\sigma_n n'_Q$, with n'_I and n'_Q two centred Gaussian random variables with unitary variance. Thanks to Gaussian properties, the squared sum of these new centred Gaussian random variables becomes a new statistic, which follows a Chi-square distribution, with 2M degrees of freedom (M+M). As a consequence, T_0 / σ_n^2 is a random variable following a Chi-square distribution with $2M$ degrees of freedom. Given a probability of false alarm P_{fa} defined as the probability that the statistic T_0 is greater than a predetermined threshold T_h, $P_{fa} = \Pr[T_0 > T_h]$, it is then possible to compute that decision threshold T_h using the inverse of the chi-square cumulative distribution function.

Opposite, in presence of the GPS signal to acquire, the test statistic T becomes:

$$T_1 = \sum_{k=1}^{M} \left[\begin{array}{l} \left(\frac{A}{2} d_k R_{c_f c}(\varepsilon_\tau) \frac{\sin(\pi \Delta f T_p)}{\pi \Delta f T_p} \cos(\varepsilon_\theta) + n_I(k) \right)^2 \\ \qquad + \left(\frac{A}{2} d_k R_{c_f c}(\varepsilon_\tau) \frac{\sin(\pi \Delta f T_p)}{\pi \Delta f T_p} \sin(\varepsilon_\theta) + n_Q(k) \right)^2 \end{array} \right] \tag{2.12}$$

where:

- $\varepsilon_\tau = \tau - \hat{\tau}$ is the residual code delay uncertainty.
- $\varepsilon_\theta = \theta - \hat{\theta}$ is the residual phase shift uncertainty.

Following the same approach as in the previous case, it can be shown that the test statistic T_1 / σ_n^2 follows a non-central Chi-square distribution with 2M degrees of freedom, whose non-centrality parameter is given below in equation (2.13). The probability of successful detection P_d is then defined as $P_d = \Pr[T_1 > T_h]$.

$$\lambda = \mathrm{E}[T_1] = \frac{2M}{f_p}\frac{C}{N_0}R_{c_f c}^2(\varepsilon_\tau)\left(\frac{\sin(\pi\Delta f T_P)}{\pi\Delta f T_P}\right)^2 \tag{2.13}$$

where:

– C is the power of the RF signal. $C = A^2/2$.

2.1.2.1.3 Performance and Mean Acquisition Time

The choice of the coherent and non-coherent integration times is of tremendous importance. The higher the coherent integration time T_p, the lower the decision threshold because the correlator output noise power will be lowered. However, this time can not exceed the GPS data bit duration, which is 20ms. Moreover, selecting a high value for the coherent integration time implies the reduction of the Doppler bin size, thus the increase of the number of frequency bins to explore. As a consequence, the acquisition time needed to successfully detect a GPS signal will increase significantly. The non-coherent integration time has also a great impact on the acquisition performance. It is used to enhance the property of noise power reduction of the coherent integration time (which can not exceed 20ms) but with less efficiency. There is a close relationship between this time and the mean acquisition time through the dwell time τ_d, as it can be seen in equation (2.14) [4]:

$$\overline{T} = \frac{2+(2-P_d)\cdot(q-1)\cdot(1+K\cdot P_{fa})}{2P_d}\tau_d \tag{2.14}$$

where:

– q is the uncertainty region, which is defined as the number of cells to explore to achieve the code acquisition. It is then the product of both the number of code and Doppler bins.
– K is the penalty factor, $K\tau_d$ being the time spent by the tracking loops to try and track a non existing signal.

For both coherent and non-coherent integration times, a trade off has then to be found. As an example, Figure 2.6 illustrates the probability of detecting a signal, assuming no interferences, no residual Doppler effect ($\Delta f = 0$), and no residual code delay uncertainty ($\varepsilon_\tau = 0$). The figure shows clearly that the larger the coherent integration time, the more the signal detection stage will succeed in processing GPS signals with low C/N_0.

One the other hand, this statement has to be balanced with the increase of the acquisition time. Indeed in Figure 2.7 is plotted the mean acquisition time for several couples (M,T_p) so that the dwell time stays always equal to 20ms. For this simulation, a 12 kHz Doppler range has been taken into account, with a Doppler bin of $1/2T_p$, so that the uncertainty region equals $40920000T_p$ cells. The penalty factor has been chosen such as $K\tau_d = 1$s. For a constant dwell time, performances in terms of time to acquire are better with a small coherent integration time and a high non-coherent integration time. These integration times have opposite effects on the performance of the acquisition process. Their tuning has then to be carefully according to the aimed application.

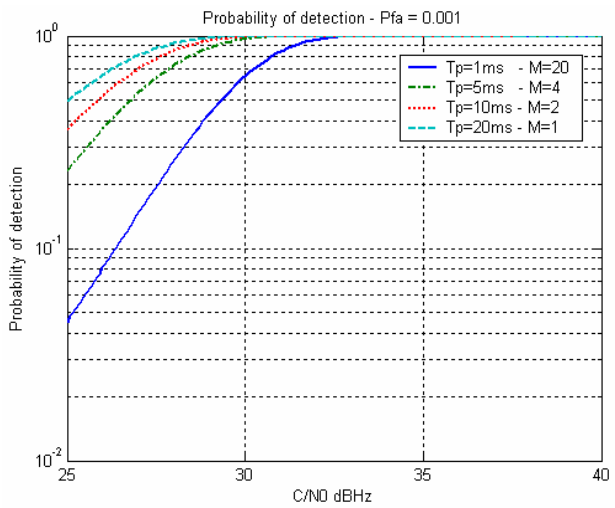

Figure 2.6: Probability of detection for a constant dwell time of 20ms.

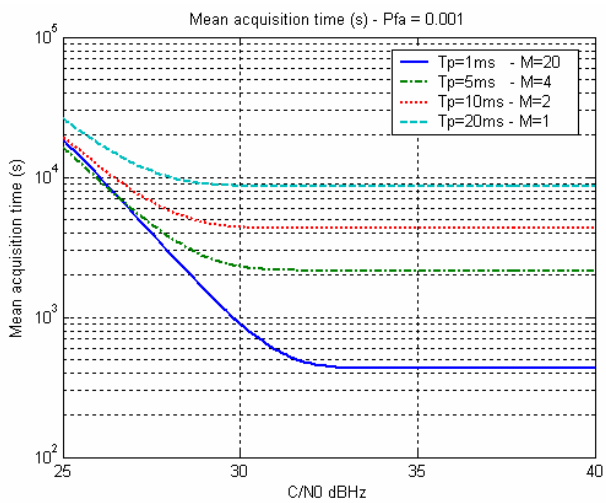

Figure 2.7: Single dwell serial search mean acquisition time for a constant dwell time of 20ms

2.1.2.2 GPS Signal Tracking

To continuously estimate the code delay and the phase shift in order to enable the demodulation of the signal, the tracking of the signal around the initial estimates provided by the acquisition stage has to be done. This tracking is achieved trough the use of two different loops. The first one is the carrier tracking loop (PLL) dedicated to track the carrier phase. A frequency loop can be used instead depending on the receiver's requirements. The second loop is the code tracking loop (DLL), which tracks the code propagation delay affecting the received signal. Both loops are described in the following. Only the basics are presented here.

2.1.2.2.1 Phase Lock Loop

Figure 2.8 illustrates the block diagram of a carrier tracking loop.

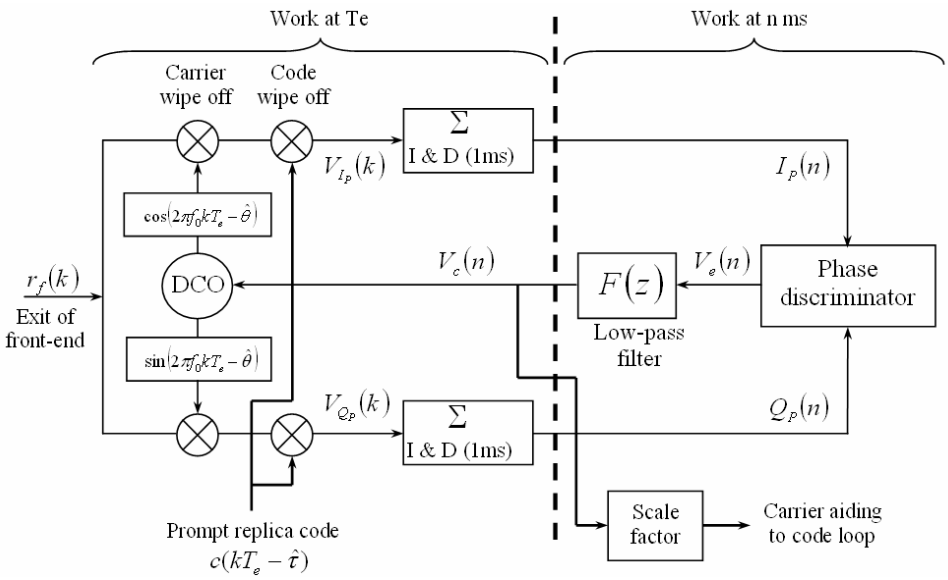

Figure 2.8: Generic Phase Lock Loop architecture [3].

This loop is mainly composed of Integrate and Dump filters, a carrier loop discriminator and a carrier loop filter F. These three components determine also the carrier loop thermal noise error, and the maximum dynamic stress threshold of the loop. The left hand side part of the loop works at the sampling frequency and generally is hardware implemented in the GPS receiver. The right hand side part is software implemented. The software processing rate is generally different from the hardware one, and closely related to the dwell time used in the loop.

The purpose of the PLL is to generate a local carrier, whose phase $\hat{\theta}$ shall be as identical as possible to the one of the received carrier θ. The main difficulty remains in the estimation of the Doppler affecting the received signal. The output of the prompt in-phase channel and prompt quadrature channel are given by the equations (2.8) and (2.9). These two outputs are then processed in a discriminator in order to determine the phase offset between the received and the local phase.

The configuration of the carrier tracking loop depends on the dynamic of the signal to be tracked. Indeed, to tolerate dynamic stress, the pre-detection integration time should be short, the discriminator should be a FLL, and the carrier loop filter bandwidth should be wide. On the other hand, to better resist noise and have accurate Doppler phase measurements, a PLL discriminator should be taken with a long pre-detection integration time and a narrow loop filter noise bandwidth.

The discriminator used in the carrier tracking loop defines the type of loop as PLL, Costas PLL (which is a PLL, whose discriminator tolerates the presence of data bits in the baseband signal) or FLL (Frequency Locked Loop). PLL and Costas PLL are the more accurate, but also more sensitive to the dynamic stress than FLL. Their discriminators output phase errors, whereas FLL discriminator output frequency errors. Most of GPS receivers use a Costas carrier tracking loop because of its insensitiveness to 180-deg phase reversal. Indeed, the 50Hz navigation message, which is composed of "+1/-1" remains after carrier and code have been wiped off.

<u>Product or Costas Discriminator:</u>

The output of the phase discriminator V_e is the result of the multiplication of the prompt in-phase and the quadrature channels, so that V_e is equal to equation (2.15):

$$V_e(n) = I_P(n) \cdot Q_P(n) = \frac{A^2}{8} R_{c_f c}(\varepsilon_\tau) \sin(2\varepsilon_\theta) \left(\frac{\sin(\pi \cdot \Delta f \cdot T_p)}{\pi \cdot \Delta f \cdot T_p} \right)^2 + n_e(n) \tag{2.15}$$

This discriminator is near optimal at low Signal to Noise Ratio (SNR). V_e is a π-periodic signal, so that we can zero the sine without having exactly $\theta = \hat{\theta}$, but rather $\theta = \hat{\theta} + k\pi, k \in \mathrm{Z}$. It emphasizes the fact that the tracking loop can lock on the phase of the received signal with an ambiguity of π. Furthermore, this discriminator depends directly on the power of the received signal. In order to get rid of the signal amplitude, this discriminator is usually normalised. Assuming that the variation between the Doppler shift and the estimated Doppler Δf is small, and considering a small phase tracking error, equation (2.15) can be approximated by equation (2.16) [6], as given below:

$$V_e(n) \approx \varepsilon_\theta + n_e^{'}(n) \tag{2.16}$$

From equation (2.16), it is obvious that to lock the phase loop, the estimated phase and the received phase need to be equal. In the receiver, this is done by zeroing V_e. Indeed, if $V_e > 0$ then the

loop filter F commands the DCO trough the signal V_c to increase the estimate of the phase. Conversely, if $V_e < 0$, then the loop filter commands the DCO to decrease the estimate of the phase. The control signal V_c is the filtering result of V_e through the low-pass filter (or loop filter) F.

The variance of the noise affecting the phase estimate $\hat{\theta}$ is equal to [2] (in rad):

$$\sigma_{\varepsilon_\theta}^2 = \frac{B_L}{C/N_0}\left[1+\frac{1}{2\,C/N_0 \cdot T_c}\right] \tag{2.17}$$

where:

– B_L is the PLL bandwidth.

<u>Arc Tangent Discriminator:</u>

This discriminator is the two quadrant arctangent discriminator. It is optimal in the sense of the maximum likelihood estimator, especially at high and low SNR. It is defined as given in equation (2.18).

$$V_e(n) = \arctan\left(\frac{Q_P(n)}{I_P(n)}\right) \tag{2.18}$$

Given the expression of Q_p and I_p, it is straightforward to expand equation (2.18). At first order, equation (2.18) can be rewritten as equation (2.19). This discriminator does not depend on the signal amplitude itself.

$$V_e(n) = \varepsilon_\theta(n) + n_e(n) \tag{2.19}$$

The variance of the noise affecting the phase estimate $\hat{\theta}$ of the PLL implementing such a discriminator is well approximated by equation (2.17) [2]. As an illustration, Figure 2.9 shows the performance of some PLL discriminators.

It can be seen that the more the discriminator is linear, the better is the correction that is applied on the local generated carrier phase. The figure opposite is plotted under the assumption that no noise is affecting the discriminators. In the case of the presence of additive noise, these plots are flattened.

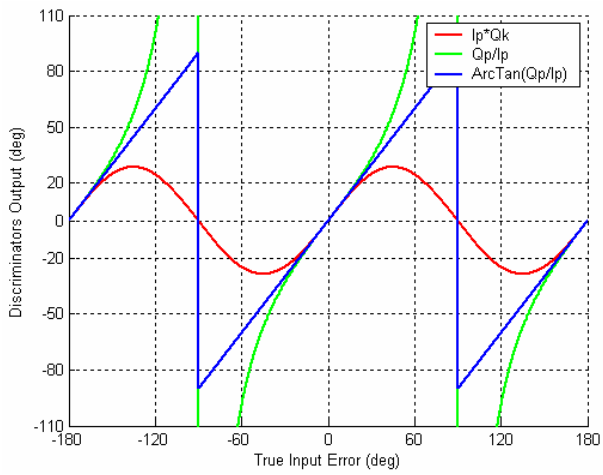

Figure 2.9: Performance of several Costas PLL discriminators.

2.1.2.2.2 Delay Lock Loop

Figure 2.10 illustrates the block diagram of a code tracking loop. This loop requires more

Integrate and Dump filters than the phase tracking loop, since an early and late version of the same PRN code is needed to find the code delay affecting the received signal. As for the phase tracking loop, the left hand side part works at the sampling frequency and is generally hard implemented in the GPS receiver. The right hand side part is soft implemented. The processing rate is generally different from the hard one, and is closely related to the dwell time used in the loop. The discriminator is completely different from the previous ones described above.

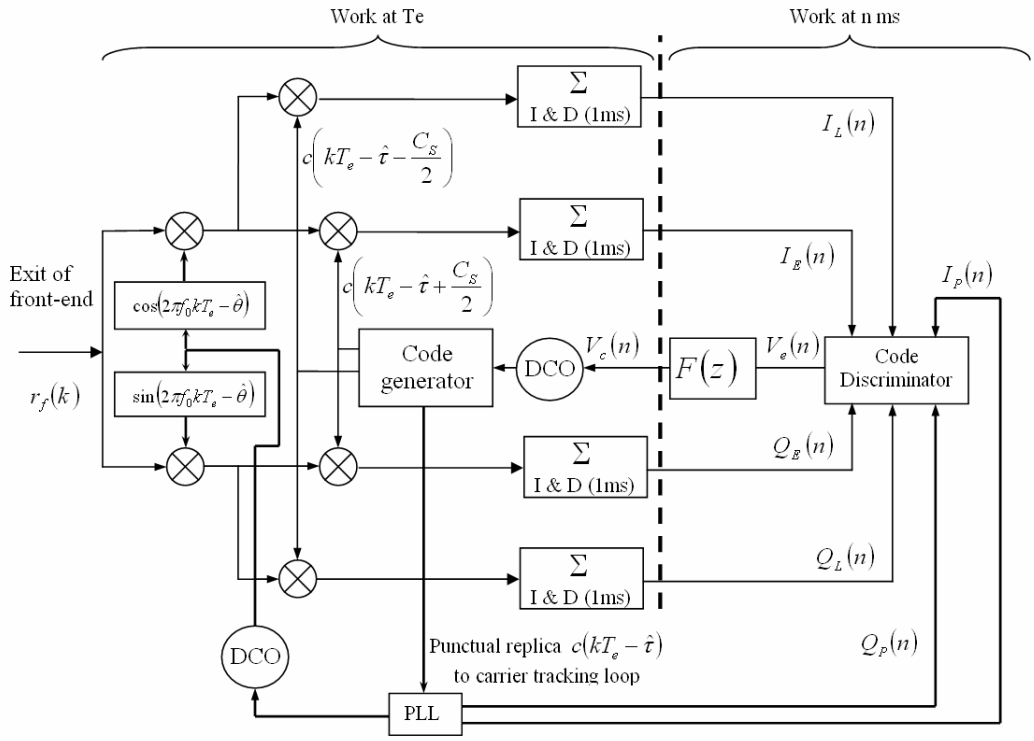

Figure 2.10: Generic Delay Lock Loop architecture [3].

The DLL can be coherent or non-coherent. A DLL is said coherent if it requires a quite accurate estimation of the carrier phase or carrier frequency to work properly. A non-coherent DLL is a loop which can estimate the code delay without having a good estimation of the phase shift or frequency shift. According to Figure 2.10, the signals in the in-phase (I) and quadrature (Q) Early and Late channels are given respectively in equations (2.20) and (2.21).

$$\begin{cases} I_E(n) = \frac{A}{2} d_n R_{c_f c}\left(\varepsilon_\tau + \frac{C_s}{2}\right)\left(\frac{\sin(\pi \Delta f T_p)}{\pi \Delta f T_p}\right)\cos(\varepsilon_\theta) + n_{I_E}(n) \\ I_L(n) = \frac{A}{2} d_n R_{c_f c}\left(\varepsilon_\tau - \frac{C_s}{2}\right)\left(\frac{\sin(\pi \Delta f T_p)}{\pi \Delta f T_p}\right)\cos(\varepsilon_\theta) + n_{I_L}(n) \end{cases} \tag{2.20}$$

$$\begin{cases} Q_E(n) = \frac{A}{2} d_n R_{c_f c}\left(\varepsilon_\tau + \frac{C_s}{2}\right)\left(\frac{\sin(\pi \Delta f T_p)}{\pi \Delta f T_p}\right)\sin(\varepsilon_\theta) + n_{Q_E}(n) \\ Q_L(n) = \frac{A}{2} d_n R_{c_f c}\left(\varepsilon_\tau - \frac{C_s}{2}\right)\left(\frac{\sin(\pi \Delta f T_p)}{\pi \Delta f T_p}\right)\sin(\varepsilon_\theta) + n_{Q_L}(n) \end{cases} \tag{2.21}$$

where:
– C_s is the chip spacing between Early and Late channels. $C_s < 2$.

Early Minus Late Power Discriminator:

The Early minus Late Power discriminator is defined has follows:

$$V_e(n) = I_E^2(n) + Q_E^2(n) - I_L^2(n) - Q_L^2(n) \tag{2.22}$$

As a first approximation, it is here again assumed that the cross-correlation between the filtered code and the local generated code equals the autocorrelation of the code ($R_{c_f c} \approx R_c$). It is also assumed that the Doppler frequency residual Δf is small. At the end of the acquisition process, the propagation delay tracking error ε_τ can be considered low enough to have $|\varepsilon_\tau| < C_s/2$ (a basic value of chip spacing C_s is T_c, some narrow correlators have chip spacings of $0.1T_c$). As a consequence, the error signal V_e can be approximated by equation (2.23) [6]:

$$V_e(n) \approx -\frac{A^2}{2} \cdot \frac{\varepsilon_\tau}{T_c}\left(2 - \frac{C_S}{T_c}\right) + n_e(n) \tag{2.23}$$

The error signal V_e is independent from the phase tracking error ε_θ, so that this discriminator is said to be non-coherent. However, the error signal V_e depends on the signal power. Therefore, the use of the normalised Early minus Late Power is often preferred.

The variance of the noise affecting the code delay estimate $\hat{\tau}$ of a DLL using this discriminator is given by equation (2.24), [2] (in chips):

$$\sigma_{\varepsilon_\tau}^2 = \frac{B_L C_s}{2C/N_0}\left(1 + \frac{2}{(2 - C_s)C/N_0 \cdot T_c}\right) \tag{2.24}$$

Dot Product Discriminator:

This discriminator uses all the three code replicas of the in-phase and quadrature channels. It is defined as given in equation (2.25):

$$V_e(n) = (I_E(n) - I_L(n)) \cdot I_P(n) + (Q_E(n) - Q_L(n)) \cdot Q_P(n) \tag{2.25}$$

Again, assuming $R_{c_f c} \approx R_c$ and $|\varepsilon_\tau| < C_s/2$, the output of the discriminator is given by:

$$V_e(n) = -\frac{A^2}{4} \cdot \left[1 - \frac{|\varepsilon_\tau|}{T_c}\right] \cdot \left(-\frac{2\varepsilon_\tau}{T_c}\right) + n_e(n) \tag{2.26}$$

Equation (2.26) is not linear, not normalised but is independent from the phase tracking error, so that it is a non-coherent discriminator. Once linearised and normalised, it represents the most popular DLL discriminator. The variance of the noise affecting the code delay estimate $\hat{\tau}$ is

given in equation (2.27) in unit of chips. Compared to the previous one of equation (2.24), it is obvious that for signals with low C/N_0, this kind of DLL is less affected by noise.

$$\sigma_{\varepsilon_\tau}^2 = \frac{B_L C_s}{2C/N_0}\left(1+\frac{1}{C/N_0 \cdot T_c}\right) \tag{2.27}$$

2.1.3 GPS Measurements

The basic GPS principle and the main processing stages of a GPS receiver have been described. This section deals with the measurements that are used to compute the location of the receiver's antenna. Basically, one civilian user can process three measurements by satellite to get its position: the code phase, or pseudorange, the carrier phase and the Doppler. The carrier phase measurements offer the best accuracy (centimetre-level) when used to compute the user's location compared with pseudoranges. It is however a more complex processing implementation that requires a rover and a master receiver to process data differentially, and at least 5 satellites in order to remove the phase ambiguity. It is typically used in high-accuracy application such as geodetic surveying. It does not cover the scope of this thesis, so that no further details are given about it in the following. Many references are available on this topic, as for example [7]. The next subsections describe the measurements that are used in this thesis and detail their respective models.

2.1.3.1 Pseudorange Measurement

As discussed in the above section, GPS receivers measure the propagation time of the transmitted signal from the satellite to the user, taking into account the fact that both user and satellite clocks are not accurate and not synchronised. This propagation time once multiplied by the velocity of light represents an apparent distance, which is called pseudorange. The pseudorange to satellite i is thus the true range between the receiver's antenna and the satellite's antenna, plus the offset between receiver and satellite clock converted into distance. The general pseudorange model is given in equation (2.28) [3]:

$$\rho^i = c(t_u - t_s^i) + cb_u + \Delta D^i - c\Delta b^i + c\left(\Delta T^i + \Delta I^i + \Delta v^i\right) + \mu + n_\rho \tag{2.28}$$

where:

- t_u is the user time at time of reception (s).
- b_u is the user clock bias (s).
  $t_u' = t_u + b_u$ is thus the actual user clock time at time of reception.
- t_s^i is the time of transmission of the ith satellite (s).
- Δb^i is the ith satellite clock bias (s).
  $t_s^{i\prime} = t_s^i + \Delta b^i$ is thus the actual satellite clock reading.
- ΔD^i is the ith satellite position bias error effect on range (m). This term has to be taken into account if the position of the satellites is modelled with some error.
- ΔT^i is the tropospheric delay regarding satellite i (s).
- ΔI^i is the ionospheric delay regarding satellite i (s).
- Δv^i is the relativistic time correction for satellite i (s), usually negligible.

- μ is the multipath affecting the measurement (m).
- n_ρ is the noise affecting the pseudorange measurement (m).
- c is the velocity of light. c=299792458 m/s.

All the above errors terms will be briefly discussed in the next section. For practical considerations, the measured pseudorange of equation (2.28) can be rewritten as equation (2.29).

$$y^i = \sqrt{\left(x_u - x_s^i\right)^2 + \left(y_u - y_s^i\right)^2 + \left(z_u - z_s^i\right)^2} + cb_u + e^i \tag{2.29}$$

- y^i is the pseudorange to satellite i at time of reception.
- x_u, y_u, z_u are the user position in ECEF coordinates.
- x_s^i, y_s^i, z_s^i are the satellite position in ECEF coordinates.
- e^i is the vector containing all the residual errors affecting the measurement of the geometric distance (except receiver clock bias) after correction using double frequency measurements or models involving data transmitted in the navigation message.

The the computation of the user's position requires at least four satellite pseudoranges. The unknowns are the user's coordinate and the receiver's clock bias. Since pseudoranges involve the position of the user, they are well suited for correction purposes if used as a reference with another navigation system.

2.1.3.2 Doppler Measurement

The Doppler frequency is closely related to the instantaneous rate of change of the received carrier phase. It is usually measured in L1 cycles per second (Hz). The model used in the following is given below through equations (2.30) and (2.31).

$$f_d^{r,i} = -\frac{L_1}{c} \cdot \left[c\left(\dot{t}_u - \dot{t}_s^i\right) + c\dot{b}_u + \Delta\dot{D}^i - c\Delta\dot{b}^i + c\left(\Delta\dot{T}^i - \Delta\dot{I}^i + \Delta\dot{v}^i\right) + \dot{\mu} + n_{\dot{\rho}}\right] \tag{2.30}$$

where:
- $f_d^{r,i}$ is the Doppler affecting the received signal and measured by the GPS receiver (Hz).
- $\cdot$ is the time derivative operator.

As for pseudorange measurements, the errors terms can be regrouped into one single noise term so that equation (2.30) can be rewritten as follows:

$$f_d^{r,i} = f_d^{user} + f_d^{satellite} + f_d^{LO} + n_f \tag{2.31}$$

where:
- f_d^{LO} is Local Oscillator's Doppler contribution (Hz).
- f_d^{user} is the user's Doppler contribution (Hz).
- $f_d^{satellite}$ is the satellite's Doppler contribution (Hz).
- n_f is the overall noise affecting the measurement (Hz).

These Doppler measurements can be used as a reference in order to correct any velocity error of another navigation system.

2.1.3.3 Carrier Phase Measurement

Another measurement that can be used to compute the position of the receiver's antenna is the phase of the incoming carrier. The geometric distance from the satellite to the receiver's antenna is then the number of cycles the carrier has done when propagating. As a carrier cycle is about 20 centimetres at GPS L_1, the positioning using such a measurement provides a much better accuracy than the positioning using pseudorange measurements, the counterpart being a more complex data processing. Phase measurements are provided by the PLL. The general model is as follows:

$$\varphi = \sqrt{(x_{user} - x_{sat})^2 + (y_{user} - y_{sat})^2 + (z_{user} - z_{sat})^2} + c \cdot (b_{user} - b_{sat}) - \Delta I + \Delta T + \mu_\varphi + N \cdot \lambda + n_\varphi$$

where:
- φ is the carrier phase (in metre).
- μ_φ is the multipath contribution affecting the carrier phase measurement (0-λ/4 metre).
- N is the carrier phase ambiguity (random number).
- λ is the carrier phase wavelength.
- n_φ is the noise affecting the carrier phase measurement (≈ 1 millimetre).

Carrier phase measurements will not be used in this thesis.

2.1.4 Measurement Errors

2.1.4.1 Satellite Orbital Error ΔD

The satellite orbital errors are the discrepancies between the true satellite positions and the positions that are computed by the user's receivers. The prediction of the orbit is modelled and sent as part of the navigation message [1]. Although the satellite orbits are monitored continuously, the accuracy of the satellite position prediction model in the navigation message is limited because of the accuracy of the orbit model and the number of orbital parameters to upload per day per satellite. The error on the computed satellite position translates into an equivalent measurement error. That equivalent measurement error is equal to the projection of the user-to-satellite position error on the satellite Line-of-Sight (LoS). Therefore, that error is bounded by the satellite position error. It is usually limited to a few metres in a nominal mode.

2.1.4.2 Ionospheric Error ΔI

The ionosphere is the layer extending from the altitude of about 50 km to about 1000 km. It is composed of free electrons and ions, whose physical properties change widely between day and night [8]. The free electrons disturb the refractive indices of the various layers of the ionosphere, affecting in the same time the propagation of the GPS signals (change in propagation velocity [9]). When using double frequencies measurements, the ionospheric error can be almost completely removed (not in the scope of this thesis). To reduce the error due to the propagation through the ionosphere, special algorithms have to be used, as for example the Klobuchar algorithm. This algorithm requires coefficients that are transmitted in the navigation message in order to remove

nearly 50% of the ionospheric error [1]. In a nominal mode, the typical ionospheric error is within 0 to 50m.

2.1.4.3 Tropospheric Error ΔT

The troposphere is the neutral region of the Earth's atmosphere extending from the Earth's surface up an altitude of 50 km. The propagation delay introduced by the troposphere has a wet component and a dry component [9]. The dry component is responsible for about 90 % of the whole error and can be well predicted. The wet component is far more difficult to estimate because vapour density vary with the local weather. The typical tropospheric error is within 2-30m. There are many models to correct the tropospheric error. It has to be computed by the user, because no information is transmitted trough the navigation message. One simple model that is often used is the Hopfield model [59], [12].

2.1.4.4 Multipath μ

Multipath refers to the phenomenon of a signal reaching an antenna via two or more paths along with the direct Line-of-Sight GPS signal. It generally occurs when the user is near tall building, inside buildings, under trees… Its mitigation is very hard to completely achieve. Multipath can introduce negative and positive error on the pseudorange measurement depending on the phase of the multipath signal. The position solution accuracy may be very affected by such error, especially in urban environments. In a nominal mode, this error is bounded by ±150m [2]. For non-LoS signals, often called echo-only signals, this error is much greater than the previous one. As discussed in [10], it depends on the reflected signal geometry. Several techniques have been developed for mitigating multipath based on the design of the receiver but also the antenna. One of the most effective techniques based on the design of receiver architecture is the Narrow Correlator technique [11], which is extensively used.

2.1.4.5 Time Synchronisation Δb

Even if high accuracy clocks are used to generate GPS signals on board, the satellite clocks are affected by some drift. The clock correction for each satellite clock is transmitted in the navigation message. It is composed of several parameters that represent a second-order polynomial in time [1]. Taking also into account some relativistic effects and the group delay [1], the error introduced by satellite clock bias can be reduced to only 0.1m.

2.1.4.6 Tracking Loops Jitter

As discussed above, the tracking loops, namely PLL (or FLL) and DLL continuously estimate the carrier phase shift (or Doppler) and the code delay. Given the discriminator used in the loops, the standard deviation of the estimations may vary but whatever its type, the tracking process introduces noise on the phase shift and code delay measurements, which consequently increases at some extend the error on the pseudorange. Expressions of phase (PLL) and code (DLL) jitters due to thermal noise are given in section 2.1.2.2.

2.2 GPS Processing Enhancement

2.2.1 Positioning Technologies and Issues

The GPS is part of a series of complementary location solutions. Indeed various positioning technologies have been developed for GSM/EDGE & UMTS applications in order to enable the localisation of one person.

The Cell-Id (Cell Identity) also called COO (Cell of Origin) or CGI (Cell Global Identity) is the simplest network-based technology. The network based solutions rely only on intrinsic capabilities of the network such as the identity of the originating cell for the standard Cell-Id technology. Several other techniques are deduced from it. It is the case for Cell Id + timing advance for instance. This technique involves the timing advance measurement giving information of the distance separating the user from the BTS. Cell Id ++ is also a derivation from Cell-Id. It adds a measurement of signal strength viewed from several adjacent cells (called NMR techniques). The performances of such methods depend on the density of the cells. It can be between 100m to several kilometres.

The Time of Arrival (TOA) and Angle of Arrival (AOA) are network-based positioning technologies. Both are up-link methods where a known signal is sent by the mobile and received by three or more BTS equipped with Location Measurement Units (LMU). The Cell-Ids, TOA values and TOA measurement quality are returned to the Service Mobile Location Center (SMLC) where a hyperbolic triangulation is performed by using a Positioning Calculation Function (PCF), based on the known Relative Time Difference (RTD) and the BTS positions. The TOA method is standardised, the available standards are within GSM TS 03.71, under ETSI 101 724. It is to be noted that the BTS are not synchronised in the GSM architecture. One of a key role of the LMU is to manage the synchronisation with an external system, typically GPS. The performances are within 50m to 100m, with non negligible difficulties to enable the 3D location of the user.

The Enhanced Observed Time Difference (E-OTD) technology is one of the various handset-based technologies. It is a down-link method where the handset measures the relative time of arrival of the signals transmitted by at least 3 BTS: this difference is called Observed Time Difference (OTD) and allows triangulation computation. It is the opposite of the TOA. It is also standardised. The performances and the limitation are quite identical to the TOA.

All these solutions are complementary and each solution is more suited to the requirements of a given application. But they all involve some extra infrastructure making some solution not cost effective, and the accuracy of the position solution is medium. GPS, and even more GNSS, is more adapted to applications requiring precise positioning. It also requires no extra infrastructure but a chipset to decode and process GPS signals. As a consequence, this makes it very suitable to fulfil the location requirements of applications such as:

- Emergency services: E911, E112, guidance of rescue teams etc…
- Tracking services: fleet tracking, dangerous goods, worker safety…
- Billing: variable billing depending on the location of the user, tailoring billing etc…
- Navigation services: information to find a given destination, real time traffic information

Nevertheless, the technique has limitations due to errors that affect the incoming signals. Indeed, such Location Based Services are likely to be deployed in urban areas. High multipath may affect the signals contributing to a high position bias. Moreover, GPS signals may be blocked or

faded by buildings, which consequently will decrease the availability of the positioning service. Improvements are thus needed.

2.2.2 High Sensitivity GPS

2.2.2.1 Principle

To deal with weak GPS signals, new techniques have been developed since now several years. As discussed in the above section dealing with the GPS processing core, the noise power affecting the incoming GPS signal is reduced after the correlation with a local replica of the spreading code to detect. For a given integration duration, the higher the coherent integration time, the better the reduction of the noise power at the output of the correlator, i.e. the higher the probability of detection (see Figure 2.6).

To enhance the sensitivity and thus the availability of the position solution using GPS, High Sensitivity techniques based on the use of long integration times have been developed [13], [14]. The processing gain is tremendously increased with such long coherent / non-coherent integration times so that the processing of signal with power as low as -188 dBW is possible, as done with current HS chipset (see for instance [23] or [24]).

One of the main drawbacks of such technique is the computational burden that tremendously increases for a typical 12 channels receiver trying to process weak GPS signals. As shown in Figure 2.11, the acquisition of signals with very low C/N_0 (let say below 25dBHz) requires long dwell time. As a consequence, the time needed to successfully acquire such signals dramatically increases, as shown in Figure 2.12 for the typical single dwell serial search technique. Computation resources are also needed to fight heavy multipath and cross-correlations that affect the incoming signals.

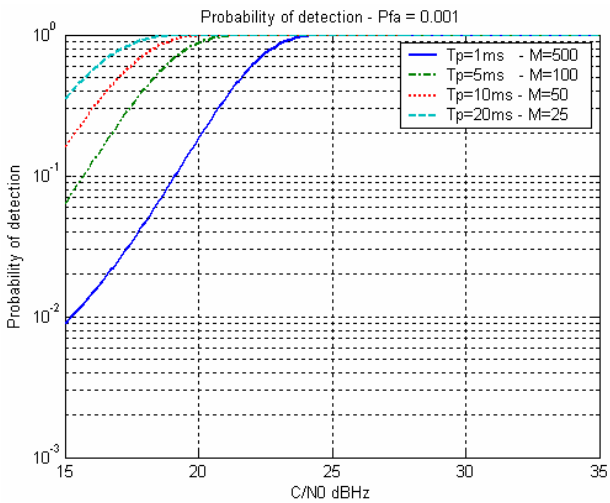

Figure 2.11: Single dwell serial search probability of detection for a constant dwell time of 500ms.

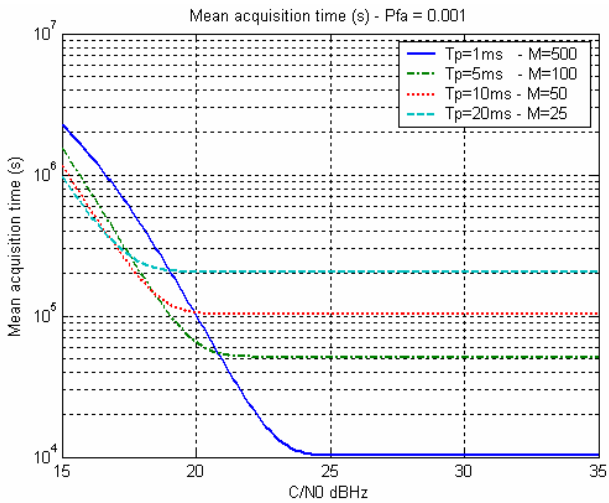

Figure 2.12: Single dwell serial search mean acquisition time for a constant dwell time of 500ms

To face the increase of the computational load due to the processing of signals with very weak power, two techniques are mainly used. The first one handles the computational issue by integrating hundred thousands correlator in a single die [15]. The massive correlation capabilities of such hardware designed HSGPS receiver allow the navigation in light indoor-like environments as well as in most of urban streets.

The second technique is rather based on a software implementation of the correlation process. To reduce the acquisition time, a technique based on the Wiener-Kinchtine relation and basic Fast Fourier Transform (FFT) is used. Instead of having a coherent integrator where the spreading codes are correlated, the new method based on FFT performs directly the correlations for all code bins at once. To compute the cross-correlation, we need at least one period samples of the spreading code. If not, only partial correlation can be computed, which decreases the performances. Since the spreading code is periodic with period N, the cross-correlation is also periodic with the same period. It is then possible to express the cross-correlation function of the spreading code as a function of Discrete Fourier Transforms (DFT). The digital cross-correlation function of a spreading code can be written as given in equation (2.32).

$$R_c(m) = \frac{1}{N}\sum_{n=0}^{N-1} c(n)c(n-m) \tag{2.32}$$

where:

- $c(n) = \frac{1}{N}\sum_{k=0}^{N-1} C(k)e^{i2\pi\frac{kn}{N}}$
- N is the period of the C/A spreading code (1ms).

The cross-correlation of the spreading code is thus as given in equation (2.33):

$$R_c(m) = \frac{1}{N}\sum_{k=0}^{N-1}\sum_{l=0}^{N-1}\frac{1}{N^2}C(k)C(l)e^{-i2\pi\frac{lm}{N}}\sum_{n=0}^{N-1}e^{i2\pi\frac{(k+l)n}{N}} \tag{2.33}$$

Given the fact that the sum of complex exponentials is equal to zero if $k+l$ is different from zero, the cross-correlation of the spreading code is thus as follows:

$$R_c(m) = \frac{1}{N^2}\sum_{k=0}^{N-1} C(k)C(-k)e^{i2\pi\frac{km}{N}} = \frac{1}{N}DFT^{-1}\left[DFT[c(n)]\cdot\overline{DFT[c(n)]}\right] \tag{2.34}$$

where:

- $\overline{DFT[c(n)]}$ is the complex conjugate of the DFT of the spreading code.

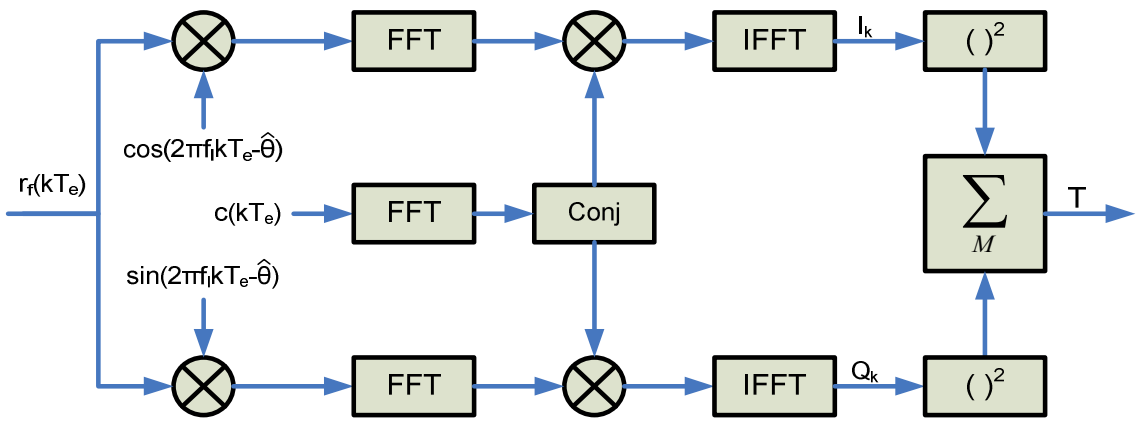

Figure 2.13: FFT-based acquisition scheme.

Once the received signal has been cumulated over T_p seconds, the FFT process is engaged to

compute the correlation between the incoming signal and the locally generated spreading code. Since T_p equals at least the period of the spreading code, we obtained after one processing the cross-correlation function over the coherent integration time T_p for a given Doppler shift. The basic scheme of an FFT acquisition structure is shown below in Figure 2.13.

2.2.2.2 Performance Overview

Even with the increase of correlation computation capabilities, the sensitivity of HSGPS found its limitation in the tracking of weak signals. Once the signal is acquired, the time and the frequency shall indeed be tracked and the navigation data have to be retrieved. The most prone to difficulties steps are on the one hand the carrier phase tracking for sensitivity purposes and on the other hand the data demodulation for sensitivity reasons as well but also for Time to First Fix.

The first limitation is the phase tracking. The jitter of a typical Costas PLL applied to a GPS L1 signal is given in equation (2.17). Given the typical use case of a tracking loop bandwidth of 20Hz and an integration time of 20ms, the 3-sigma tracking jitter is represented in Figure 2.14. A good rule of thumb for such a tracking loop is that the 3-sigma jitter shall not exceed 45° to keep the loop locked. This yields the working threshold of such a PLL to be approximately 25dBHz. As a consequence, the carrier phase tracking of signal weaker than 25dBHz is not possible. HSGPS performs then code-only tracking.

The second limitation comes from the demodulation of the data. To be able to compute a position, the receiver shall demodulate a number of absolutely necessary data such satellite ephemeris, satellite clock corrections, handover word (HOW), ionosphere corrections (even if it is not absolutely necessary if we can tolerate an error of several metres). This limitation is also twofold. First, for a functioning point of view, where the probability of making no error on the demodulation of the ephemeris/clock block is higher than 0.9 (i.e. with a very low Bit Error Rate), the minimum required signal to noise ratio is 25dBHz, as shown in Figure 2.15. Second, the TTFF is at least 30 seconds since the ephemeris and the clock block are broadcast every 30 seconds, as it was explained in a previous section.

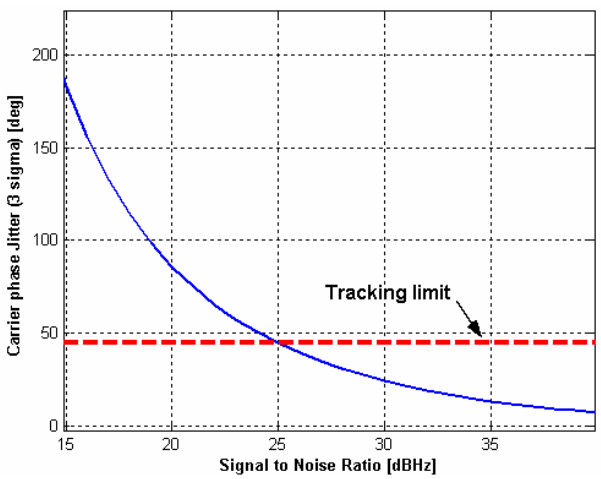

Figure 2.14: Costas Phase Lock Loop tracking performance.

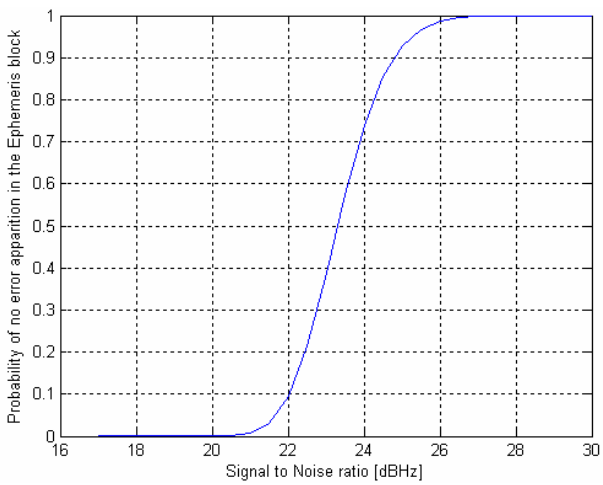

Figure 2.15: Probability of no error (BER of 0) in the demodulation of the ephemeris/clock block (White Gaussian Noise Channel).

An overview of the performance that can be achieved with a HSGPS receiver is shown opposite. In this test, a HSGPS SiRF Star III based receiver was put on the dashboard of a car. In the same time, a geodetic grade GPS receiver OEM4 from Novatel was also embedded with its own antenna set outside the vehicle. The test took place in a residential area of Toulouse with medium buildings and streets bordered with trees. The OEM4 position solution is clearly not relevant of the true trajectory followed during the test (shown in grey). Opposite, the red path of the HSGPS position solution is far more relevant of the true trajectory, even if in some areas large multipath affect the solution. The HSGPS outperforms the geodetic grade receiver in such urban environment.

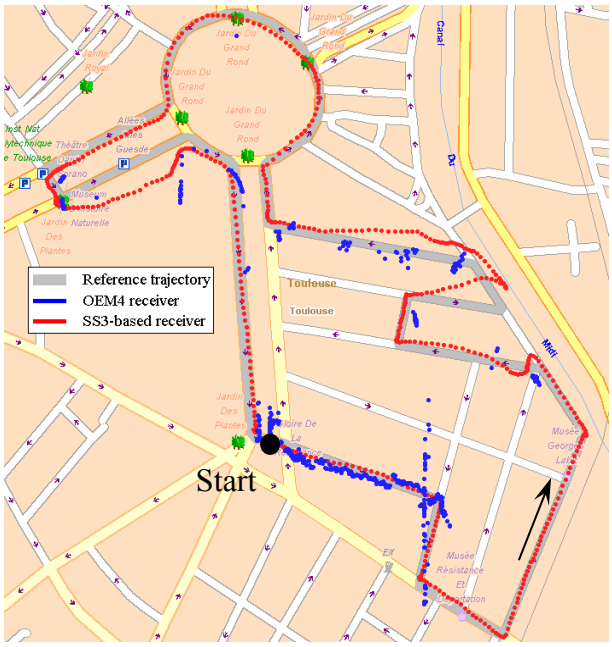

Figure 2.16: Comparative navigation test in urban environment.

2.2.3 Assisted GPS

2.2.3.1 Principle

The Assisted GPS (AGPS) technology appeared in recent years and represents a key turning point. It stands indeed for the technology which paves the way for mass-market-location-oriented applications. The great success of such a technology finds its origins in a powerful hybridisation between a world wide location means – GPS – and a mass market communications means – GSM/UMTS. AGPS is a break-even technology since it significantly compensates the major difficulties encountered when processing weak signals using High Sensitivity techniques.

AGPS is a positioning system sharing the same processing core as HSGPS, but using external sources to help the receiver to perform ranging measurements and position computation. These external sources are mainly composed of an assistance server and a reference network. The assistance data provided to the AGPS receiver by the assistance server are transmitted through the reference network. The assistance from the network makes the AGPS receiver operate faster than it would unassisted, as for example HSGPS, because a set of task it would normally handle is shared with the assistance server.

Basically, AGPS provides the user with some interesting features compared with standard GPS and HSGPS:

- It reduces the TTFF (very short latency) to get a position by sending satellite data much more rapidly through the mobile network instead of demodulating the GPS signal in space. As a consequence, AGPS improves the power consumption of the GPS chipset.
- It increases the sensitivity, and then increases the availability of the location service, particularly in dense urban area and indoor environments

As presented earlier, the principle of assisted-GPS consists of coupling satellite positioning and communication networks, sending assistance data to the receiver to improve its performance. Its basic principle is illustrated in Figure 2.17 and described in details below.

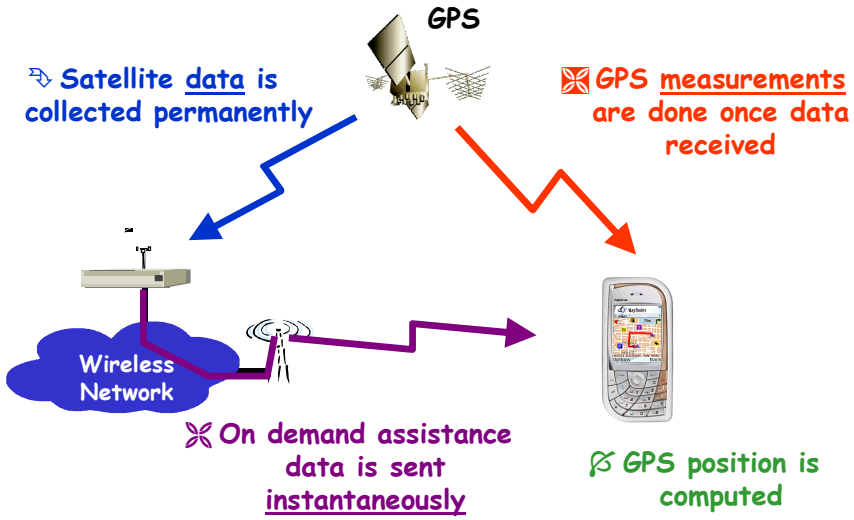

Figure 2.17: Assisted-GPS basic principle.

Step 1:
The AGPS server is integrated in the mobile operator network and collects permanently the satellite data provided by the GPS constellation.

Step 2:
The location can be requested by the mobile user or by an external application on the network. To help its location process (satellite signals acquisition, pseudo ranges (PR) measurement), the mobile phone requests some assistance data to the Assisted GPS server. The mobile chooses the type of assistance data it requires among the standardised data defined in the 3GPP TS 44.031 for GSM/EDGE and TS23.371 for UMTS.

Assistance data help improving both acquisition and tracking of GPS signals. For the acquisition phase, the sensitivity and the TTFF are tremendously improved. The very first step of the acquisition phase is to synchronise on the GPS signal in space. This process is based on a time-frequency search in a given domain, as illustrated in Figure 2.18.

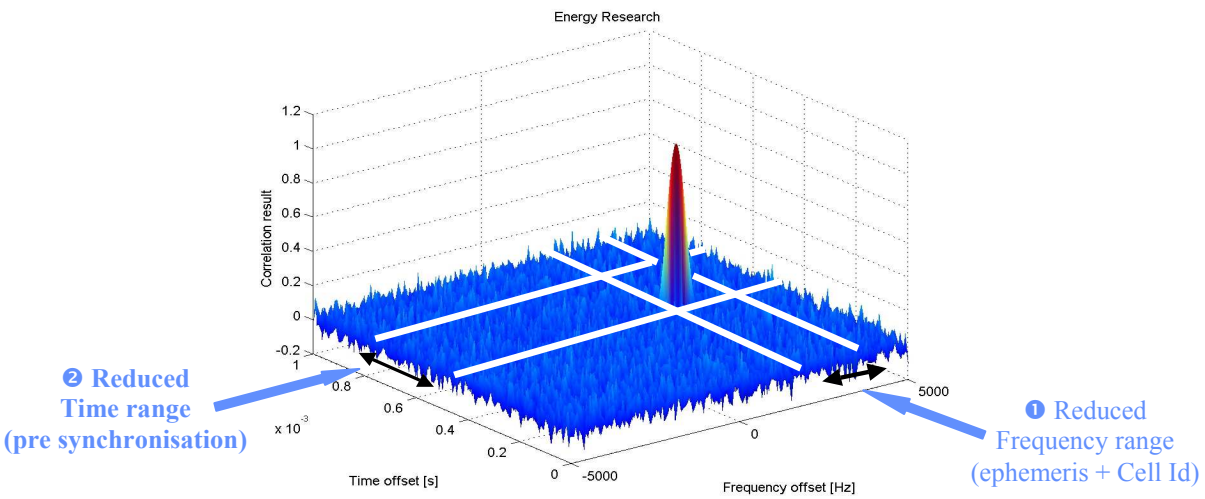

Figure 2.18: AGPS acquisition enhancement.

The frequency range research is linked to uncertainties coming from the preponderant

unknown satellites Doppler, the local oscillator drift, and the user dynamic. The sensitivity, and the complexity of the receiver processing are directly linked to the frequency range to be checked. The assistance data allows a terminal to pre compute the satellite Doppler, and to remove the local oscillator drift. The reduction of the scanned frequency domain directly improves the sensitivity and the time to fix. In the same sense the time uncertainty to be swept is directly linked to the time uncertainty of the receiver. The assistance data allows the receiver to reduce this time uncertainty and then to focus even more the processing on the smaller time-frequency domain, and then improve the sensitivity.

After the first step of the acquisition process and before being able to provide a position solution, a standalone receiver shall demodulate the navigation model. The necessary data are broadcast every 30 seconds, which presents a TTFF limitation for a standalone GPS receiver. This limitation is completely removed thanks to the assistance data. In addition, the demodulation of the SIS data presents a great limitation in terms of sensitivity. The constraints being removed thanks to the assistance data, the sensitivity is also improved.

For the tracking phase, the sensitivity is again increased. Thanks to the assistance data, the processing can be improved in order to focus on the code tracking. It tremendously improves the tracking sensitivity with respect to a standard standalone processing.

The A-GPS server elaborates and sends the assistance data with respect to the data requested and the location of the users. For the time being, there are two standardised ways to transmit the assistance data:

- Control plane implementation. This implementation uses the signalling layers of the communication network to convey the assistance data to the mobile phone and to retrieve position information from the telephone. The protocol is standardised in the TS44.031 (RRLP) for GSM and the TS23.371 (RRC) for UMTS. The advantage of the control plane implementation is precisely that it uses the low layers of the communications which means that assistance data can be conveyed to the users even if they have no SIM cards (E112 emergency calls requirements).
- Secure User plane Implementation; This implementation uses the high level layers of the communication network, i.e. the applicative layers. This is dealt with by the OMA standardisation group. Nevertheless the protocol used for assistance data transmission is the protocol defined at 3GPP level (RRLP for 2nd generation cellular networks, RRC for 3rd generation cellular networks). The data are then exchanged through IP. The advantage of such a solution is that the applicative layer has a much higher data rate. Nevertheless, the user can access to this layer only if it has subscribed, which raises an issue when it is question to deal with emergency calls.

Step 3 and 4:
The handset equipped with the AGPS receiver processes the GPS satellites signals and computes its position. There are two ways to compute the location:

- MS-Based: the AGPS chipset in the mobile phone computes itself the location.
- MS-Assisted: the pseudoranges are sent back to the server. The server computes the location that is sent back to the handset.

2.2.3.2 Enhanced AGPS

The Enhanced AGPS is the technology developed by Alcatel Alenia Space that enhances

AGPS in using EGNOS data to add in the standard assistance data. EGNOS is a system for which Thales Alenia Space is the prime contractor. It is composed of a network of stations deployed world-wide, collecting GPS data and measurements to deliver measurement corrections, end user accuracy estimation and alarms to any user via 3 geostationary satellites. The system is operational since 2005.

The Enhanced AGPS technology provides a number of enhancements compared to the standard AGPS. First, the accuracy is improved thanks to the corrections computed by the EGNOS system (correction of the propagation errors as well as satellite orbital and onboard clock errors) and transmitted to the handset receiver. It enables to reach the best achievable accuracy performances thanks to an optimal combination of the local differential data and the EGNOS wide area data. Moreover, EGNOS may enable the increase of the position solution, particularly in urban areas where the receiver faces an important masking angle, so that the satellite geometry may be very poor leading to a degraded accuracy. As an example, for an ideal receiver the accuracy over France with only one AGPS server is illustrated in Figure 2.20.

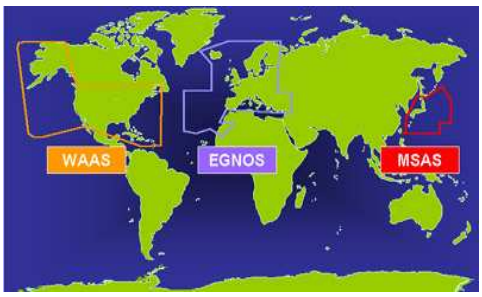

Figure 2.19: EGNOS coverage.

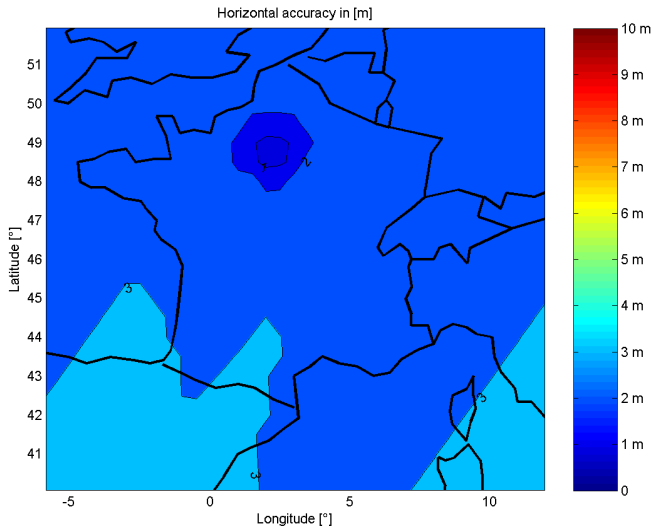

Figure 2.20: Positioning server accuracy.

EGNOS also allows the increase of integrity thanks to the detection and correction of any GPS system failure using EGNOS integrity function even in indoor conditions, typically where classical RAIM techniques fail [50].

2.2.3.3 Acquisition Performance

To analyse the performance of the acquisition stage of an AGPS receiver in terms of time to successfully acquire one signal, several statistic simulations are conducted. More specifically, the analysis focuses on the performance of a software-based acquisition stage. As described in a previous section and also detailed in [16], it is possible to give an expression of the test statistic T at the output of the acquisition stage given in equations (2.11) and (2.12). Therefore, it is possible to simulate the entire acquisition process by directly generating the output T as a function of the coherent integration time and non-coherent integration time. Consequently, in order to estimate the performance of the acquisition stage to successfully acquire one GPS signal, the output of the acquisition loop is generated according to a randomly chosen correlation peak position and given the number of non-coherent integrations, coherent integrations as well as the C/N_0 of the signal to

acquire and the residual Doppler.

Once the criterion T is generated, the detection process based on maximum peak detection is done. If the detection fails, the dwell time is increased until the correlation peak is successfully detected. For each C/N_0 within the range 17dBHz – 30 dBHz (which is considered as typical C/N_0s encountered indoors and in urban environements), the acquisition procedure is repeated 10000 times to get a statistic estimate of the required signal duration Probability Density Function (PDF) and Cumulative Density Function (CDF). Simulations are run for a static user and typical indoor C/N_0s (C/N_0s values have to be understood as C/N_0s at the output of the quantifier stage, which is the last filter of the RF front-end part).

For each simulation, the mean time required to have a successful acquisition is computed. Figure 2.21 presents these mean times as a function of the C/N_0, given a false alarm probability of 10^{-5} and for three different coherent integration times of 1ms, 10ms and 20ms (20ms being the upper coherent integration limit due to the navigation message data bit transition). As expected, the higher the coherent integration time, the lower the length of signal that has to be processed. Signal durations are very small compared to the ones obtained with a standard single dwell serial search procedure (see Figure 2.7). This demonstrates that the FFT acquisition strategy based on a maximum detection test is much more efficient.

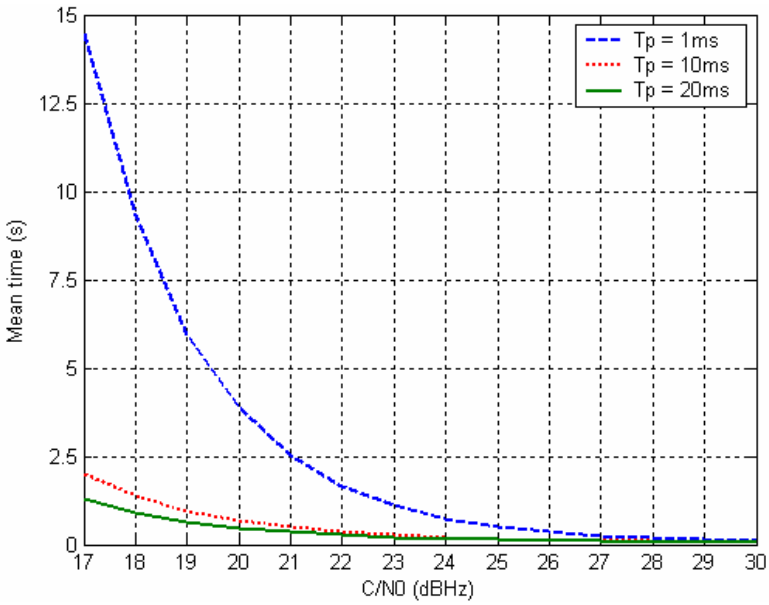

Figure 2.21: Mean signal duration required for a successful acquisition. Pfa = 1e-5, no frequency error.

Following the result of the above simulation, the overall time needed to acquire one satellite with respect to its C/N_0 is deduced. This time can be divided into two parts, the first one being the useful signal duration (or required signal duration, as estimated above), the second one the time needed to process that signal. The processing time is related to the performance of the processor used for computations. This time can not be neglected since many FFT operations are done in the acquisition stage. In the following the processing time is estimated based on the mean signal duration as shown in Figure 2.21.

The time needed to process the required mean signal duration is analysed with the characteristics of a TMS320C55x DSP from Texas Instruments with a clock speed of 168MHz. The overall mean acquisition time taking into account both the mean signal duration and the processing

time for three coherent integration times is plotted in Figure 2.22. For light indoor environment where C/N_0s are typically between 20dBHz and 30dBHz, the overall time needed to successfully acquire one satellite is well below 5 seconds for large coherent integration times, and less than 8 seconds for the other cases. Obviously, the lower the C/N0s, the greater the time to successfully acquire one signal.

From these simulations, it is interesting to notice that long coherent integration times are needed in order to acquire and consequently use weak signals to compute the position of the user in indoor environments. Even if the computational power has well increased in the up-to-date chipsets which makes possible the use of such long integration times, it nevertheless makes the receivers very sensitive to the user's dynamic. Any motion may indeed change the position of the correlation peak in the search matrix as shown in Figure 2.18 while performing long integrations, which in turn may reduce the correlation processing gain at the output of the correlation stage. Such an effect is partially handled with the computational power available in the receiver, but still is one major issue in harsh environments.

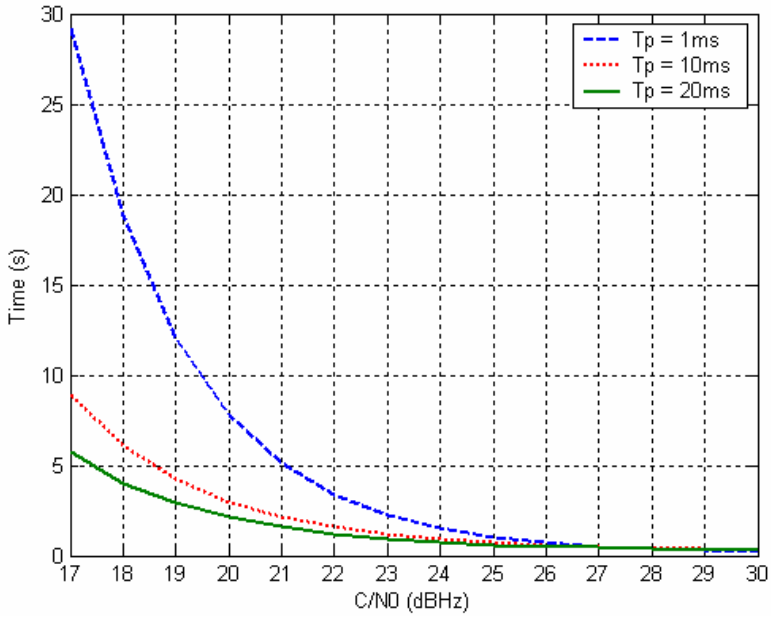

Figure 2.22: Mean acquisition time for a successful acquisition. Pfa=1e-5, no frequency error.

2.3 HS-GPS / AGPS Performance Analysis

2.3.1 HSGPS / AGPS Modules

In order to analyse the performance of AGPS versus HSGPS, a comparative test campaign has been conducted within the Thales Alenia Space field trial. A complete report of the test campaign can be found in [17]. It consists in using an A835 and A1000 Motorola handset, an assisted GlobalSat BT338 and an HP 6515 handset connected to the Thales Alenia Space server that provides with assistance data. The aforementioned handsets are fully implemented with AGPS technology. Pictures as well as basic characteristics are given below. The performance of the different navigation modules are compared with those obtained with a standalone HSGPS bluetooth BT 338 module. In all the following test cases, it is considered that a valid position fix is obtained when the location procedure (including protocols with the assistance data server, if any) ends up

with at least 4 acquired satellites and position solution accuracy better than the cell size the user relies on.

HP 6515
(Global Locate)
MS-Based

GlobalSat BT338
(SiRF star III)
Standalone / MS-Based

Motorola A835
(SiRF star II)
MS-Based

Motorola A1000
(Motorola)
MS-Based

2.3.2 Performance Assessment

The performances of the AGPS modules are assessed through the position accuracy with respect to a reference position, the TTFF and the availability of the position solution. The reference position is whether computed using geodetic grade receiver whose antenna is placed outdoors approximately at the vertical of the position of the indoor handsets, or using a reference point on a digital map. In both cases, the accuracy of the reference point is known at most within ±3 metres.

2.3.2.1 Accuracy

The accuracy of the position solution is characterised by three different quantities. The first one is the RMS error computed according to equation (2.35), which involves as a first approximation the latitude and longitude errors. The 2D bias affecting the different position solutions is defined according to equation (2.36), whereas the sigma 2D error is computed according to equation (2.37).

$$error_{RMS} = \sqrt{\frac{1}{N}\left(\sum_{i=1}^{N}\left(long_error^2 + lat_error^2\right)\right)} \tag{2.35}$$

where:
- N is the number of valid position fixes
- long_error is the longitude difference [m] between the ‘true’ position and the measured one.
- lat_error is the latitude difference [m] between the ‘true’ position and the measured one.

$$bias_{2D} = \frac{1}{N}\sum_{i=1}^{N}\sqrt{long_error_i^2 + lat_error_i^2} \tag{2.36}$$

$$\sigma_{2D} = \sqrt{\sigma^2(long_error) + \sigma^2(lat_error)} \tag{2.37}$$

where:
- λ_k, φ_k are the longitude and latitude result of the kth trial.

- φ_{ref} is the latitude of the reference position.
- R_t is the earth's radius at equator.
- $\sigma(long_error) = \sqrt{\frac{1}{N}\sum_{k=1}^{N}\left(\lambda_k - \left(\frac{1}{N}\sum_{k=1}^{N}\lambda_k\right)\right)^2} \cdot \cos(\varphi_{ref}) \cdot R_t$
- $\sigma(lat_error) = \sqrt{\frac{1}{N}\sum_{k=1}^{N}\left(\varphi_k - \left(\frac{1}{N}\sum_{k=1}^{N}\varphi_k\right)\right)^2}$

2.3.2.2 Time-To-First-Fix

It corresponds to the time to get a valid position fix when activating the location function. It is only relevant when performing a cold start fix. For the AGPS receivers, the TTFF includes the transmission duration of the assistance data from the AGPS server to the AGPS handset.

2.3.2.3 Availability

It corresponds to the ratio between the number of valid fixes and the total number of trials. It is expressed in percentage. A fix is considered valid only if it is computed with at least 4 satellites and within 2 minutes timeout.

2.3.3 Comparative Test Results

The tests are performed in two types of environments. The first environment is light indoors in the office of a building with steel walls, as shown in Figure 2.23. The second environment is a urban canyon as illustrated in Figure 2.26. Outdoors tests under clear sky conditions have also been conducted, but since the positions where all accurate, no detail about the performance of the different location modules are given in the following. This section ends with kinematic tests.

2.3.3.1 Light Indoor Environment

Table 2.1 gives the cold start results inside the light indoor environment shown in Figure 2.23 of the three types of handsets. As expected, the MS-based handsets give the best performance in terms of TTFF (21s for the Motorola A835, 15s for the BT-338) compared to the reference HSGPS (BT-338 in standalone mode). The accuracy of the first position solution depends on the chipset that is used, but comparing handsets using the same SiRF star III processing core, the AGPS solution is of better accuracy than those of the HSGPS reference receiver, maybe due to a better Dilution of Precision.

These results are just an illustration of the performance that can be achieved with such receivers and shall not be considered as typical cold start performance, as the number of trials is sometimes quite small.

Figure 2.23: Light indoor environment.

Handset	A835	BT-338 Standalone	BT-338 MS-Based
Nb of trials	200	4	4
Bias 2D	5.21m	3.5m	0.1m
Bias 3D	5.9m	-	-
σ2D	57m	0.2m	0.6m
σ3D	45m	0.7m	2.9m
TTFF	21s	68s	15s
Availability	100%	100%	100%

Table 2.1: Light indoor cold start test results.

The tracking test results are summarised in Table 2.2 for all the handsets used in the field trial. All the receivers give an accurate position solution (except the A1000 handset). The solution provided by the assisted receivers is less noisy, as it is shown in Figure 2.24 and Figure 2.25. This may be explained by the better DOP experienced by AGPS receivers that improves the accuracy of the position solution.

Handset	A835	BT-338 Standalone	BT-338 MS-Based	HP 6515	A1000
Nb of trials	152	200	645	182	264
RMS Error	9.9m	11.8m	1.1m	6.9m	35m
Bias 2D	9m	3m	0.6m	7m	23m
Bias 3D	9m	9m	-	11m	35m
σ2D	4m	11m	0.9m	1m	26m
σ3D	23m	20m	2.6m	1.7m	60m
Availability	100%	99%	100%	99.5%	100%

Table 2.2: Light indoor tracking test results.

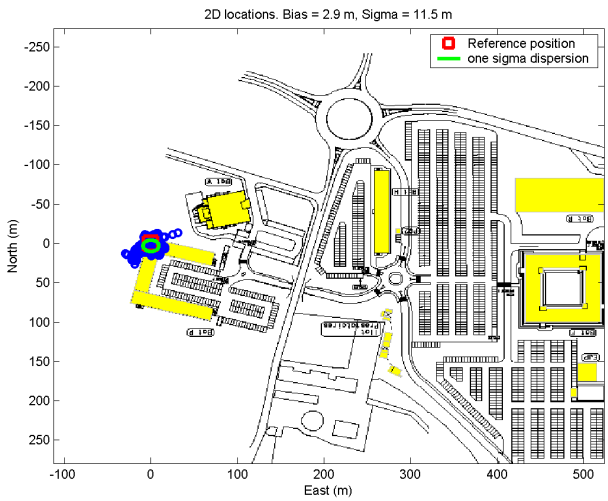

Figure 2.24: 2D plot of BT-338 (standalone) in light indoor environment.

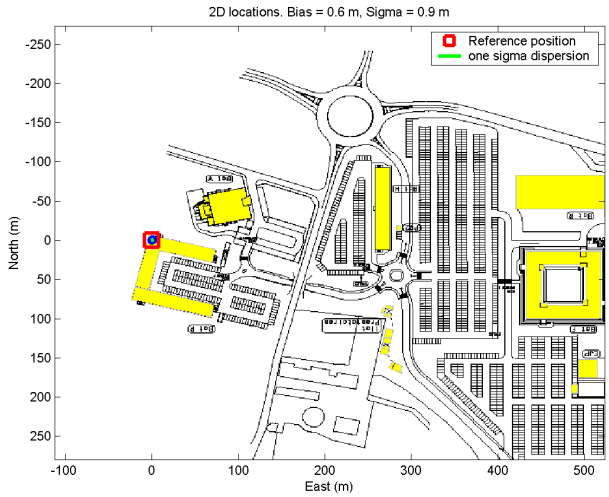

Figure 2.25: 2D plot of BT-338 (MS-based) in light indoor environment

2.3.3.2 Urban Street Environment

This test was conducted in a very narrow street in Toulouse, France. Figure 2.26 and Figure 2.27 give an overview of the location where the test was conducted. All the handsets were put on the roof of a vehicle so that the antennas were pointing to the sky with no obstacle.

Figure 2.26: Urban street environment (heading north).

Figure 2.27: Urban street environment (heading south).

In a first time, static cold start positioning was tested. Results are given in Table 2.3 using a mask angle of 5 degrees. It is obvious that the AGPS receivers outperform the HSGPS reference receiver in terms of TTFF. Providing through the cellular network the ephemeris of the satellite in visibility is a clearly advantage that faces quite well the issue of the reduction of the noise power as well as the demodulation of the navigation message for each satellite.

Handset	A 835	BT-338 Standalone	BT-338 MS-Based
Nb of trials	85	5	4
TTFF	42s	2min30s	31s
Availability	76%	100%	100%

Table 2.3: Urban street cold start test results

The tracking of the position of the user shows again that AGPS receiver gives the more accurate position solution in such harsh environment, as it can be seen in Table 2.4.

Handset	A 835	BT-338 Standalone	BT-338 MS-Based	HP 6515
Nb of trials	152	>1000	79	>1000
RMS Error	18.8m	23m	8.5m	17.5m
Bias 2D	17m	20m	8.3m	5m
σ2D	7m	10m	1.8m	17m
Availability	100%	100%	100%	100%

Table 2.4: Urban street tracking test results.

The different position solutions are again less noisy with AGPS receivers. As a comparison,

the position solutions computed with both BT-338 (one HSGPS, one AGPS) are plotted in Figure 2.28 and in Figure 2.29. To explain such results, it would have been useful to analyse to number of satellites used to compute the position as well as the Dilution of Precision. However, both quantities were not available in the data recorded during the trials.

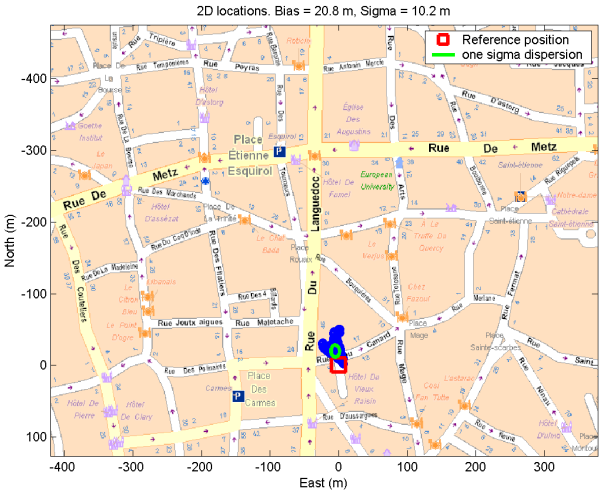

Figure 2.28: 2D plot of BT-338 (standalone) in urban street environment.

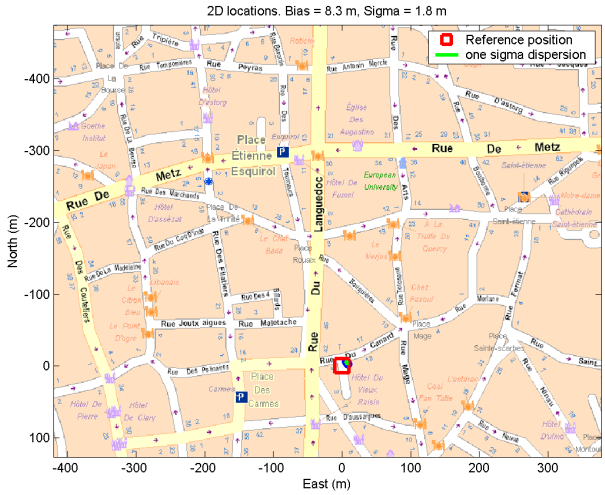

Figure 2.29: 2D plot of BT-338 (MS-based) in urban street environment.

2.3.3.3 Kinematic Urban Test

A dynamic test has been conducted in dense urban area to assess the tracking capabilities of the different chipsets. It clearly appears that once again, AGPS outperforms HSGPS, as illustrated in Figure 2.30 and in Figure 2.31.

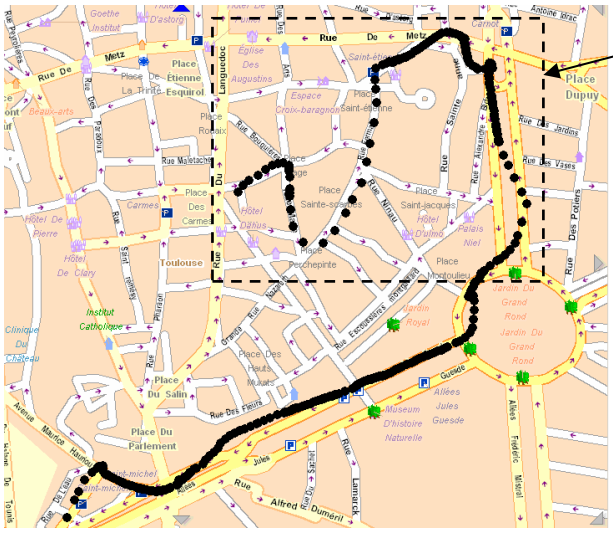

Figure 2.30: 2D plot of BT-338 (standalone) in urban dynamic test.

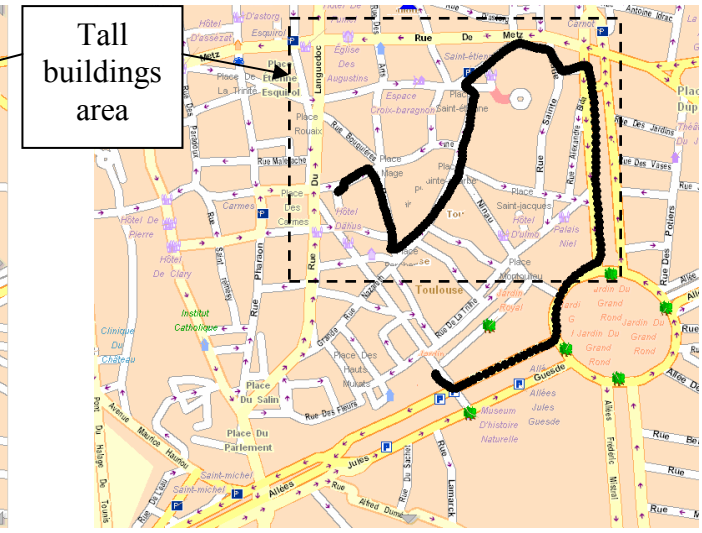

Figure 2.31: 2D plot of BT-338 (MS-based) in urban dynamic test.

There is indeed no need to demodulate the ephemeris of the satellite in visibility since they are transmitted through the assistance data. As a consequence, as soon as a satellite is acquired and tracked, it can be integrated into the set of measurements used to compute the user's position. This is a clear advantage of AGPS against HSGPS. The DOPs are therefore better in that case, which in

part explains why the position solution is more smoothed and accurate.

2.3.3.4 Indoor Test

The performances of AGPS and HSGPS receivers in harsh environment have been finally tested. The results presented hereafter have been obtained using one GlobalSat BT338 module which can be configured whether in AGPS or in HSGPS mode.

The tracking result of a pedestrian going inside and outside buildings are shown in Figure 2.32 and in Figure 2.33 for the AGPS and HSGPS mode respectively. In both cases, the pedestrian starts its walk outside and follows the trajectory as illustrated by the yellow dashed plot in the direction indicated by the arrow. He then enters the building in 'A' and keeps walking inside until point 'B', and finishes its walk outside.

As it can be seen in the two figures, the trajectory of the pedestrian inside the building is clearly not observable with the outputs of the GPS modules. As soon as the pedestrian enters the building, the position solutions become very inaccurate due to multipath and cross-correlation that dramatically affect the position computation stage. This clearly demonstrates the need of an alternative positioning system that would replace GPS during outages in order to provide positions inside buildings.

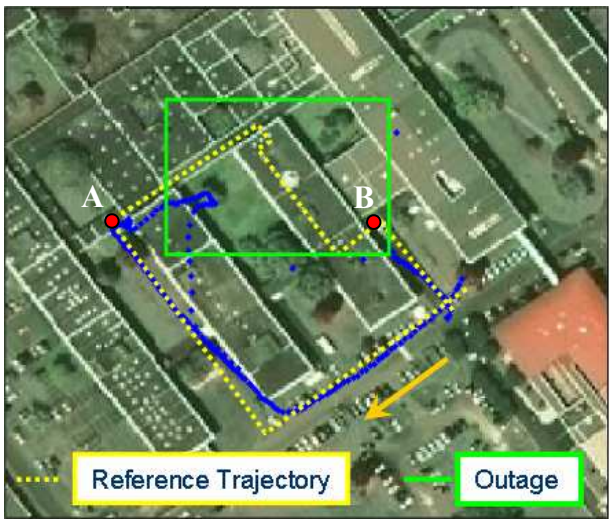

Figure 2.32: AGPS tracking result of a pedestrian going outside / inside buildings.

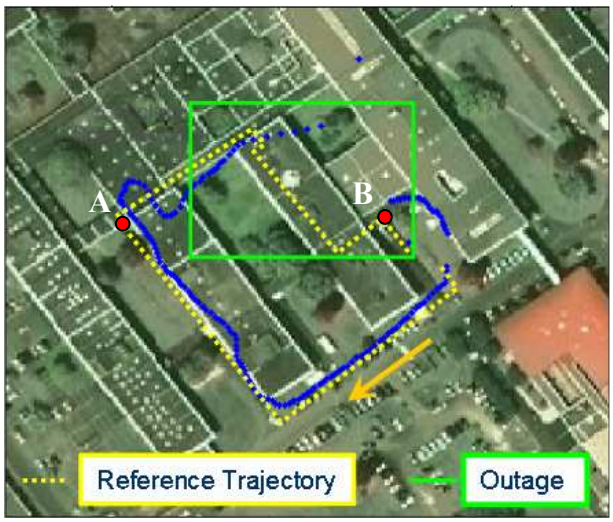

Figure 2.33: HSGPS tracking result of a pedestrian going outside / inside buildings.

2.4 Conclusion

This section recalled the basics of the GPS positioning technique. The typical issue (weak signal processing, multipath and cross-correlation impact, quality of the position solution…) encountered when using GPS to locate people in urban areas (even indoor) have been discussed. New GPS architectures designed to face these issues such as HSGPS and AGPS have been presented, and their performance have been analysed in terms of time to acquire, time to fix and position accuracy. Both AGPS and HSGPS have shown sensitivity and availability improvement as compared to standard GPS. Even if the number of trials that have been excersised are not large

enough to draw definitive conclusions, it nevertheless tends to demonstrate they both are suitable for urban positioning, although their respective accuracy degrades when the receiver operates close to tall buildings or inside infrastructures.

The improvement of the processing core (HSGPS) and the architecture of the positioning system (AGPS) are somehow useless in very harsh environments such as inside big buildings or in deep urban areas, as shown with the two latter position solutions in Figure 2.32 and Figure 2.33. There is therefore a needed for augmentations if one would like to increase the position availability.

In the frame of this thesis, the alternative system used to support or replace GPS during outages will be made of low-cost inertial sensors. The next chapter will present navigation algorithms based on these sensors.

Chapter 3: Inertial Navigation Systems

This chapter describes the navigation algorithms that can be used with inertial sensors (i.e. accelerometers and gyroscopes). In a first time the basics on inertial navigation are recalled and notations used throughout this thesis are defined. A particular attention is then paid to the sensors, their intrinsic accuracy and expected performance with respect to their grade. In particular, the sensors unit assembly used in this thesis (the MTi IMU made by Xsens) is analysed. As the typical inertial sensors issues are described, this chapter details then the standard Inertial Navigation System (INS) mechanisation and discusses its performance regarding the sensors that are used. Finally, a specific analysis of the so-called Pedestrian Dead Reckoning mechanisation is given and a performance comparison with the standard INS is done.

3.1 Inertial Navigation Overview

3.1.1 Basic principle

The inertial navigation relies on the measurements provided by sensors contained in an Inertial Measurement Unit (IMU). The IMU is basically composed of a triad of accelerometers and gyroscopes orthogonally mounted. Such sensors can be integrated into two main types of inertial systems, namely gimbaled and strap-down systems. Gimbaled systems are actuated platforms, whose principle is to maintain the platform frame aligned with a specific navigation coordinate system. When achieved, the accelerometers mounted on the platform are used to measure the specific force along the navigation axes. These measurements are then processed to compute the position of the vehicle. The attitude of the vehicle is measured as the relative angles between the platform and the vehicle axes. Gimbaled systems are expensive and often used for high accuracy applications (aircraft, spacecraft…).

In strap-down systems, the inertial sensors are fixed to in the vehicle itself, rather than in a stabilised platform. The sensors measure the dynamic of the vehicle so that the relationship between the measurements and the navigation state of the vehicle must be permanently computed. As a result, the computation load is increased compared to gimbaled systems. Such a drawback is currently of no problem due to major improvements in computer technology. Moreover, strap-down systems allow the reduction of the IMU size as well as its cost but at the expense of some accuracy. More details about gimbaled and strap-down systems can be found in [18] and [19]. Strapdown systems will be used within the scope of the study, since they are less expensive and more suited to miniaturisation.

An Inertial Navigation System (INS) is a system composed of an IMU and a computer. It estimates the position of a mobile the IMU is mounted on by processing the measurements of the sensors contained in the IMU. It relies on Newton's laws of motion. Any external force applied to an IMU generates acceleration and a rotation signal that are expressed in a specific reference frame. These measurements are processed to get the position, velocity of the vehicle in a coordinate system adapted to the navigation of the vehicle. Several coordinate systems and transformations are thus required to enable a relevant processing of the inertial data.

3.1.2 Frames and Coordinates

The relationship of the inertial measurements with the navigation state of a vehicle involves four reference frames.

<u>Inertial Reference Frame ***(I)***:</u>
It is a non-rotating Galilean frame, attached to the centre of the Earth with the Z_I axis pointing toward the North Pole, whereas X_I and Y_I axes both lie in the plane of equator, with the X_I axis pointing toward the vernal point direction (i.e. the intersection between the orbital plane and the equatorial plane). The three axes are always pointing toward their respective direction. The inertial reference frame is illustrated in Figure 3.1.

<u>Earth-Centred Earth-Fixed (ECEF) Reference Frame ***(e)***:</u>
The ECEF reference frame is linked to the Earth. It is deduced from the inertial reference frame by

a rotation around the common Z axis (Z_I or z_{ECEF}) of angle Ω_E. x_{ECEF} of the ECEF coordinates is on the Greenwich meridian. The ECEF frame is illustrated in Figure 3.1.

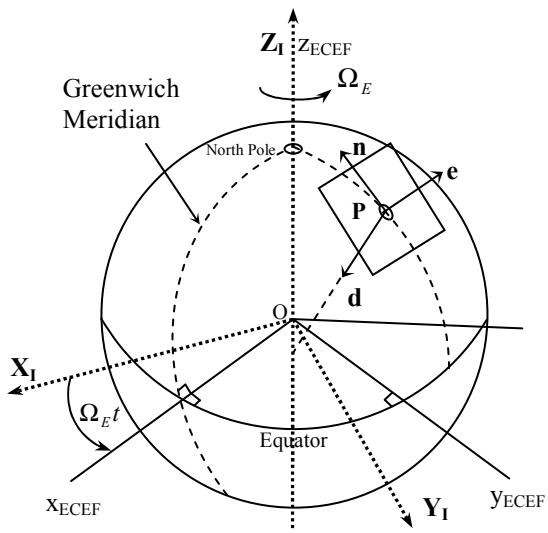

Figure 3.1: Inertial *(I)*, ECEF *(e)* and navigation *(n)* frames.

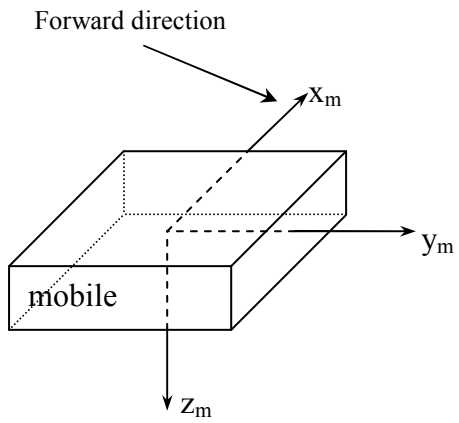

Figure 3.2: Navigation *(n)* frame.

Local Geodetic Reference Frame or Navigation Frame ***(n)***:
It is defined by a tangent plane, which is attached to a fixed point on the surface of the Earth. This point is the origin of the local frame. The north axis points toward the true north, the east axis points to the east and the down axis completes the right handed coordinates system pointing toward the interior of the Earth, but not necessary to the Earth's centre. The down axis is perpendicular to the reference ellipsoid. The navigation frame is illustrated in Figure 3.1.

Mobile Reference Frame ***(m)***:
The mobile reference frame is defined by the orthogonal triad (x_m, y_m, z_m) of Figure 3.2 attached to the mobile. The axes are assumed aligned with the IMU frame. In case where x_m is defined as the forward axis, i.e. the axis in the direction of displacement, x_m is called the roll axis. y_m is then defined as the pitch axis and z_m completing the direct reference frame is the yaw or heading axis.

3.1.3 Sensors

3.1.3.1 Accelerometer

A simple and quite general way of understanding the principle of an accelerometer is to imagine it as a device that measures the force applied on a proof mass to accelerate it. Rigidly mounted in a vehicle, it then measures its acceleration. Details about various accelerometer operation principles can be found in [18], but basically, it can be considered as a spring with a proof mass μ at an extremity (the other being linked to the host vehicle). According to the fact that the proof mass is a punctual mass at position M , the second Newton's law applied to the proof mass in an inertial reference frame ***(I)*** yields the following equation:

$$\mu \cdot \vec{a}_{M/I} = \vec{F}_R + \vec{F}_D + \mu \cdot \vec{G}_M \tag{3.1}$$

where:
- $\vec{a}_{M/I}$ is the inertial acceleration of the punctual proof mass μ at position M, relative to ***(I)***.
- $\vec{F}_R$ is the resulting force applied on the proof mass by the restoring spring, and caused by the vehicle movement.
- $\vec{F}_D$ is a disturbing force regrouping all effects caused by friction, mechanical damping…
- $\vec{G}_M$ is the universal gravitational force, applied at M on the mass μ.

Neglecting the disturbing force $\vec{F}_D$, equation (3.1) can be rewritten as follows:

$$\vec{f} = \vec{F}_R / \mu = \vec{a}_{M/I} - \vec{G}_M \tag{3.2}$$

where:
- $\vec{f}$ is called the specific force. It is the true acceleration that is measured by the accelerometer.

The accelerometers are orthogonally mounted into a measurement unit, whose axes can be as illustrated in Figure 3.2. Since this measurement unit is also rigidly mounted on the vehicle, the acceleration measurement is done in the reference frame linked to the mobile (the vehicle), i.e. the mobile frame. As a consequence, the accelerometer does measurements with respect to the inertial frame ***(I)*** that are expressed in the mobile frame ***(m)***.

Due to the manufacturing process of the sensor, the measurements are affected by errors that vary with time, temperature, as well as the motion experienced by the sensor. The impact of these errors on the measurements accuracy is closely related to the quality of the sensor and the technology used. Nevertheless, a common output model can be derived in all cases. Equation (3.3) gives the general first order accelerometer output model:

$$a^{out} = (1 + SF_a) \cdot f + b_a + n_a \tag{3.3}$$

where:
- a^{out} is the output of the accelerometer.
- SF_a is the scale factor affecting the true acceleration.
- b_a is the bias affecting the measurement.
- n_a is the accelerometer noise.

3.1.3.2 Gyroscope

The gyroscope is the sensor used to compute the attitude of an Inertial Navigation System. It senses the rotation rate along the axis it is placed with respect to the inertial frame ***(I)***. As for accelerometers, the rotation rate is expressed in the frame the sensors are attached, i.e. the mobile frame ***(m)***. Details about various gyroscope technologies and principles of operation can be found in, for example, [18] and [19]. The general first order output model of a gyroscope is given in equation (3.4):

$$\omega^{out} = (1 + SF_\omega) \cdot \omega^{true} + b_\omega + n_\omega \tag{3.4}$$

where:
- ω^{out} is the output of the gyroscope.
- ω^{true} is the true rotation rate experienced by the sensor.
- SF_{ω} is the scale factor affecting the true rotation rate.
- b_{ω} is the bias affecting the measurement.
- n_{ω} is the gyroscope noise.

3.1.3.3 Measurements Errors

Both gyroscope and accelerometer measurements are affected by the same type of errors. The impact of these errors on the accuracy of the measurements is very dependent on the quality of the sensors that are used. Compared to the dynamic that is measured by the sensors, these errors have quite low magnitude, but since measurements are likely to be integrated, they dramatically decrease the inertial navigation performance as time increases.

The noise affecting the measurement is the result of the electronic equipment needed for the sensor to work properly. It has random properties and usually can not be removed with deterministic models. It is rather considered as a first approximation as zero mean white Gaussian noise. In datasheets, it is often characterised by velocity random walk for accelerometers and angular random walk for gyroscopes, with a density expressed in unit of signal / √Hz.

The bias is mainly composed of two parts. The first one is the turn-on bias, which varies every time the sensor is powered on. The repeatability of this part is quite poor for typical low-cost sensors, and thus should often be estimated. The second part is the in-run bias, whose variation is closely related to the motion experienced by the sensor. The latter contribution is the more difficult to estimate since the movement of the sensor is unpredictable. It will consequently introduce non-negligible systematic errors in the measurements and thus must be modelled. Both bias components depend also on the operating temperature.

The scale factor is the ratio usually expressed in PPM that characterises the non linear change in the output with respect to the change in the input, as shown in equations (3.3) and (3.4). It is a non deterministic error that also depends on the motion and the temperature experienced by the sensor.

The IMU performance is driven by the three main errors described above. However, it also depends on the manufacturing process in the construction of the sensor triad. As a result of the possible misalignment of the sensors, each axis is affected by measurements of the other two axes in the body frame. Usually, such error is calibrated in laboratory by the manufacturer quite accurately. This kind of error is therefore not taken into account in the following.

3.2 Strap Down Attitude Computation

As described above, navigation and motion measurements are done in two different frames. It is usual to express the navigation status such as position and velocity in the navigation frame ***(n)*** North, East, Down rather than in any other reference frame. As part as inertial sensors properties, measurements are done in the mobile frame ***(m)*** that is attached to the vehicle. To express the

measurements in the navigation frame and perform inertial navigation, the relative orientation between these two frames has to be known.

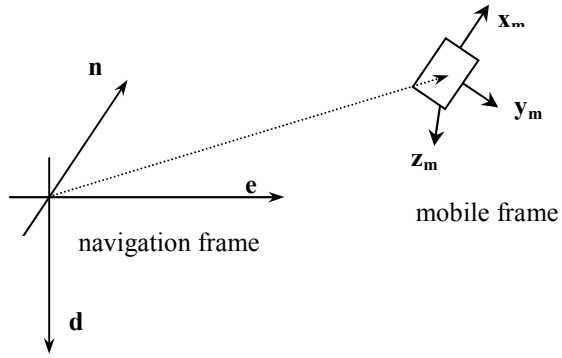

This relationship can be fully described by the position of the mobile frame origin expressed in navigation coordinates and the rotation matrix from the mobile frame to the navigation frame involving Euler's angles. Euler's angles are defined as three distinct rotations around particular axes, as shown below in Figure 3.3. They also are known as roll, pitch and yaw (heading) angles.

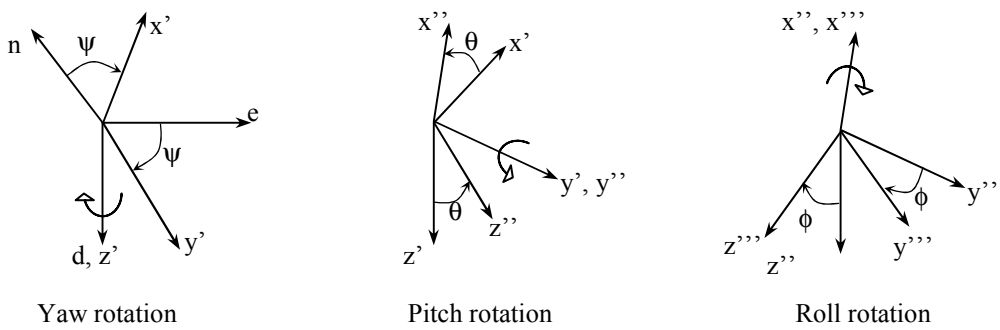

Figure 3.3: Euler's angles definiton.

The triad of gyroscopes in the IMU provides the rotation rates along the three axes of the mobile frame. The global rotation rate of the vehicle the IMU is mounted on is thus given by equation (3.5):

$$\vec{\Omega}_{m/I}^{(m)} = p \cdot \vec{x}_m + q \cdot \vec{y}_m + r \cdot \vec{z}_m \tag{3.5}$$

where:

- $\vec{\Omega}_{m/I}^{(m)}$ is the global rotation rate vector of the mobile with respect to the inertial frame expressed in the mobile frame.
- p is the roll angle rate as measured by the gyroscope along the x_m axis.
- q is the pitch angle rate as measured by the gyroscope along the y_m axis.
- r is the yaw angle rate as measured by the gyroscope along the z_m axis.

3.2.1 Attitude Algorithm

Several methods exist to compute the attitude of a mobile with respect to a particular frame.

Among them, the most well known and widely used are Euler's angles and the rotation quaternion. Euler's angle methodology was the first method used to continuously track the attitude of a vehicle. It relies on the integration of non linear differential equations as given in equation (3.6) [20]. However, this method requires numerous trigonometric operations and singularity issues may affect the computation of the Euler's angles, especially for pitch angles of ±90°.

$$\begin{bmatrix} \dot{\phi} \\ \dot{\theta} \\ \dot{\psi} \end{bmatrix} = \begin{bmatrix} 1 & \sin(\phi)\tan(\theta) & \cos(\phi)\tan(\theta) \\ 0 & \cos(\phi) & -\sin(\phi) \\ 0 & \sin(\phi)\cdot\cos^{-1}(\theta) & \cos(\phi)\cdot\cos^{-1}(\theta) \end{bmatrix} \cdot \begin{bmatrix} p \\ q \\ r \end{bmatrix} \tag{3.6}$$

A more convenient and efficient method based on Hamilton quaternion [21] is used throughout this thesis. A Quaternion is a hyper-complex number invented by W.R. Hamilton for mathematical purposes. It is a combination of real and complex values, and is often written as given in equation (3.7). The real part of a quaternion is called the scalar part, whereas the imaginary part is often called the vector part. The unit vectors are the complex numbers i, j, k.

$$\vec{q} = \underbrace{q_0}_{scalar\ part} + \underbrace{q_1 \cdot \vec{i} + q_2 \cdot \vec{j} + q_3 \cdot \vec{k}}_{vector\ part} \tag{3.7}$$

The quaternion as defined above can also be used to represent a rotation of a vector in a three dimensions space. The rotation of angle θ about the fixed axis *D* can be represented by the quaternion q, whose corresponding definition (equivalent to that of equation (3.7)) is given below in equation (3.8). A rotation quaternion is thus of unitary magnitude.

$$q = \cos\left(\frac{\theta}{2}\right) + \vec{u}\sin\left(\frac{\theta}{2}\right) \tag{3.8}$$

where:
– $\vec{u}$ is a unit vector of the rotation axis *D*.

According to quaternion operation rules, it can be demonstrated that for a small rotation, the time derivative of quaternion q can be expressed as a function of itself and the rotation rates of the mobile to characterise [21]. The classical quaternion differential equation, as given in equation (3.9) is used as the input of the quaternion-based attitude determination algorithm detailed in [20] and recalled in appendix B. It allows then the computation of the rotation quaternion from ***(m)*** to ***(n)*** in real time.

$$\dot{q} = \frac{1}{2} q \circ \omega_{m/n}^{(m)} \tag{3.9}$$

From a practical point a view, once the rotation quaternion has been computed, the relationship with the more convenient Euler's angles is used for navigation. As it is shown in [20] or [21], the rotation matrix from the mobile frame ***(m)*** to the navigation frame ***(n)*** can be expressed as a function of quaternion's components but also as a function of Euler's angles. The two expressions are given below, where this rotation matrix from ***(m)*** to ***(n)*** is noted R_{m2n}, a cosine is noted c and a sine s.

$$R_{m2n} = \begin{bmatrix} c(\theta)\cdot c(\psi) & s(\varphi)\cdot s(\theta)\cdot c(\psi) - c(\varphi)\cdot s(\psi) & c(\varphi)\cdot s(\theta)\cdot c(\psi) + s(\varphi)\cdot s(\psi) \\ c(\theta)\cdot s(\psi) & s(\varphi)\cdot s(\theta)\cdot s(\psi) + c(\varphi)\cdot c(\psi) & c(\varphi)\cdot s(\theta)\cdot s(\psi) - s(\varphi)\cdot c(\psi) \\ -s(\theta) & s(\varphi)\cdot c(\theta) & c(\varphi)\cdot c(\theta) \end{bmatrix} \tag{3.10}$$

$$R_{m2n} = \begin{bmatrix} q_0^2 + q_1^2 - q_2^2 - q_3^2 & 2(q_1 q_2 - q_0 q_3) & 2(q_1 q_3 + q_0 q_2) \\ 2(q_1 q_2 + q_0 q_3) & q_0^2 + q_2^2 - q_3^2 - q_1^2 & 2(q_3 q_2 - q_0 q_1) \\ 2(q_1 q_3 - q_0 q_2) & 2(q_2 q_3 + q_0 q_1) & q_0^2 + q_3^2 - q_1^2 - q_2^2 \end{bmatrix} \tag{3.11}$$

It is then straightforward to determine the attitude angles based on the rotation matrix expressions as a function of quaternion's components. The three equations are given below:

$$\theta = \arcsin(-2(q_1 q_3 + q_0 q_2)) \tag{3.12}$$

$$\phi = \arctan\left(\frac{2(q_3 q_2 - q_0 q_1)}{-1 + 2(q_0^2 + q_1^2)}\right) \tag{3.13}$$

$$\psi = \arctan\left(\frac{2(q_1 q_2 - q_0 q_3)}{-1 + 2(q_0^2 + q_3^2)}\right) \tag{3.14}$$

3.2.2 Attitude Initialisation

One issue dealing with gyroscopes measurements is that only relative rotation rates are sensed. The angles of attitude have thus to be initialised first before any real time tracking can be done. The initialisation of these angles is of tremendous importance since it can introduce some permanent angle offsets in the estimated attitude. The attitude initialisation can be divided into two procedures. They are the horizontal and azimuth alignment. The horizontal or inclination initialisation is often performed with the use of accelerometer measurements. Indeed, when the IMU is not moving, the accelerometers are likely to sense the gravity vector, as shown with equation (3.15). One can then use the gravity vector components to determine the inclination, i.e. the roll and pitch angles experienced by the IMU, as given in equation (3.16) and (3.17).

$$\begin{bmatrix} a_x \\ a_y \\ a_z \end{bmatrix}^{(m)} = R_{n2m} \cdot \begin{bmatrix} 0 \\ 0 \\ g \end{bmatrix}^{(n)} = g \cdot \begin{bmatrix} -s(\theta) \\ c(\theta)\cdot s(\phi) \\ c(\theta)\cdot c(\phi) \end{bmatrix} \tag{3.15}$$

$$\hat{\phi} = \arctan(a_y / a_z) \tag{3.16}$$

$$\hat{\theta} = \arctan\left(-a_x \Big/ \sqrt{a_z^2 + a_y^2}\right) \tag{3.17}$$

The accuracy of the inclination estimation is very dependent on the quality of the accelerometers that are used. The inclination measurement procedure is illustrated in Figure 3.5. Assume an accelerometer whose measurements are affected by a bias, the estimated inclination angle may be corrupted depending on the intensity of that bias. In Figure 3.4 is shown the impact of typical biases on the estimation of the inclination angle (whether the pitch or roll angle) given typical true inclination angles. Obviously, the larger the bias, the larger the error on the estimation of the inclination. Moreover, the error increases as the inclination to estimate increases as well.

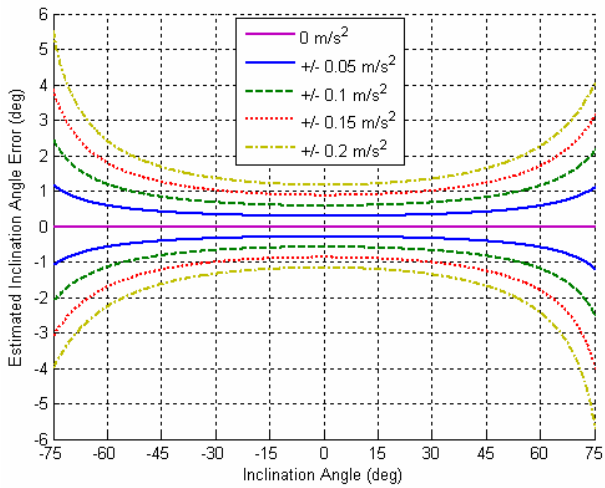

Figure 3.4: Estimated inclination angle error as a function of several accelerometer biases.

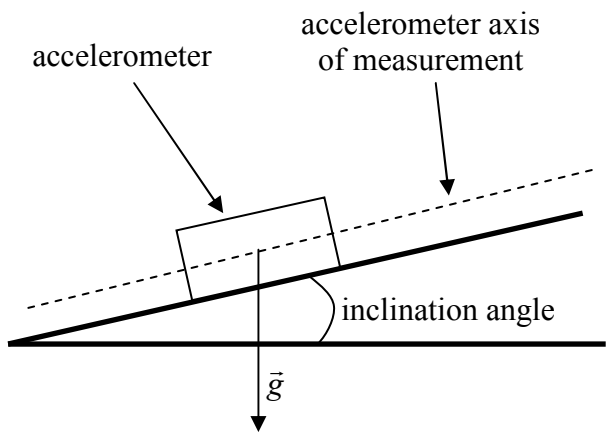

Figure 3.5: Accelerometer inclination measurement scheme.

Azimuth initialisation requires fairly accurate gyroscope sensors to perform gyrocompassing [19]. In such an initialisation method, gyros affected by a drift rate far below the Earth's rotation are required. Other methods using external sensors such as GPS or magnetometers can be employed for azimuth initialisation. The GPS-based method is the most robust one but needs special conditions to give accurate results. First, GPS azimuth is only available while the mobile is in motion, so that no static calibration can be done. Second, measurements are likely to be affected by noise and multipath in harsh environment such as indoors or in urban canyon, so that the GPS heading information may be very noisy as well.

Magnetometers can also be used to initialise the heading computed based on IMU measurements. The magnetic heading is computed using the Earth's magnetic field vector horizontal components (i.e. perpendicular to the gravity vector). This heading differs from the geographic north by an angle called declination, which is known and can be found for example in [22]. The magnetic heading accuracy depends on the quality of the magnetic measurements and on the interferences that may occur. It is also related to the accuracy of the inclination angles (i.e. roll and pitch angles) used to rotate the measurements from the mobile frame ***(m)*** to a horizontal frame.

3.2.3 Euler's Angles Singularity Issue

The usual definition of the rotations associated to Euler's angles φ, θ and ψ are given below. The rotation matrix R_{n2m} from ***(n)*** to ***(m)*** is the successive composition of the three rotations defined above, i.e. $R_{n2m}=R_{\varphi}\times R_{\theta}\times R_{\psi}$. The rotation matrix R_{m2n} from ***(m)*** to ***(n)*** is computed by transposing the transposition of R_{n2m}.

Roll rotation R_{φ}

$$\begin{bmatrix} 1 & 0 & 0 \\ 0 & \cos(\varphi) & \sin(\varphi) \\ 0 & -\sin(\varphi) & \cos(\varphi) \end{bmatrix}$$

Pitch rotation R_{θ}

$$\begin{bmatrix} \cos(\theta) & 0 & -\sin(\theta) \\ 0 & 1 & 0 \\ \sin(\theta) & 0 & \cos(\theta) \end{bmatrix}$$

Yaw rotation R_{ψ}

$$\begin{bmatrix} \cos(\psi) & \sin(\psi) & 0 \\ -\sin(\psi) & \cos(\psi) & 0 \\ 0 & 0 & 1 \end{bmatrix}$$

When the pitch angle θ reaches ±90°, which may occur especially if the IMU is carried in a handheld device, singularities appear in the definition of the other attitude angles so that both roll

and heading angles computed based on equations 3.14 and 3.15 are no more relevant of the true ones. Indeed, as defined in equation 3.11, the rotation matrix R_{n2m} for such extreme values of pitch becomes as follows:

$$R_{m2n}\big|_{\theta=\pm 90^\circ} = \begin{bmatrix} 0 & s(\varphi)c(\psi)-c(\varphi)s(\psi) & c(\varphi)c(\psi)+s(\varphi)s(\psi) \\ 0 & s(\varphi)s(\psi)+c(\varphi)c(\psi) & c(\varphi)s(\psi)-s(\varphi)c(\psi) \\ -1 & 0 & 0 \end{bmatrix} = \begin{bmatrix} 0 & s(\varphi-\psi) & c(\varphi-\psi) \\ 0 & c(\varphi-\psi) & -s(\varphi-\psi) \\ -1 & 0 & 0 \end{bmatrix}$$

Only the difference between the roll and heading angles is observable. Both angles can not be extracted as individual values from this matrix. This issue is also well addressed if equation (3.6) is used to compute the attitude angles. Figure 3.6 illustrates the problem of the attitude angles restitution. In this test, the IMU is intended to be moved such as the pitch angle reaches 90°. As the pitch experiences extreme values, both roll and yaw (heading) are no more reliable.

To get rid of this singularity issue, a basic idea is to virtually rotate the IMU when the pitch angle crosses a pre-determined threshold. If the pitch angle goes above this threshold, the IMU is rotated by an angle θ' along the pitch axis while keeping both yaw and roll constant to decrease the pitch angle value. The attitude is computed taken into account this virtual rotation in order for the attitude angles to be relevant of the true attitude experienced by the IMU. The new rotation matrix available for Euler's angles estimation is then as follows:

$$R_{m2n}^{new} = R_{m2n} \times R_{\psi'}^{T} \times R_{\theta'}^{T} \times R_{\varphi'}^{T} \tag{3.18}$$

where:

- $R_{\psi'}^{T}$ is yaw rotation with $\psi' = 0$. Thus $R_{\psi'}^{T} = I_3$.
- $R_{\theta'}^{T}$ is the virtual pitch rotation. $\theta' = -(\theta - threshold)$.
- $R_{\varphi'}^{T}$ is roll rotation with $\varphi' = 0$. Thus $R_{\varphi'}^{T} = I_3$.

The effectiveness of this method is illustrated in Figure 3.7. Corrected angles are plotted using thick lines. As the pitch angle reaches ±90°, both roll and yaw are still observable and can be used for navigation purposes. The efficiency of such an algorithm is also demonstrated in chapter 6 in the case of a pedestrian navigation where the IMU is worn in a pocket with a random attitude.

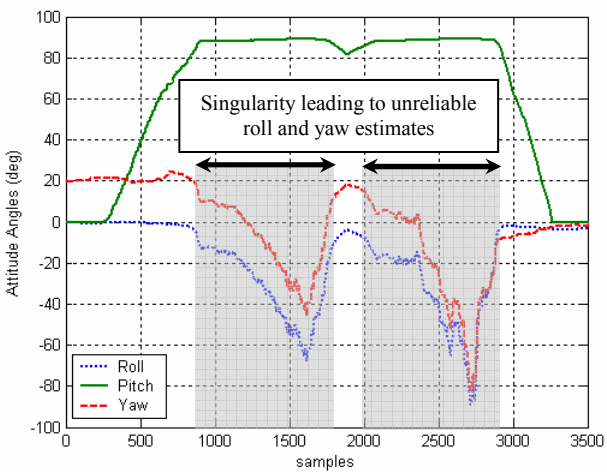

Figure 3.6: Euler's angles singularity issue.

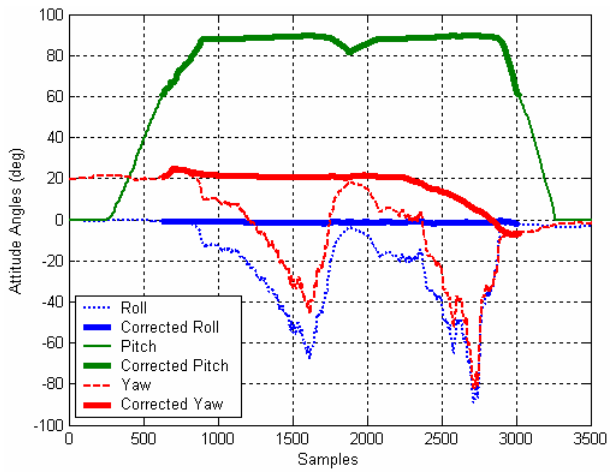

Figure 3.7: Euler's angles singularity resolution.

3.3 MEMS Sensor Unit Performance Overview

The objective of this subsection is not to build a measurement unit from sensors in order to meet any size constraint, sensors assembly cost or accuracy requirements, but rather to analyse the performance of a typical current off-the-shelf IMU. As a consequence, no detail is provided in the following about the sensors technology or the integration issues. The focus is rather put here on the errors that affect the different measurements of the sensors assembly. The Xsens Mti sensors assembly was selected regarding its cost and size for any possible further integration in a handheld device. As a consequence, the MEMS technology is of particular interest. The following presents the IMU used throughout the thesis.

3.3.1 Xsens Motion Tracker

The off-the-shelf IMU used in this thesis is a typical low-cost MEMS-based IMU. Figure 3.8 presents the Xsens Motion Tracker as well as the sensors performance as given by the manufacturer. This IMU is composed of a triad of accelerometers, a triad of gyroscopes and a triad of magnetometers. A temperature sensor and a micro-controller are also comprised in the sensors package. This measurement unit is capable of outputting raw measurements affected by noise, temperature and bias, as performed by an Inertial Sensor Assembly (ISA), as well as calibrated data as done by an IMU.

		rate of turn	acceleration	magnetic field	temperature
Unit		[deg/s]	[m/s^2]	[mGauss]	[°C]
Dimensions		3 axes	3 axes	3 axes	-
Full Scale	(units)	+/- 300	+/- 17	+/- 750	-55…+125
Linearity	(% of FS)	0.1	0.2	0.2	<1
Bias stability	(units 1σ)	5	0.02	0.5	0.5
Scale factor stability	(% 1σ)	-	0.05	0.5	-
Noise density	(units √Hz)	0.1	0.001	0.5 (1σ)	-
Alignment error	(deg)	0.1	0.1	0.1	-
Bandwidth	(Hz)	40	30	10	-

Figure 3.8: Xsens motion tracker and sensors performance.

Laboratory calibration procedures are done to minimise the impact of the measurements errors such as biases, scale factors or temperature dependency. As a consequence, they contribute to the increase of the overall IMU cost. The Xsens MTi price is about $2000, which still makes it a low-cost IMU, because each sensor is about $10 if bought in large volume.

Since the IMU is made of low-cost MEMS sensors, its performance can be expected to be low as well. The next subsections deal with the sensors of the MTi as part of the IMU, i.e. accelerometers and gyroscopes, and give a rough overview of their intrinsic performance.

3.3.1.1 Accelerometer

The accelerometer triad of the IMU is composed of a set of Analog Devices accelerometers orthogonally mounted [27], [28]. According to the corresponding datasheet, they are capable of

0.001 m/s²/√Hz noise for a bandwidth of 30 Hz. To roughly characterise the turn-on biases and scale factors that affect the accelerometer measurements, 10 data sets have been collected while the IMU was idling. The procedure was to let each axis of measurement idle while sensing the gravity vector along the local vertical upwards and then downwards. The biases and scale factors affecting the measurements are estimated according to the following equations:

Measurement n°1 : $m_1 = (1+SF)g + b$	Estimated turn-on bias : $b = (m_1 + m_2)/2$
Measurement n°2 : $m_2 = -(1+SF)g + b$	Estimated Scale Factor : $SF = (m_1 - m_2 - 2g)/2g$

To limit the impact of the noise on the bias estimation, the output of the each accelerometer is averaged for 1 minute for both upward and downwards measurements. Then, bias and scale factors are estimated based on these averaged measurements. The procedure is repeated for each of the three axes of the IMU. Results are given in Figure 3.9 and in Figure 3.10.

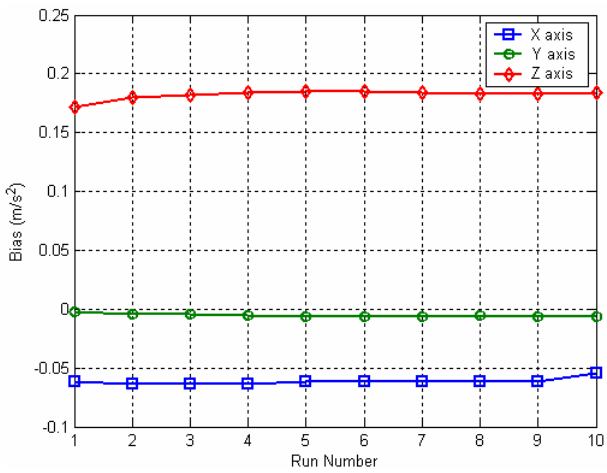

Figure 3.9: Accelerometers turn-on bias.

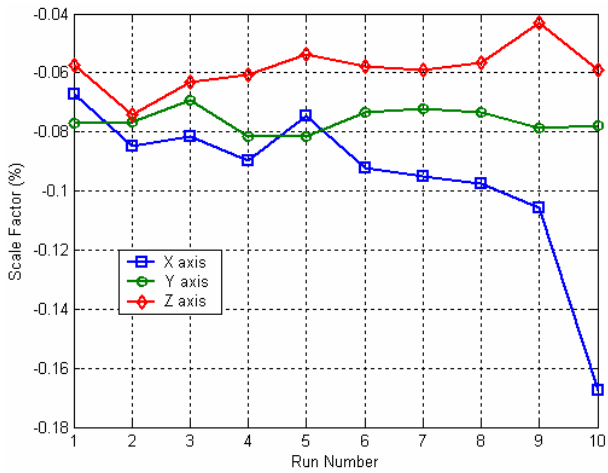

Figure 3.10: Accelerometer turn-on scale factor.

Table 3.1 summarises the errors as mean value and standard deviation for each axis of measurement. Turn-on biases and scale factors are quite stable regarding the quality of the sensors.

	X axis		Y axis		Z axis	
	Bias	*S.F.*	*Bias*	*S.F.*	*Bias*	*S.F.*
Mean	-0.061 m/s²	-0.096 %	-0.005 m/s²	-0.076 %	0.182 m/s²	-0.058 %
Std	0.003 m/s²	0.028 %	0.001 m/s²	0.004 %	0.004 m/s²	0.008 %

Table 3.1: Accelerometer triad turn-on biases and scale factors.

3.3.1.2 Gyroscopes

The gyroscopes of the IMU are also from Analog Devices [26]. They are affected by a 0.1 deg/s/√Hz noise for a bandwidth of 40 Hz. The turn-on bias of the three sensors is characterised using the above 30 measurements by averaging each gyroscope static output. The scale factor of each sensor can be theoretically computed as given in the table below. However, measurements are affected by noise such as the Earth's rotation rate (of the order of 4.10^{-3}) is not distinguishable, as illustrated in Figure 3.12. Therefore, no valuable scale factor estimation was found possible using this methodology, and consequently no characterisation has been done.

Measurement n°1 : $m_1 = (1+SF)\cdot\Omega_E \sin(\lambda)+b$	
Measurement n°2 : $m_2 = -(1+SF)\cdot\Omega_E \sin(\lambda)+b$	
Estimated turn-on bias : $b = (m_1+m_2)/2$	
Estimated Scale Factor : $SF = (m_1 - m_2 - 2\Omega_E \sin(\lambda))/2\Omega_E \sin(\lambda)$	

Figure 3.11 shows the results of the gyroscopes turn-on biases estimation. Compared to the results obtained for accelerometers, the stability of the gyroscopes turn-on bias is worse. Nevertheless, it can be considered to stay within acceptable limits regarding the quality of the sensors. Table 3.2 summarises the bias mean and standard deviation for each axis of measurement.

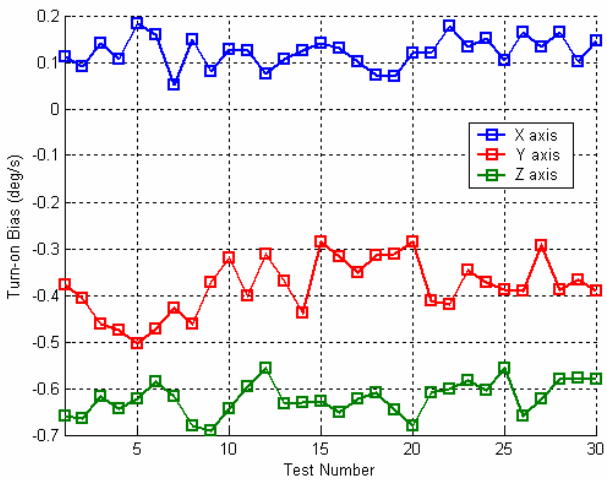

Figure 3.11: Gyroscopes turn-on bias.

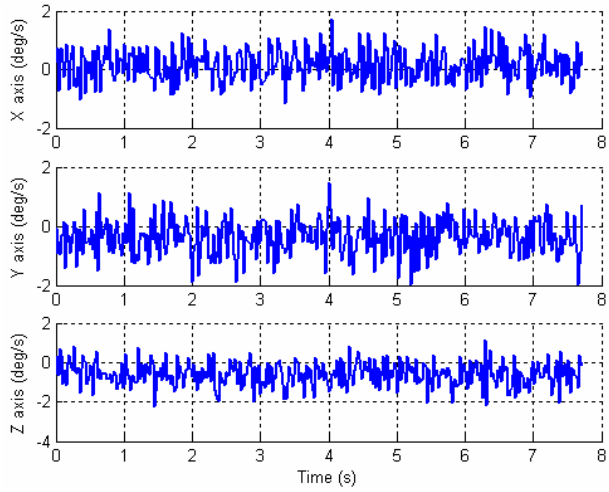

Figure 3.12: Gyroscope triad static outputs.

	X axis	Y axis	Z axis
Mean	0.122 deg/s	-0.381 deg/s	-0.622 deg/s
Std	0.033 deg/s	0.060 deg/s	0.036 deg/s

Table 3.2: Gyroscope triad turn-on biases.

3.3.2 Gyroscope Output Approximation

As pointed out in the above section, the output of each gyroscope is used to update the rotation quaternion that characterises the attitude of the IMU. The rotation rates of the IMU with respect to the navigation frame ***(n)*** is then required. Omitting the effect of the noise, bias and scale factor, the output of a gyroscope can be decomposed as given in equation (3.19).The rotation rate of the mobile with respect to the navigation frame ***(n)***, expressed in the mobile frame ***(m)*** is more specifically detailed.

$$\omega_{m/n}^{(m)} = \omega_{m/I}^{(m)} - R_{n2m}\left(\omega_{n/e}^{(n)} + \omega_{e/I}^{(n)}\right) \tag{3.19}$$

The rotation rate of the Earth (i.e. ECEF frame with respect to Inertial frame) is well known and is equal to ω_E. Using the coordinate transformation as detailed in [9], the rotation rate of ***(e)*** with respect to ***(I)*** and expressed in ***(n)*** is given in equation (3.20). Figure 3.14 illustrates the components in the navigation frame of such a rotation rate for typical latitude angles. The maximum

rate is obtained either when the centre of the navigation frame is at the equator or at the Earth's pole. It is equal to the Earth's rotation rate magnitude 4.17×10^{-3} deg/s.

$$\omega_{e/I}^{(n)} = R_{e2n} \cdot \omega_{e/I}^{(e)} = \omega_E \cdot \begin{bmatrix}\cos(\lambda) & 0 & -\sin(\lambda)\end{bmatrix}^T \tag{3.20}$$

where :

- ω_E is the Earth rotation rate. ($\approx 7.2924\cdot10^{-5}\, rad/s = 4.17\cdot10^{-3}$ deg/s)

The rotation rate of ***(n)*** with respect to ***(e)*** and expressed in the navigation frame ***(n)*** is application dependent. In the navigation frame, the rotation vector can be expressed as given in equation (3.21) [9]:

$$\omega_{n/e}^{(n)} = \begin{bmatrix}\dot{\Phi}\cos(\lambda) & -\dot{\lambda} & -\dot{\Phi}\sin(\lambda)\end{bmatrix}^T \tag{3.21}$$

where :

- λ is the geodetic latitude of the mobile.
- Φ is the geodetic longitude of the mobile.
- $\dot{\lambda}$ is the latitude rate.
- $\dot{\Phi}$ is the longitude rate.

The longitude and latitude rates are not directly used as measurements. It is rather preferred to introduce the velocity of the mobile in the navigation frame, using the basic three relationships given below [9]. Consequently, the rotation vector from ***(n)*** with respect to ***(e)***, expressed in ***(n)*** is given by equation (3.22).

1. $\dot{\lambda} = \dfrac{v_{North}}{R_\lambda + h}$ with $R_\lambda = \dfrac{a(1-e^2)}{\sqrt[3/2]{1-e^2\sin^2(\lambda)}}$
2. $\dot{\Phi} = \dfrac{v_{East}}{(R_\Phi + h)\cdot\cos(\lambda)}$ with $R_\Phi = \dfrac{a}{\sqrt{1-e^2\sin^2(\lambda)}}$
3. $\dot{h} = -v_{Down}$

where :

- h is the geodetic height of the mobile.
- R_λ is the radius of curvature in a meridian.
- R_Φ is the transverse radius of curvature.
- a is the semi-major axis of the WGS-84 ellipsoid.
- e is the eccentricity of the WGS-84 ellipsoid.

$$\omega_{n/e}^{(n)} = \begin{bmatrix}\dfrac{v_{East}}{R_\Phi + h} & -\dfrac{v_{North}}{R_\lambda + h} & -\dfrac{v_{East}\tan(\lambda)}{R_\Phi + h}\end{bmatrix}^T \tag{3.22}$$

In Figure 3.13 is plotted the corresponding three components and the rotation rate magnitude, assuming no altitude (h=0) and North and East velocities of 140 km/h, such that the velocity magnitude is roughly equal to 200 km/h, which is an extreme use case given the

application field of personal positioning. For a gyroscope used in medium latitudes (as it is the case for France), it can be considered that the upper bound does not exceed 1.4×10^{-3} deg/s.

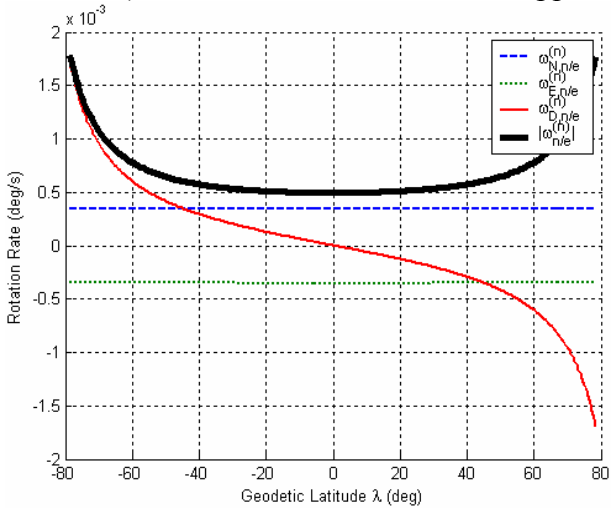

Figure 3.13: Rotation rate of *(e)* with respect to *(I)* expressed in *(n)*. $v_N=v_E=140$ km/h, h=0.

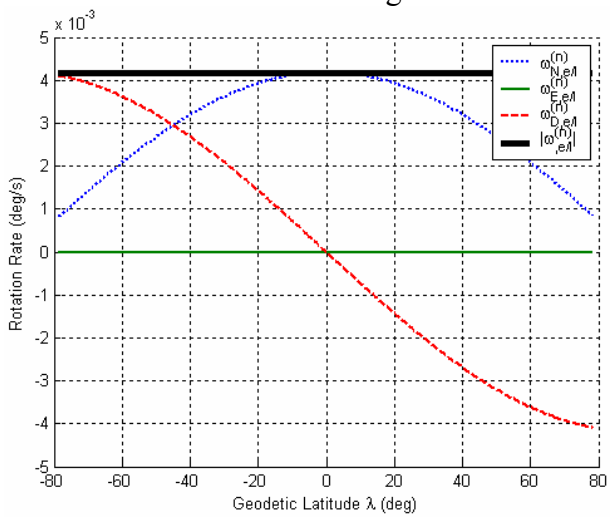

Figure 3.14: Rotation rate of *(e)* with respect to *(I)* expressed in *(n)*.

From the previous statements and taking into account the performance of the gyroscopes in the IMU, the two above rotation rates can be considered of negligible magnitude. In other words, they can be considered as acting as a constant bias b_{rr} of magnitude about 5.5×10^{-3} deg/s, which is far below the noise affecting the measurements.

As a consequence, it is assumed throughout the thesis that the rotation rate of the mobile with respect to the navigation frame can be approximated by the output of the gyroscope, i.e. the rotation rate of ***(m)*** with respect to ***(I)***, as written below in equation (3.23).

$$\omega_{m/n}^{(m)} = \omega_{m/I}^{(m)} + b_{rr} \approx \omega_{m/I}^{(m)} \tag{3.23}$$

3.4 Classical Inertial Navigation System

In this section, the relationship between the specific force sensed by the accelerometers as defined in equation (3.2), and the velocity of the mobile with respect to ***(e)*** expressed in ***(n)*** is derived in order to establish the basic INS mechanisation. In the following, superscript between brackets will stand for the coordinate system in which vectors are expressed, whereas index will stand for frames in which the expressions are computed.

3.4.1 Fundamental Inertial Differential Equation

Let M be a point of a moving mobile, O the origin of the inertial frame ***(I)***, and O' those of the ECEF frame ***(e)***. The time derivative of the vector associated to the position of M with respect to ***(I)*** and expressed in ***(I)***, is given by equation (3.24).

$$\left(\frac{d}{dt}\vec{M}^{(I)}\right)_I = \left(\frac{d}{dt}R_{e2I}\vec{M}^{(e)}\right)_I = \vec{v}_{m/e}^{(I)} + \vec{\Omega}_{e/I}^{(I)} \wedge \vec{M}^{(I)} \tag{3.24}$$

where :
- R_{e2I} is the rotation matrix from ***(e)*** to ***(I)***.
- $\vec{M}^{(I)}$ is the position vector of the mobile, expressed in ***(I)***.
- $\vec{M}^{(e)}$ is the position vector of the mobile, expressed in ***(e)***.
- $\vec{\Omega}_{e/I}^{(I)}$ is the rotation vector of ***(e)*** relative to ***(I)***, expressed in ***(I)***.
- $\vec{v}_{m/e}^{(I)}$ is the velocity of the mobile relative to ***(e)***, expressed in ***(I)***.
- ^ is the cross-product operator.

The acceleration of M expressed in the inertial frame ***(I)*** is then deduced from equation (3.24) as its time derivative. Its expression is given below in equation (3.25).

$$\left(\frac{d^2}{dt^2}\vec{M}^{(I)}\right)_I = \left(\frac{d}{dt}\vec{v}_{m/e}^{(I)}\right)_I + \vec{\Omega}_{e/I}^{(I)} \wedge \vec{v}_{m/e}^{(I)} + \vec{\Omega}_{e/I}^{(I)} \wedge \left(\vec{\Omega}_{e/I}^{(I)} \wedge \vec{M}^{(I)}\right) \tag{3.25}$$

The accelerometers measure a specific force as described in equation (3.2), which is the acceleration of the mobile the sensors are mounted on with respect to ***(I)*** and expressed ***(m)***. On the other hand, the acceleration of the mobile relative to ***(I)*** and expressed in ***(m)*** is also given by equation (3.26).

$$\vec{a}_{m/I}^{(m)} = R_{I2m} \cdot \left(\frac{d^2}{dt^2}\vec{M}^{(I)}\right)_I \tag{3.26}$$

where :
- R_{I2m} is the rotation matrix from ***(I)*** to ***(m)***.

The combination of equations (3.2) and (3.26) yields the following equation involving the acceleration of the mobile, the specific force and the gravitational field:

$$\left(\frac{d^2}{dt^2}\vec{M}^{(I)}\right)_I = \vec{f}^{(I)} + \vec{G}_M^{(I)} \tag{3.27}$$

Equation (3.27) shows that the acceleration of the mobile can be fully expressed as a function of two known variables that are the specific force f and the gravitational field G_M. Equation (3.25) can then be transformed into equation (3.28), as detailed below:

$$\left(\frac{d}{dt}\vec{v}_{m/e}^{(I)}\right)_I = \vec{f}^{(I)} + \vec{g}_M^{(I)} - \vec{\Omega}_{e/I}^{(I)} \wedge \vec{v}_{m/e}^{(I)} \tag{3.28}$$

where:
- $\vec{g}_M^{(I)}$ is the local gravity vector, which is defined as $\vec{G}_M^{(I)} - \vec{\Omega}_{e/I}^{(I)} \wedge \left(\vec{\Omega}_{e/I}^{(I)} \wedge \vec{M}^{(I)}\right)$.

The ***(e)*** frame is used as a reference for navigation purposes (i.e. all displacements are done relative to that reference). However, it is more suitable to express the displacement directions in the navigation frame, which is more adapted to understand the change in position velocity and attitude. Consequently, equation (3.28) shall be rewritten in the navigation frame for further use.

$$\left(\frac{d}{dt}\vec{v}_{m/e}^{(n)}\right)_n = \vec{f}^{(n)} + \vec{g}^{(n)}(M) - \left(\vec{\Omega}_{n/e}^{(n)} + 2\vec{\Omega}_{e/I}^{(n)}\right) \wedge \vec{v}_{m/e}^{(n)} \tag{3.29}$$

where :

- $\vec{v}_{m/e}^{(n)}$ is the velocity of the mobile relative to ***(e)***, expressed in ***(n)***.
- $\vec{\Omega}_{n/e}^{(n)}$ is the rotation vector of ***(n)*** relative to ***(e)***, expressed in ***(n)***.
- $\vec{\Omega}_{e/I}^{(n)}$ is the rotation vector of ***(e)*** relative to ***(I)***, expressed in ***(n)***.

The rotation vector from the navigation frame ***(n)*** with respect to the ECEF frame ***(e)*** is application dependent. It has been detailed in the previous subsection and its expression is given in equation (3.22). It is obvious that the rotation vector from ***(e)*** with respect to ***(I)*** and expressed in ***(e)*** has only one component along the z axis of the ECEF frame ***(e)***. The expression of the rotation rate of ***(e)*** with respect to ***(I)*** and expressed in ***(n)*** is given in equation (3.20). All the terms in equation (3.29) are then fully described as functions of known quantities. The classical inertial differential equation involving the velocity of the mobile expressed in ***(n)*** is:

$$\begin{bmatrix} \dot{v}_{North} \\ \dot{v}_{East} \\ \dot{v}_{Down} \end{bmatrix}^{(n)} = R_{m2n} \cdot \begin{bmatrix} a_x \\ a_y \\ a_z \end{bmatrix}^{(m)} + \begin{bmatrix} \xi_g \\ -\eta_g \\ g_n \end{bmatrix}^{(n)} - \left(\begin{bmatrix} v_{East}/(R_\Phi + h) \\ -v_{North}/(R_\lambda + h) \\ -v_{East} \cdot \tan\lambda/(R_\Phi + h) \end{bmatrix} + 2 \cdot \begin{bmatrix} \Omega_E \cos\lambda \\ 0 \\ -\Omega_E \sin\lambda \end{bmatrix} \right) \wedge \begin{bmatrix} v_{North} \\ v_{East} \\ v_{Down} \end{bmatrix}_n \tag{3.30}$$

where :

- $a = \begin{bmatrix} a_x & a_y & a_z \end{bmatrix}_m^T$ is the acceleration measured by the accelerometers in ***(m)***.
- $\vec{g} = \begin{bmatrix} \xi_g & -\eta_g & g_n \end{bmatrix}^T$ is the local gravity vector, expressed in ***(n)***. The g_n component can be computed using for example the Somigliana model [20].

3.4.2 INS Mechanisation in the Navigation Frame

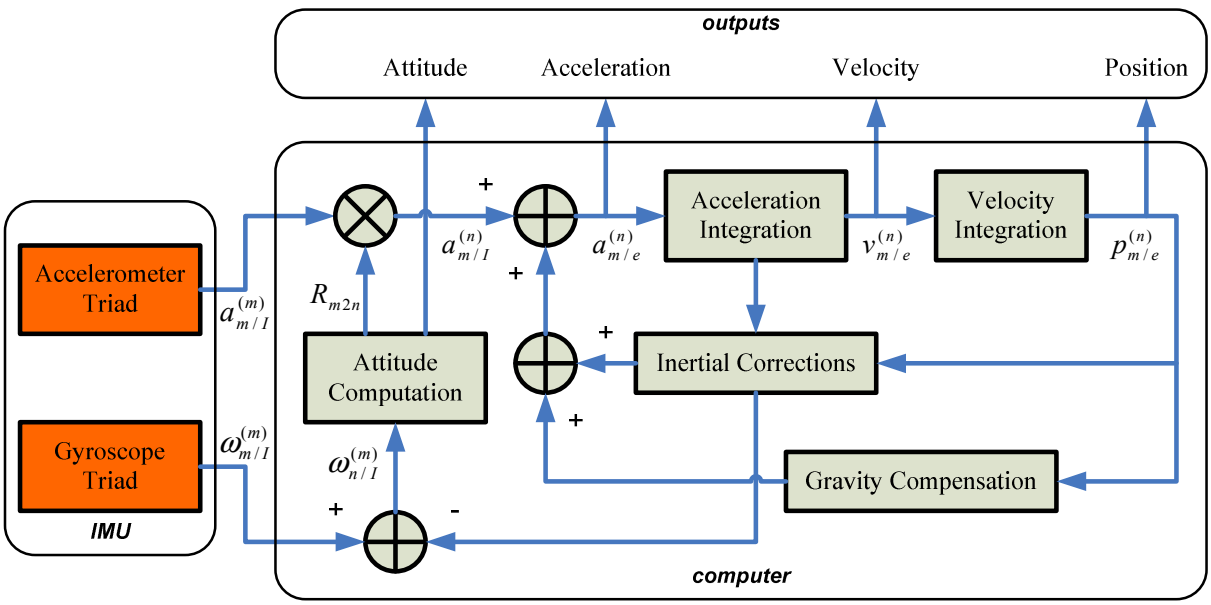

Figure 3.15: Inertial Navigation System (INS) mechanisation.

According to equation (3.30), the mechanisation of the classic inertial navigation system is illustrated above in Figure 3.15.

3.4.3 Expected Accuracy

The accuracy of the navigation system presented in Figure 3.15 mainly depends on two factors. The most important one is the quality of the sensors used in the IMU, which relies on the manufacturing process and the sensor technology. Both accelerometers and gyroscopes measurements are indeed affected by biases and scale factors that introduce drift at the different stages of the INS mechanisation. All these errors contribute to the decrease of the overall INS accuracy.

The second factor responsible for position, velocity and attitude errors comes from the approximations made in the INS mechanisation. These approximations are twofold: the first order Taylor expansion models used to compute some parameters (as for example quaternion), and the use of some quantities estimated at epoch k for the computation process at epoch k+1. These approximations are nevertheless considered negligible with respect to the impact of the biases.

In order to model the performance of such a mechanised Inertial Navigation System, a propagation error methodology is used. The derivation of the dynamic error model of the INS in the navigation frame, whose mechanisation is illustrated in Figure 3.15, is fully described in [9]. No more detail about it is given in the following. According to [9], the state transition model of the position, velocity, attitude and sensors errors is those of equation (3.31), where all sub-matrices are developed in details in [9].

$$\begin{bmatrix} \delta\dot{p} \\ \delta\dot{v} \\ \delta\dot{\rho} \\ \delta\dot{\varepsilon}_a \\ \delta\dot{\varepsilon}_g \end{bmatrix} = \begin{bmatrix} Fpp & Fpv & F_{p\rho} & 0 & 0 \\ Fvp & Fvv & Fv\rho & F_{v\varepsilon_a} & 0 \\ F\rho p & F\rho v & F\rho\rho & 0 & F_{\rho\varepsilon_g} \\ 0 & 0 & 0 & F_{\varepsilon_a\varepsilon_a} & 0 \\ 0 & 0 & 0 & 0 & F_{\varepsilon_g\varepsilon_g} \end{bmatrix} \cdot \begin{bmatrix} \delta p \\ \delta v \\ \delta\rho \\ \delta\varepsilon_a \\ \delta\varepsilon_g \end{bmatrix} + \begin{bmatrix} n_p \\ n_v + n_{\varepsilon_a} \\ n_\rho + n_{\varepsilon_g} \\ n_{\varepsilon_a} \\ n_{\varepsilon_g} \end{bmatrix} \tag{3.31}$$

where:
- δp is the position error in the navigation frame.
- δv is the velocity error in the navigation frame.
- $\delta\rho$ is the attitude error.
- $\delta\varepsilon_a$ is the accelerometers bias and scale factor error.
- $\delta\varepsilon_g$ is the gyroscope bias error.

The minimal state vector is augmented by accelerometers errors $\delta\varepsilon_a$ including bias and scale factor models, and gyroscopes errors $\delta\varepsilon_g$ only including the bias model. The performance of the IMU can then be assessed using the propagation model of equation (3.31) and the sensors errors as determined in subsections 3.3.1.1 and 3.3.1.2. Gyroscope scale factors are not modelled in the following since no actual characterisation has been done, as justified in subsection 3.3.1.2.

The horizontal RMS position error predicted through the propagation of the INS errors is illustrated in Figure 3.16. It corresponds to the dashed blue plot. Given the low-cost sensors used in the IMU, the horizontal RMS error is predicted to be nearly 570 metres after 60 seconds.

In order to assess this simulation result, real data were collected from the idling Xsens IMU over 60 seconds and processed through the navigation algorithm of Figure 3.15. Prior to data collection, the IMU was switch on about 10 minutes in order for the temperature inside the sensors assembly to be quite homogenous, preventing in-run biases from introducing additional errors. The resulting horizontal RMS error is plotted Figure 3.16 as the red solid curve. Both horizontal RMS errors are close from each other. There is only a slight difference mainly due to the accuracy of the stochastic models chosen for biases and scale factor modelling, which certainly do not match perfectly the reality. Nevertheless, the error propagation model matches quite well the INS static behaviour so that the error model is used in the following to find ways for improving the navigation solution.

To analyse the contribution of each error factor onto the overall horizontal RMS error, three independent error propagation simulations are conducted. They all involve only one error parameter among accelerometer bias, accelerometer scale factor and gyroscope bias to avoid any interference between these factors. The values used in the different error models are again these determined in subsections 3.3.1.1 and 3.3.1.2. The results of the three simulations are plotted in Figure 3.17. Among the three error sources, the bias affecting the gyroscope measurements has the highest impact on the horizontal RMS accuracy, as shown by the blue solid curve (more than 650 metres error due to gyroscope bias only). It significantly degrades the INS position accuracy. Opposite, the accelerometer scale factor has a very little effect on the overall accuracy. The impact of the accelerometer bias is non negligible (about 100 metres per minute) but less important than the gyroscope one.

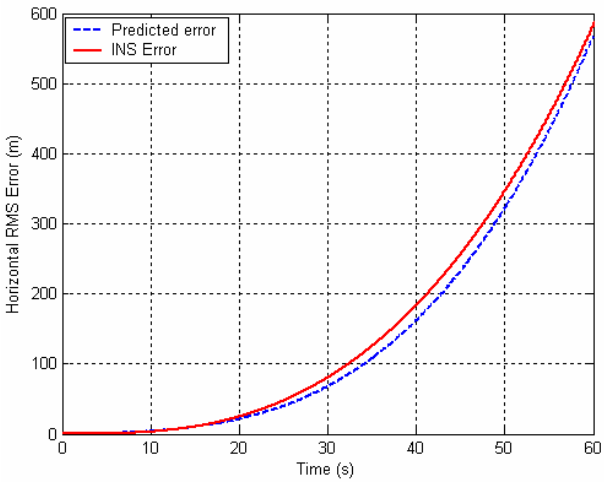

Figure 3.16: Predicted and actual INS horizontal RMS error.

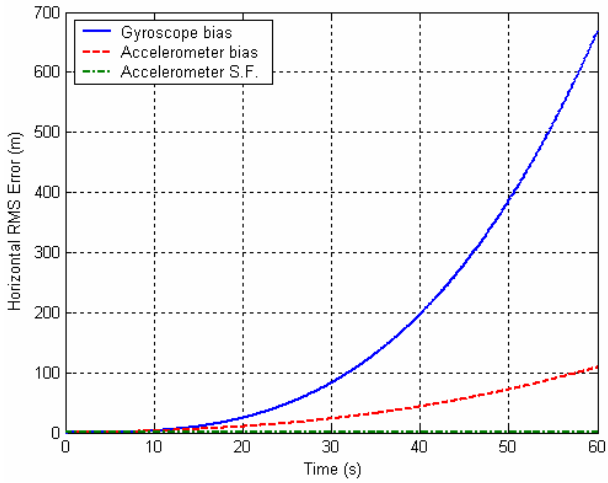

Figure 3.17: Biases and scale factor impact on INS horizontal accuracy.

As a consequence of the above simulations, the improvement of the navigation algorithm relies first on the reduction of the effect of the gyroscope bias and then accelerometer bias. Scale factor effect will be neglected in the following.

3.5 The Particular Case of the Pedestrian Navigation

According to the previous results, the inertial navigation using a low-cost IMU as for instance the Xsens's MTi is very sensitive to large errors that affect all the computation stages of a

classic Inertial Navigation System. In order to enhance the accuracy of a low-cost INS, errors affecting the sensors have to be accurately modelled. This section focuses on the particular case of the pedestrian navigation, which aims at avoiding the double integration of the acceleration in the navigation frame to limit the impact of the different biases. It presents another approach consisting in the modification of the classic mechanisation taking into account the relationship between the acceleration of the pedestrian and its velocity or step length.

3.5.1 Mechanisation in the Navigation Frame

According to medical researches as introduced for instance in [29] and [30], one can establish a relationship between the velocity or step length of a walking pedestrian and some parameters that characterise the acceleration experienced by this pedestrian. The basic relationships are given below in equation (3.32) and equation (3.33).

$$s_p = f_1(\textit{individual parameters}) \tag{3.32}$$

$$v_p = f_2(\textit{individual parameters}) \tag{3.33}$$

where:

- s_p is the step length of the walking pedestrian.
- v_p is the velocity of the walking pedestrian.
- f_1, f_2 are the model functions. They both can be linear or non linear.
- *individual parameters* are the processing result of the acceleration magnitude. They are detailed in the following.

The individual parameters used to model the actual pedestrian velocity / step length are computed based on the measured acceleration of the walking pedestrian. However, this acceleration is biased by the gravity vector so that the sensors mounted onto the pedestrian do not exactly measure the actual acceleration. Moreover, the acceleration may change very much depending on the measurement direction [29] (the longitudinal acceleration pattern of a pedestrian is completely different from the lateral one). To get rid of the orientation of the IMU containing the accelerometers, the characterisation of the pedestrian velocity / step length is done using the global acceleration signal (i.e. the acceleration magnitude) defined below in equation (3.34):

$$a_k = \sqrt{\left(a_{x,k}^{(m)}\right)^2 + \left(a_{y,k}^{(m)}\right)^2 + \left(a_{z,k}^{(m)}\right)^2} \tag{3.34}$$

where:

- a_k is the global acceleration magnitude sensed by the IMU at epoch k.
- $a_{x,k}^{(m)}$ is the acceleration along the x axis of the IMU, expressed in ***(m)*** at epoch k.
- $a_{y,k}^{(m)}$ is the acceleration along the y axis of the IMU, expressed in ***(m)*** at epoch k.
- $a_{z,k}^{(m)}$ is the acceleration along the z axis of the IMU, expressed in ***(m)*** at epoch k.

Based on the global acceleration signal of equation (3.34), the individual parameters (as defined in the following) are computed to model the velocity / step length of the walking pedestrian. These parameters are chosen in such a way they reflect the behaviour of the walk (a non exhaustive

list is given in the next subsection 3.5.2.1). To fit the mathematical model with the actual velocity/step length model, a regression algorithm (Least Squares) is then applied on the computed parameters, which requires an external positioning source to give a reference for velocity measurements or travelled distance.

In the application aimed within this thesis (localisation of one user indoors), the user is likely to go in locations where GPS measurements are very affected by multipath. It is well known that Doppler measurements are less affected in such environments, so that it is theoretically more interesting to use velocity measurements rather than position measurements for the model calibration. As a consequence, the focus is from this point put on the modelling of the pedestrian velocity, which can be expressed as given in equation (3.35). The curvilinear distance travelled by the pedestrian is then estimated by integrating the modelled velocity.

$$v_p = \alpha_1 \cdot Param_1^{\beta_1} + \cdots + \alpha_i \cdot Param_i^{\beta_i} \tag{3.35}$$

where:
- i is the index of the parameters used to model the pedestrian velocity.
- α_x and β_x are the regression coefficients.
- $Param_x$ are the parameters computed based on the total acceleration.

The azimuth of displacement must then be estimated to reconstruct the trajectory followed by the pedestrian. There are two typical ways of estimating the azimuth of displacement, depending on the motion of the IMU, i.e. whether it follows those of the pedestrian or not. In the first case, the heading computed by the IMU is the displacement direction biased by an additive constant due to the non alignment of the IMU heading axis with the direction of walk of the pedestrian. In the second case, the true azimuth of displacement is not the heading provided by the IMU, since the IMU has got its own movement relative to the pedestrian. This use case is very difficult to handle. It is specifically addressed in subsection 3.5.4.

Finally, once the curvilinear travelled distance and the displacement direction are estimated, the trajectory can be reconstructed through a classical Dead Reckoning algorithm, whose equations are given below.

$$N_{k+1} = N_k + d_{[k,k+1]} \cdot \cos(\psi_k) \tag{3.36}$$

$$E_{k+1} = E_k + d_{[k,k+1]} \cdot \sin(\psi_k) \tag{3.37}$$

where :
- ψ_k is the azimuth of displacement at epoch k.
- N_k is the position of the pedestrian at epoch k.
- E_k is the position of the pedestrian at epoch k.
- $d_{[k,k+1]}$ is the curvilinear distance travelled between epoch k and k+1.

The following focuses on the parameters used in the model, the choice of their combination and the model to estimate the velocity of the pedestrian. The stability of the regression coefficient and the minimum amount of information needed to build an accurate pedestrian velocity model are also addressed.

3.5.2 Travelled Distance Estimation

3.5.2.1 Parameters

A non-exhaustive list of potential parameters that may be used to model the pedestrian velocity is given below. As explained above, all the parameters are computed based on the total acceleration expressed in equation (3.34) to get rid of the IMU orientation. These parameters can be computed over one stride or over a predetermined time window depending on the time tag that is chosen to update the position solution. The parameters used in the following of the document are defined in Table 3.3 and given according to a time-tagged reference time. It is straightforward to derive the corresponding expressions for a step-tagged navigation system (i.e. navigation systems based on step occurrences).

Parameter	Equation	Comments
MEAN	$\frac{1}{n+1}\sum_{i=k-n}^{k} a_i$	This parameter is the mean of the signal computed at epoch k over n samples
VAR_1	$\mathrm{var}\left(a_{[k-n,k]}\right)$	This parameter is the variance of the signal computed from the last n samples of the total acceleration
VAR_2	$\sum_{i=k-n+1}^{k} \frac{\left(a_i - MEAN_k\right)^2}{n}$	This parameter is slightly different from the above VAR_1 parameter. It represents the jerk relative to the mean of the total acceleration during the time span n instead of the jerk relative to contiguous samples.
RMS_1	$\sqrt{VAR_{1,k}}$	This parameter is the square root of VAR_1 at epoch k.
RMS_2	$\sqrt{VAR_{2,k}}$	This parameter is the square root of VAR_2 at epoch k.
ABS	$\sum_{i=k-n+1}^{k} \frac{\left\lvert a_i - MEAN_k \right\rvert}{n}$	This parameter is the absolute value of the acceleration amplitude over n samples at epoch k.
AMP	$\frac{\max(a)_{step_k}}{\max(a)_{step_k} - \min(a)_{step_k}}$	This parameter is the relative amplitude of the total acceleration in a window of length n. This parameter is more adapted to system with step-based reference time, in which it is defined as the relative amplitude of the acceleration signal in one stride.
M_3	$\sum_{i=k-n+1}^{k} \frac{\left(a_i - MEAN_k\right)^3}{n}$	This parameter is the third order moment computed from the total acceleration signal. Its main benefit is that the sign of this parameter depends on the jerk of the signal used for computation.
FREQ	– Step detection – Periodogram – HR techniques – Kalman filtering	This parameter is the frequency of the acceleration signal that can be estimated using the four methods listed opposite over a specific time window. The efficiency of the four methods is discussed in appendix D

Table 3.3: Candidate parameters to the pedestrian velocity model.

Once the parameters are defined, one has to choose some of them to establish a velocity model. The selection is based on a correlation analysis between these candidate parameters and the pedestrian velocity. In order not to get the model too complex and also avoid redundancy, a second correlation analysis between the selected parameters is also conducted.

Two sets of data have been collected for parameters selection. For these two records, the IMU was placed in a pocket of the pedestrian and not moved. The walks took place in a flat surface with various paces in order to cover the whole velocity spectrum of a pedestrian, as shown in Figure 3.18 and Figure 3.19 (another solution would have been to collect data for several tests done with different constant velocities and then process these tests together to find the best parameters). The velocity of reference is computed in each test by differentiating the post-processed DGPS positions. Both rover and base station GPS data are recorded at a sampling rate of 4Hz, and then re-sampled to match the sampling frequency of IMU data (50 Hz). The Shannon requirement is not met by the GPS sampling rate, but the true mean velocity of displacement is nevertheless very accurately estimated. Only the typical oscillations of the walk are not clearly observable due to the low GPS sampling rate, but this will not impact the identification of the best parameters.

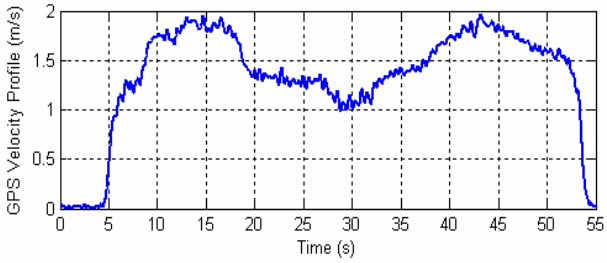

Figure 3.18: DGPS velocity of reference. Walk n°1.

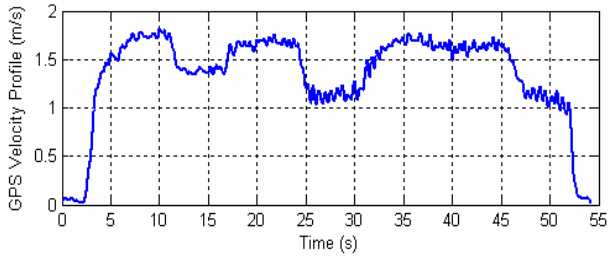

Figure 3.19: DGPS velocity of reference. Walk n°2.

The correlation coefficient used to characterise each parameter is defined in equation (3.38). Correlations are computed before the regression process, as explained in section 3.5.2.3. If a linear or non-linear regression process would have first been applied to fit the parameters' shape to the velocity of reference, the correlation result would have been better. Nevertheless, the way the correlations are computed provides results representative of the importance of the different parameters.

$$R_{p_i,v_{ref}} = \frac{\mathrm{cov}(p_i, v_{ref})}{\sqrt{\mathrm{cov}(p_i, p_i)\cdot \mathrm{cov}(v_{ref}, v_{ref})}} \tag{3.38}$$

where :

- p_i is the ith parameter.
- v_{ref} is the velocity of reference.
- cov is the covariance operator.

The focus is first put on the characterisation of the parameters based on a step-tagged reference time. In this approach, the parameters are computed between step occurrences. The correlation results for the parameters computed each step using the signal between two successive step occurrences are presented in Table 3.4. The frequency FREQ is the only parameter that matches the variations of the reference velocity quite well, whatever is the test walk. The MEAN and ABS parameters have the next two best (but poor) correlation coefficients.

The correlation results for the parameters computed every two steps using the acceleration signal between three successive step occurrences are detailed in Table 3.5. All the parameters are well suited to model the reference velocity, except the parameter M_3. The averaging effect of processing a signal with a longer duration increases the correlation property of the parameters with

respect to the actual pedestrian velocity. However, this reduces the capability of estimating high dynamic changes in the pace of the pedestrian, so that a trade-off shall be found. From the various tests that have been conducted, it has been found that a 2 steps smoothing can be considered as the upper bound of an averaging time window.

Parameters	MEAN	FREQ	VAR_1	VAR_2	RMS_1	RMS_2	ABS	AMP	M_3
Walk n°1	0.726	0.944	0.405	0.404	0.403	0.400	0.440	0.358	0.247
Walk n°2	0.692	0.942	0.379	0.379	0.399	0.386	0.421	0.419	0.269

Table 3.4: Correlation results. Parameters computed each step.

Parameters	MEAN	FREQ	VAR_1	VAR_2	RMS_1	RMS_2	ABS	AMP	M_3
Walk n°1	0.919	0.968	0.924	0.924	0.940	0.940	0.949	0.821	0.536
Walk n°2	0.897	0.966	0.894	0.893	0.908	0.906	0.939	0.906	0.567

Table 3.5: Correlation results. Parameters computed every 2 steps.

For both reference walk n°1 and n°2, the parameters with the highest correlation coefficient are plotted in Figure 3.20 and Figure 3.21. The relationship between the parameters and the true displacement velocity computed with DGPS measurements is clearly observable. Among all, the frequency FREQ is the best one that closely matches the pedestrian displacement velocity.

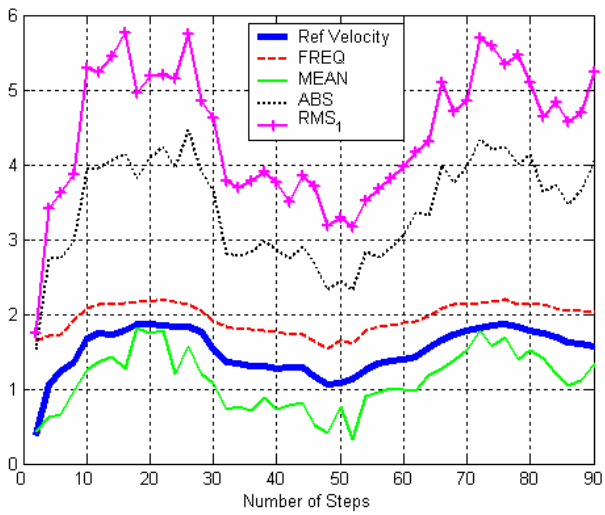

Figure 3.20: Best parameters computed every 2 steps. Walk n°1.

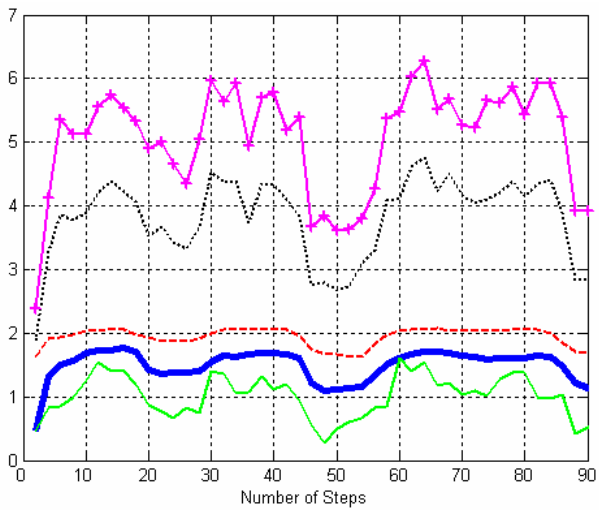

Figure 3.21: Best parameters computed every 2 steps. Walk n°2.

As a first conclusion for systems based on step occurrences, the parameters that are suitable to model the velocity of the pedestrian are FREQ, MEAN, VAR_1 or VAR_2, RMS_1 or RMS_2 and ABS. Among these parameters, some may be correlated to each other so that it would be worth to decrease the model complexity at the expense of some loss of accuracy by removing some of them.

The cross-correlation between the selected parameters has been computed for every couple of parameters. Results are given in Table 3.6 for parameters computed each step, and in Table 3.7 for parameters computed every two steps. From these tables, it can be seen that the parameter ABS has a good correlation with all the three other parameters, whatever the computation time window.

As a consequence, ABS is no more considered as part of the pedestrian velocity model. The remaining and retained parameters are thus MEAN, FREQ and RMS_1.

	MEAN	FREQ	RMS_1	ABS
MEAN	1	0.602	-0.027	-0.026
FREQ	0.602	1	0.463	0.498
RMS_1	-0.027	0.463	1	0.989
ABS	-0.026	0.498	0.989	1

Table 3.6: Cross-correlation coefficients (1 step).

	MEAN	FREQ	RMS_1	ABS
MEAN	1	0.871	0.821	0.876
FREQ	0.871	1	0.895	0.922
RMS_1	0.821	0.895	1	0.982
ABS	0.876	0.922	0.982	1

Table 3.7: Cross-correlation coefficients (2 steps).

The same selection method is applied using a time-tagged reference. Several time windows have been tested (spans of 1s, 2s and 5s), on which the parameters are computed with a rate equal to the IMU sampling rate. This high computation rate allows a better dynamic restitution of the velocity of the pedestrian, as it is illustrated in Figure 3.22 and Figure 3.23. The accuracy of the model is thus increased. The same conclusion as for step occurrences based analysis can be drawn. The parameters FREQ, MEAN, RMS_1 and ABS have the best correlation coefficients and the cross-correlation between the parameters shows that ABS can be removed from the parameters set that match the better the dynamic of the pedestrian velocity.

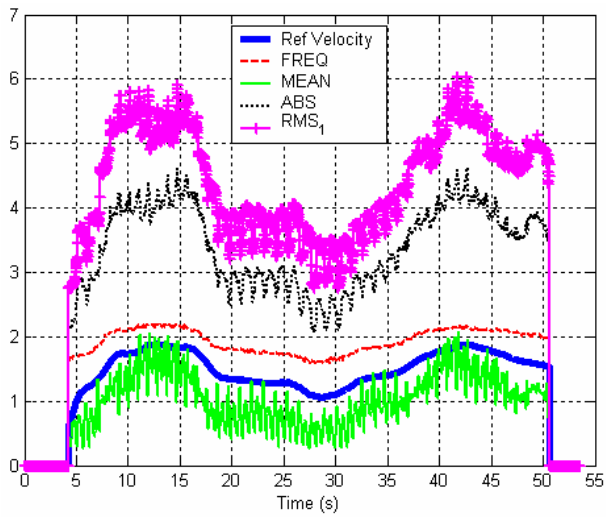

Figure 3.22: Best parameters computed over 2s. Walk n°1.

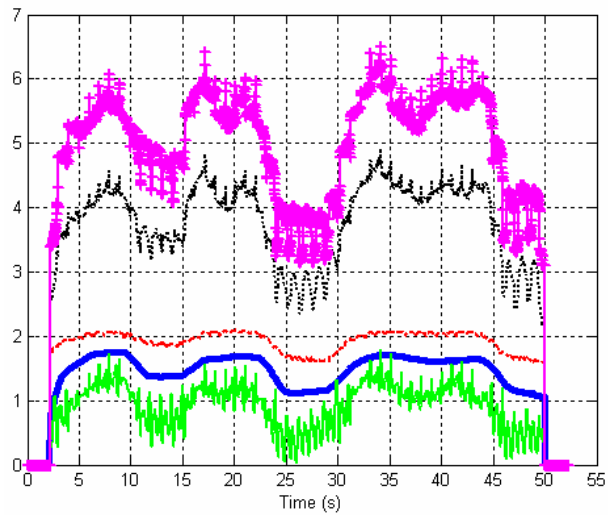

Figure 3.23: Best parameters computed over 2s. Walk n°2.

3.5.2.2 Velocity Models

The selection of the parameters as discussed in the previous subsection focused on the correlation between the parameters and the GPS velocity of reference. Because the computed correlation value is relevant of a linear correlation, the parameters MEAN, FREQ and RMS_1 shall be part of a linear model of the pedestrian velocity. However, a non-linear model might give better results. Consequently, the two possible models are studied in the following. The general velocity model is given in equation (3.39), whereas the simpler linear model is given in equation (3.40).

$$v_p = \alpha_1 \cdot Mean^{\beta_1} + \alpha_2 \cdot Freq^{\beta_2} + \alpha_3 \cdot RMS_1^{\beta_3} \tag{3.39}$$

$$v_p = \gamma_1 \cdot Mean + \gamma_2 \cdot Freq + \gamma_3 \cdot RMS_1 \tag{3.40}$$

where:

- α_i and β_i are the regression coefficients of the non linear pedestrian velocity model.
- γ_i are the regression coefficients of the linear pedestrian velocity model.

3.5.2.3 Regression Coefficients

The purpose of this subsection is to assess the efficiency of the velocity models defined in equations (3.39) and (3.40). It also aims at analysing whether it is worth using a non linear model or a linear model, regarding the expected performance with respect to the increase of complexity.

3.5.2.3.1 Impact of the Velocity

This subsection analyses the impact of the velocity of walk on the regression coefficients. Several straight test walks with different paces were recorded for that purpose. In all the tests, the IMU is placed in a pocket of the pedestrian and not moved. Three typical velocity ranges (namely low, normal and high) have been more specifically tested, as illustrated in Figure 3.28. The blue plot with squares stands for the mean pedestrian velocity computed based on DGPS measurements. The dashed red plot is the averaged velocity for typical tests in the same range of velocity.

The non-linear model is first analysed. For that purpose, both non-linear iterative least square estimation (ILSQ, see Appendix C) method and the Matlab least square (LSQ) curve fitting function have been tested. The two methods have been tested on the data recorded during the trials and it sometimes appeared that the non-linear model could not be estimated because of the divergence of the LSQ algorithm. To cope with this issue, the non-linear regression was performed independently for each parameter and the model was reconstructed with equal weight for all the single regression models. Even if the methodology is not rigorous, it can nevertheless be used as a first approximation.

The regression coefficients associated to the non-linear velocity model computed from the eleven reference tests are plotted in Figure 3.24. As it can be seen on the figure, they are sometimes badly estimated. The coefficients associated to the parameter MEAN are indeed erroneous for tests 1, 4, 6, 7 and 9. The reasons of this bad estimation lie in the non-linear estimation which does not seem robust enough, especially in that case where the parameters are well correlated between each other. However, the other regression coefficients have been estimated correctly. Their variations are zoomed in Figure 3.25. Obviously, they can not be considered constant whatever the velocity of walk. Even for the same velocities of walk, these coefficients are not constant, especially the power of the FREQ parameter.

The linear velocity model is studied following the same principle as for the non-linear one. Two regression techniques are here again tested, whether the regression is performed for all parameters at once or for each one separately. The results of the first method are plotted in Figure 3.26. The estimation method seems more robust since the regression succeeded for all the reference tests. As expected from the non-linear regression results, the coefficients are not constant whatever

the velocity of walk.

To avoid any interference due to the cross-correlation effect between the selected parameters, separate least square estimations are done for each parameter and the three results are then combined to obtain the velocity model. The pedestrian velocity model could have been composed of only one of the three selected parameters, but this would have been at the expense of the model accuracy. Therefore, this second method is test even if it is not optimum. Results are illustrated in Figure 3.27. The regression coefficients seem in that case constant over the three GPS velocity ranges identified in Figure 3.28. The dashed lines are the mean of the regression coefficients on the three tested velocity ranges.

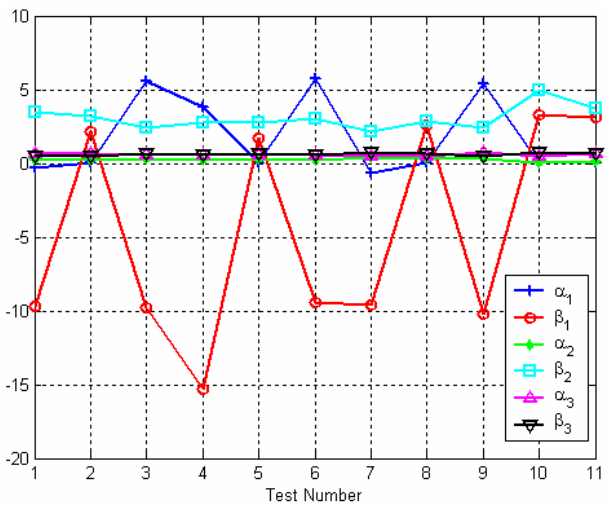

Figure 3.24: Regression coefficients. Non-linear model.

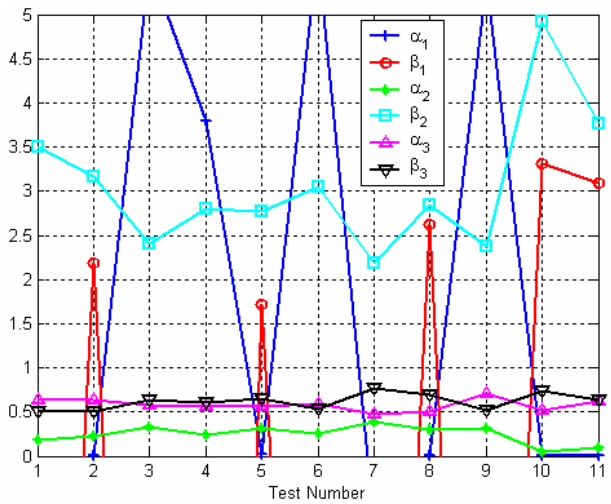

Figure 3.25: Regression coefficients. Non-linear model (close-up).

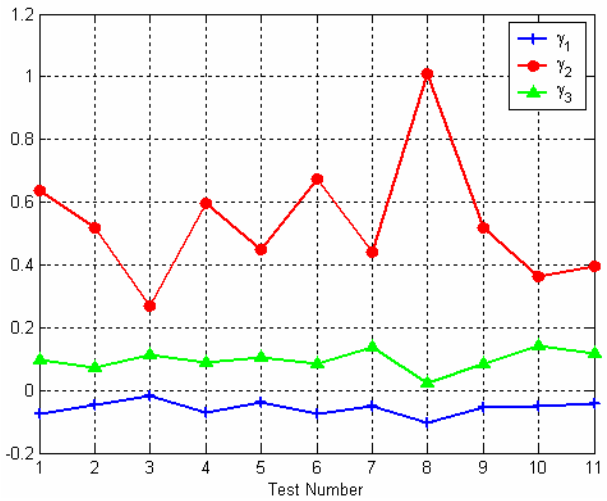

Figure 3.26: Regression coefficients. Linear model. 1st method.

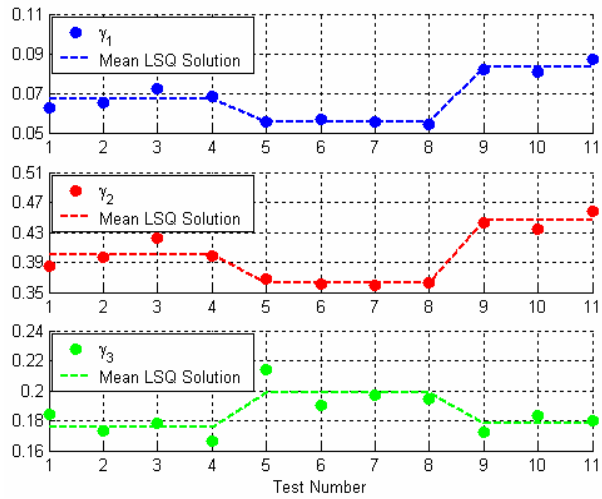

Figure 3.27: Regression coefficients. Linear model. 2nd method.

According to the above tests, the non-linear model does not seem robust enough to support the modelling of the pedestrian velocity. Opposite, the linear model gives good results in terms of robustness, i.e. there is always a suitable solution for any of the reference tests. As a consequence, the non-linear model will not be used in the following and the linear model will be preferred. Two methods can be used to match the linear velocity model to the DGPS measurements. It has been

shown that the second method based on the separate fitting of the parameters is interesting since it provides computed parameters that do not vary very much for a given velocity of walk. However, it could be expected that the final model of the pedestrian velocity is less accurate than the model obtained using the global least square estimation method.

Figure 3.29 illustrates the accuracy of both methods on the eleven reference tests. The distance resulting from the integration of the estimated velocity modelled using the computed regression coefficients is compared to the DGPS reference. The azimuth used to get the pedestrian trajectory is provided by the processing of DGPS measurements in order to analyse more specifically the impact of the velocity models. The distance estimation error is then computed and expressed in percent of the true travelled distance, which is computed with DGPS measurements. Figure 3.29 shows the improvement brought by the second method as compared to the first one, even if this difference is not of great importance.

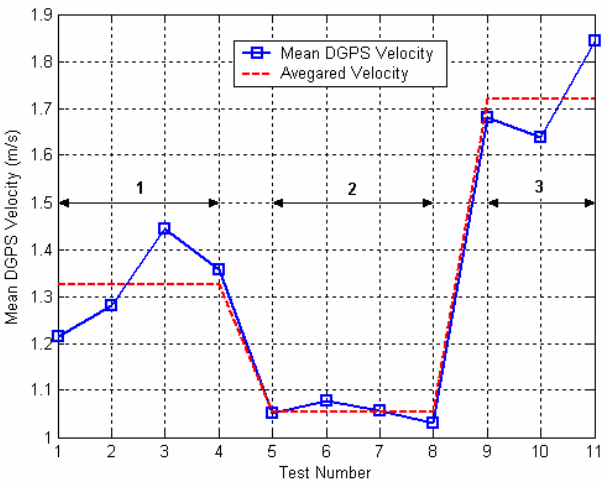

Figure 3.28: Mean DGPS velocity profile of the eleven reference tests.

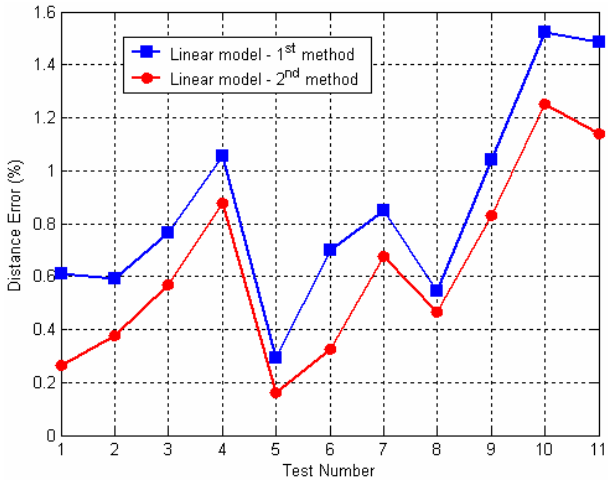

Figure 3.29: Curvilinear distance estimation error with respect to DGPS measurements.

As said above, the second method has the property of providing constant coefficients for typical ranges of velocity. This property is very interesting within the scope of a pedestrian navigation algorithm since it would allow the off-line establishment of a velocity model for different velocity ranges. That is if one is able to estimate the current state of the pedestrian pace, one could use a predetermined model for distance estimation until external measurements are available to determine a more accurate velocity model. The FREQ parameter can be used to fulfil this requirement, since it is has the best correlation with the velocity of the pedestrian, as demonstrated in Table 3.4 and Table 3.5. Once the frequency of walk estimated, the navigation system could find in a table the most adequate velocity model for the navigation. As an illustration, a model implementing the mean value of the regression coefficients computed for low velocities (trials from 5 to 8) is tested. Following the same procedure as above, the travelled distance is then estimated using these mean regression coefficients and compared to the reference distance as shown in Figure 3.29. The corresponding accuracies are given below in Table 3.8. The error is at most 2.92 percent of the true travelled distance, which can be considered as fairly good.

Test Number	5	6	7	8
Distance Error (regression coefficients)	0.18 %	0.37 %	0.71 %	0.43 %
Distance Error (mean regression coefficients)	-2.92 %	1.23 %	1.78 %	1.85 %

Table 3.8: Distance estimation accuracy – Method 2.

3.5.2.3.2 Impact of the User

This sub-section analyses the impact of the identity of the pedestrian using the navigation system on the regression coefficient as defined above. Only the linear velocity model is studied here. Four normal walks were recorded for two different people walking a straight and flat path. The corresponding mean DGPS velocities are plotted in Figure 3.30.

The regression coefficients are plotted in Figure 3.31. The pedestrian n°1 corresponds to the four first tests (1 to 4), whereas the second pedestrian corresponds to the four last tests (5 to 8). For both users, the coefficients are stable but differ from each other. This is basically due to the behaviour of the users while walking. Indeed, the movement's frequency of the legs is dependent on the height of the person. To keep an identical velocity of walk, a small person should move his legs faster than a taller one. To reduce this anatomical difference, it could be interesting to normalise the velocity of reference. However, the results conducted with the references trials showed that the regression coefficient were still different. No general velocity model can consequently be found for several users, because regression coefficients are dependent on the identity of the person.

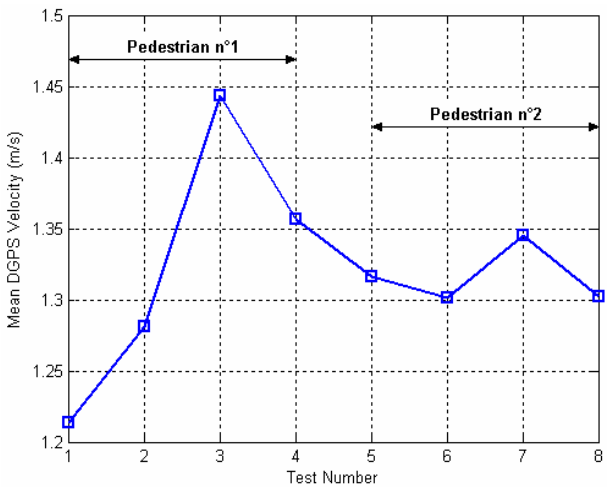

Figure 3.30: Mean DGPS velocity profile of the eight reference tests.

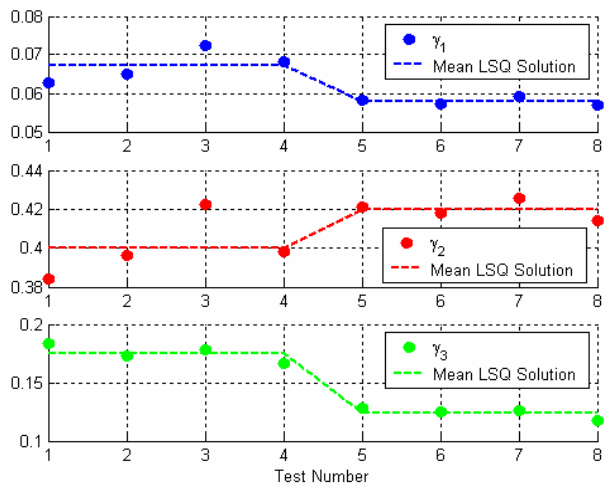

Figure 3.31: Regression coefficients. Linear velocity model. 2nd method.

3.5.2.3.3 Impact of the Reference Measurement Quality

In this subsection, the impact of the quality of the external measurements on the computation of the regression coefficient is analysed. The DGPS reference measurements used in the above subsections were the result of the post-processing of the rover and base station phase measurements using the GraphNav software.

In the particular case of the pedestrian navigation, it is unlikely to have differential measurements to calibrate the velocity model. A trial in an environment prone to multipath is thus done to simulate a typical urban navigation. Only the measurements of the rover are used for calibration. Figure 3.32 shows the reference velocities. The blue solid plot stands for the DGPS velocity, whereas the red dashed plot stands for velocity estimated using the rover receiver measurements only. As it can be seen, the standalone solution is very noisy and inaccurate compared to the DGPS one, with a 2D standard deviation of respectively about 4m and 0.04m.

The single point velocity solution yields a distance estimation error of 27% when using the linear velocity model presented in subsection 3.5.2.2 compared to the true travelled distance computed with DGPS measurements. This error is reduced to 1% if the pedestrian velocity model is calibrated with DGPS data. This test is very representative of an initialisation in urban or in indoor environments. It also reveals the need of an alternative calibration procedure in such harsh environments, as for example the procedure relying on the FREQ parameter as described at the end of subsection 3.5.2.3.1.

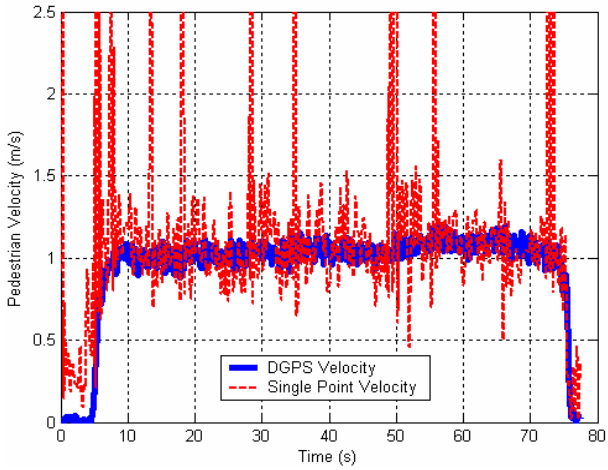

Figure 3.32: Reference velocity used for regression.

3.5.2.3.4 Impact of the Amount of Data Used for Calibration

The impact of the amount of reference data on the accuracy of the pedestrian velocity model is analysed in this subsection. The analysis is addressed through the reference test presented in Figure 3.19 and in Figure 3.33 (upper part) with a different scale. Only a percentage of the reference velocity is used to calibrate the velocity model, which goes from 2% up to 100%. For each regression, the error made on the travelled distance is estimated relative to the true DGPS distance of reference. Both linear regression methods are studied hereafter (as defined in subsection 3.5.2.3.1). Results are plotted in Figure 3.33 (lower part). Figure 3.34 clearly shows the convergence of the regression coefficients as soon as about 20% of GPS data are used. There is therefore no need of a large amount of data to enable the estimation of the travelled distance with an acceptable accuracy (error within ±5% of the true travelled distance).

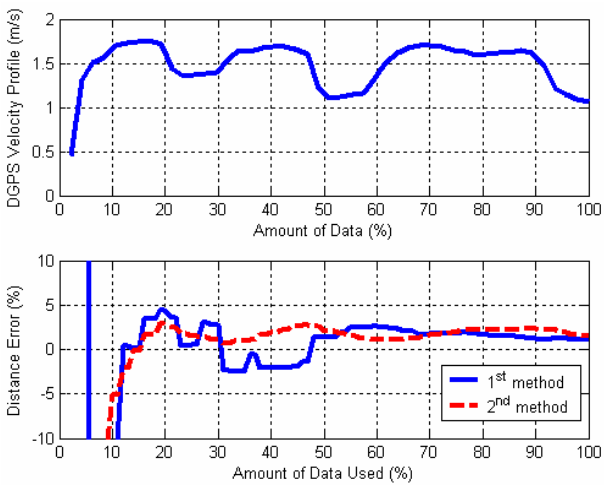

Figure 3.33: DGPS velocity profile (up) and distance estimation error (down).

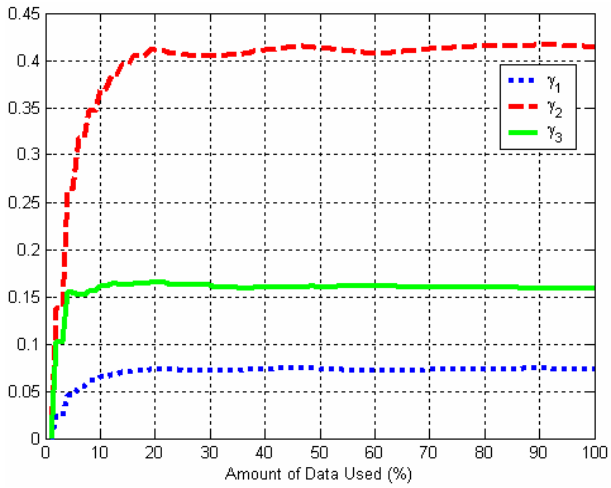

Figure 3.34: Regression coefficients. Linear model. 2nd method.

3.5.3 Displacement Direction Estimation

As presented in subsection 3.5.1, the pedestrian navigation relies on the distance estimation

and the displacement direction (i.e. heading) estimation. The heading estimation is a process completely independent of the distance estimation. It relies on gyroscopes measurements as described in section 3.2.

Among the three attitude angles, only the heading angle is used as an input of the Pedestrian Dead-Reckoning (PDR) algorithm. Pitch and roll angles shall nevertheless be properly initialised in order to allow a good computation of the heading. Accelerometers are well suited for that purpose. They allow an autonomous inclination initialisation, whose accuracy is closely related to the bias affecting the measurements. According to the characterisation of the sensors as described in subsection 3.3.1.1 and summarised in Table 3.1, it can be assumed a remaining turn-on bias in the accelerometer measurements of less than 0.05 m/s². As plotted in Figure 3.4, the inclination of the IMU can thus be estimated within an accuracy of ±1°. If magnetometers are used to initialise the heading, this inclination error budget will introduce a bias of about ±1° as illustrated in chapter 4, which remains within acceptable limits according to the quality of the sensors of the IMU.

The heading accuracy relies on the gyroscopes biases that vary in time in relationship with the operating temperature and the motion experienced by the sensors. Due to the low-cost property of the sensors, it is likely that the computed displacement direction will drift over time. One improvement would be to limit that drift using external measurements as for example those of the magnetometers. This improvement is discussed in great details in chapter 4.

3.5.4 Unconstrained Navigation Issue

The crucial point of the pedestrian mechanisation lies in the close coupling of the IMU with the pedestrian. In other words, any movement of the IMU with respect to the user's body will dramatically impact the algorithm performance in terms of travelled distance and displacement direction estimation. This is one of the main drawbacks of such mechanisation, which consequently is more similar to a constrained navigation. The issue is thus raised when the purpose is to locate a pedestrian as the inertial sensors can be put inside a handheld device such as a cell phone or a PDA. The constrained assumption is no more valid so that all the benefits brought by the new mechanisation (i.e. no double integration of the acceleration biases) may be lost.

As detailed in the above subsections, the distance estimation relies on the computation of parameters that characterise the dynamic of the pedestrian. Figure 3.35 illustrates the selected parameters computed during a walk where the IMU was moved twice. The test starts with the IMU in the pocket of the pedestrian, then the unit is moved to the ear as a cell phone would be and finally the IMU is replaced in the pocket. As it can be seen in the figure, the parameters do not have the same shape as the velocity of reference provided by DGPS measurements. This is also clearly observable in Figure 3.36 where parameters such as MEAN are plotted with the acceleration magnitude. The FREQ parameter is nevertheless the most reliable whatever the location of the IMU and even in the transition periods. There are however periods of inaccuracy mainly due to the fact that the pedestrian step frequency is blurred by the intrinsic motion of the IMU.

The displacement direction of the pedestrian may differ from the heading of the IMU if the measurement unit is moved while walking. It is of tremendous importance to keep the sensors assembly closely attached to the pedestrian or the vehicle in order to avoid any undetectable heading offset. Indeed, the unconstrained navigation implies that the orientation of the heading axis of the IMU and the direction of walk are not correlated, making the tracking of the IMU heading no more relevant.

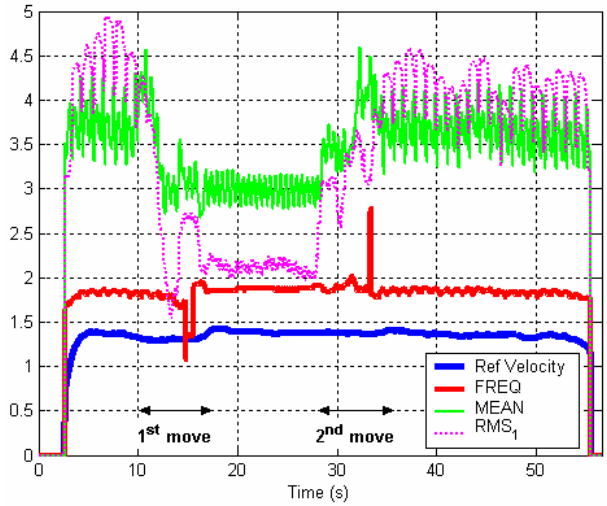

Figure 3.35: Parameters of the velocity model (unit m/s). IMU is moved while walking.

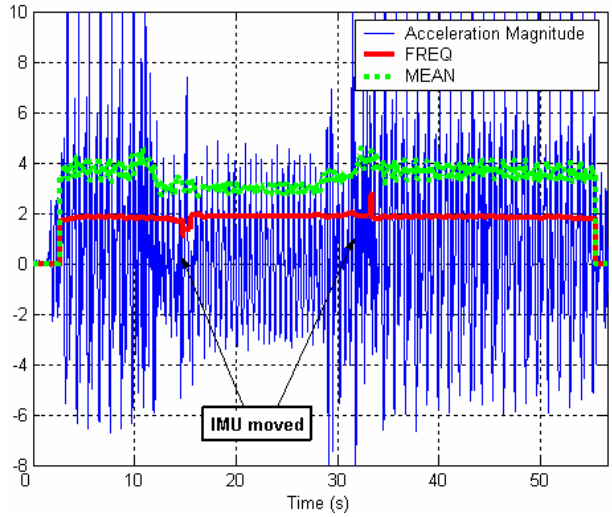

Figure 3.36: Relationship between the acceleration magnitude and the parameters (unit m/s^2).

As an alternative solution, the true displacement direction can be computed based on the north and east velocity components. The velocity model elaborated with IMU measurements is the velocity of the IMU relative to the ground directly expressed in the navigation frame ***(n)***. It can be decomposed as follows:

$$v^{(n)}_{IMU/ground} = v^{(n)}_{IMU/user} + v^{(n)}_{user/ground} \tag{3.41}$$

where :

- $v^{(n)}_{IMU/ground}$ is the velocity of the IMU with respect to the ground, expressed in ***(n)***.
- $v^{(n)}_{IMU/user}$ is the velocity of the IMU with respect to the user, expressed in ***(n)***.
- $v^{(n)}_{user/ground}$ is the velocity of the user with respect to the ground, expressed in ***(n)***.

Assuming the velocity of the IMU relative to the user negligible compared to those of the user relative to the ground, the east and north velocity components can then be used to compute the true displacement azimuth α, as given in equation (3.42).

$$\alpha = \arctan(v_E / v_N) \tag{3.42}$$

These components are not directly available. However, it is possible to project the acceleration measurements in the navigation frame using the rotation matrix from the mobile frame to the navigation frame. Assuming a non-drifting attitude and avoiding the integration of these projected accelerations to limit the impact of the biases (i.e. estimating the north and east velocities as it is done with the pedestrian velocity), it is then possible to get an estimate of the different velocity components, and consequently the true displacement direction.

The unconstrained navigation is much more complex to handle than the constrained one. Even if the travelled distance can be estimated through the parameter FREQ with medium accuracy, the tracking of the true displacement direction is more difficult to achieve. Moreover, the estimation of the north and east components relies on the rotation matrix from the mobile frame to the navigation frame, which is very sensitive to gyroscopes biases.

3.5.5 PNS Mechanisation

Figure 3.37 summarises the Pedestrian Navigation System mechanisation as described above. It mainly relies on the processing of the low cost IMU data together with GPS velocity for calibration purposes.

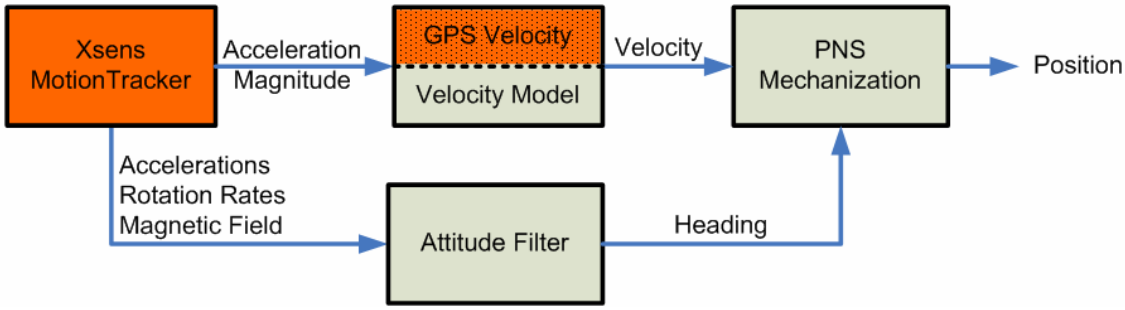

Figure 3.37: Pedestrian Navigation System (PNS) mechanisation.

3.5.6 Expected Accuracy

The pedestrian mechanisation aims at avoiding the double integration of the acceleration in the navigation frame to limit the impact of the biases (from gyroscopes and accelerometers) that rapidly degrades the performance of the positioning system. Errors are nevertheless done while estimating the velocity of the pedestrian as well as the azimuth of displacement. The following proposes a simple analysis of the performance that can be achieved with such a mechanisation.

It is very difficult to analyse the performance of the positioning technique for a pedestrian walking freely, so that the straight walk test case is more specifically addressed. The worst case is considered, since the error affecting the velocity is assumed to be a constant bias as well as the heading rate error, and the pedestrian is assumed to be continuously walking. In addition, the particular case of a Gaussian heading error is also assumed in order to predict the performance that can be achieved if a stable attitude algorithm is used to compute the heading.

It is assumed in the following that the error on the 2D position of one user can be decomposed into two non-correlated contributions (distance error and heading error). In a first time, the error due to the velocity model parameters estimation is discussed. Assuming the estimated pedestrian velocity is affected by a constant bias (which obviously represents the worst error case), the true velocity can be written as given in equation (3.43).

$$v_t = \hat{v} + \sigma_v \tag{3.43}$$

where:

- v_t is the true velocity of the pedestrian.
- $\hat{v}$ is the estimated velocity.
- σ_v is the constant error affecting the estimated velocity.

It is then straightforward to estimate the error made on the travelled distance, as it is defined in equation (3.44).

$$\sigma_{d,k} = \sigma_v \cdot k \tag{3.44}$$

where:

– $\sigma_{d,k}$ is the error made on the travelled distance at epoch k.

The error due the estimation of the heading is twofold. It depends on the type of error affecting the measurements. Considering the first case of a constant and maximum heading rate bias, the error trajectory is illustrated in Figure 42. The red and blue paths are respectively the error trajectory due to a positive and negative constant heading rate bias. The heading error contribution at epoch k is thus defined as follows:

$$\sigma_{h,k} = \sum_{n=1}^{k} \sigma_{h,n} = \sum_{n=1}^{k} d_n \cdot \sin\left(\int_{t_1}^{t_n} \dot{\alpha}_{\max} dt\right) \tag{3.45}$$

where:

– $\sigma_{h,k}$ is the heading error contribution at epoch k

– $\dot{\alpha}_{\max}$ is the maximum heading rate bias.

– d_n is the true travelled distance at epoch n.

In the second case of a constant heading bias, the corresponding error trajectory is plotted in Figure 43 with the same notations as for Figure 42. At each estimated position P_i, the heading error is here assumed to be within a specific range which depends on the accuracy of the algorithm that would estimate the heading. Equation (3.46) gives the expected heading error contribution.

$$\sigma_{h,k} = \sum_{n=1}^{k} \sigma_{h,n} = \sum_{n=1}^{k} d_n \cdot \sin(\alpha_{\max}) \tag{3.46}$$

where:

– $\alpha_{\max}$ is the maximum heading bias.

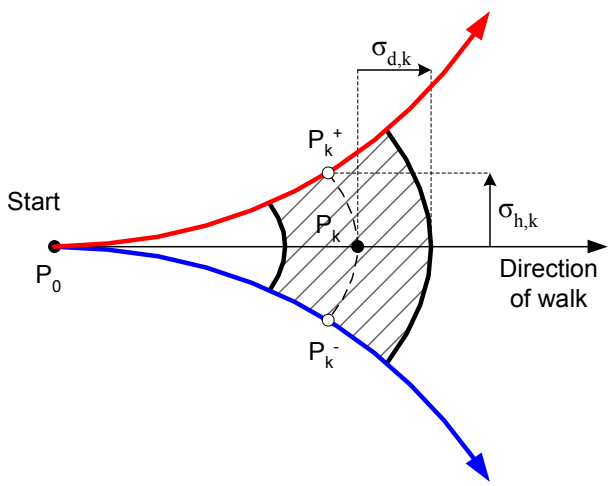

Figure 3.38: Error of a pedestrian walking a straight path assuming constant velocity and heading rate biases.

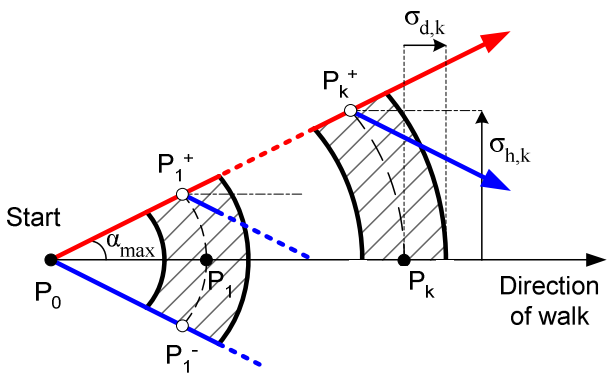

Figure 3.39: Trajectory error of a pedestrian walking a straight path assuming constant velocity and heading biases.

Once the two contributions are computed, the overall upper bound 2D RMS error that characterises the position accuracy is deduced according to equation (3.47).

$$\varepsilon_{2D} = \sqrt{\sigma_{d,k}^2 + \sigma_{h,k}^2} \tag{3.47}$$

The performance of the pedestrian mechanisation is illustrated in Figure 3.40 and in Figure 3.41 for typical errors relevant of low-cost MEMS sensors given in Table 3.9. During the whole simulation, the pedestrian is assumed walking (i.e. no stop for 10 min).

Parameters	Type	Value
Heading Bias	Constant	5°
Heading Rate Bias	Constant	300°/hour
Velocity Bias	Constant	2.0 m/s
Simulation Time	-	10 min

Table 3.9: Pedestrian mechanisation simulation parameters.

Whatever the heading error model, the pedestrian mechanisation outperforms the classical INS, whose static performance is shown in Figure 3.16. Figure 3.40 shows that typical errors of about 300m / 120m 2D after 10 minutes of navigation can be achieved compared to 600m 2D after 1 minute of navigation for a standard INS mechanisation. It is obviously not rigorous to compare the results of the PDR mechanisation (which assume a walking pedestrian) to the static results of the INS. However, this can be justified as one can expect a worse dynamic accuracy of the INS because of the biases introduced during the motion of the IMU.

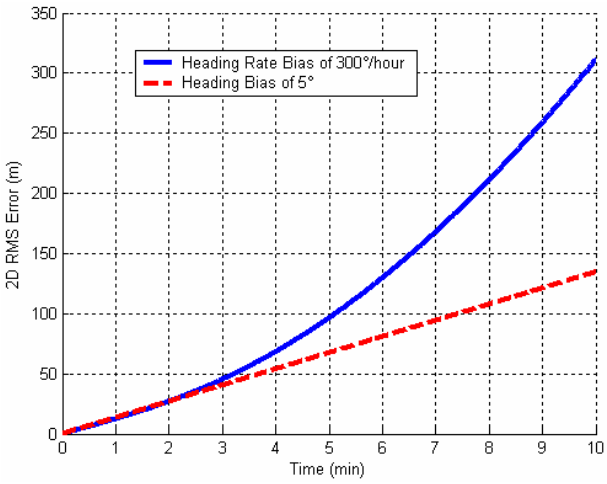

Figure 3.40: 2D upper bound position error assuming a constant velocity bias.

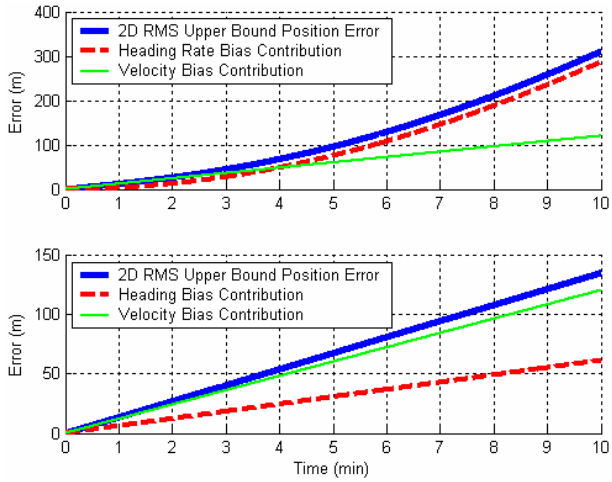

Figure 3.41: Detail of the contributions of each 2D upper bound position error.

The simulated position error is smaller in the case of a heading affected by a constant bias, as illustrated in Figure 3.40. In this case, there is indeed no memory effect since there is no drift at all. The position accuracy is increased and the availability of the positioning service is extended.

3.6 Conclusion

This chapter recalled the basics of the inertial navigation principles. In a first time, the sensors characterisation was introduced for further performance analysis. Both accelerometers and gyroscopes were studied as part of an off-the-shelf IMU used throughout this thesis (Xsens's MTi). The standard inertial navigation system mechanisation was then derived and its performance relative to the quality of the sensors embedded in the Xsens's MTi assessed. It has been shown that the use of low-cost sensors makes the standalone inertial navigation only reliable for a very short time.

The particular case of the pedestrian navigation has been exhaustively detailed. It has been shown that the mechanisation can provide substantial benefits to improve the reliability of the system working without any external update. The accuracy of the standalone Pedestrian Navigation System depends on two specific and distinct contributions: the travelled distance error and the pedestrian heading error. The performance of such a mechanisation relative to a constant velocity bias and several types of heading errors was discussed. It was demonstrated that a system affected by a constant heading bias would give better long term accuracy than those affected by a drifting heading angle.

Chapter 4: Sensor-Based Augmentations

As discussed in chapter 2, GPS-based positioning systems are a good mean to enable the location of one user in many environments. Deep indoor and deep urban canyons are nevertheless very harsh environments in which the availability and the accuracy of the GPS position solution decreases dramatically. As an augmentation to replace GPS during outages in the aforementioned environments, inertial navigation systems have been presented in Chapter 3. The weakest points as well as the advantages of such navigation systems have been discussed. The particular case of the pedestrian navigation has also been addressed to mitigate the impact of the low-cost sensors bias. Such a mechanisation increases the navigation performance, but as for the classical mechanisation, the position is drifting due to the accumulating effect of heading drift and velocity errors.

In order to improve the different computation stages of the INS and also the performance of GPS/INS hybridised systems, the addition of several low-cost MEMS sensors is studied in this chapter. More particularly, the use of a pressure sensor and a triad of magnetometers are addressed. In a first time, the two sensors are described, their expected performance discussed, and the way they can be used to improve the GPS, INS or GPS/INS position solution is presented. In a second time, an algorithm developed in the frame of this thesis that fuses the information of the different sensors in order to enhance the attitude computation based on IMU data is detailed.

4.1 Pressure Sensor

4.1.1 Principle and Output Model

As a low-cost sensor, the pressure sensor is very well suited to improve the position accuracy and especially the vertical channel. It measures the ambient pressure at the operating level, which can then be converted into altitude. The basic pressure-to-altitude relationship is given in equation (4.1). This model does not take into account special weather conditions like temperature inversion as they often appear during the winter season, and also atmospheric pressure changes caused by changes in the weather.

$$z(P) = \frac{T_0}{\gamma} \cdot \left(\frac{P}{P_0} \right)^{-\frac{R_a \cdot \gamma}{g_0}} - \frac{T_0}{\gamma} \tag{4.1}$$

$$P(z) = P_0 \cdot \left(1 + \gamma \frac{z}{T_0} \right)^{\frac{-g_0}{R_a \cdot \gamma}} \tag{4.2}$$

where:

- z is the altitude provided by the pressure sensor, and P is the pressure at altitude z.
- $P_0 = 1013.25 hPa$.
- T_0 is the temperature at 1013,25hPa. $T_0 = 15°C = 288.15K$.
- γ is the gradient of temperature, fixed for $z \leq 11km$ to $\gamma = dT/dz = -6.5°C/km$.
- R_a is a constant. For dry air, $R_a = 287.1 J/kg/K$.
- g_0 is the gravity acceleration at MSL and latitude 45°N. $g_0 = 9.80665 m/s^2$.

The pressure measured by the sensor converted into an altitude z is referenced from the 1013.25hPa pressure surface. Under standard conditions, the 1013.25hPa pressure surface is considered to be the Mean Sea Level (MSL) and as a consequence, the altitude provided is the height from that MSL to the operating level. Usually, the MSL and the 1013.25hPa surface do not match, as illustrated in Figure 4.1.

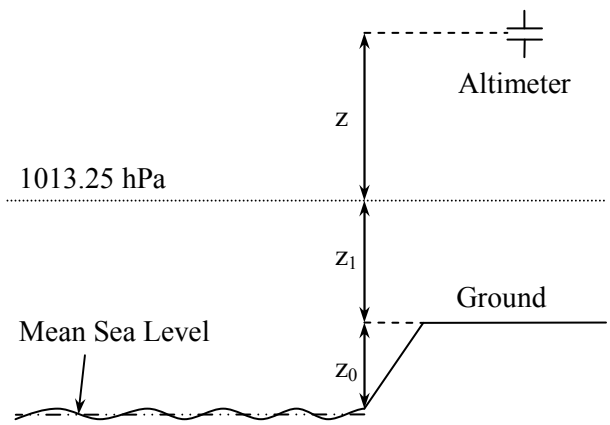

Figure 4.1: Pressure measurement principle.

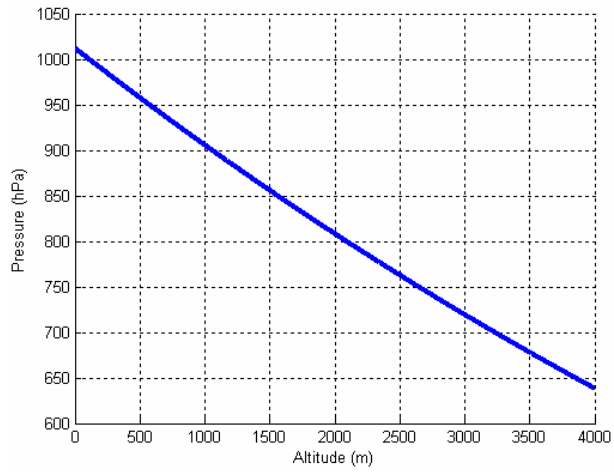

Figure 4.2: Altitude-to-pressure relationship.

The pressure sensor used throughout the thesis is an Intersema MS5534 [31]. It is a stable and temperature compensated sensor capable of 1 mbar (0.1 hPa) resolution (as illustrated in Figure 4.3), which approximately corresponds to 1 metre (as illustrated in Figure 4.4) with a precision within ±0.5 mbar once calibrated (i.e. ±0.5 m).

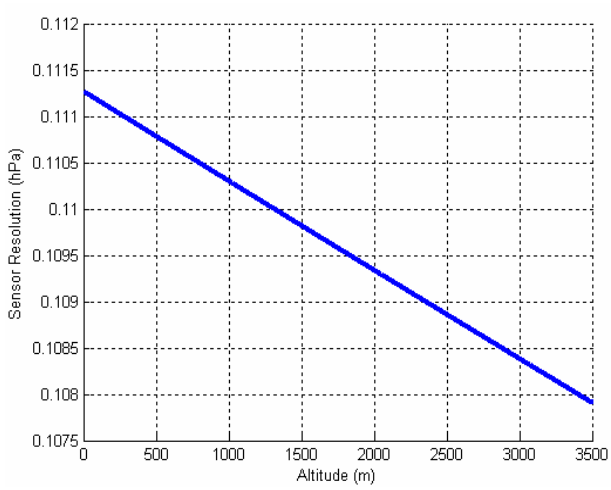

Figure 4.3: Required pressure resolution to enable a 1m vertical resolution.

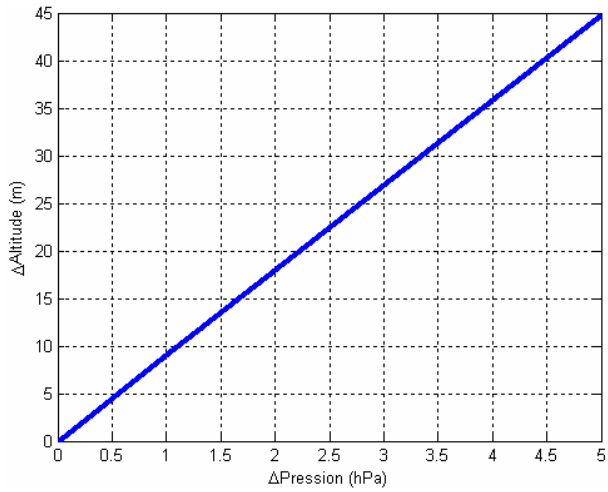

Figure 4.4: Impact of the pressure variation on the computed altitude.

The output model of a pressure sensor can be written as given in equation (4.3). The scale factor has a negligible effect on the altitude restitution. Opposite, the bias and the perturbations due to the changes of weather dramatically affect the accuracy and the reliability of the measurements.

$$p^{out} = \left(1 + SF_p\right) \cdot p^{true} + b_p + P^{weather} + n_p \tag{4.3}$$

where:

- p^{out} is the output of the pressure sensor.
- SF_p is the scale factor affecting the measurements.
- p^{true} is the true pressure that should be outputted by the sensor.
- b_p is the bias affecting the pressure measurements.
- $P^{weather}$ is the perturbation due the weather changes.
- n_p is the noise affecting the pressure measurements.

4.1.2 Performance assessment

To analyse the quality and the stability of the measurements, the pressure sensor is placed in a closed room for about 13 hours, with an initial altitude artificially set to 0 metre. The data recorded during this static trial are plotted in Figure 4.5. Both temperature and pressure converted into altitude according to equation (4.1) are presented. The sensor internal temperature needs about 2 hours before it converges to a stable value. The computed altitude varies around the initial value with a standard deviation of 1.8 metres. There is apparently no relationship between the variations of the altitude and the temperature, which tends to prove that the temperature calibration is efficient. The observable variations are thus mainly due to the bias affecting the pressure measurements.

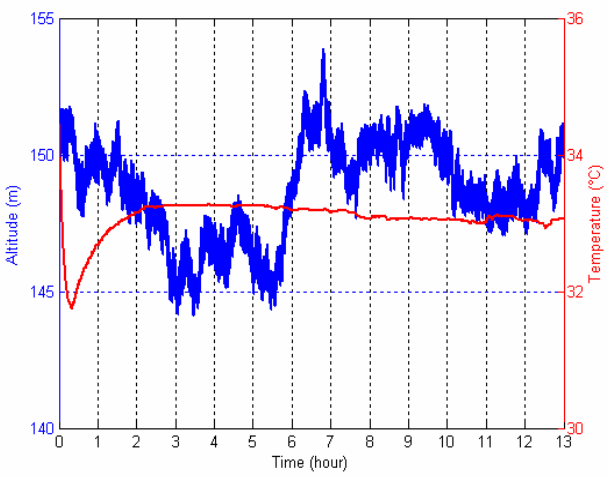

Figure 4.5: Altitude and temperature variations recorded over 13 hours in a closed room.

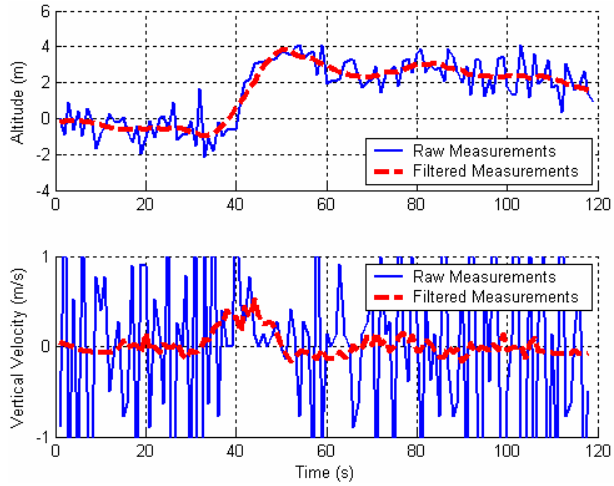

Figure 4.6: Vertical velocity computed with the pressure sensor measurements.

As an illustration of the pressure sensor performance, Figure 4.6 shows the altitude recorded during a trial inside a building where the pedestrian was walking from the ground floor up to the first floor using staircases. According to the upper part of Figure 4.6, the two floors are separated from approximately 3.5 metres, which is consistent with the actual height (4 metres). The measurements are very noisy as illustrated by the vertical velocity computed from the raw measurements, as shown in the lower part of Figure 4.6 in blue.

The filtered measurements (averaging over 5seconds) plotted in dashed red in both graphs are rather more accurate, especially the vertical velocity computed from the altitude measurements. The period where the pedestrian is climbing stairs is clearly observable, with a vertical velocity of about 0.4 m/s, which is consistent with the true vertical velocity, since 4 metres were climbed in 10 seconds. The pressure sensor measurements shall then be filtered (averaging over a time window for instance) in order to provide useful information, especially if the vertical velocity is used as a reference measurement.

4.1.3 Improvement of the Position Solution

There are several ways of using the pressure sensor in order to limit the error on the vertical channel. A first approach would be to use the pressure measurements converted into altitude measurements at a low level in the position computation process. In other words, the altitude could be used as the geometric distance from the user to a fictitious satellite centred at the Earth's centre. This additive pseudorange (not affected by the receiver clock bias) could then be integrated with the true satellite pseudoranges and processed to compute the user's position. However, this pseudorange is very likely to be affected by errors due to the measurement accuracy. Moreover, the height computed from the pressure sensor measurements is the height with respect to the 1013.25hPa reference surface, whose altitude may vary depending on the weather conditions. Such a discrepancy is of the order of about ±20hPa, which translates into ±200m. Consequently, the absolute measurements of the altimeter can not be used directly to provide an accurate pseudorange measurement. A first calibration using for example a GPS 3D position solution is thus required.

The above requirement stands also for the use of a pressure sensor providing the vertical user's position component. The number of unknown to find is then reduced to three (east, north

components and receiver clock bias) in the case of a 3D position computation. However, introducing a ±200m vertical error in the vertical component will impact as much the predicted measurements and thus the two others user's components (north and east). A first calibration of the barometer is thus required.

In both cases, it is consistent to assume that once the barometer is calibrated, the error made on the altitude estimate does not vary very much over a medium time slot. If no strong weather change occurs, any vertical displacement larger than the sensor resolution and accuracy will thus be detected. To analyse the benefits of the pressure measurements on the accuracy of the position solution, three different Least SQuare (LSQ) position computations are done (see appendix C). The first method (case 1) uses only four satellites to compute the user's position, whose measurements are generated with a standard deviation of 3 metres according to a known user reference position on Earth. The second method (case 2) uses the pressure measurement as a fictitious pseudorange and the third method (case 3) uses the altitude data as the vertical component of the user, reducing to three the number of unknowns in the LSQ algorithm. Errors from 0 to 50 metres are introduced in the altitude provided by the pressure sensor. For each pressure measurement error, 1000 LSQ computations are done. The three mean 3D RMS errors are plotted in Figure 4.7.

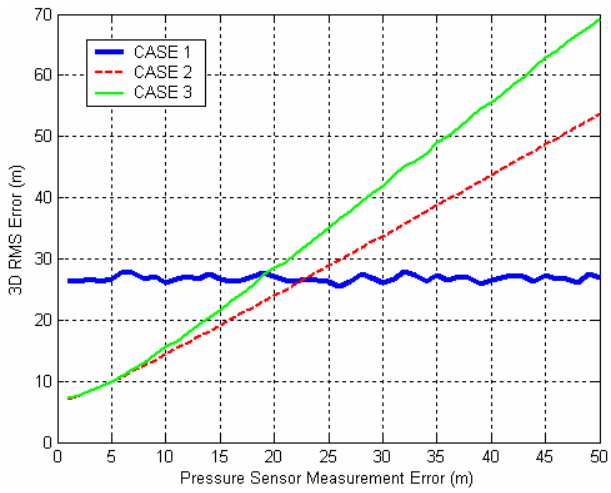

Figure 4.7: 3D RMS position error using pressure measurements with three different computations methods.

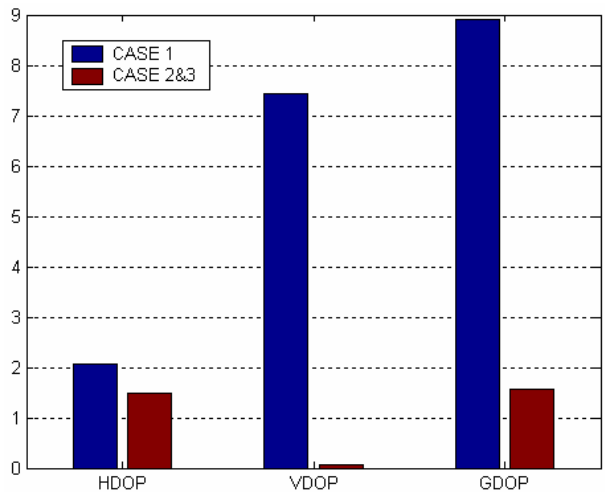

Figure 4.8: DOPs improvement due to the processing of the pressure measurements.

The blue horizontal line is the position error computed with method n°1. Figure 4.8 shows in blue the different DOPs characterising the satellite configuration, which in that case is quite bad. As soon as the vertical information is added in the LSQ algorithm, the DOPs logically decrease (especially the vertical DOP), as shown in Figure 4.8. The position solution 3D RMS error is well reduced when using the pressure measurement, especially if the added information from the pressure sensor is not very affected by errors (less than 15 metres error for a GPS pseudorange standard deviation of 3 metres). Method n°2 outperforms method n°3 especially for large altitude information errors, which tends to demonstrate that using the altitude measurement as a fictitious pseudorange is more efficient than using it as a vertical coordinate estimate. However, method n°2 implies to process pseudoranges in order to compute the position of the user, which can not always be possible, especially if GPS modules providing information through NMEA frames are used for navigation. In that case, method n°3 still is an effective mean of improving the position accuracy.

When altitude measurements are very affected by errors (a typical threshold would be between 15 and 20 metres according to Figure 4.7 for typical GPS pseudoranges standard deviation

of 3 metres) and as soon as four satellites are available, it should be preferred not to take into account the pressure sensor in the position computation as the overall accuracy decreases. However, it is very difficult to detect whether the pressure measurements are reliable or not, especially if no pure GPS 3D fix can be computed or if only pure GPS 3D fix with high uncertainty is available (as for example typical fixes computed with indoors signals).

4.2 Magnetic Field Sensor

4.2.1 Earth Magnetic Field

One of the particular characteristic of the Earth is that anywhere around its centre, it is possible to measure a magnetic field. This field has properties that slowly vary in time (at the scale of years) so that they can be considered locally constant. Figure 4.9 and Figure 4.10 illustrate some of the Earth's magnetic field characteristics and Table 4.1 gives typical values for the Earth's magnetic field at Toulouse, France for year 2005.

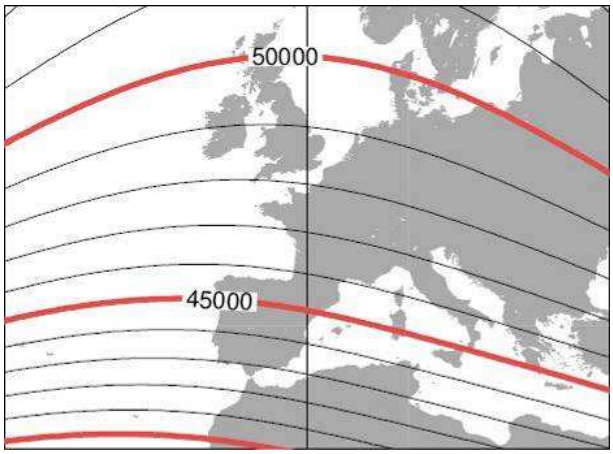

Figure 4.9: Earth's magnetic field intensity [22].

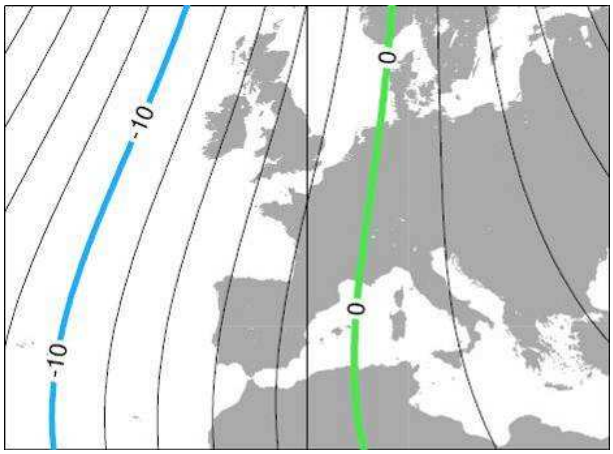

Figure 4.10: Earth's magnetic field declination [22].

Figure 4.11 presents the Earth's magnetic field vector H_e in a horizontal reference frame (x,y,z). It is characterised by its inclination or dip angle δ, which is the angle between the horizontal projection H_h of H_e and the magnetic field vector H_e. The inclination depends on the location on the Earth but is locally constant. For a given area, it can be found for example in [22].

If magnetic measurements are rotated into a horizontal frame, the magnetic heading α can be computed. It is the angle between the heading axis x and the horizontal projection H_h of H_e. This angle differs from the true geographic north by a locally constant angle known as the declination λ. The declination is also a locally constant characteristic of the Earth's magnetic field. Typical values for a given area can be found in [22] for example.

Dip angle	58,73°	-
Declination	-1,299°	-
Magnitude	42921,18 nT	1 (normalised)
Horizontal magnitude	22279,17 nT	0,5191 (normalised)

Table 4.1: Toulouse Earth's magnetic field characteristics (year 2005) [22].

4.2.2 Sensor Output Model

Magnetometers are used to sense the Earth's magnetic field. The low-cost Xsens measurement unit MTi comprises a triad of such sensors. The general magnetometer output model is given in equation (4.4). Altough the Scale factor SF_m and the bias b_m are temperature dependent, their respective variations are not taken into account in the following of this report. The temperature calibration done by Xsens is assume enough accurate.

$$m^{out} = (1 + SF_m) \cdot m^{true} + b_m + I_m + n_m \tag{4.4}$$

where :
- m^{out} is the output of the magnetometer.
- SF_m is the scale factor affecting the true quantity to measure.
- m^{true} is the true quantity to measure.
- b_m is the bias affecting the measurement.
- I_m is the magnetic interference that may occur during the measure.
- n_m is the noise affecting the measurement.

4.2.3 Magnetic Heading

The magnetic heading (also called magnetic azimuth) α is computed using the two horizontal components of the Earth magnetic field H_e as presented in Figure 4.11 and expressed in equation (4.5). Measurements have thus to be rotated into a horizontal plane prior to any heading estimation. Its accuracy depends on the quality of the data (biases, scale factors) as well as the accuracy of the inclination angles used to rotate the measurements into the local horizontal plane.

$$\alpha = \arctan(H_y / H_x) \tag{4.5}$$

where:
- H_x is the Earth's magnetic field component along the horizontal x axis standing for the heading axis (i.e. the axis with respect to whom the angle is computed) of the horizontal frame (x,y,z).
- H_y is the Earth's magnetic field component along the y axis of the horizontal frame (x,y,z).

The impact of the measurement biases and scale factors on the magnetic heading is detailed in [25]. This contribution can be partially handled with a calibration procedure (detailed in the next subsection) so that it is assumed negligible compared to the error introduced by the tilting of the magnetometer triad. According to [25], the magnetic heading error as a function of the inclination error is given by the following equation:

$$\varepsilon_{\psi_{mag}} = \arctan(\tan(\delta) \cdot \sin(\tau)) \tag{4.6}$$

where:
- $\varepsilon_{\psi_{mag}}$ is the magnetic heading error.
- δ is the dip angle, as illustrated in Figure 4.11.
- τ is the inclination error.

The magnetic heading error depends on the location of the measurement unit on Earth through the dip angle δ. In France, the dip angle is comprised between 50° and 60°. The corresponding heading error is then plotted in Figure 4.12. This figure shows that the tilt estimation plays a crucial role in the heading accuracy since small tilt errors introduce large heading errors.

Under static conditions, the tilt accuracy (i.e. the accuracy of both pitch and roll) depends on the quality of the accelerometers measurements. Accelerometers sense the gravity vector, so that pitch and roll angles can be computed using the corresponding projections onto the mobile frame ***(m)***, as explained in chapter 3. Assuming a residual turn-on bias in the accelerometer measurements of less than 0.05 m/s² after calibration, the inclination of the IMU can thus be estimated within an accuracy of ±1° (detailed in chapter 3). If magnetometers are used to initialise the heading, this inclination error budget will introduce a bias of about ±1°, as illustrated in Figure 4.12, which remains within acceptable limits according to the quality of the sensors of the IMU.

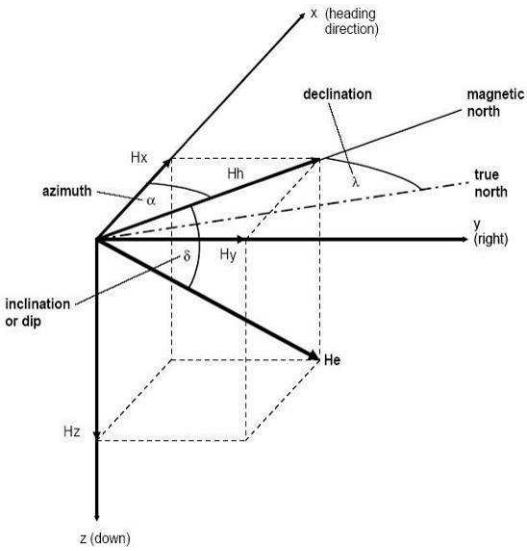

Figure 4.11: Earth magnetic field [25].

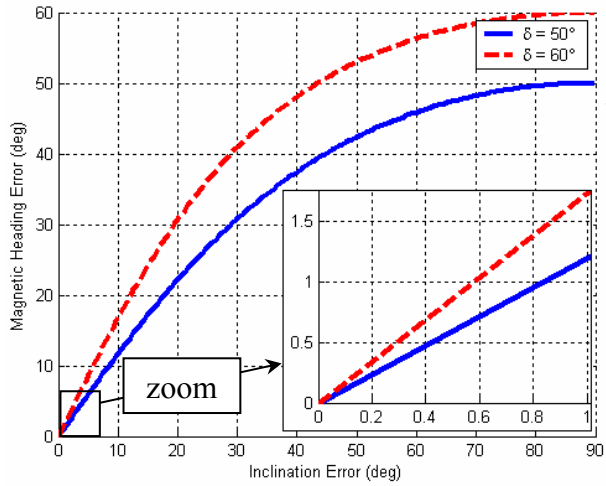

Figure 4.12: Magnetic heading error with respect to inclination error.

In a dynamic mode, the tilt accuracy is very dependent on the real time estimation of the true acceleration of the pedestrian or the vehicle. No tilt compensation can be done since typical inclinometers are disturbed by the motion of the IMU. Such a dynamic tilt compensation algorithm has been developed. Details are given in the next section.

4.2.4 Calibration Procedures and Magnetic Interferences

The scale factor and the bias as defined in equation (4.4) introduce errors in the magnetic heading. These errors need to be estimated in order to increase the heading accuracy. However, the magnetic heading is computed once the measurements are rotated in a horizontal plane. Thus, the correction needed to limit the impact of both errors can be applied into the mobile frame ***(m)*** or in the horizontal levelled frame (as shown in Figure 4.11). In the following, the components of the magnetic field in the local horizontal plane are corrected for biases and scale factors.

If the measurements were perfect in the local horizontal plane after describing a whole 360° rotation about the vertical axis of the navigation frame, the H_x versus H_y plot should be a perfect circle centred in (0, 0) with a radius equal to the local horizontal Earth's magnetic field H_h (i.e. 0.5191 in Toulouse). The scale factor is responsible for the distortion of the circle into an ellipse

and the bias de-centres the ellipse. Thus, in an environment with no magnetic interference, the calibration procedure of the magnetometers consists in finding the calibrated horizontal magnetic components, as given in equation (4.7).

$$\begin{aligned} H_x^{calibrated} &= X_{SF} \cdot H_x + H_{x0} \\ H_y^{calibrated} &= Y_{SF} \cdot H_y + H_{y0} \end{aligned} \tag{4.7}$$

where:

- $H_x^{calibrated}$, $H_y^{calibrated}$ are the calibrated horizontal Earth's magnetic field components.
- X_{SF}, Y_{SF} are the scale factors affecting the measurements in the horizontal plane.
- H_{x0}, H_{y0} are the biases affecting the measurements in the horizontal plane.

The calibration procedure allows also the mitigation of permanent magnetic interferences. Such typical perturbations occur when the magnetic sensors of the measurement unit are placed nearby iron objects. These objects produce a constant magnetic field that disturbs those of the Earth. In the calibration diagram, hard interference decentres the circle and act as biases on the horizontal components of the sensed magnetic field.

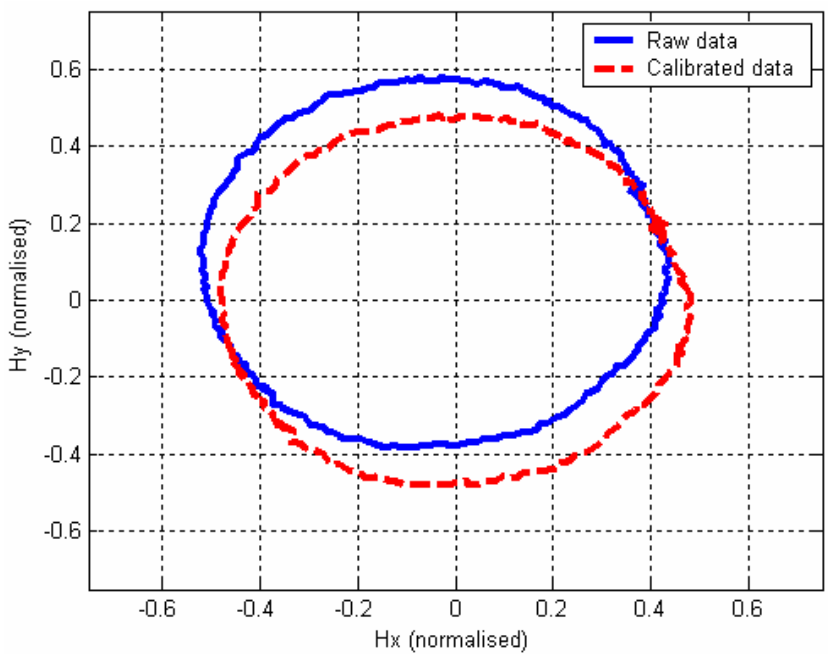

Figure 4.13: Calibration test diagram in a non perturbed magnetic environment.

As an example, Figure 4.14 and Figure 4.15 illustrate such hard iron interference effect on the sensed magnetic field. The particular case of the land vehicle is more specifically shown since it involves the strongest magnetic interferences.

In Figure 4.14 are plotted the magnetic field magnitude (the upper blue plot) and the acceleration magnitude (the lower red curve). Five parts are clearly observable on the magnetic field magnitude. The 1st and 5th part are epochs where the measurement unit is in the vehicle with engine off. As it can be seen, the magnitude is not equal to one but constant and equal to approximately 0.82. This typically illustrates the intrinsic hard interference property of the vehicle. The 2nd part of the plot stands for the pre-start of the diesel engine. The 3rd part is the start of the

engine. The vehicle shakes a little, as it can be seen in the acceleration pattern. Finally, the 4th part is for engine started. The vibrations of the vehicle are clearly observable in the acceleration plot but not in the magnetic field magnitude one, which remains constant.

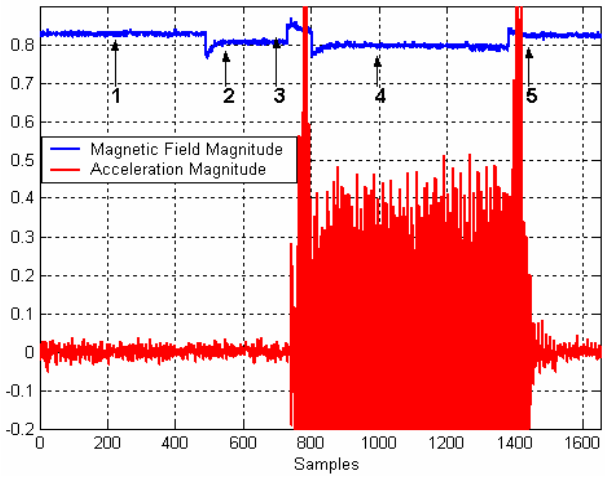

Figure 4.14: Magnetic field magnitude variation during the different vehicle engine start.

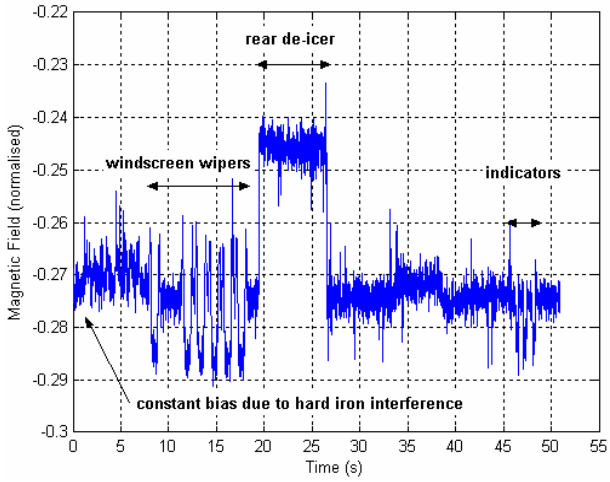

Figure 4.15: Magnetic interferences due to the dashboard equipments of a vehicle.

Figure 4.15 illustrates typical interferences that may occur while driving and that can not be mitigated through a calibration procedure due to their random property. In such cases, the magnetic heading is biased and can not be used as a correction source for the drifting gyro-based heading.

4.3 Drift-Free Attitude Filter

As discussed in chapter 3, the inertial navigation is a short term reliable navigation method, whose error budget can be split into a heading error contribution and a travelled distance error contribution. The position drift due to accelerometer biases can be partially managed with the use of modified mechanisations as for example those for pedestrians presented in chapter 3. The position accuracy can also be improved with the use of external sensors such as a pressure sensor to limit the vertical drift or wheel speed sensors in the land vehicle case, as demonstrated in [32].

In both inertial navigation cases (i.e. the classical INS or the PNS), the attitude drift is still remaining and thus degrades significantly the position solution when no GPS measurement is available for update. As the measurement unit studied within the scope of the thesis is composed of a triad of accelerometers, gyroscopes and magnetometers, it is possible to limit the impact of the gyroscopes bias on the heading accuracy by fusing the information provided by all these low-cost sensors of MEMS type.

The recent progresses in the manufacturing of MEMS type sensors make components such as integrated 3-axis accelerometers and 3-axis magnetometers very attractive for navigation purposes. As an example of the prices foreseen in the next few years, Analog Devices expects to provide a 3-axis accelerometer for $1 [56], AKM produces a 3-axis magnetometer for about $5 [57] and the new InvenSense 2-axis gyroscope foreshadows new improvements in the integration of MEMS gyroscopes in a single die [55], which until these days remains the most expensive sensor. Besides the fact that the price of the aforementioned sensors is expected to decrease, their respective performance is foreseen to stay at the same level of quality as it currently is. Especially low-cost

gyroscopes are likely to still provide measurements affected by errors that would degrade the computation of the IMU attitude. Therefore, it could be relevant to use the magnetometers and the accelerometers to compensate for the rotation rate errors. Their combination with gyroscopes could indeed give a great deal of performance for a minimal additive cost on the overall sensors assembly.

The attitude of the IMU is usually represented by the intuitive Euler's angles (φ roll, θ pitch, ψ yaw or heading), as described in chapter 3. Within the frame of this thesis, the quaternion-based method is used to compute the orientation of the IMU using the gyroscopes measurements. It has the advantage of being defined whatever the angles the sensors assembly experiences and its computation does not require trigonometric functions, which in turn decreases the overall computation complexity.

The accelerometers used as inclinometers are likely to provide information about the inclination of the IMU. As a consequence, they can be used to estimate the pitch and roll drifts. Once rotated into a horizontal plane, the magnetometers measurements can be used to estimate the heading drift of the IMU. Inclination and heading estimations are thus two separate processes where corrections are done with two independent sensors.

The following presents a sensor fusion algorithm aiming at improving the reliability and the accuracy of the attitude of a low-cost IMU. The inclination and the heading estimations are performed in two consecutive Kalman filters ([44], [45], Appendix C). This has got the advantage of reducing the size of the matrices involved in the filter, which is profitable for real time implementation perspectives. It also allows a more flexible heading estimation, enhanced for magnetic interference mitigation.

4.3.1 Inclination Filter

4.3.1.1 State Transition Models

The inclination filter relies on the fusion of accelerometers and gyroscopes data. The attitude is computed with the quaternion method. According to the notation of equation (3.7) and equation (3.10), the discrete model used in the Kalman filter for the quaternion propagation is given below in equation (4.8). This equation is obviously not linear since it involves the product of true rotation rates with quaternion components, but it is far easier to get it linear than equation (3.6).

$$q_{k+1} = \left(1 + \omega_k^{true,(m)}/2\right) \circ q_k \tag{4.8}$$

where:

- q_k is the rotation quaternion at epoch k.
- $\omega_k^{true,(m)}$ is the true rotation rate vector of the mobile with respect to the ***(I)*** at epoch k.
- $\circ$ is the quaternion product.

Quaternion q_k at epoch k represents the rotation of the measurement unit from the mobile frame to the navigation frame. The rotation rates $\omega_k^{true,(m)}$ involved in equation (4.8) should be the true rotation rates of the measurement unit with respect to the navigation frame. As justified in chapter 3, these quantities are approximated by the output of the gyroscopes. Given the sensors resolution and sensitivity, the residual error is indeed neglected. However, the true rotation rates are not directly accessible since gyroscopes are affected by biases. As a consequence, both gyroscopes

bias and true rotation rates will be modelled in the inclination part of the attitude filter. In the following, the in-run biases of the gyroscope sensors are assumed to follow a 1st order Gauss-Markov process, whose discrete expression is given below in equation (4.9).

$$b_{k+1}^{\omega} = e^{-\beta_{\omega} T_s} \cdot b_k^{\omega} + \frac{1}{\beta_{\omega}} \cdot \left(1 - e^{-\beta_{\omega} T_s}\right) \cdot w_k^{b\omega} \tag{4.9}$$

where:
- T_s is the sampling period.
- b_k^{ω} is the bias vector affecting the gyroscopes measurements at epoch k.
- β_{ω} is the inverse of the time constant of the 1st order discrete Gauss-Markov process.
- $w_k^{b\omega}$ is the Gauss-Markov driving noise with variance $\sigma_{b\omega}^2$.

The true rotation rate model depends on the motion experienced by the IMU. Figure 4.16 illustrates two typical use cases, namely the pedestrian navigation (upper part) and the land vehicle navigation (lower part). For both cases, the dynamic experienced by the IMU is completely different. A rigorous approach would be to adapt the true rotation rate model as a function of the detected motion, but this would require extra processing. In the following, the model is rather designed to match the highest dynamic the IMU can experience (pedestrian navigation).

In Figure 4.17 is plotted in blue the PSD of the rotation rate measurements of the three axes of the IMU recorded during a pedestrian trial. For these three PSD, the basic shape is similar to those that could be obtained with a signal composed of multiple sinusoids, whose frequencies are related to the frequency of the steps. However, such a characteristic can not be generalised as for example in the land vehicle case. As a consequence, general models are rather used with simpler PSD shapes, as it is the case with the first order Gauss-Markov process and the second order band-pass filter. Both PSD expressions are given respectively in equation (4.10) and in equation (4.11).

$$PSD_{BPF}(f) = \left| \frac{A \cdot 2j\pi f}{(2\pi f_0)^2 + 2j\pi f \cdot BW + (2j\pi f)^2} \right| \tag{4.10}$$

where:
- A is the band-pass filter gain.
- f_0 is the centre frequency of the band-pass filter.
- BW is the filter bandwidth.

$$PSD_{GM}(f) = \frac{\sigma_{\omega}^2}{1 + \left(c_k^{\omega}\right)^2 - 2 \cdot c_k^{\omega} \cdot \cos\left(2\pi \tilde{f}\right)} \tag{4.11}$$

where:
- c_k^{ω} is the time constant setting the bandwidth of the ω^{true} process.
- σ_{ω}^2 is the variance of the driving noise setting the magnitude limit of the modelled motion.
- $\tilde{f}$ is the frequency normalised by the sampling rate. $\tilde{f} = T_s \cdot f$

Figure 4.17 clearly shows that the dynamic of the measurements depends also on the axis of

measurement. There is indeed less power in the signal along the Z axis than in the signal along the X axis. Here again, the true rotation rate model should take into account each component property of the sensor triad. However, in a first approximation, a same model will be used for all of the axes of measurement. Consequently, the different parameters of the PSD presented in equation (4.10) and (4.11) must be tuned according to the maximum dynamic of the motion experienced by the sensors assembly.

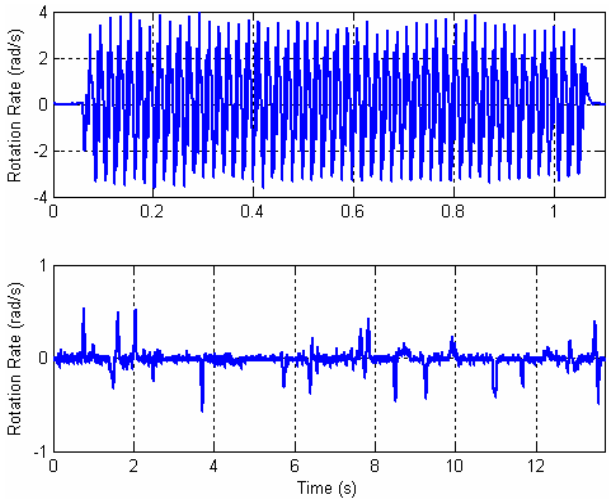

Figure 4.16: Typical rotation rate patterns for pedestrian navigation (upper part) and land vehicle navigation (lower part).

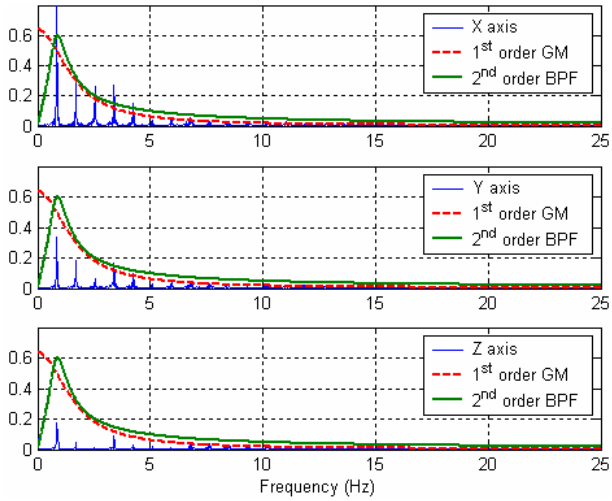

Figure 4.17: PSD of the three rotation rate components in the mobile frame *(m)*, 1st order GM and 2nd order band-pass filter.

The PSD of the Gauss-Markov (GM) and the 2nd order band-pass filter (BPF) adapted to the X axis data (worst dynamic) are plotted in Figure 4.17 for the three axes of measurements. The PSD of the band-pass filter is the best match for the PSD of the true rotation rates. However, the centre frequency f_0 must be adjusted depending on the characteristic frequency of the signal in order for the model to take advantage of the band-pass properties. The computation load is thus increased. The Gauss-Markov PSD approximates nevertheless quite well the true PSD. Such a model also has the advantage of being simple to integrate into a state space model (one equation to handle a component of the true rotation rate, rather than two if the 2nd order band-pass filter is used), reducing in the same time the matrices dimensions, which is interesting for a real time implementation perspective.

As a consequence of the model benefits and disadvantages, the true rotation rates are modelled as a 1st order Gauss-Markov process tuned according to the Power Spectral Density function, whose parameters namely bandwidth and magnitude are chosen according to the highest dynamic of the motion experienced by the sensors assembly (found by processing the signals from typical pedestrian walks, for different IMU location onto the body of the user). The true rotation rate model used in the inclination filter is given below in equation (4.12).

$$\omega_{k+1}^{true,(m)} = c_k^{\omega} \cdot \omega_k^{true,(m)} + w_k^{\omega} \tag{4.12}$$

where:

– $\omega_k^{true,(m)}$ is the true rotation rate vector at epoch k, expressed in the mobile frame ***(m)***.

– w_k^{ω} is the driving noise with variance σ_{ω}^2 setting the magnitude limit of the modelled motion.

The first measurements combined with the gyroscopes outputs are those provided by the accelerometers. The aim of this sensor fusion is to limit the drift in both pitch and roll angles. In the navigation frame and when no motion affects the sensors assembly, accelerometers sense the gravity vector allowing both roll and pitch estimation. However, when the sensors unit is moving, this basic inclination estimation is no more possible since the contribution of the IMU acceleration is added to those of the gravity vector. There is consequently a need to model the true acceleration experienced by the sensors assembly as well as the biases affecting the accelerometers measurements in order to track the inclination of the unit under dynamic conditions. The bias of each accelerometer is modelled as a 1st order Gauss-Markov process, according to equation (4.13).

$$b_{k+1}^{a} = e^{-\beta_a T_s} \cdot b_k^a + \frac{1}{\beta_a} \cdot \left(1 - e^{-\beta_a T_s}\right) \cdot w_k^{ba} \tag{4.13}$$

where:

- b_k^a is the bias vector affecting the acceleration measurements at epoch k.
- β_a is the inverse of the time constant of the 1st order discrete Gauss-Markov process.
- w_k^{ba} is the Gauss-Markov driving noise with variance σ_{ba}^2.

The statements made for the true rotation rates are still valid for the acceleration measurements. Figure 4.18 shows the different acceleration magnitudes recorded during a pedestrian and a land vehicle trial. As it can be seen, the dynamic is much more important in the pedestrian case than in the vehicle case. The pedestrian navigation is thus taken as a reference to choose the true acceleration model.

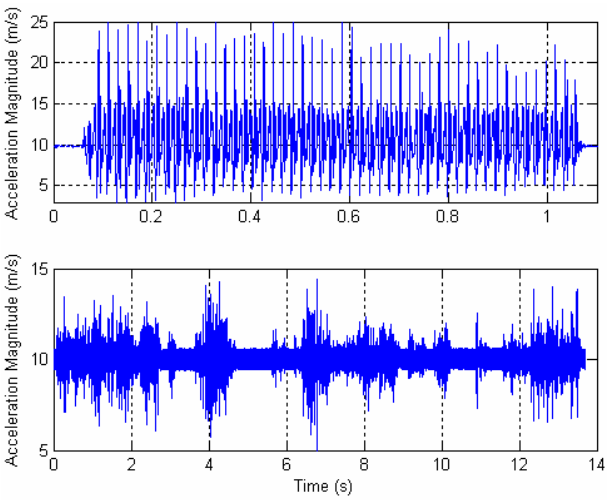

Figure 4.18: Typical acceleration magnitude patterns for pedestrian navigation (upper part) and land vehicle navigation (lower part).

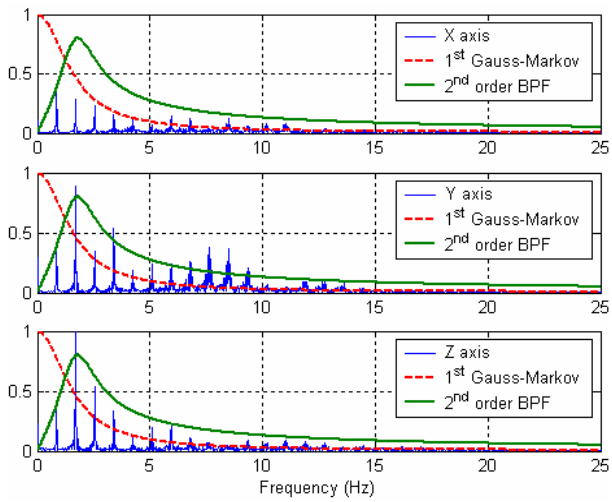

Figure 4.19: PSD of the three acceleration components in the mobile frame *(m)*, 1st order GM and 2nd order band-pass filter.

Figure 4.19 shows the different PSD adjusted to the measurement that experiences the worst dynamic (pedestrian case). Again, the 2nd order band-pass filter seems to be more adapted to model the true acceleration. However, to simplify the implementation of the inclination filter, the 1st order Gauss-Markov model is rather chosen in the following, so that the model of the true acceleration is assumed to be as given in equation (4.14).

$$a_{k+1}^{true,(m)} = c_k^a \cdot a_k^{true,(m)} + w_k^a \tag{4.14}$$

where:

- $a_k^{true,(m)}$ is the true acceleration vector at epoch k, expressed in the mobile frame ***(m)***.
- c_k^a is the time constant setting the bandwidth of the a^{true} process.
- w_k^a is the driving noise with a variance σ_a^2 setting the magnitude limit of the modelled motion.

4.3.1.2 Measurement Models

The inclination filter aims at providing stable pitch and roll angles that will be used to rotate the magnetometers measurements into a horizontal plane so as to estimate the heading drift. Three different kinds of measurements are used in order to achieve this inclination stabilisation. These measurements are used as direct inputs of the Kalman filter in order to simplify the design of the filter. The first measurements are those provided by the gyroscopes. The output model given in equation (3.4) is simplified as written below.

$$\begin{bmatrix} \omega_x^{meas.} \\ \omega_y^{meas.} \\ \omega_z^{meas.} \end{bmatrix}_k^{(m)} = \begin{bmatrix} \omega_x^{user} \\ \omega_y^{user} \\ \omega_z^{user} \end{bmatrix}_k^{(m)} + \begin{bmatrix} b_x^{\omega} \\ b_y^{\omega} \\ b_z^{\omega} \end{bmatrix}_k^{(m)} + n_k^{\omega} \tag{4.15}$$

where:

- $\omega_k^{meas.}$ is the gyroscope triad output data vector at epoch k.
- ω_k^{user} is the true rotation rate vector experienced by the user at epoch k.
- b^{ω} is the bias vector affecting the measurements at epoch k.
- n_k^{ω} is the measurement noise at epoch k.

The measurement model involving both the acceleration data and the rotation quaternion components is given below in equation (4.16). The rotation matrix as a function of the quaternion components is given in chapter 3, equation (3.12). Equation (4.16) does not clearly show that the acceleration measurements improve more specifically the inclination angles accuracy. It has however the advantage of being very simple to implement in the Kalman filter.

$$\begin{bmatrix} a_x^{meas.} \\ a_y^{meas.} \\ a_z^{meas.} \end{bmatrix}_k^{(m)} = R_{n2m} \cdot \begin{bmatrix} 0 \\ 0 \\ g \end{bmatrix} + \begin{bmatrix} a_x^{user} \\ a_y^{user} \\ a_z^{user} \end{bmatrix}_k^{(m)} + \begin{bmatrix} b_x^{a} \\ b_y^{a} \\ b_z^{a} \end{bmatrix}_k^{(m)} + n_k^{a} \tag{4.16}$$

where:

- g is the gravity vector.
- a_k^{user} is the true acceleration of the sensors assembly unbiased by the gravity vector at epoch k.
- R_{n2m} is the rotation matrix from the navigation frame ***(n)*** to the mobile frame at epoch k.
- b^a is the bias affecting the measurements at epoch k.
- n_k^a is the measurement noise at epoch k.

The last measurement equation is added to make sure the quaternion magnitude is equal to 1. Equation (4.17) gives the non-linear normalisation equation, whose notations are equivalent to those of chapter 3.

$$\sqrt{q_{0,k}^2 + q_{1,k}^2 + q_{2,k}^2 + q_{3,k}^2} = 1 \tag{4.17}$$

4.3.1.3 Inclination Filter Summary

The inclination filter principle is summarised below in Figure 4.20. It uses the state equations (4.8), (4.9), (4.12), (4.13) and (4.14). The accelerometer and gyroscope measurements are fed into the Kalman filter to enable the estimation of the roll and pitch angles drift. The measurements equations are given in (4.15), (4.16) and (4.17). In order to properly initialise the attitude angles computation, magnetic measurements are used to find the initial heading angle (as described in section 4.2.3). The inclination filter then processes only accelerometers and gyros data.

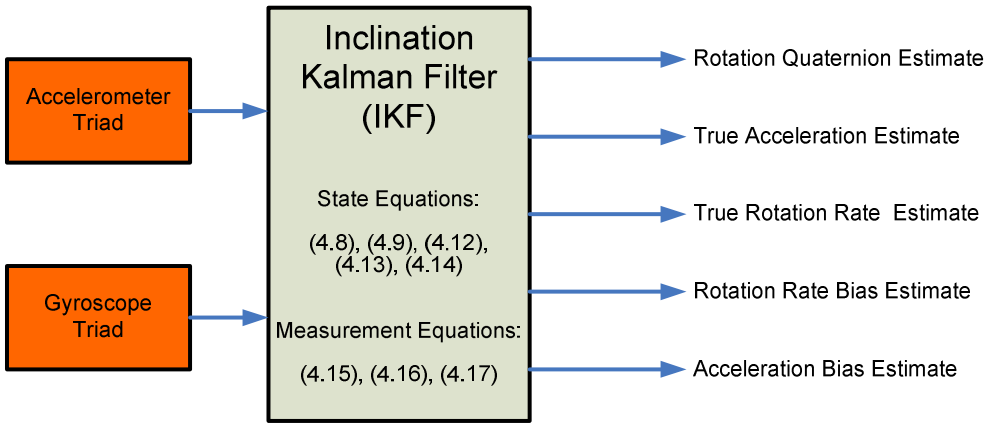

Figure 4.20: Inclination filter principle.

In the proposed filter, scale factors are deliberately assumed not to have significant variations that would introduce large errors and thus are not included in the state vector of the inclination filter. Equation (4.18) gives the state vector of the inclination filter. It involves 16 unknowns as defined in the above subsection.

$$X_{inclination} = \begin{bmatrix} q & \omega^{true} & b^{\omega} & a^{true} & b^{a} \end{bmatrix}^T \tag{4.18}$$

The outputs of the inclination filter are the quaternion components estimates from which the Euler's angles can be computed. Only roll and pitch angles are corrected for drift. The true acceleration vector, the true rotation rate vector as well as the respective biases that affect the measurements are also estimated in the filter.

4.3.2 Heading Filter

4.3.2.1 State Transition Models

The heading of the sensors assembly is computed in a second Kalman filter, which mainly

relies on magnetometers measurements if no magnetic interference is detected. It relies otherwise on the heading provided by the inclination filter. Several techniques exist to estimate the magnetic heading. In [33], a vector method using the gravity vector and the Earth's magnetic field both expressed in the mobile frame is described. More intuitively, the magnetic measurements once rotated in a horizontal plane can be used to sense the direction of the magnetic north, as for example it is explained in [34]. Another technique based on the knowledge of the components of the Earth's magnetic field in the navigation frame can be used [35].

In this study, to reduce the filter complexity and allow a flexible heading estimation, the magnetometers measurements are first rotated into a horizontal plane using the attitude provided by the inclination filter, as described earlier. Equation (4.5) gives the corresponding magnetic heading used as an external measurement.

This magnetic heading is considered as the reference in the Kalman filter. However, it may be affected by perturbations due to nearby iron objects that would distort the Earth's magnetic field. Thus, in order to mitigate those interferences, the still biased heading provided by the inclination filter is used as a backup. Its bias and scale factor will be estimated using magnetometer data. Once magnetic interferences are detected, the correction is stopped and the debiased heading is used as the main heading source. The reliability and the accuracy of the heading computed from the inclination filter will obviously decrease over time until the next update. The procedure is referred in the following as Magnetic Interference Mitigation (MIM).

Given these statements, the state vector is naturally composed of four unknowns, whose propagation models are given from equation (4.19) to equation (4.22). The true heading is assumed to follow a simple random walk process. It was found to be a good comprise between the random property of the heading variation (i.e. the IMU attitude is unpredictable) and the model complexity.

$$\psi_{k+1}^{true} = \psi_k^{true} + w_k^{\psi} \tag{4.19}$$

where:

- ψ_k^{true} is the true heading of the sensors assembly at epoch k.
- w_k^{ψ} is the driving noise of the true heading at epoch k. It is assumed to be equal to 1° as discussed in subsection 4.2.3, which roughly corresponds to the accuracy that can be achieved using non-filtered magnetic measurements to compute the heading taking into account a typical inclination error of about 1°.

The scale factor affecting the inclination heading (i.e. the heading provided by the Inclination Kalman Filter (IKF)) is also assumed to follow a random walk process. The scale factor is here taken into account since the heading may have been affected by the inclination filter processing. Its variations are nevertheless considered very small over time (variance of the driving noise set empirically according to physical considerations to 0.001°).

$$SF_{k+1}^{IKF} = SF_k^{IKF} + w_k^{SF} \tag{4.20}$$

where:

- SF_k^{IKF} is the scale factor affecting the inclination filter heading solution at epoch k.
- w_k^{SF} is the driving noise of the random walk process.

It is intuitive to think about integrated processes to model the heading bias, since the heading is computed based on the integration of the gyroscopes measurements. However, it was found in the different filter implementations that the increase of model complexity does not provide a great deal of performance as compared to the use of simpler models. Nevertheless, the heading bias is modelled as a 1st order Integrated Gauss-Markov process, as described in equation (4.21).

$$\begin{aligned} b_{k+1}^{\psi} &= b_k^{\psi} + T_s \cdot \dot{b}_k^{\psi} \\ \dot{b}_{k+1}^{\psi} &= e^{-\beta_\psi T_s} \cdot \dot{b}_k^{\psi} + \frac{1}{\beta_\psi} \cdot \left(1 - e^{-\beta_\psi T_s}\right) \cdot w_k^{b\psi} \end{aligned} \tag{4.21}$$

where:

- b_k^{ψ} is the bias (integrated Gauss-Markov) of the inclination filter heading solution at epoch k.
- $\dot{b}_k^{\psi}$ is the time derivate of the bias at epoch k, which follows a 1st order Gauss-Markov process.
- β_ψ is the time constant of the Gauss-Markov model.
- $w_k^{b\psi}$ is the driving noise of the Gauss-Markov process.

The magnetic interference model is given below in equation (4.22)

$$I_{k+1}^{\psi} = c_k^P \cdot I_k^{\psi} + w_k^P \tag{4.22}$$

where:

- I_k^{ψ} is the magnetic perturbation that affect the heading at epoch k.
- c_k^P is the time constant setting the bandwidth of the magnetic interference at epoch k.
- w_k^P is the driving noise setting the magnitude of the magnetic perturbation at epoch k, which is permanently adjusted as a function of the difference between the measured and the theoretical magnitude of the magnetic field.

The magnetic perturbation model is tuned with the parameters c_k^P and w_k^P in order to mitigate the magnetic interferences. The magnitude of the horizontal component sensed by the magnetometers as well as the magnetic inclination angle are checked and compared to the theoretical ones that can be found in database such as those provided by the National Geophysical Data Centre [22]. If the discrepancy is too high, a magnetic interference is detected and the driving noise setting its magnitude is increased. In that case, less confidence is also given in magnetometer measurements, so that the true heading estimation relies mainly on the inclination filter heading solution.

4.3.2.2 Measurements Models

As discussed above, the measurements are twofold. The heading measurements can be provided whether by the inclination filter or by the magnetometers. The magnetic heading computed according to equation (4.5) is given below in equation (4.23).

$$\psi_k^{mag} = \psi_k^{true} + I_k^{\psi} + n_k^{mag} \tag{4.23}$$

where:

– ψ_k^{mag} is the magnetic heading measurement coming from the processing of magnetometers data.

– n_k^{mag} is the magnetic heading measurement noise at epoch k. The variance of the noise is adjusted according the intensity of the magnetic interference I_k^{ψ} that may occur.

The model of the heading computed with the quaternion components estimated in the inclination filter is given in equation (4.24).

$$\psi_k^{IKF} = SF_k^{IKF} \cdot \psi_k^{true} + b_k^{\psi} + n_k^{IKF} \tag{4.24}$$

where :

– ψ_k^{IKF} is the inclination filter heading output at epoch k and used as measurement of the heading Kalman filter.

– n_k^{IKF} is the inclination filter measurement noise at epoch k.

4.3.2.3 Heading Filer Summary

The heading filter principle is summarised below in Figure 4.21. It uses the state equations (4.19), (4.20), (4.21) and (4.22). The heading drift estimation is done through the combination of the measurements coming from the inclination filter (rotation quaternion converted into Euler's angles) and the processing of the magnetometers data. The measurements equations are given in equation (4.23) and (4.24).

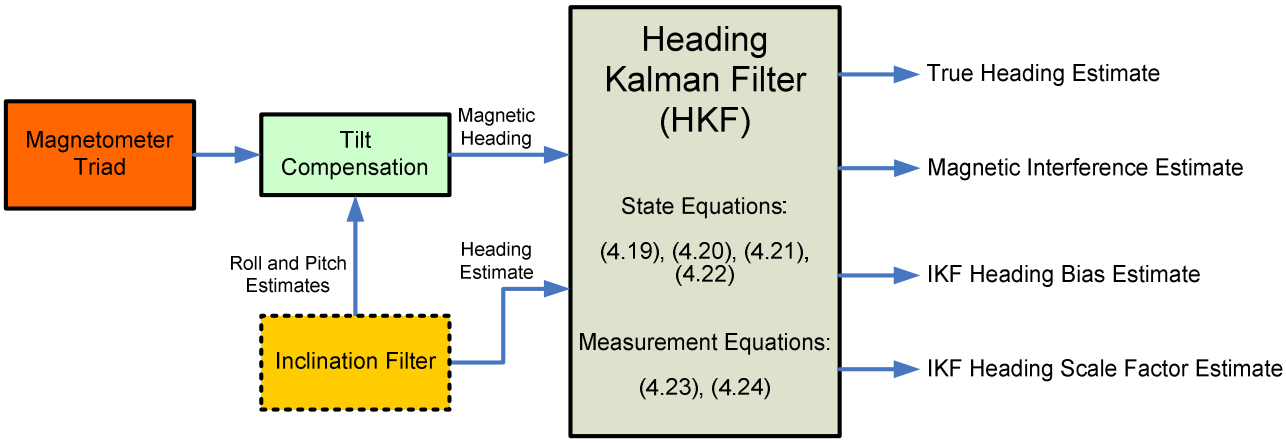

Figure 4.21: Heading filter principle.

Equation (4.25) gives the state vector of the heading filter, which involves 5 unknowns as defined in the above sub-section.

$$X_{heading} = \begin{bmatrix} \psi_k^{true} & SF_k^{IKF} & b_k^{\psi} & \dot{b}_k^{\psi} & I_k^{\psi} \end{bmatrix}^T \tag{4.25}$$

The outputs of the heading filter are the true heading estimate and the errors affecting the magnetic heading (i.e. scale factor, bias and interference).

4.3.3 Optimised Drift-Free Attitude Filter

Among all the three types of sensors used in the measurement unit, gyroscopes are the more expensive ones. Therefore, in order to reduce the overall sensors assembly cost, one could think about removing some of them. In this perspective, a single gyro mounted vertically onto the body of a pedestrian or mounted in a vehicle should provide the orientation of the sensors assembly. But due to the dynamic of pedestrians and even land vehicles, this gyro is not likely to perfectly sense the vertical rotation rate of the measurement unit, introducing some errors in the heading estimation. To avoid such alignment error, magnetometers measurements are combined with the single gyroscope. Equation (4.26) gives the basic relationship between the true rotation rate, the Earth's magnetic field and its derivative, assuming no magnetic interference.

$$dm_k^{(m)} = \omega^{true,(m)} \times m_k^{true,(m)} \tag{4.26}$$

where:

- $m_k^{true,(m)}$ is the true magnetic field vector, as defined above in equation (4.4).
- $dm_k^{(m)}$ is the time derivative vector of $m_k^{true,(m)}$, expressed in the mobile frame at epoch k.

By developing and rearranging equation (4.26), it is possible to give an expression of the rotation rates along the two axes where the sensors assembly is not equipped with gyroscopes. Assuming the only gyroscope of the measurement unit is pointing upward along the vertical axis, equation (4.26) can be developed such that:

$$\omega_{x,k}^{true,(m)} = -\frac{dm_{y,k}^{(m)} - \omega_{z,k}^{true,(m)} \cdot m_{x,k}^{true,(m)}}{m_{z,k}^{true,(m)}} \tag{4.27}$$

$$\omega_{y,k}^{true,(m)} = \frac{dm_{x,k}^{(m)} + \omega_{z,k}^{true,(m)} \cdot m_{y,k}^{true,(m)}}{m_{z,k}^{true,(m)}} \tag{4.28}$$

where:

- $dm_{-,k}^{(m)}$ is the '-' coordinate of $dm_k^{(m)}$.
- $\omega_{-,k}^{true,(m)}$ is the '-' coordinate of $\omega^{true,(m)}$.
- $m_{-,k}^{true,(m)}$ is the '-' coordinate of $m_k^{true,(m)}$.

According to equations (4.27) and (4.28), magnetic measurements can be used to compensate the tilt error due the lack of gyroscopes. The computed rotation rates around x and y axes as defined in the two above equations are then used as measurements that are fed into the inclination Kalman filter. However, when magnetic interferences disturb the Earth's magnetic field so that magnetometer measurements are no more reliable, the two above equations may introduce large errors in the heading estimation. To mitigate the effect of these perturbations, magnetometer measurements are only used when they are found to be reliable enough. In that case, the attitude is computed without errors and the calibration of the heading computed based on the single gyroscope can be performed. When interferences occur, the heading provided by the filter is the one computed using the calibrated gyroscope.

4.3.4 Drift-Free Attitude Filter

4.3.4.1 Design n°1: Attitude Filter using all the Sensors

The global attitude filter is the combination of the two above filters. However, a well-known issue with Euler's angles rises when the sensors assembly experiences roll angles of $\pm\pi/2$. This use case may occur especially if the sensors assembly is put with a random attitude on the body of a user or on the dashboard of a vehicle. In that case, both pitch and heading angles are no more defined. This typical singularity disturbs the visual restitution of the attitude of the sensors assembly. Thus, an Euler's Angles Singularity Resolution (EASR) algorithm (detailed in chapter 3) is implemented at the output of the inclination filter to detect and correct this issue. It also provides a reliable heading estimate whatever the attitude of the sensors unit [36].

The principle of the algorithm using all the sensors of the measurement unit is summarised in Figure 4.22. The first Kalman filter is dedicated to inclination estimation. Its state vector is composed of 16 unknowns. Then angles are checked to avoid singularities and heading estimation is done through a second Kalman filter of 5 states.

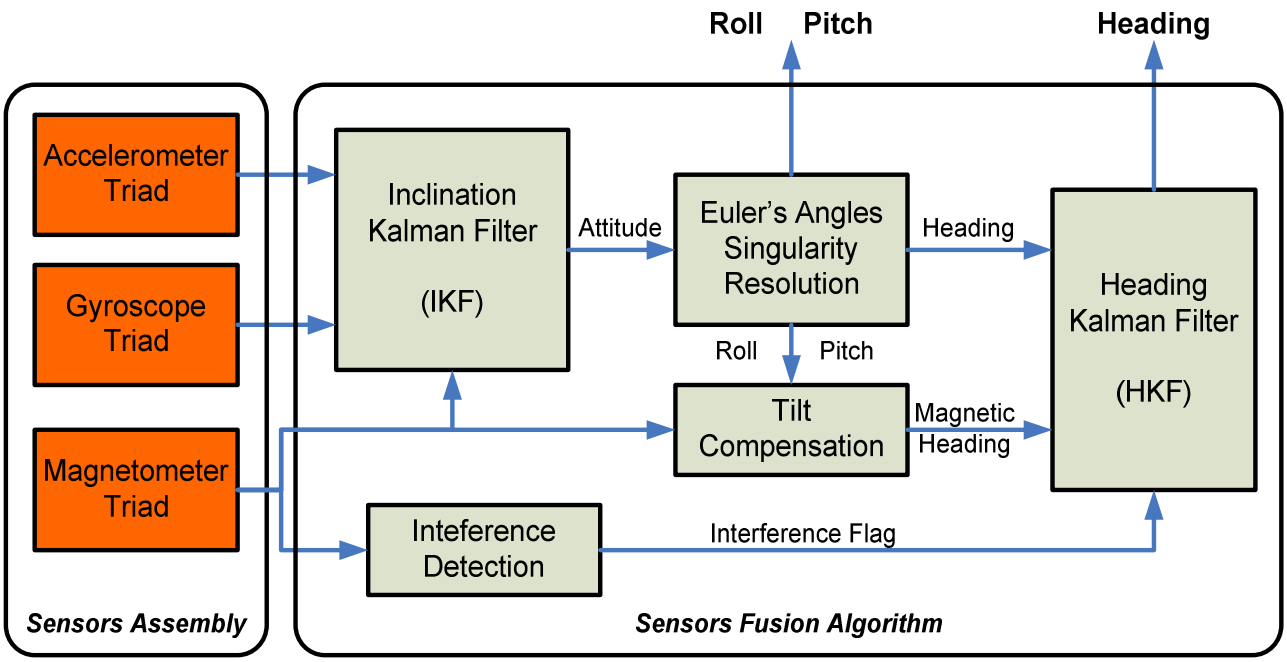

Figure 4.22: Attitude filter algorithm using all the sensors.

4.3.4.2 Design n°2: Attitude Filter using only 1 Gyroscope

Figure 4.23 summarises the algorithm in the case of the use of only one gyroscope mounted vertically. In such a use case, the EASR algorithm may not be useful since the measurement unit is assumed to be closely attached to the vehicle / pedestrian to localise.

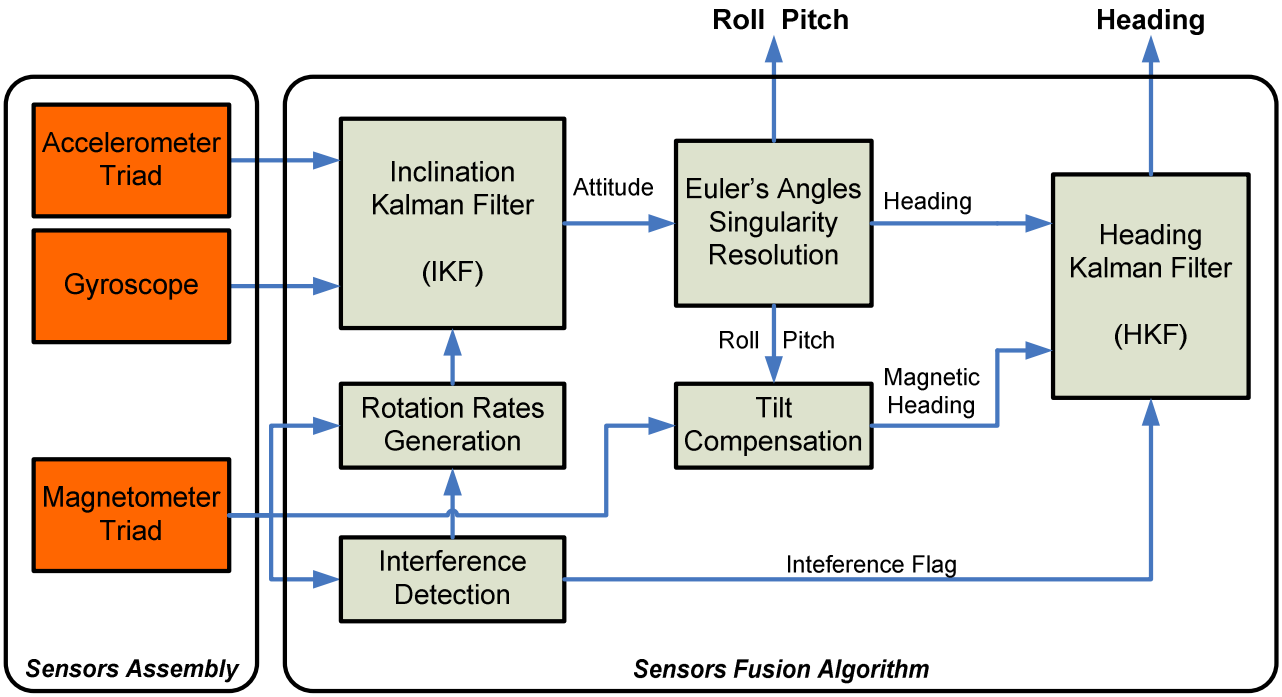

Figure 4.23: Attitude filter algorithm with only 1 gyroscope in the sensors unit.

4.3.5 Test Results

This section presents the results of the trials exercised in actual conditions using the sensors of the MTi. The attitude filter is tested for both pedestrian and land vehicle navigation under dynamic conditions. The purpose of these tests is to analyse the accuracy of the attitude provided by the filter and more specifically the accuracy of the heading. As a reference, GPS measurements collected during trials are processed differentially to have as accurate as possible heading and trajectory references. As a consequence, the tests took place on an open sky car parking lot of a supermarket with lots of idling and moving cars to make sure that GPS measurements can be differentially processed. Furthermore, such a testing environment allows magnetic interferences to disturb the Earth's magnetic field.

The pedestrian navigation is first tested. In that case, the sensors will be assumed to remain fixed with respect to the body. The dynamic experienced during the walk may change depending where the sensors are placed. The filter should thus be able to adapt the different propagation models according to the pedestrian motion. In the particular case where the sensors are attached to the body with a pre-determined attitude (for example, belt mounted with one axis of the sensors assembly pointing toward the local vertical), the possibility of using only one gyro, allowing in the same time a reduction of the global sensors assembly cost, is more specifically studied.

The land vehicle navigation is tested in second. The IMU is likely to be placed with a random attitude on the dashboard of the car or elsewhere. In that case, the sensors assembly will thus be considered to remain fixed with respect to the car, as for the pedestrian navigation. The possibility of reducing the number of sensors used to provide the attitude of the unit is also addressed. The four different use cases tested in the following are summarised in Table 4.2

Navigation mode	Pedestrian		Land Vehicle	
Test Case	Case 1	Case 2	Case 3	Case 4
Sensors configuration	3 Gyroscopes 3 Accelerometers 3 Magnetometers	1 Gyroscope 3 Accelerometers 3 Magnetometers	3 Gyroscopes 3 Accelerometers 3 Magnetometers	1 Gyroscope 3 Accelerometers 3 Magnetometers

Table 4.2: Measurement unit configuration given typical test cases.

As presented in Figure 4.18 through the acceleration magnitude patterns, the dynamic due to the motion of pedestrians and land vehicles are very different. As a consequence and according to this dynamic, equations (4.12) and (4.14) have to be tuned adequately. In the attitude filters described above, the adaptation of the models to the motion experienced by the sensors assembly is performed online using the variance and the time derivative of accelerations and rotation rates. Furthermore, the magnetometers of the sensors assembly are calibrated against hard interferences caused by nearby iron objects prior to perform the different trials, according to the procedure detailed in subsection 4.2.4.

4.3.5.1 The Pedestrian Navigation Case

4.3.5.1.1 Case 1 Test Results

In this trial, the sensors assembly is put inside the user's trouser pocket with a random attitude. The pedestrian walked a short path in the middle of parked cars. The filter using all the sensors is first tested. Figure 4.24 presents the heading provided by the attitude filter with and without the Euler's Angle Singularity Resolution algorithm detailed in chapter 3. As it can be seen, the sensors assembly experiences many positions where the pitch angle reaches critical values (i.e. $\pm\pi/2$), disturbing the restitution of the estimated heading. The non corrected heading solution plotted in blue is biased and very noisy. Its variance between time 160 and 190 reaches about 30 degrees, which is clearly not realistic of a pedestrian walk.

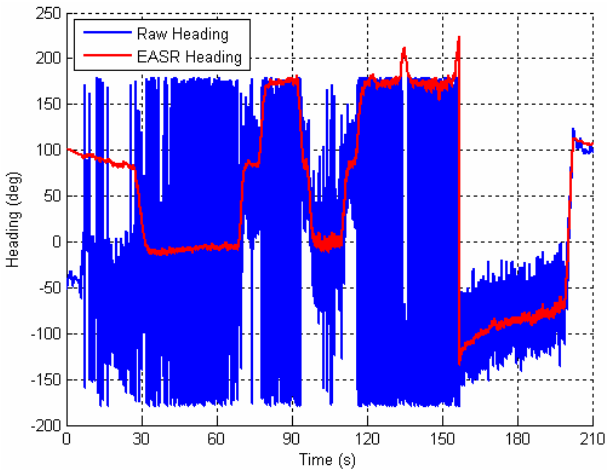

Figure 4.24: Attitude filter heading solution.

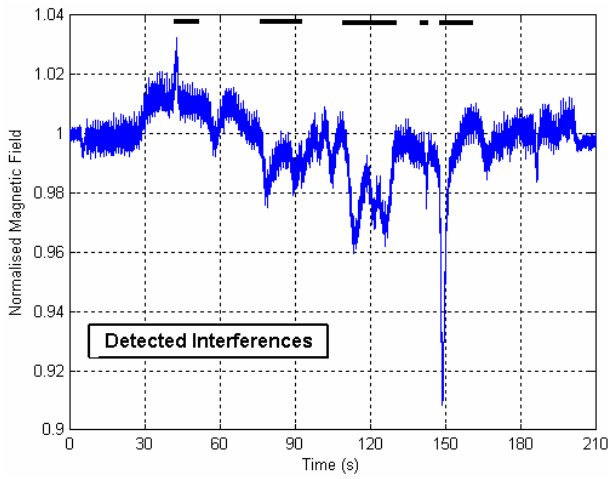

Figure 4.25: Normalised magnetic field magnitude.

Figure 4.25 shows the magnetic field magnitude as recorded during the trial. Perturbations have been automatically detected according to the procedure described at the beginning of the

chapter. They are identified by the black lines in Figure 4.25. It can also be noticed that the magnitude of these interferences is not very high and their duration never exceeds 15 seconds. As a consequence, they are expected not to introduce large errors in the heading estimation.

To analyse the accuracy of the heading provided by the attitude filter, DGPS measurements are used as reference. Since the pedestrian has got a low velocity while walking, the DGPS reference is quite noisy with a standard deviation of about 3 degrees.

Figure 4.26 presents the heading error with respect to the DGPS measurements of both the attitude filter in blue and the classical strapdown gyro-based algorithm in green. The gyro-based heading solution is clearly drifting at a rate of about 5°/min. On the contrary, the heading provided by the attitude filter seems stable.

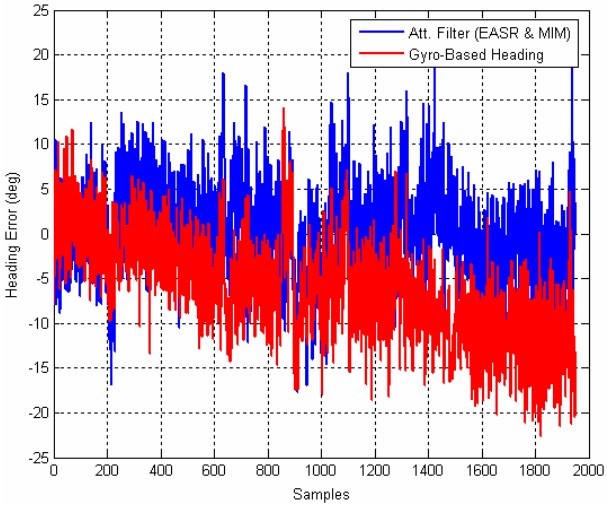

Figure 4.26: Attitude filter and gyro-based heading errors. All sensors are used.

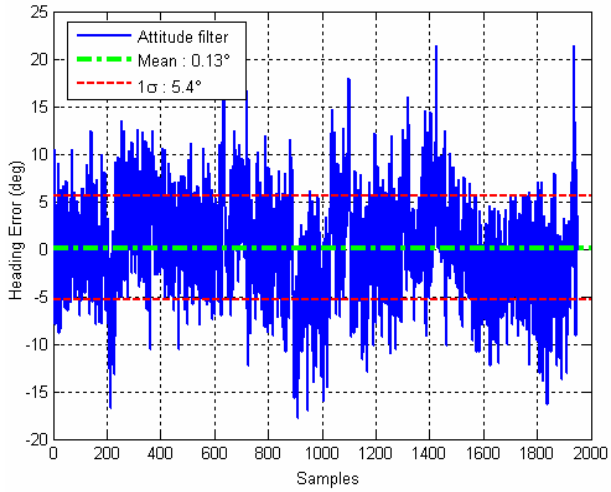

Figure 4.27: Attitude filter heading error. All sensors used.

Figure 4.27 gives a focus on the error made in the estimation of the heading as done by the attitude filter. The error is nearly centred with a mean value of 0.13 degree over the whole trial duration. The standard deviation is about 5.4 degrees, which is quite high. However, it can be assumed that the reference heading is mainly responsible for that.

To assess the impact of the attitude filter heading accuracy on the position solution provided by an inertia-based navigation system, the trajectory of the pedestrian is reconstructed following a dead-reckoning methodology, whose basic equation is given in equation (4.29). The trajectory uses the heading estimated with the different algorithms whereas the curvilinear travelled distance is computed with the DGPS measurements. The observed error in the reconstructed trajectories can thus be entirely attributed to the accuracy of the estimated heading.

$$\begin{aligned} N_{k+1} &= N_k + d_{[k,k+1]} \cdot \cos(\psi_k) \\ E_{k+1} &= E_k + d_{[k,k+1]} \cdot \sin(\psi_k) \end{aligned} \tag{4.29}$$

where:

– N_k is the north position of the user at epoch k.

– E_k is the east position of the user at epoch k.

– $d_{[k,k+1]}$ is the travelled distance between epoch k and k+1 provided by DGPS measurements.
– ψ_k is the heading at epoch k.

Figure 4.28 illustrates the different trajectories reconstructed using different heading sources.

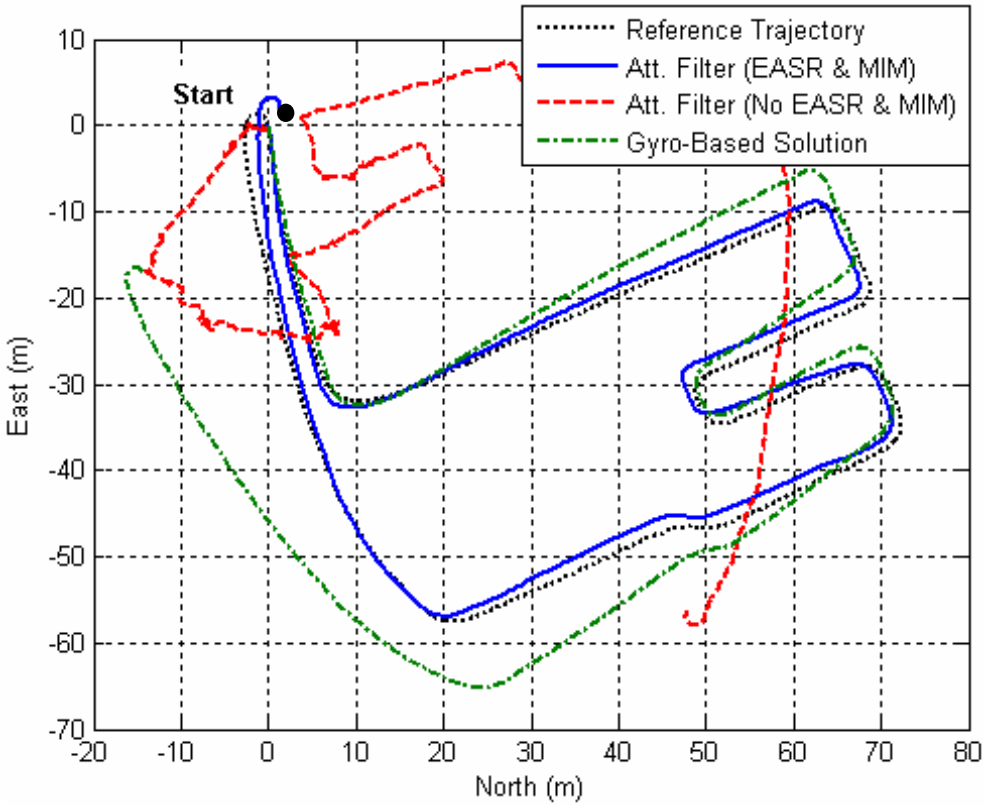

Figure 4.28: Trajectories using different heading sources. Pedestrian case with the triad of gyroscopes.

The black dotted plot is the DGPS reference path. The red plot is the trajectory reconstructed with the heading affected by Euler's angles singularities. The path is obviously not relevant of the true one, which justifies the implementation at some computational expense of an angle ambiguity resolution algorithm (as for example the EASR, as detailed in chapter 3). The green plot represents the trajectory using the heading computed with the classical strapdown algorithm, which is based on gyroscope measurements. The green path is obviously drifting. The blue path is the trajectory using the attitude filter heading solution enhanced with the Magnetic Interference Mitigation (MIM) procedure described earlier. The corresponding trajectory matches the best the true path followed during the trial.

4.3.5.1.2 Case 2 Test Results

In the above pedestrian trial, the x axis of the sensors unit was found to point approximately towards the local vertical during the whole test. The attitude restitution using only the gyroscope along the x axis of the measurement unit is then tested in the following.

Figure 4.29 illustrates the heading errors with respect to the DGPS reference when only one

gyroscope is used in the attitude filter, the other rotation rates being computed using the magnetometer data. The blue plot stands for the attitude filter error with only one gyroscope, whereas the red plot illustrates the vertical gyroscope-based heading error (without compensation due to tilt error and rotation rate bias). As shown in the figure, the gyroscope-based heading is clearly drifting at a rate of about 8°/min. This drift rate is higher than the drift rate of the strapdown solution since the vertical gyroscope is not perfectly aligned with the true vertical axis. It follows indeed the movement of the leg, which introduces non negligible tilt errors in the computed heading solution and contributes to the overall decrease of heading accuracy.

To analyse the effect of the magnetic interferences onto the rotation rates generated with the magnetometers data, an example of gyro bias estimation in the inclination filter is shown in Figure 4.30. The internal Kalman standard deviation is also plotted in black. When interferences occur, the Kalman covariance increases suddenly so that the gyro bias estimate error increases, and as a consequence the tilt angle estimation error as well.

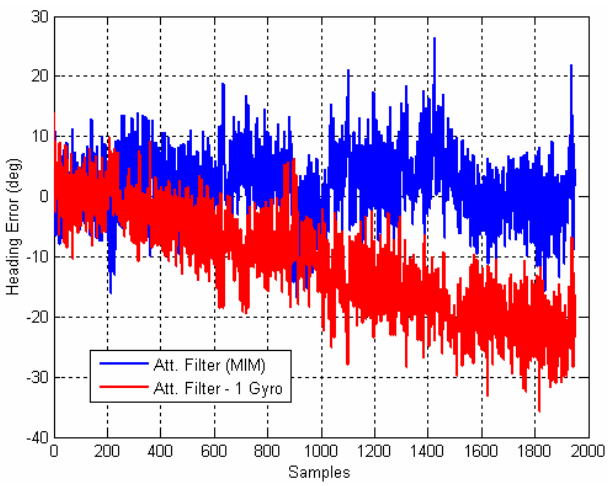

Figure 4.29: Attitude filter and gyro-based heading errors. Only one gyroscope is used.

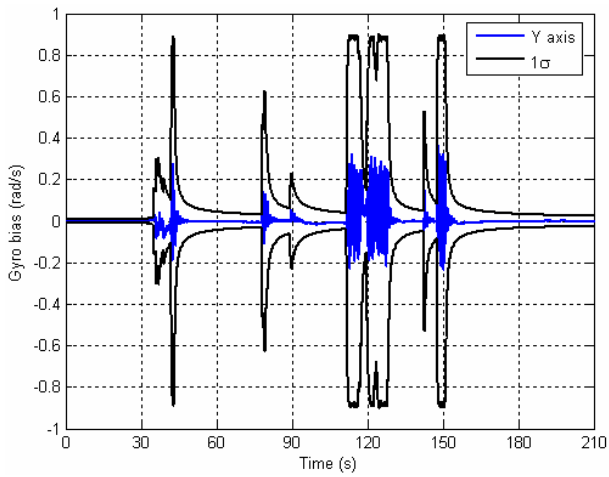

Figure 4.30: Y axis gyro bias estimate of the Inclination Kalman Filter (IKF).

What is also interesting to notice is that the Kalman filter needs time to converge to a more accurate bias estimate (10s after the end of the magnetic interference to go back to a bias standard deviation of less 0.05rad/s). This means that the heading provided by the filter relies on the debiased vertical gyro measurements during the perturbation but also a certain amount of time after this perturbation is detected in order for the filter to converge towards accurate estimates.

As a consequence of the above statements, it can be expected that the sensors assembly using only one gyro will rely exclusively on gyroscope data more often that in the previous case because of the time needed for the filter to converge to stable bias estimates (as illustrated above in Figure 4.30).

Figure 4.31 illustrates the trajectories reconstructed using different heading sources. The gyro-based position solution is plotted in green, the attitude filter heading in blue and the attitude filter using only one gyroscope in red. The red path experiences small drift when the heading solution relies exclusively on gyroscope measurements. This drift is not observable in Figure 4.29 due to the too high variance of the DGPS heading reference.

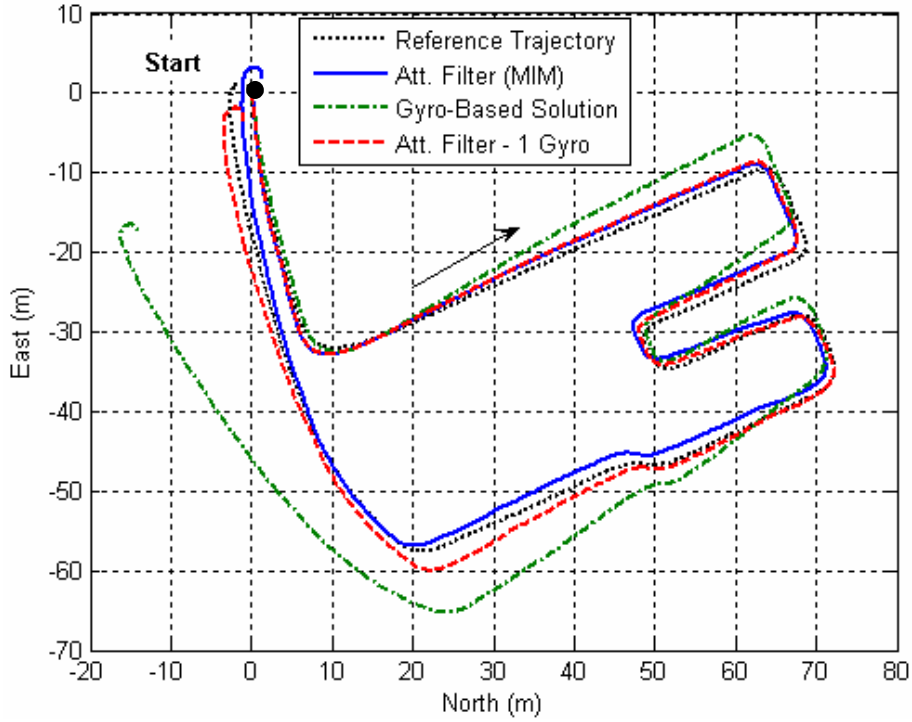

Figure 4.31: Trajectories using Different Heading Sources. Pedestrian Case with only one Gyroscope.

4.3.5.2 The Land Vehicle Navigation

4.3.5.2.1 Case 3 Test Results

The attitude filter algorithm is then tested for typical land vehicle dynamics. As in the pedestrian navigation case, the test took place with a car driven on the car parking lot of a supermarket with lots of moving and idling cars. In a first time, the attitude filter is tested using all the sensors of the measurement unit. Then the performance of the configuration using only one gyroscope is analysed.

In the conducted trial, the standard deviation of the reference DGPS heading was found to be approximately 0.8 degree, which is better than in the pedestrian case. This is mainly due to the medium velocity of the car, much higher than those of a pedestrian, which in turn decreases the sensitivity of the velocity measurements with respect to the noise of the GPS signals.

The different heading errors with respect to the DGPS reference are plotted in Figure 4.32. High errors are observable near sample 700, but this is due to a stop of the car, making the velocity measurements very noisy and as a consequence, the GPS-based heading quasi unobservable.

The green plot stands for the heading computed with gyroscope measurements following a gyro-based strapdown algorithm. The inherent drift is again clearly observable with a rate of about 3°/min, which is less than in the pedestrian case. This can be justified by the dynamic of the vehicle which is quite low, so as a consequence, the in run bias which varies as a function of the temperature and the motion affecting the sensor has less impact on the overall heading error. The red plot stands for the heading computed using the magnetometers data once they are rotated in a horizontal plane using the inclination filter outputs (EASR enabled). As it can be seen in the figure, the magnetic interferences strongly affect the heading estimation. The blue plot is the heading

computed with the attitude filter. The mean of the error is equal to 0.9°, and the standard deviation is equal to 3.3°. No drift is remarkable in the solution provided by the filter.

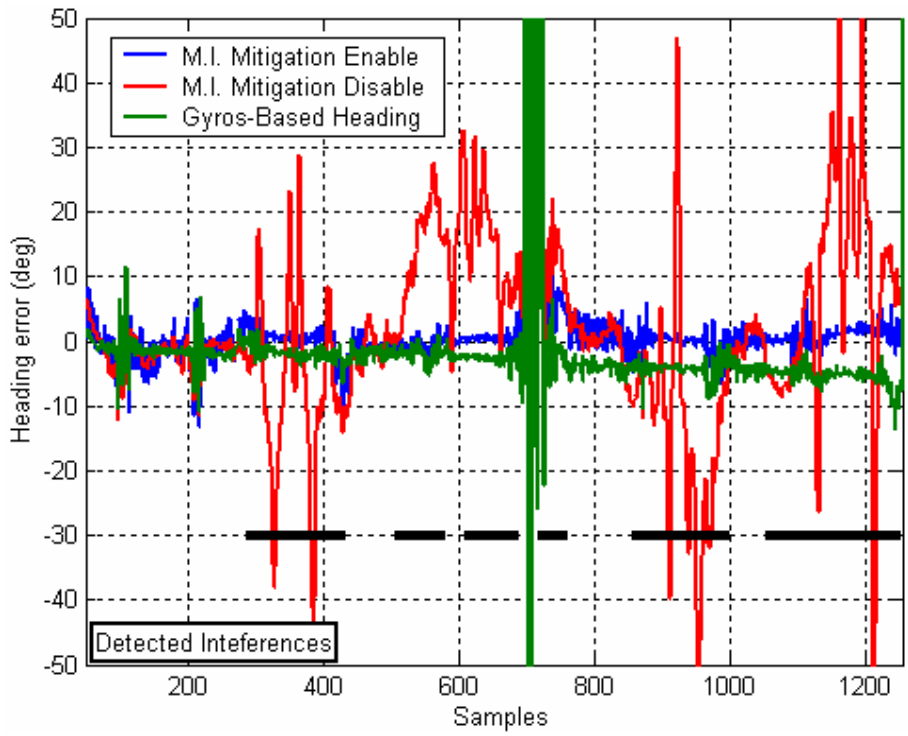

Figure 4.32: Heading errors with respect to the DGPS reference. All the sensors are used.

The reconstructed paths using the above estimated headings are plotted in Figure 4.33.

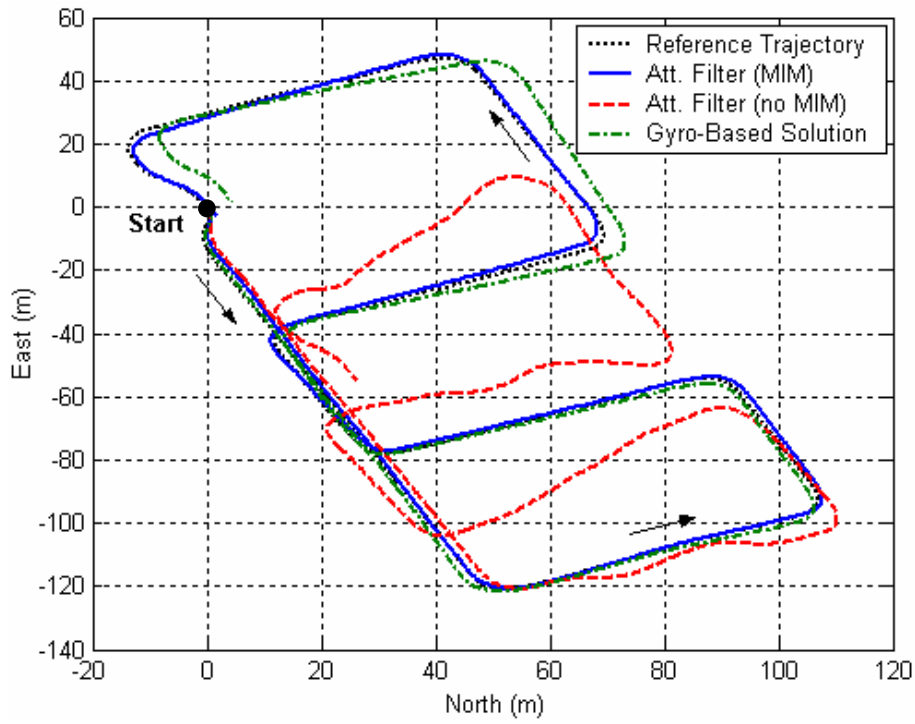

Figure 4.33: Trajectories using different heading sources. Land vehicle case with three gyroscopes.

The reference DGPS path is plotted as the dashed black line. The red path is the trajectory

computed with the magnetic heading once tilt compensation has been applied on the magnetometers measurements. It is obvious that the magnetic interferences that occur during the trial affect the trajectory, which still remains recognisable but exhibits a very poor accuracy.

Opposite, the attitude filter solution plotted in blue is more relevant of the true trajectory followed during the trial. The Magnetic Interference Mitigation (MIM) performs well. As a comparison, the trajectory using the gyro-based heading is also plotted in green. A low drift is observable in this path. This drift is lower than in the pedestrian case, due to the smoother acceleration experienced by the sensors assembly that does not modify the in run bias significantly. This also explains why the attitude filter provides an accurate heading solution during the numerous periods where the magnetometers data are flagged as unreliable, as shown in Figure 4.32.

4.3.5.2.2 Case 4 Test Results

The filter is then tested using only the gyroscope of the measurement unit that is pointing toward the local vertical during the whole trial. The resulting trajectory computed with this new heading source is plotted in Figure 4.34. In order to compare the performance of the different position solutions, the path computed with all the sensors is also plotted in blue and the gyroscope-based strapdown solution in green. As discussed above in subsection 4.3.3, once a magnetic interference is detected, the rotation rates generated by the processing of the magnetometers data are considered corrupted so that the heading provided by the inclination filter is no more reliable. Some time is needed for the filter to converge toward a stable solution, even after the end of the magnetic interference. Meanwhile, the vertical gyroscope is the only sensor capable of providing useful information to compute the heading of the vehicle.

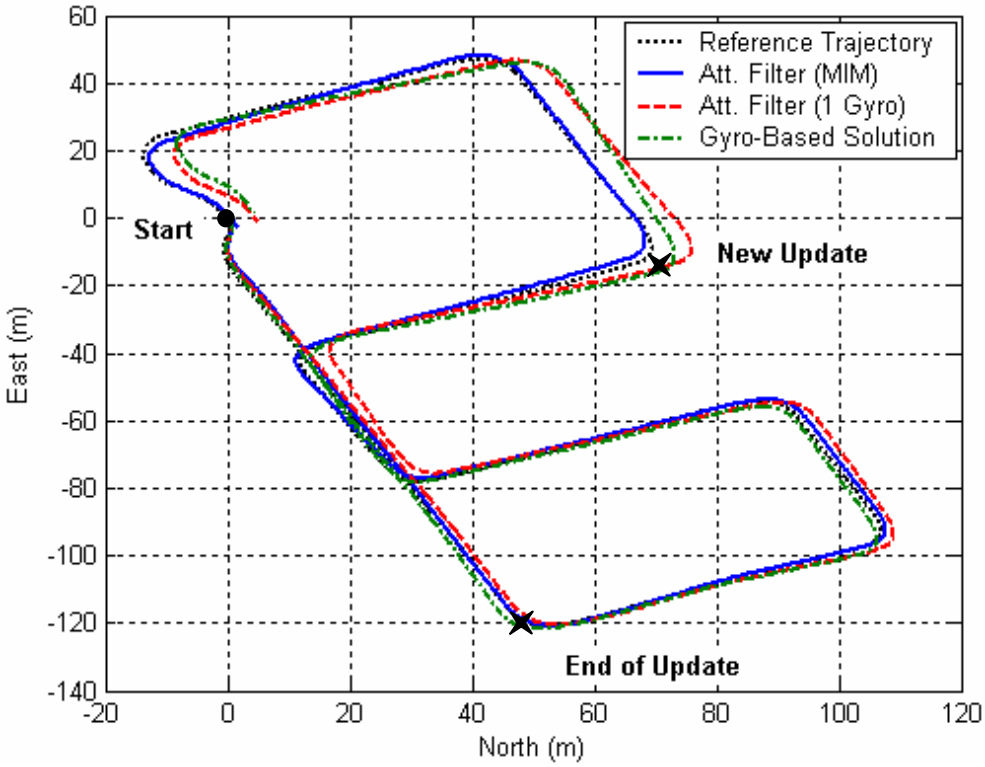

Figure 4.34: Trajectories using different heading sources. Land vehicle case with only one gyroscope.

As a consequence and according to Figure 4.32, the update of the gyroscope-based heading

can only be performed at the beginning of the trial and around sample 800. The red plot standing for the position solution using the heading computed with one vertical gyroscope follows indeed quite well the true path from the beginning to the point marked as “End of Update”, because magnetometers are used to estimate the vertical gyroscope drift. The trajectory experiences then small drift due to gyroscope measurements affected by bias and tilt error, and that can not be corrected. The next update is performed around samples 800 at the “New Update” point, where magnetometer data are declared reliable to enable the estimation of the heading errors (bias and tilt).

4.4 Other Augmentation Techniques

The beginning of the chapter presented some sensor-based augmentations that could yield an increase of availability and accuracy of GPS-based positioning systems when integrated with the GPS sensor. The following described another improvement that can be brought by such low-cost sensors as their information can be fused into one filter in order to limit the impact of the gyroscopes bias, even if the IMU is in motion, and thus increase the computed attitude. This section presents finally some improvements that are rather in relationship with the type of motion experienced by the IMU, and that do not require the use of extra sensors.

4.4.1 Zero velocity UPdaTe (ZUPT)

As detailed in chapter 3 and recalled in this chapter, the main issue involved in the INS is the impact of the sensors bias (accelerometers and gyroscopes) on the different INS computation stages. Basically, these errors can be estimated either if an external accurate source is available to perform corrections, or if the motion of measurement unit can be independently characterised. The latter case requires a motion detection algorithm, but it can give a great deal of performance for a minimal computational cost.

It is straightforward to infer some properties of what should be measured by the sensors if the IMU is at rest. Indeed, and whatever the accuracy of the error model of the different sensors, it is obvious that once the IMU is idling, the gyroscopes output should be equal to zero, and the acceleration sensed by the triad of accelerometers should be exclusively the gravity vector. In such a use case, the estimation of the gyroscope bias is easy to do by averaging the output of the sensor.

It is more difficult to estimate the biases affecting the accelerometer triad. However, it is straightforward to estimate the error made on the velocity computed from the acceleration measurements [38]. When the IMU is detected to be idling, the velocity components can indeed be set to zero since no motion affects the measurement unit (Zero velocity UPdaTe - ZUPT).

Figure 4.35 shows the basic principle of the zero velocity update for updates every 30s, 60s and 90s. Once the IMU is found idling, the velocity components computed through the integration of the accelerations are set to zero. The figure is plotted according to a typical accelerometer bias of 0.04m/s², which is the average bias affecting the accelerometers measurements as characterised in chapter 3. The effect on the position accuracy is illustrated in Figure 4.36.

Such an algorithm will not be used within the scope of this thesis.

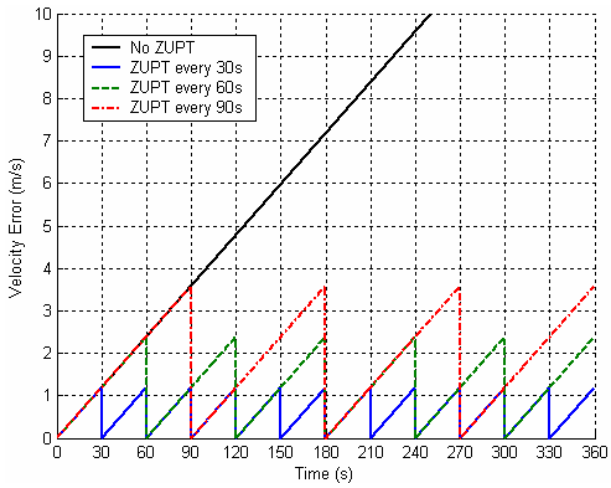

Figure 4.35: ZUPT. Theoretical velocity error profiles.

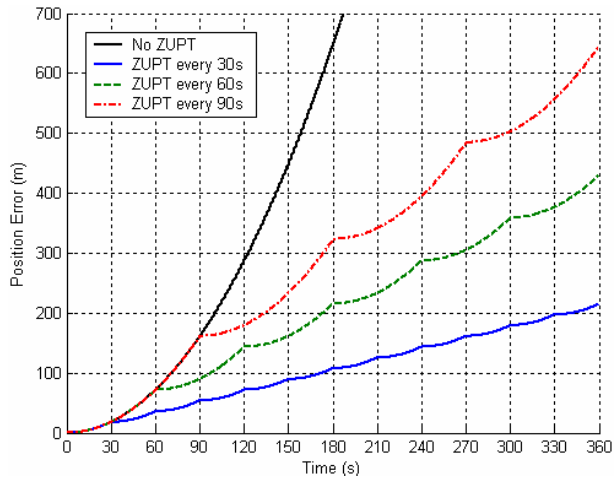

Figure 4.36: ZUPT. Theoretical position error profiles.

4.4.2 Velocity and Height Constraints

In most navigation cases, the measurement unit is attached to the pedestrian or vehicle to localise. In such a use case, it is possible to find the displacement direction and the orientation of the IMU with respect to it. In the particular case of the vehicle navigation, it can be assumed that the measurement axes perpendicular to the displacement direction do not provide any useful information (assuming also that the vehicle does not slip and stays on the ground). In other words, the velocity components onto these axes can be set to zero [37]. It is more difficult to hold the same assumption for pedestrian navigation, since the pedestrian may walk a step backward or forward, but also laterally, which makes the velocity constraints obsolete. Such a kind of algorithm-based augmentation will be used only for vehicle navigation.

The height constraint follows the same principle as the velocity constraint. For a typical travel, the height solution does not vary very much, at most by more than few tens of metres. If the height is provided by a pressure sensor for example, the position solution accuracy may increase in both 2D and 3D dimensions, especially in urban canyon environments, where GPS signals are weak and affected by large multipath. Such an improvement will be assessed in chapter 6.

4.5 Conclusion

This chapter presented some sensor-based augmentations in order to improve the position accuracy of both INS and GPS. The pressure sensor has first been introduced. Its performance have been assessed and more specifically the altitude and vertical velocity accuracy. It has been found that the altitude provided was quite stable with a standard deviation of about 2 metres. Despite the known sensitivity of the pressure measurements to the weather conditions, the numerous tests that have been conducted did not demonstrate such a relationship. This may be first explained by the weather conditions during the trial (no major changes between outside and inside), and second by the calibration procedure implemented in the evaluation board that applies corrections to the measurements as a function of the temperature sensed at the pressure sensor level. The vertical velocity accuracy was also analysed. It was found very noisy if computed based on the raw altitude

measurements. However, as soon as the altitude is filtered through a simpler averaging window for example, the velocity becomes more accurate and suitable for further integration. Different integration techniques have been studied more specifically at the altitude level. The integration of the altitude measurements as an additive pseudorange measurement was found to give the best improvements in terms of 3D position accuracy. In the perspective of an integration of GPS with inertial sensors, height constraint seems however more adapted to give a great deal of performance for a minimal increase of algorithm complexity.

The benefits of the magnetometers measurements have been detailed. The Xsens' MTi has the advantage of including in the small sensors package such components, so that the improvement of the heading accuracy is easier to do. Since the increase of accuracy of the heading provided by the measurement unit leads to an increase of the INS performance as demonstrated in chapter 3 for both classical and pedestrian mechanisations, an algorithm has been developed. The sensors fusion detailed in this chapter was dynamically tested to assess its performance for typical motions such as pedestrian and land vehicle. The models implemented in the attitude filter are dependent on the dynamic experienced by the sensors. The models tuned according to the worst case (pedestrian navigation) shows good heading accuracy capabilities. A dynamic accuracy of less than 1° was found achievable according the results of the trial conducted for pedestrian navigation. The mitigation of the magnetic interferences shows also good results, with an efficient and reliable detection procedure. However, according to the methodology followed in the design of the filter, the heading output relies exclusively on gyroscope measurements during magnetic interferences, which introduces drift as long as no update can be performed. The example of land vehicle navigation is a typical use case where the magnetometers are not often reliable enough to enable the gyroscopes bias estimation. It was nevertheless shown that according to the conducted trials, the availability of the magnetic measurements was good enough. As the vehicle did not experience high dynamic, the in-run gyroscope bias varied much slowly than in the pedestrian case, allowing long and reliable navigation periods without the need of a regular heading update.

The possibility of reducing the number of sensors has also been addressed. The performance of the attitude filter has been shown to be quite worse than the full sensors one, according to the trial exercised, even if results are within acceptable limits according to the gyroscope-based attitude solution.

Others techniques based on the dynamic of mechanical displacement properties of the user / vehicle to localise have been discussed. Their performances are likely to be demonstrated in chapter 6, which addresses the INS/GPS integration, as well as the benefits brought by the attitude filter. The next chapter will also show the advantage of such a sensor combination.

Chapter 5: Sensors Aiding for GPS Acquisition

This chapter discusses the possibility of using low-cost sensors of MEMS type in order to decrease the acquisition complexity of GPS signals by reducing the user's Doppler uncertainty. The extension to general GNSS signals is straightforward. Among all the processing stages involved in the position computation process, it seems that the acquisition stage is the more appropriate to benefit from the sensors assembly information. As detailed in chapter 3 and chapter 4, the MEMS sensors can provide orientation and velocity information, whose respective accuracies mainly depend on the mechanisation used for standalone inertial navigation (i.e. classical INS or PNS mechanisation) as well as the filters used to limit the impact of sensors errors (as for example the attitude filter detailed in chapter 4).

In a first time, the principle of the tight coupling of the GPS receiver with the low-cost MEMS sensors is described. The algorithm aiming at estimating the user's Doppler in order to improve the acquisition of GPS signals is discussed and justified. A detailed Doppler contribution is provided with respect to the user, the receiver clock and the satellite to acquire. The sensor fusion algorithm is then tested in actual conditions and results are presented.

5.1 Introduction

The recent improvements in the manufacturing of Micro-Electro-Mechanical-Systems (MEMS) have made the use of such sensors very common in many areas. Indeed, despite their low accuracy, their low consumption, small size and low cost make them very attractive for many applications and services. Among them, Location-Based Services (LBS) may experience significant improvements in both reliability and availability since GNSS-based location products dedicated to pedestrian or land vehicle navigation are likely to be augmented with a set of complementary MEMS. However, such an augmentation mainly relies on the quality of the sensors used in the hybridised system. Because they usually are low-cost, enhanced algorithms have to be implemented to cope with their intrinsic low-performance.

The traditional sensors fusion approach focuses on the correction of the position using a reference navigation system, for instance a HSGPS or AGPS receiver. Figure 5.1 illustrates such a system combination without getting into the details of the integration algorithm. The usual integration part is the data fusion algorithm highlighted in green, whose different architectures are described in details in the next chapter. The aim of this chapter is rather to study the performance that can be achieved in the reduction of the GPS processing complexity using external information provided by the low-cost MEMS sensors, which is illustrated by the thick red line.

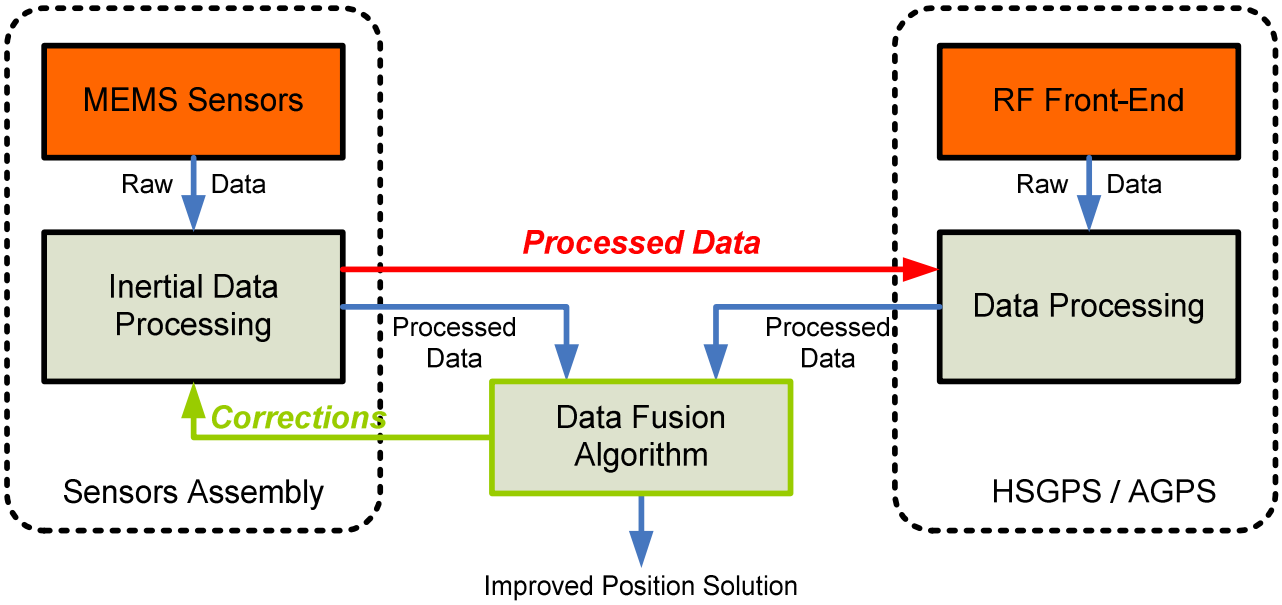

Figure 5.1: Navigation systems integration principle.

As discussed in chapter 1, the basic processing stages of a GPS receiver are the acquisition and tracking stages. The improvement of the tracking loops with external information is well known and often termed as ultra-tight integration. The Doppler derived from the inertial measurements is used to drive the phase and code loops in order to improve the dynamic response of the integrated system. More details can be found in the large available related literature ([60] and [61] for instance). Such an integration level requires high quality inertial sensors, and therefore will not be discussed in this study. The following rather focuses on the acquisition enhancement and more specifically using a triad of low-cost accelerometers, magnetometers and gyroscopes.

The approach followed in this chapter concentrates on how acquisition can be improved through the reduction of the user dynamic uncertainty by using information from MEMS sensors [52]. Such an issue is of dramatic importance especially in the use case of weak signal acquisition that involves tiny Doppler bins, which in turn increases the total number of search bins, and the overall computation load. The navigation system considered throughout the chapter is composed of two parts. The first one is the GPS receiver, which is assumed to work in the previously described assisted mode. The second part of the navigation system is composed of a low-cost MEMS-based measurement unit, which is mounted onto the pedestrian or the land vehicle.

The different components of the navigation system have already been described in details in chapters 2 and 3. Because the mobile – whether the pedestrian or the land vehicle – is likely to move in harsh environments such as deep urban canyons or even tunnels, many signal disruptions may affect the GPS-based position solution availability. Moreover, a lot of GPS signal re-acquisitions may be performed in those environments, increasing the power consumption and the computation load too. The proposed integration algorithm takes into account all the aforementioned issues by using MEMS sensors information to enhance GPS signal acquisition. The result of the processing of MEMS data is directly used in the GPS signal processing core to minimise errors and maximise processing efficiency. A detailed description of the methodology followed to integrate the inaccurate sensors information into the GPS acquisition stage is given. Tests in actual conditions are then conducted for both pedestrian and land vehicle navigation and their respective results analysed.

Two use cases would be of interest, either the acquisition is done in the so-called “cold start” mode, or in the “hot/warm start” mode. Hot and warm starts show the same issues. In both cases a fix has just been computed so that the receiver’s clock synchronisation is done, the Doppler contribution of the Local Oscillator is estimated as well as the user one. Consequently, depending on the accuracy of the receiver’s clock model, there would be no need of extra information to speed up the next acquisition process. A typical example would be the re-acquisition of a GPS signal after a short outage.

This chapter rather concentrates on the cold start acquisition aiding under typical dynamics encountered in personal navigation (i.e. typical pedestrian and land vehicle motions). The acquisition phase is a two dimensions search process so that the acquisition aiding mainly consist in the reduction of time and frequency search spans for every GPS signal. In synchronised cellular network, it is possible to make the reference time consistent with GPS time, so that the time uncertainty can be reduced to only several chips. In non-synchronous cellular networks, the accuracy of the reference time provided in the assistance message is only accurate to several seconds (typically ±2 seconds), which does not allow any time uncertainty reduction. As a consequence, it will not be studied in the following of this chapter.

The focus is put on the frequency uncertainty reduction. Assistance provided by external means can help reducing the frequency search span. The frequency uncertainty is composed of three independent contributions coming from the motion of the GPS satellites, the receiver’s Local Oscillator drift and the motion of the user. The first contribution can be estimated using external data (c.f. AGPS positioning). The receiver’s LO drift can be modelled using a mathematical model, but its accuracy is not good enough to allow the estimation of the Doppler contribution over medium even short time duration. The user Doppler contribution can not be estimated without external information, thus is considered to be unknown as well. Consequently in the following, the acquisition aiding will be achieved through the estimation of both LO and user Doppler contributions.

5.2 Receiver Doppler Uncertainty

Basically, the carrier of the GPS signal is affected by the relative motion of the transmitting satellite with respect to the receiver's antenna, and the drift of the clocks used at both sides of the transmission channel. As a consequence, for a single channel of a GPS receiver, the Doppler affecting the carrier of the signal to acquire can be written as given in equation (5.1).

$$f_{receiver}^{carrier} = f_{L_1} + f_d^r \tag{5.1}$$

where:

- $f_{receiver}^{carrier}$ is the apparent carrier frequency of the signal to acquire.
- f_{L_1} is the true carrier frequency of the signal to acquire.
- f_d^r is the overall receiver Doppler effect affecting the carrier of the signal to acquire.

As detailed in equation 2.35 of chapter 2, the Doppler of the received signal is composed of several contributions. All these contributions are more specifically analysed in the following subsections.

$$f_d^r = f_d^{user} + f_d^{satellite} + f_d^{LO} + n_f$$

where:

- f_d^{user} is the user's Doppler contribution (Hz).
- $f_d^{satellite}$ is the satellite's Doppler contribution (Hz).
- f_d^{LO} is Local Oscillator's Doppler contribution (Hz).
- n_f is the overall noise affecting the measurement (Hz).

5.2.1 Satellite Contribution

The satellite Doppler contribution can be predicted when the ephemeris of the satellite to acquire is known, as well as the position of the receiver's antenna and the GPS time. In the particular case of an A-GPS positioning system, the ephemeris are transmitted though the assistance data. The rough GPS time information is also given with a rough user's position whose accuracy is consistent with the cell size the mobile phone relies on. The satellite Doppler contribution is computed according to equation (5.2). It involves the satellite velocity expressed in the navigation frame ***(n)*** or in the ECEF frame ***(e)***.

$$f_d^{satellite} = -\frac{L_1}{c}\vec{u}^{(e)} \cdot \vec{v}_{sat}^{(e)} = -\frac{L_1}{c}\vec{u}^{(n)} \cdot \vec{v}_{sat}^{(n)} \tag{5.2}$$

where :

- $\vec{u}$ is the LOS unit vector between the user and the satellite.
- $\vec{v}_{sat}$ is the satellite velocity vector.

- L_1 is the true carrier frequency.
- c is the velocity of light.

According to Figure 5.2, the LOS unit vector can be expressed as given in equation (5.3). The coordinates are related to the position of the user through the well known parameters that are the satellite elevation and azimuth. The unit vector is expressed in the navigation frame ***(n)***.

$$\vec{u}^{(n)} = \cos(E)\cos(Az)\cdot\vec{n} + \cos(E)\sin(Az)\cdot\vec{e} + \sin(E)\cdot\vec{d} \tag{5.3}$$

where :
- E is the elevation of the satellite.
- Az is the azimuth of the satellite.
- $\vec{n},\vec{e},\vec{d}$ are the unit vectors of the navigation reference frame ***(n)***.

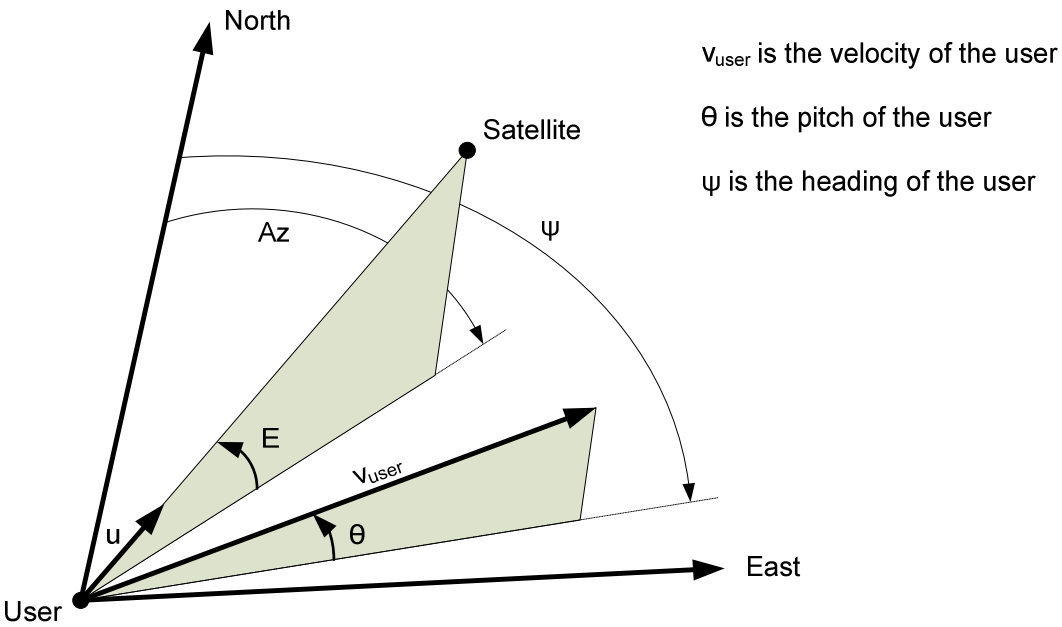

Figure 5.2: Satellite position definition with respect to the user's position.

Using equations (5.2) and (5.3), the satellite Doppler contribution is then fully described by equation (5.4), as detailed below:

$$f_d^{satellite} = -\frac{L_1}{c}\left[\cos(E)\cos(Az)\cdot v_{sat}^{north} + \cos(E)\sin(Az)\cdot v_{sat}^{east} + \sin(E)\cdot v_{sat}^{down}\right] \tag{5.4}$$

The ephemeris data are used to compute the velocity of the satellite in the ECEF reference frame at the GPS time transmitted in the assistance message. Thus, since the time information accuracy is within ±2 seconds (typical assistance time uncertainty in a non-synchronous network), errors are introduced in both satellite velocity and position prediction.

The impact of the time accuracy on the satellite Doppler prediction is illustrated in Figure 5.3. In this simulation, the user is assumed static, located at a perfectly known position that is used as a reference (ENAC laboratory). The YUMA almanac for week 254 is used in order to simulate the satellite positions and velocities. PRN 1 has been arbitrarily chosen for the simulation. As it can

be seen, the uncertainty due to the inaccuracy of the GPS time available in the assistance data is quite small and never exceeds 1.5 Hz.

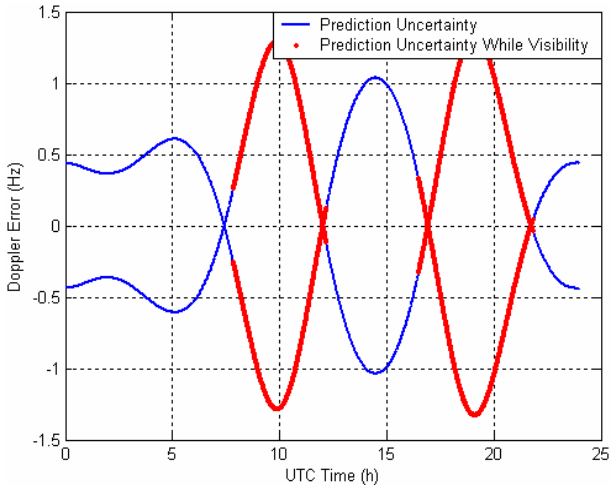

Figure 5.3: Satellite Doppler uncertainty. GPS time known at ±2s.

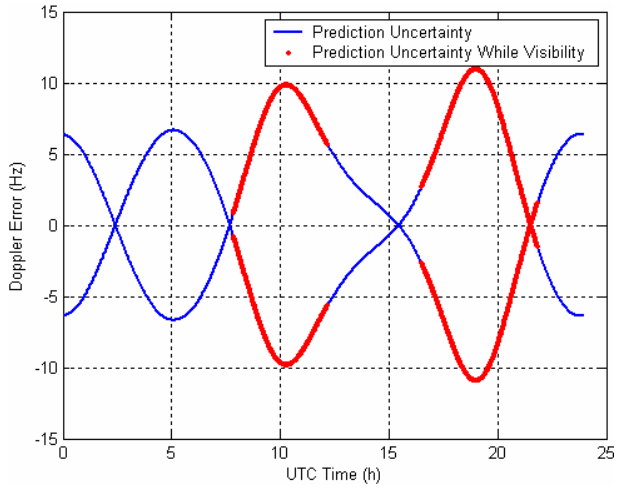

Figure 5.4: Satellite Doppler uncertainty. User's position uncertainty of ±15km.

The impact of the user's position uncertainty is rather more important, as shown in Figure 5.4. For the highest horizontal uncertainty of ±15km (the maximum size of a GSM cell), the error made on the prediction of the satellite Doppler can reach up to 13 Hz. In Figure 5.5 is shown the combined effect of the inaccurate position and reference time in the satellite Doppler prediction. The error is very close to the one plotted in Figure 5.4, due to the very limited impact of the time uncertainty. The typical remaining uncertainty is reduced to several tens of Hertz.

Figure 5.6 gives an example of the satellite Doppler estimation accuracy obtained through the processing of ephemeris data recorded in actual conditions. The GPS receiver used for that purpose is a Novatel ProPak GLplus receiver operating under clear sky conditions. In this simulation, the exact user's position is known. For Doppler prediction accuracy analysis, several position uncertainty values are applied to that reference position. Results are plotted in Figure 5.6. They are consistent with the previous conclusions drawn when considering almanacs (see Figure 5.3 and Figure 5.4).

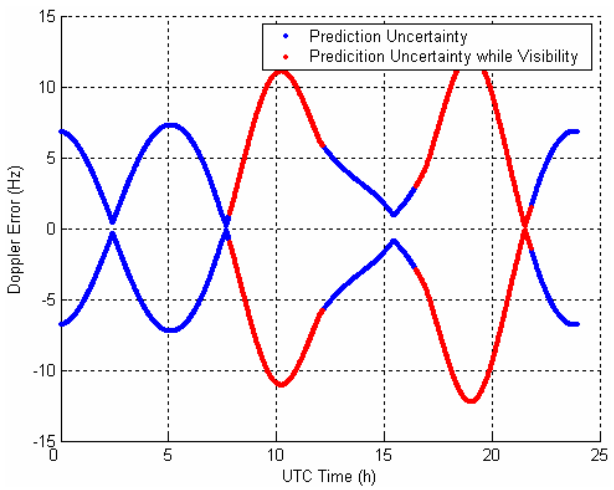

Figure 5.5: Satellite Doppler uncertainty. GPS time known at ±2s. User's position uncertainty of ±15km.

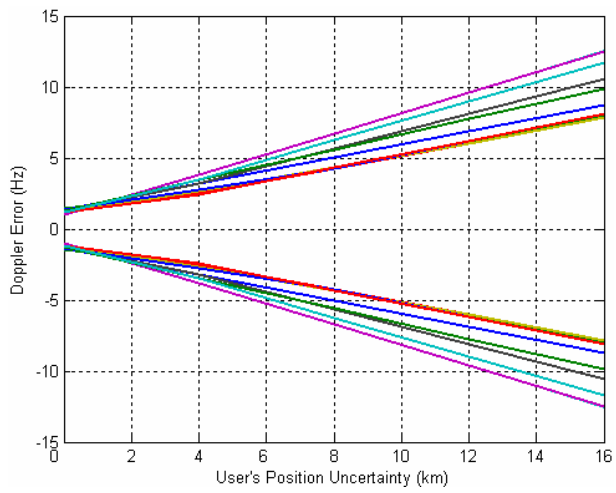

Figure 5.6: Satellite Doppler uncertainty. GPS time known at ±2s. Results with real GPS ephemeris.

As a conclusion on the satellite Doppler contribution, it can be assumed that once the predicted satellite Doppler is obtained using the information provided by the assistance message inherent to the AGPS technology, the remaining satellite Doppler estimation error stays within ±15 Hz at most.

5.2.2 Local Oscillator Contribution

The contribution of the Local Oscillator (LO) depends on its quality. A typical 1ppm accurate LO introduces an uncertainty of about $\pm 10^{-6} \times L_1$ Hertz at L_1 (approximately ±1.5kHz), which is likely to be the case of the components embedded in mobile phones. In the standard conditions of a cold start and as soon as four satellites are acquired or tracked, the LO Doppler uncertainty can be removed. During the acquisition of the first four satellites, no useful information can be used in order to remove such an uncertainty, which as a consequence remains in the overall Doppler affecting the carrier frequency.

The analysis of the LO of the Novatel ProPak GL2plus GPS receiver has been conducted in order to assess the performance of a typical GPS clock (such a component is obviously not typical of a cell phone LO unit). Under static conditions, the clock drift has been recorded for about 2 hours. Figure 5.7 illustrates such a drift over time. No particular steering of the clock is done during the data collection, so that what is plotted can be considered as the real on-board receiver clock drift. The receiver is said to have a clock stability better than ±0.5 ppm, which means for the L1 carrier a frequency accuracy within about $\pm 0.5 \cdot 10^{-6} \times L_1$ (approximately ±800 Hz), which is consistent with the measurements shown in Figure 5.7 (-19 m/s represents about -100 Hz).

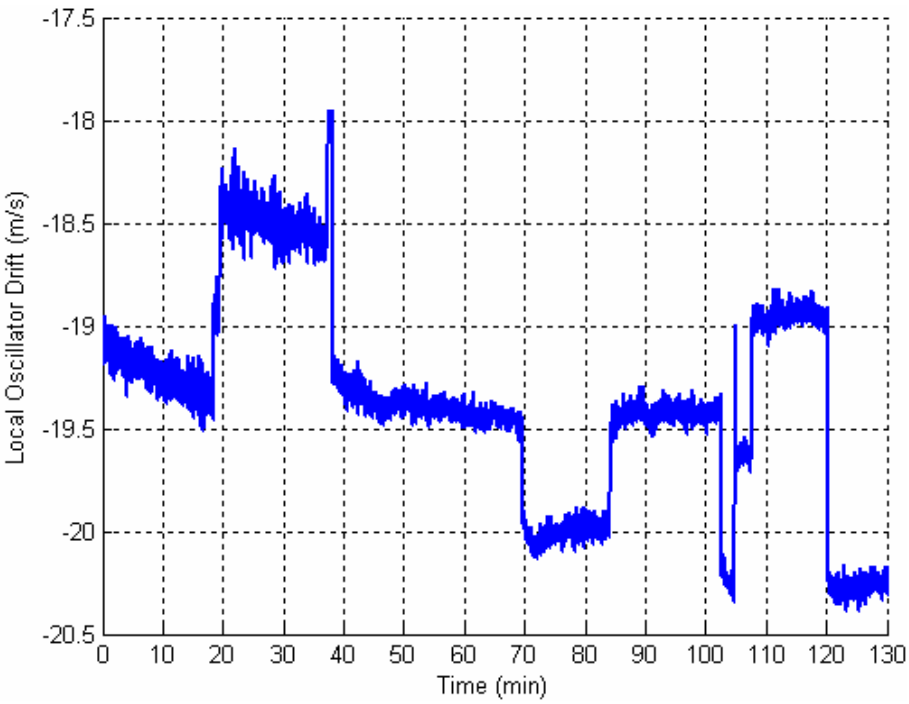

Figure 5.7: Local Oscillator drift (ProPak GL2plus, static test case).

Despite some jumps that are clearly noticeable (mainly due to the number of satellite used in the position computation stage as well as the quality of the measurements), the LO drift remains bounded around its initial value which tends to demonstrate its stability. This is of particular interest

since as soon as the LO Doppler contribution has been estimated (i.e. as soon as four satellites are acquired and tracked), there is no need to include it again into the overall Doppler uncertainty in order to optimise the acquisition stage (its accurate estimation is nevertheless required in the position computation stage since the position solution will otherwise drift over time. Such a result should also be balanced with respect to the LOs used for mass market receivers, or LOs embedded in portable devices).

5.2.3 User Contribution

The final contribution to the overall Doppler affecting the carrier frequency is the user's Doppler. Such a contribution is totally unpredictable since the movement of the user is unknown. The typical use cases within the scope of the thesis are pedestrian and land vehicle dynamics. Assuming a maximum user's velocity of 180 km/h (in the obvious land vehicle use case), the upper bound of user's Doppler contribution is about 250 Hz.

For a given total integration duration, the higher the coherent integration time, the better the sensitivity. The frequency slots are nevertheless all the more thinner as the coherent integration is long. In order to bound the energy loss to 1dB, their width shall not exceed half the inverse of the coherent integration time [2]. Figure 5.8 illustrates the different frequency bins that are used in relationship with the different coherent integration times covering the whole 20ms data bit duration (vertical bars). In the figure is also plotted the number of frequency bins to explore assuming a user's Doppler uncertainty of ±250 Hz. As it can be seen in the figure, the larger the coherent integration time, the more the frequency bins to explore. As the acquisition and the tracking of weak signals require long coherent integration times in order to decrease the noise power level, the computation load required to process weak GPS signals is greater than the computation load needed for signals with nominal power. The impact on the time to fix is obvious: the overall processing time is all the more increased as the number of frequency bins to explore is high. Thus, any reduction of the frequency search range will improve the processing time performance.

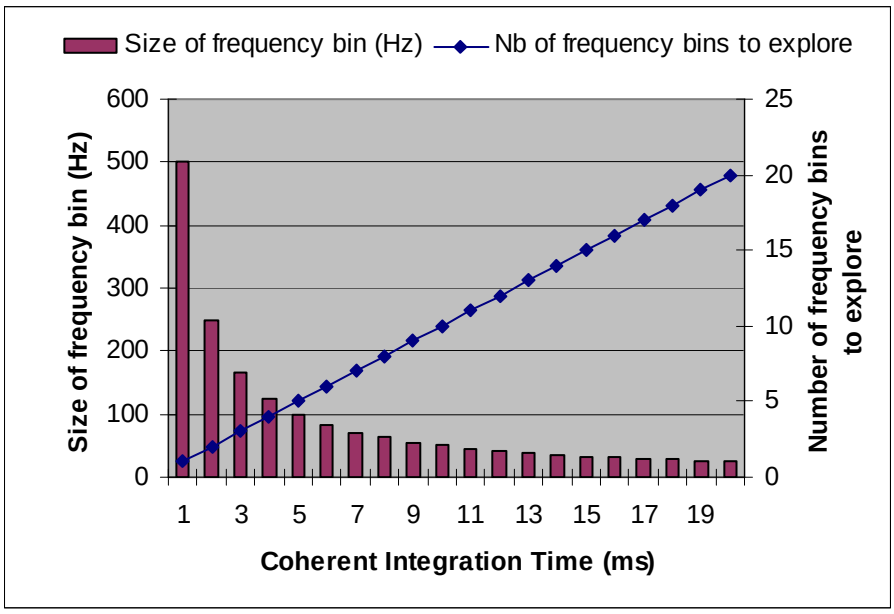

Figure 5.8: Frequency bins and number of frequency bins to explore with respect to a user Doppler uncertainty of +/- 250 Hz.

The purpose of this chapter is to analyse the possibility of providing any useful information using the MEMS-based sensors assembly in order to decrease the acquisition processing time. The aim of the sensors assembly is to enable the reduction at its minimum of the residual frequency uncertainty due to the user's motion. The following describes the sensors combination and integration scheme that is used to reduce the number of frequency bins to explore.

5.3 Sensors Aiding for Doppler Uncertainty Reduction

This section presents the methodology followed to estimate the user's Doppler contribution onto the overall Doppler. First, a basic motion recognition method using the information provided by the sensors assembly is discussed. This step allows a first reduction of the user's Doppler uncertainty. A more accurate methodology is then detailed together with its inherent issues that degrade the overall Doppler prediction performance.

5.3.1 Motion Recognition

Given the above statements, the acquisition improvement can only be achieved through the reduction of the frequency range. Two typical use cases are mainly studied in the following, namely pedestrian navigation and land vehicle navigation. Both navigation methods experience completely different dynamics and displacement velocities (up to 10 km/h for pedestrians, much more for land vehicles), as shown in Figure 4.18 of chapter 4.

Since a vehicle goes faster than walking people, the possibility of detecting if the GPS receiver is carried by a person or mounted onto a vehicle is of tremendous importance in the reduction of the number of frequency bins needed to estimate the user's Doppler contribution. As discussed in chapters 3 and 4, a motion can be characterised by the variance of the acceleration (see Figure 4.16 and Figure 4.18).

Figure 5.9 illustrates the processing of the acceleration magnitude in different trials that have been exercised. The left-hand side of the figure shows the sliding window variances computed on different acceleration magnitude. The computation step is equal to the sampling period, and the length of the window used for variance estimation is 2 seconds. The upper green and red plots show the sliding window variance of the acceleration magnitude recorded during a pedestrian walk where the sensors assembly was located respectively in the pocket and on the belt of the pedestrian (5 stops occurred in the trial plotted in green). The blue plot illustrates the sliding window variance of the acceleration magnitude recorded during a land vehicle trial. In this test, the measurement unit was fixed onto the dashboard of the vehicle and not moved during the whole trial. The right-hand part of Figure 5.9 presents a close-up on the low values of the sliding window variances. It clearly shows that the variance of the acceleration of an idling pedestrian (green plot) is lower than those of a vehicle, whatever its dynamic.

The analysis of the two figures provides means to distinguish the two typical motions. These two figures show indeed that thresholds can be adjusted in order to detect two main motions, namely an idling and a walking pedestrian (as the biases that affect the acceleration measurements are varying slowly, it can be reasonably assumed that they will not impact the computation of these two thresholds). An idling pedestrian is characterised by a quite low sliding window variance, as shown in the right-hand figure with the green plot (5 stops), whereas a walking pedestrian is rather

characterised by a high sliding window variance, as shown with the red and green plots in the left-hand figure. Threshold 1 and Threshold 2 can thus be adjusted in order to distinguish from the different motion areas. Between the two thresholds, the motion can be either those of a vehicle or a pedestrian starting to move. As a consequence, the considered velocity range will be the worst, i.e. that of a vehicle (the dynamic that implies the highest velocity and consequently the highest Doppler contribution).

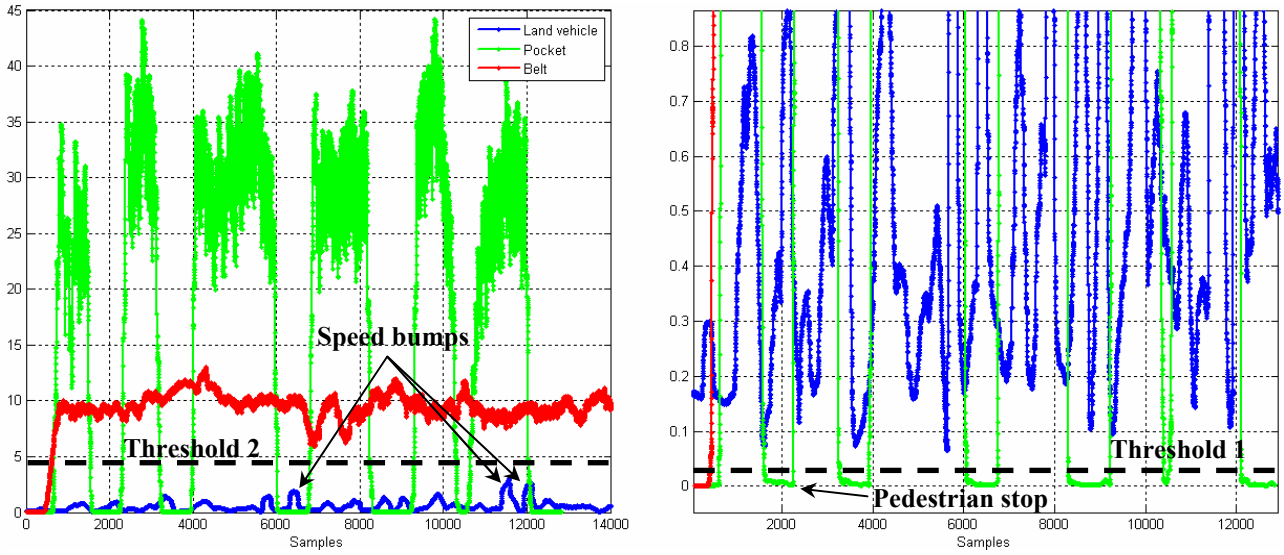

Figure 5.9: Sliding window variances computed from three different acceleration magnitude sources.

The ability of detecting the motion experienced by the sensors assembly allows a first reduction of the user's Doppler uncertainty. Given the fact that a pedestrian is likely to go up to approximately 10 km/h, it represents a Doppler contribution at most equal to ±14 Hz. A vehicle is supposed to go obviously faster. The upper bound of ±250 Hz is thus in that case rather considered.

5.3.2 Sensor Fusion & Integration Scheme

As discussed in the previous sections, the information provided by the MEMS sensors assembly is used in this study to estimate the user's Doppler contribution. Taking into account that ephemeris data are known since they are transmitted in the assistance message, the computation of the satellites position and Doppler contribution is straightforward. The remaining unknowns are the Local Oscillator and the user's contributions. The user's Doppler contribution can be estimated given the elevation and azimuth of one satellite, the direction of the land vehicle or the pedestrian and the along track velocity. According to the notations of Figure 5.2, the user's Doppler contribution can be expressed as follows:

$$f_d^{user} = -L_1/c \cdot \vec{u} \cdot \vec{v}_{user} = -L_1 \cdot \left[u^{north} \cdot v_{user}^{north} + u^{east} \cdot v_{user}^{east} + u^{down} \cdot v_{user}^{down}\right]/c \tag{5.5}$$

Equation (5.5) can be expanded to equation (5.6), which involves the along track velocity magnitude of the user, the pitch θ and heading ψ of the user (or vehicle) the measurement unit is attached on.

$$f_d^{user} = -\frac{L_1}{c} \cdot v_{user} \cdot \left[\cos(Az)\cos(E)\cos(\theta)\cos(\psi) + \sin(Az)\cos(E)\cos(\theta)\sin(\psi) + \sin(\theta)\sin(E)\right]$$

$$f_d^{user} = -\frac{L_1}{c} \cdot v_{user} \cdot [\cos(\theta)\cos(E)\cos(\psi - Az) + \sin(\theta)\sin(E)] \tag{5.6}$$

where:

– v_{user} is the true along track velocity in the navigation frame.

An example of the impact of the user's position and GPS time uncertainties on the elevation and azimuth angles is given below. The worst case is here taken into account, meaning that the position uncertainty is ±15km and the GPS time uncertainty is ±2s. For the simulation, almanacs are downloaded from satellites in visibility at the ENAC laboratory. They are preferred to ephemeris data since the latter are only valid for 4 hours and their processing outside their validity range are expected to give bad results in terms of satellite position and velocity accuracy.

Figure 5.10 illustrates the error made on the estimation of the elevation angle and the azimuth for a whole day. It can be seen that the elevation error stays below 0.05 degree (worst case), which may not have a significant impact on the accuracy of the user's Doppler contribution as given in equation (5.6). Opposite, the azimuth error is sometimes quite large (a few degrees), even if in the presented case, the largest error occurs when the satellite is not visible. As soon as the subsatellite point nears the location of the user (i.e. when the elevation angle reaches 90 degrees) the azimuth can be inaccurate to several degrees and therefore may introduce non negligible errors in the computation of the user's Doppler contribution.

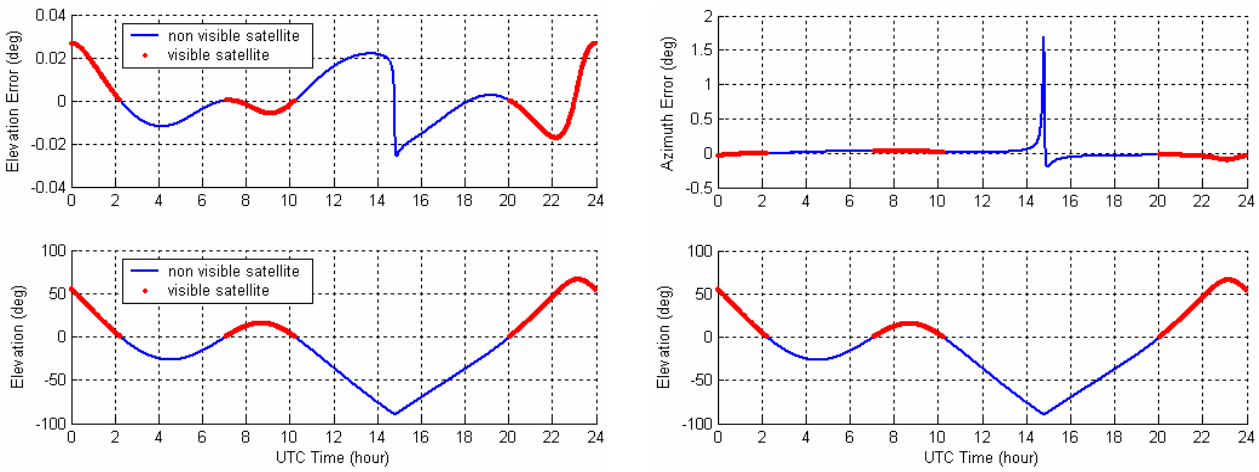

Figure 5.10: Illustration of elevation (left) and azimuth (right) errors for a user's position uncertainty of ±15km and a GPS time of ±2s.

Because the sensors of the measurement unit are affected by random errors such a bias and scale factor, the computation of the pitch and heading angles is likely to introduce large errors in a short time. To compensate for those drifts, the attitude angles involved in equation (5.6) are computed using the drift-free attitude filter presented in the previous chapter. It can then be expected to enable the long term prediction of the user's Doppler onto other LoS. As a consequence, there are only two unknowns remaining in equation (2.35) of chapter 2, namely the LO Doppler contribution and the true along track velocity. At this point, as soon as two satellites are acquired, it is possible to enable the prediction of the user's Doppler contribution onto the carrier of the other GPS signals to acquire.

In the pedestrian navigation case, the along track velocity can be estimated using the dynamic properties of the acceleration magnitude, as detailed in chapter 3. Moreover, there is a

close relationship between the frequency of walk of a pedestrian and its velocity. Consequently, it is also possible to calibrate the velocity model relative to the frequency of walk by loading pre-recorded regression coefficients computed off-line for typical velocities of walk. Even if this method is not as accurate as the online calibration using GPS measurements (about ±0.3m/s accuracy in the trials exercised), it allows the velocity estimation as soon as the measurement unit is switched on, even in deep indoor environments. This has for main consequence to enable the estimation the user's Doppler contribution as soon as the measurement unit is powered on and the attitude filter has converged to stable attitude estimates.

The case of the land vehicle navigation is more complex to handle since no reliable along track velocity estimate is available through the processing of the measurements of the sensors assembly due to the gyroscopes and accelerometers biases. These biases do not allow even short term (about 20seconds) accurate estimate, as it is possible in the particular case of the pedestrian navigation.

5.3.3 Satellite Geometry Issue

To ease the understanding, equation (2.35) can be rewritten as given below in equation (5.7).

$$f_d^r = f_d^{satellite} + f_d^{LO} + g\left(v_{user}, \alpha_{AT/LoS}\right) + n_f \tag{5.7}$$

where:

- g is the function used to compute the user's Doppler contribution as given in equation (5.6).
- v_{user} is the true along track velocity given in the navigation frame ***(n)***.
- $\alpha_{AT/LoS}$ is the along track to LoS projection coefficient as given in equation (5.6).

The projection coefficient is a function of the pitch and heading angles computed either with the gyroscope measurements or the attitude filter (both elevation and azimuth angles are assumed deterministic and do not significantly affect the accuracy of the projection coefficient, as shown previously). It is then considered as a known variable which may nevertheless be affected by some errors due to long term magnetic interferences for instance.

Equation (5.7) clearly shows that two unknowns need to be computed in order to enable the Doppler prediction onto the other GPS signals to acquire (the LO Doppler contribution and the along track velocity of the user). As discussed in the previous subsection, the along track velocity is available in the pedestrian navigation case but not in the land vehicle navigation due to the biases that affect the velocity measurements. As a consequence, there is a need to acquire at least two satellites in order to estimate the user's velocity and thus the user's Doppler contribution, and thanks to the stable attitude provided by the sensors assembly, the corresponding prediction onto new signals as well. However, once two satellites are acquired, the combination of their respective Doppler measurements according to equation (5.7) may lead to an unobservable estimated user velocity if the two projection coefficients are equal. Such a typical case of bad satellite geometry configuration is illustrated in Figure 5.11. Assuming satellite 1 and satellite 2 equally positioned from both sides of the user's heading. The geometric distance between the two satellites with respect to the user may be different, but in such a configuration, their respective rates of change are likely to be the same so that the Doppler affecting the two signals may be the same as well. With such a configuration, the two-equation system based on equation (5.7) can obviously not be solved to estimate the user's velocity and the LO Doppler.

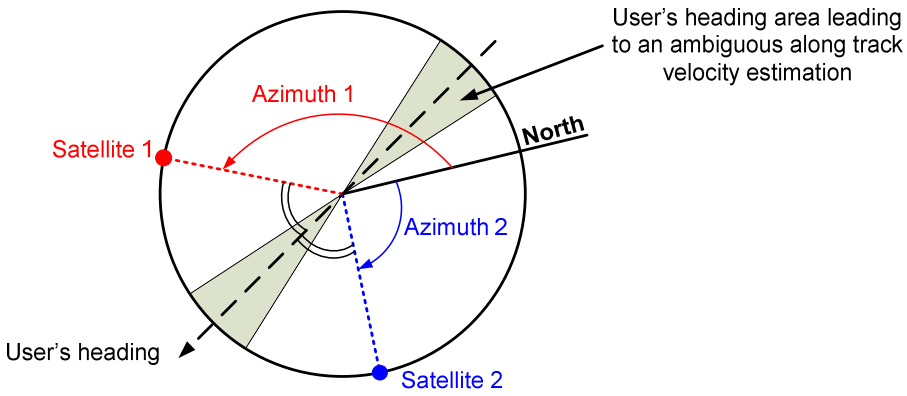

Figure 5.11: Bad satellite geometry configuration with respect to the user's heading.

Figure 5.12 shows the along track velocity estimation in the case of land vehicle using two satellites (PRN 3 and PRN 11) during a real urban test. The ephemeris data of the satellites are collected with the embedded GPS receiver, and the attitude is provided by the processing of the sensors assembly measurements. The upper part shows the azimuth of the satellites as well as the heading of the vehicle. The black dashed lines represent the theoretical heading leading to an ambiguous estimation of the velocity. It can be seen on the lower plot that when the upper user's heading curve crosses the black dashed lines the velocity profile experiences sudden variations.

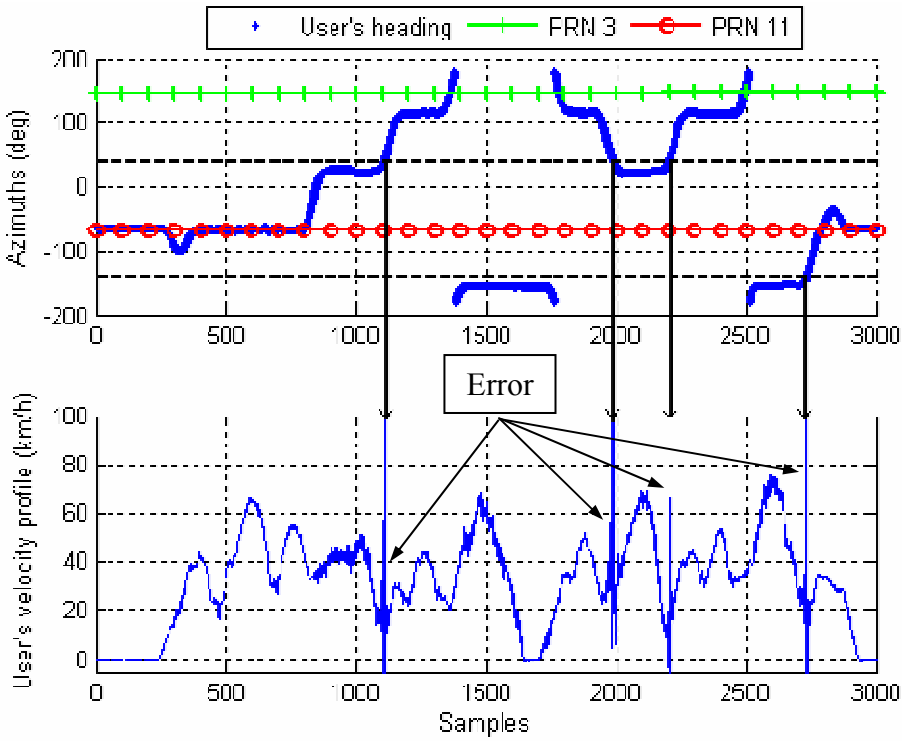

Figure 5.12: Typical issue of the user's velocity estimation. Land vehicle case.

A protection criterion shall then be implemented to avoid this bad velocity estimation. However, this will decrease the user's Doppler prediction availability, especially if such a configuration lasts quite long. Inertial measurements can then be used to estimate the true velocity of the vehicle, but it will not provide reliable estimate due to the rapid drift introduced by the integration of the different biases.

5.3.4 On-Demand Doppler Estimation

A typical cold start implies the need for an estimation of the user's Doppler on demand. According to what has just been detailed, the estimation of such a contribution is completely dependent on the ability of the drift-free attitude filter to provide a stable attitude. In order for the attitude filter to provide reliable information, an initialisation step where the sensors assembly is not moving is required. An issue may arise in the case of a sensor-aided acquisition demand while the sensors assembly is moving. The purpose of this subsection is then to assess the feasibility of an acquisition aiding under dynamic conditions (i.e. dynamic initialisation of the attitude filter).

When the attitude estimation is required while the sensors assembly is moving, the attitude filter is initialised according to the principle described in Figure 5.13. The data provided by the sensors are averaged in order to smooth the dynamic due to the motion and limit its impact on the initial estimation of both inclination and heading. The initialisation of the covariance matrix is done empirically according to the variance of the signals. If the variance is high, it is assumed the sensors assembly experiences a quite high dynamic so that the variance on the initial values of the state vector is high as well, and conversely. The only quantities that are not estimated when in-motion initialisation is requested are the gyro biases, which consequently remain completely unkown.

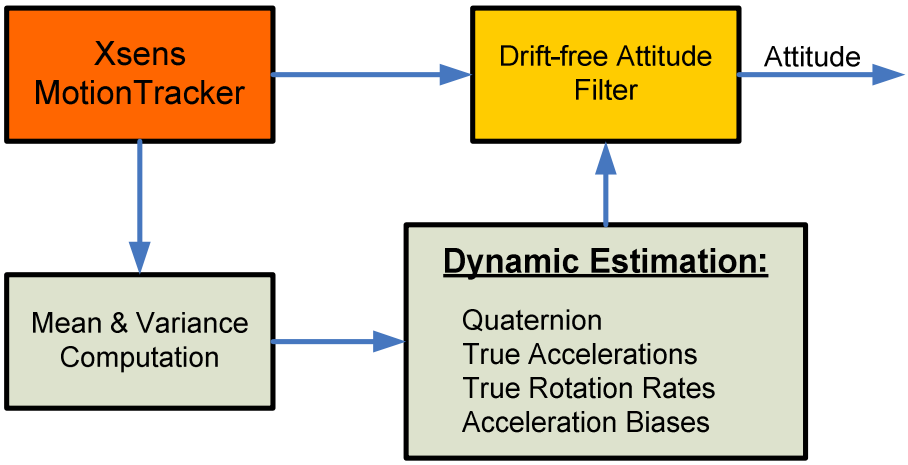

Figure 5.13: Drift-free attitude filter with in motion alignment aiding.

The proposed aiding method for the in-motion initialisation of the developed drift-free attitude filter is tested hereafter for the worst dynamic case, i.e. the pedestrian navigation. The acceleration experienced by the sensors assembly is indeed very high in such a navigation mode, making the in-run initialisation very inaccurate.

To assess the performance of the proposed initialisation method, a trial has been exercised in three steps. First, the pedestrian is not moving allowing the "standard" initialisation of the attitude filter, then the pedestrian walks for a certain time, and finally he stops. The attitude computed with these measurements is used as a reference; even if it is affected by some errors (no other means of characterising the attitude was available). Based on the data recorded during the trial, another attitude computation is done, but initialising the filter during a dynamic period (i.e. when the pedestrian is already walking). The two attitudes are then synchronised in order to be compared. Figure 5.14 show the result of the attitude angles estimation difference.

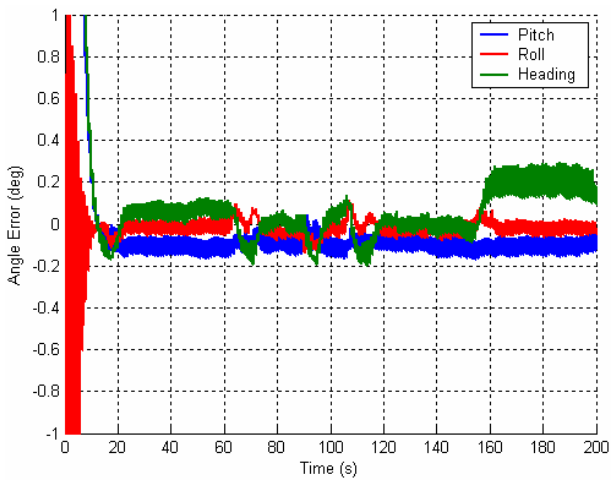

Figure 5.14: Attitude angles error with respect to the estimated angles with a static initialisation of the filter.

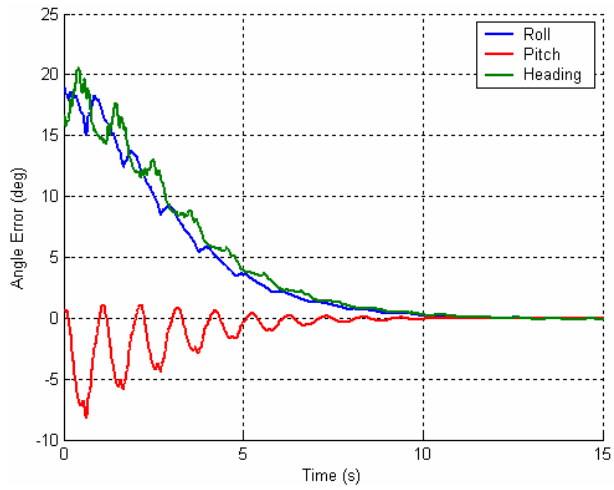

Figure 5.15: Close-up on the first epochs. The convergence of the filter is shown here and lasts about 10 seconds.

The close-up in Figure 5.15 shows that the filter needs less than 10 seconds to give a stable attitude estimate, which may be too long for real time applications but still demonstrates the feasibility of the principle. The attitude angles converge then very closely to what is obtained with the filter initialised at rest, as illustrated in Figure 5.14. Small constant deviations are however noticeable due to the error in the inclination initialisation that impact the heading too.

5.3.5 Doppler Reduction Procedure

Figure 5.16 summarises the user's Doppler uncertainty reduction using the combination of MEMS sensors data. A first Doppler uncertainty reduction is done through the motion detection procedure. Then, depending on the detected motion, the user's Doppler contribution can be estimated without GPS measurements (pedestrian navigation case), or using at least two satellites (land vehicle navigation case).

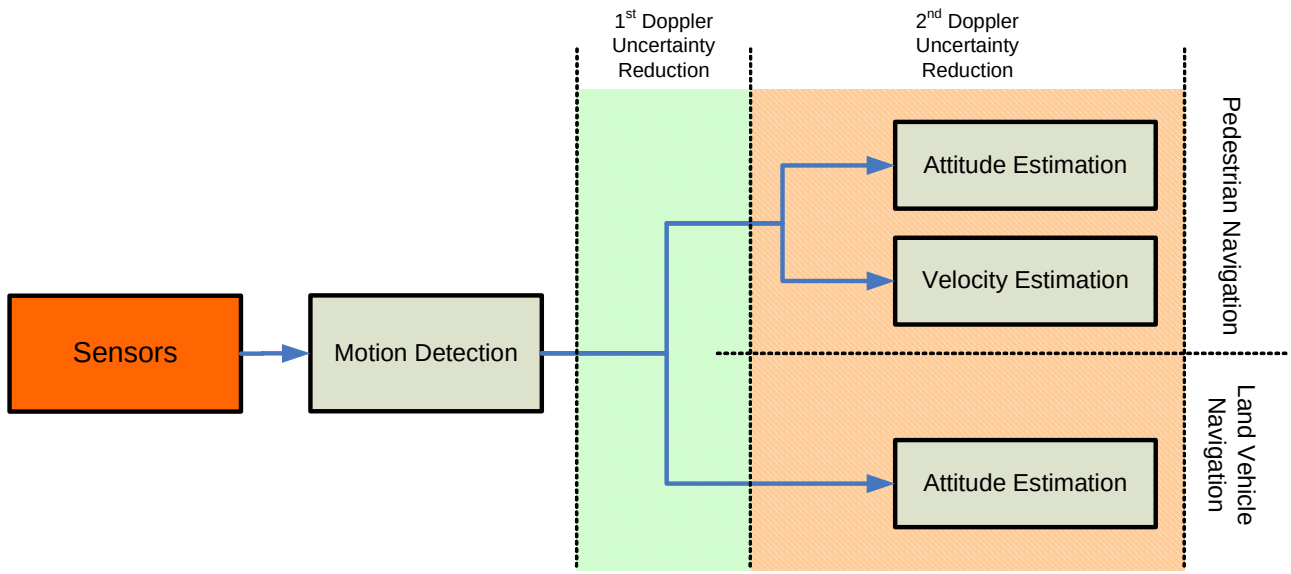

Figure 5.16: User's Doppler uncertainty reduction procedure.

5.4 Test Results

The integration scheme proposed in this paper is not directly tested in real time with a HSGPS or an AGPS receiver since none capable of outputting raw measurements (including Doppler) were available at the time the trials were conducted. The ephemeris data of each satellite in visibility is rather collected with a base station operating under clear sky conditions and post processed together with the sensors assembly data, allowing a realistic MEMS/AGPS integration simulation. The base station is used to make sure that all the ephemeris data are available. The two GPS receivers used for data collection are the Novatel ProPak GL 2 plus (rover) and Novatel OEM4 (base station).

The algorithm presented above is tested in actual conditions. Test results are presented in this section for both pedestrian and land vehicle navigation. These two navigation modes are studied separately to clearly identify the benefits of the user's Doppler estimation algorithm. For each case, the sensors assembly was first calibrated against hard iron magnetic interference and the initial heading offset was solved using first GPS measurements.

5.4.1 The Pedestrian Navigation Case

In a first trial, a pedestrian walks in the car parking lot of a supermarket with the sensors assembly put inside his trouser's pocket with a random attitude. Thanks to the motion detection and recognition, the sensors assembly detects the unit is carried by a walking pedestrian and the velocity of walk is consequently modelled as described in the section above. To avoid the calibration using GPS measurements, the velocity is modelled using regression coefficients stored in memory and recorded during off-line trials operated at different velocities of walk to cover the whole pedestrian velocity spectrum (5 significant runs with different paces). The velocity of the pedestrian was then found to be accurate within ±0.3 m/s from the true velocity (computed through post processing of DGPS measurements).

The left plot in Figure 5.17 shows the user's Doppler prediction accuracy onto the LoS of the visible satellites (PRNs 1, 3, 11, 14, 19 and 20) and using the filtered attitude that is provided by the fusion of all MEMS data. As it can be seen and even if the pedestrian velocity is accurate within ±0.3 m/s, the user's Doppler prediction error onto the LoS of the satellites in visibility stays within ±6 Hz, with 100% availability. It tremendously reduces the initial uncertainty which was ±250Hz. This improvement is all the more important the coherent integration time is high. Indeed, assuming a 20ms coherent integration, Doppler bins of 25Hz large shall be explored for a total amount of 20 given the initial uncertainty of ±250Hz. Opposite, only one Doppler bin can be searched if information provided by the sensors assembly is used, which consequently represents a complexity reduction of 95%. Figure 5.17 (b) shows the user's Doppler estimation on the same LoS, using the same pedestrian velocity model but with the attitude computed based on gyroscope measurements whose initial biases have been removed (the attitude filter is not used in that case). As the path is travelled, biases introduce drift in the attitude angles that are used to compute the projection coefficients. This clearly impacts the user's Doppler prediction accuracy over time.

Figure 5.18 shows the user's Doppler prediction accuracy using the prediction method based on equation (5.7) for the same trial as the one presented above. In this use case at least, two satellites are needed to be able to compute the user's Doppler contribution onto every LoS of the satellites in visibility. Given the fact that 6 satellites are visible all the time during the trial, the

combination of the satellites measurements that leads to the less accurate user's velocity estimate was taken into account. This most inaccurate velocity estimation once combined with the different projection coefficients allows the prediction of the user's Doppler onto the different LoS. In this test, the combination of PRN 1 and 3 was found to give the poorest velocity estimate.

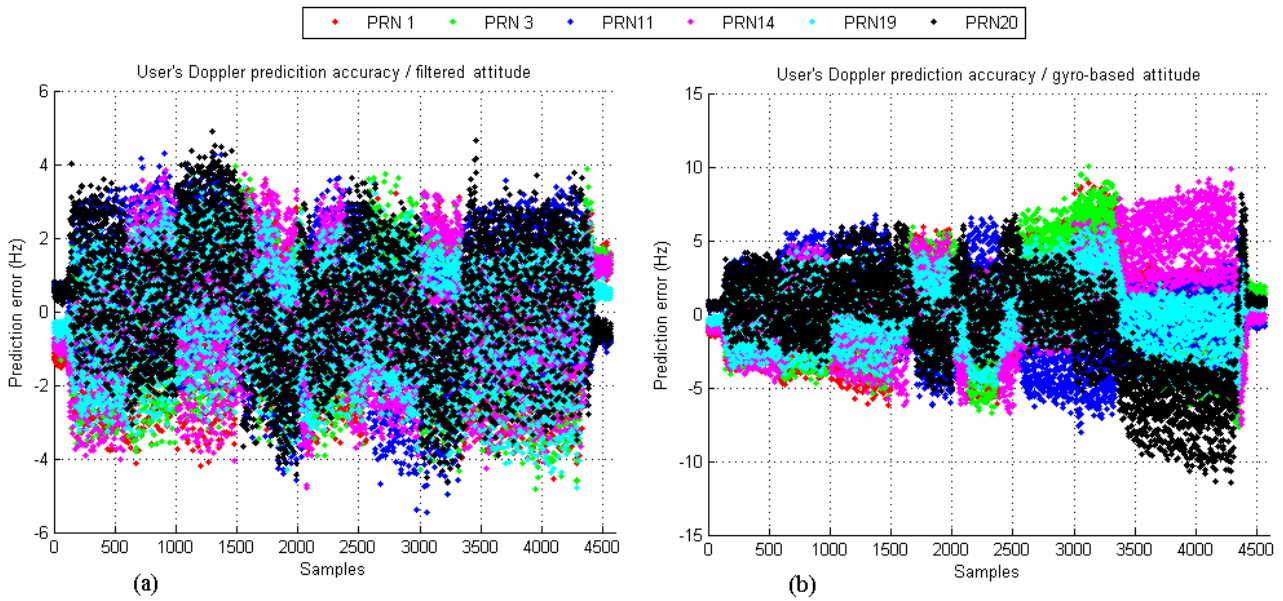

Figure 5.17: User's Doppler prediction accuracy using filtered (a) and gyro-based (b) attitude as well as the modelled pedestrian velocity. The reference user's Doppler is taken from GPS measurements.

Figure 5.18 (a) illustrates the user's Doppler prediction accuracy using the filtered attitude provided by the attitude filter with bad satellite geometry detection criterion enabled. On the one hand, the overall Doppler prediction is less accurate than in the previous case of Figure 5.17. Indeed, the error stays within ±11 Hz. On the other hand, the availability of the Doppler prediction is reduced, as it is indicated by the dots located on the top of the figure and circled in black. In this trial, the largest unavailability slot never exceeded 1 second (there are indeed numerous holes in the apparent straight unavailability lines circled in black).

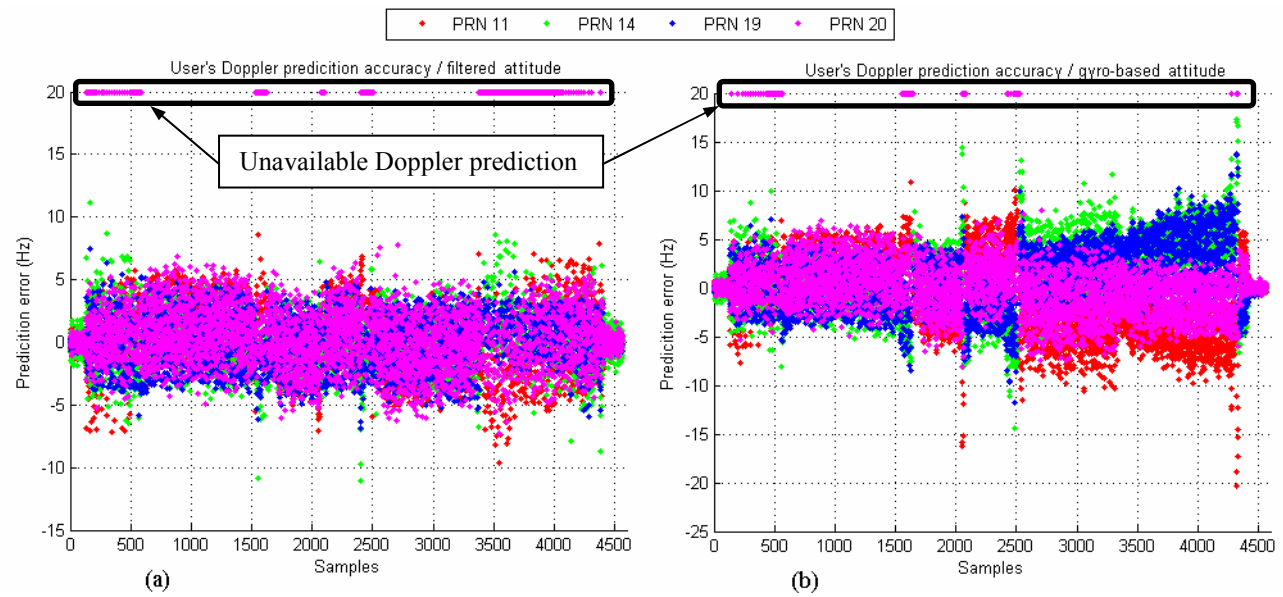

Figure 5.18: User's Doppler prediction accuracy using filtered and gyro-based attitude and the Doppler model of equation (5.7). The reference user's Doppler is taken from GPS measurements.

Figure 5.18 (b) shows the same user's Doppler prediction accuracy, but using the gyro-based attitude. Again, the accuracy decreases compared to the previous results due to both user's velocity estimation and projection coefficients computation. The drifting properties of the Doppler prediction error make such estimation not reliable for medium to long term use.

Table 5.1 summarises the results obtained for pedestrian navigation. Using the modelled velocity of walk and the stable attitude provided by the attitude filter, the number of frequency bins required to search the user's Doppler is well reduced. The greater the coherent integration time, the more interesting the combination of MEMS sensors with the GPS acquisition stage. Furthermore, the availability of the prediction is in that case 100%. Figure 5.19 illustrates the results of Table 5.1.

Coherent Integration Time (ms)		1	2	4	6	8	10	12	14	16	18	20
Size of Frequency Bin (Hz)		500	250	125	83	63	50	42	36	31	28	25
Nb of Frequency Bins to Explore	GPS Standalone	1	2	4	6	8	10	12	14	16	18	20
	MEMS & Modelled Ped. Vel.	1	1	1	1	1	1	1	1	1	1	1

Table 5.1: Number of frequency bins to explore given an initial user's Doppler uncertainty of ±250Hz. Pedestrian navigation case.

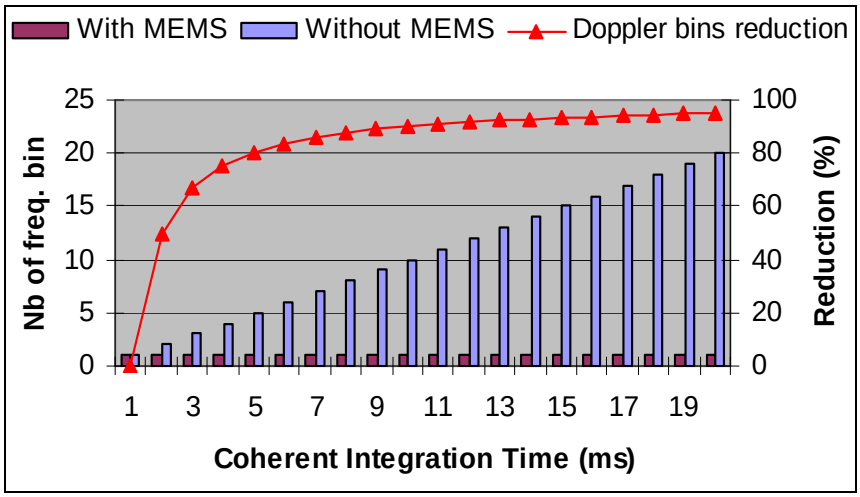

Figure 5.19: Reduction of the number of user's Doppler bins with respect to different coherent integration times for an initial uncertainty of ±250 Hz using data provided by MEMS senors.

5.4.2 The Land Vehicle Navigation Case

The Doppler prediction methodology is then tested for the land vehicle navigation case. Opposite to the pedestrian navigation, it is not possible to use a reliable estimate of the vehicle velocity mainly because of the biases that affect the accelerometer measurements, making the estimated velocity biased as well. Therefore, the improvement on the acquisition of GPS satellites through the prediction of the user's Doppler is analysed assuming two satellites already acquired.

Figure 5.20 illustrates the user's velocity estimation error using all possible combinations of two Doppler measurements, according to the satellites in visibility. The upper part shows the estimated velocity error without avoiding satellite configurations that lead to unobservable user's Doppler. In that case, the error can reach up to 1500 m/s. The lower part is a close-up of the upper part, showing that bad satellite configuration can not be neglected as they occur quite often and are very large. In this trial, PRN 3, 11, 19, 20 and 28 were visible all the time. In the following, the

satellite combination that leads to the less accurate user's velocity estimate assuming a good geometry is used for Doppler prediction (in the present test, it is the combination of PRNs 3 and 11).

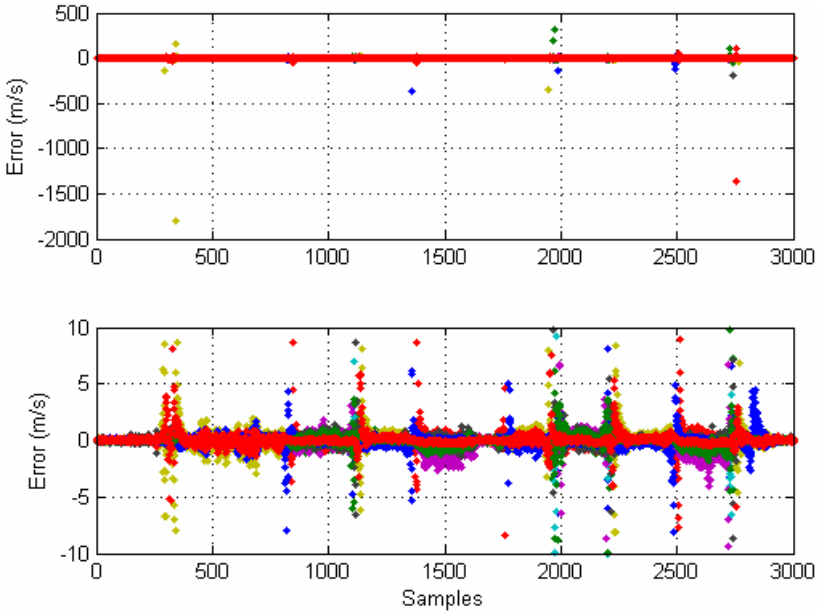

Figure 5.20: User's velocity estimation using all possible combinations of measurements from two GPS satellites.

Figure 5.21 shows the user's Doppler prediction accuracy using the filtered heading and the estimated velocity based on the measurements from PRN 3 and 11. The lower part shows the user's Doppler prediction error using all the possible combinations of satellite without taking into account the position of the satellites with respect to the vehicle heading in order to avoid unobservable cases (as explained in subsection 5.3.3). Large errors are made in the estimation (up to 100 Hz). The upper part shows the user's Doppler prediction accuracy when the detection criterion is applied. The prediction accuracy stays within ±20 Hz during the entire test, but the availability of prediction decreases below 100%. In the trial, the largest prediction unavailability slot never exceeded 1s.

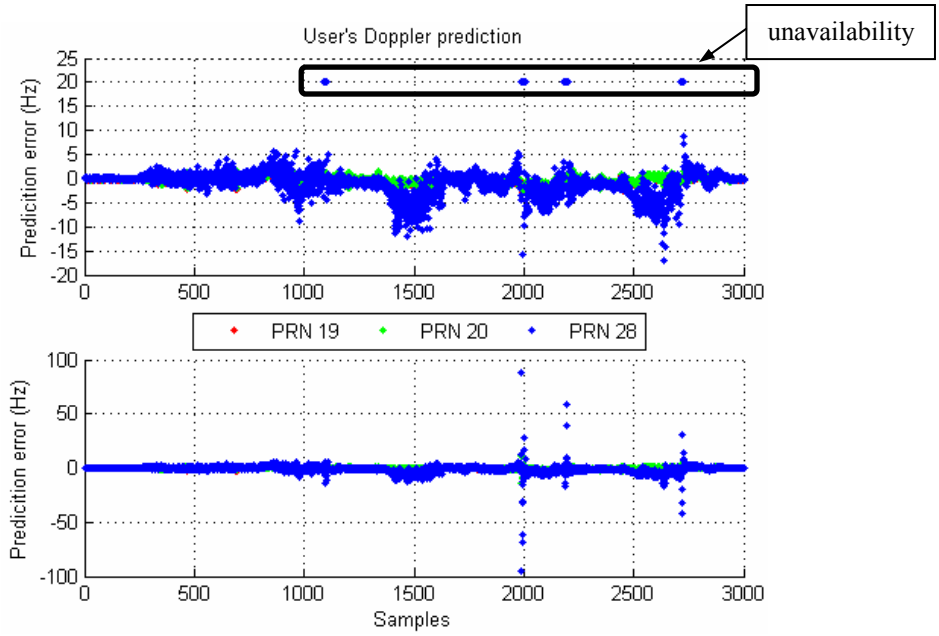

Figure 5.21: User's Doppler prediction accuracy using the filtered attitude.

Table 5.2 summarises the results obtained for land vehicle navigation. Using the stable attitude provided by the attitude filter and as soon as two satellites are acquired, the number of frequency bins required to find the user's Doppler is well reduced. As for the pedestrian navigation case, the information provided by MEMS improves all the more the acquisition performance as the coherent integration time is long. One weak point in the methodology used to predict the user's Doppler is that the availability of the prediction closely depends on the configuration of the two satellites used with respect to the user's heading.

Coherent Integration Time (ms)		1	2	4	6	8	10	12	14	16	18	20
Size of Frequency Bin (Hz)		500	250	125	83	63	50	42	36	31	28	25
Nb of Frequency Bins to Explore	GPS Standalone	1	2	4	6	8	10	12	14	16	18	20
	MEMS & 2 Satellites	1	1	1	1	1	1	2	2	2	2	2

Table 5.2: Number of frequency bins to explore given an initial user's Doppler uncertainty of ±250Hz. Land vehicle navigation case.

Figure 5.22 illustrates the results presented above in Table 5.2.

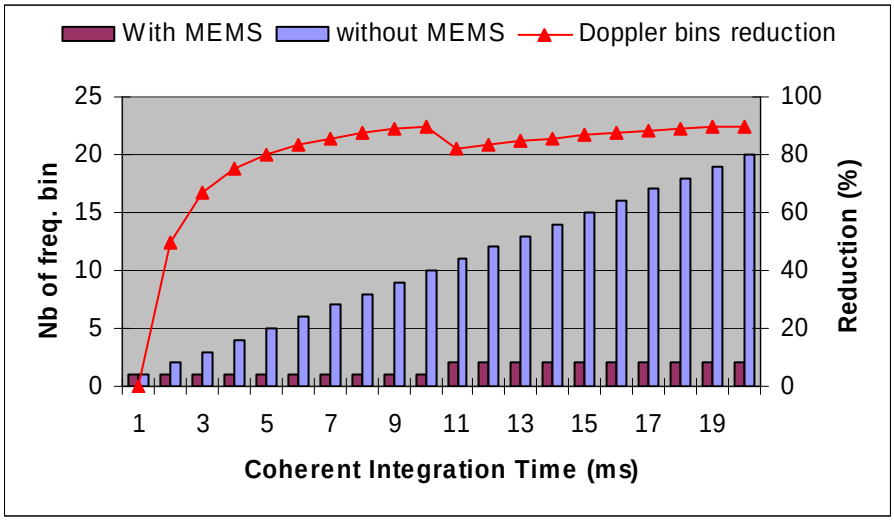

Figure 5.22: Improvement of the combination of MEMS.

5.5 Conclusions

This chapter focused on the improvement of the acquisition process through the use of MEMS type sensors. It seems obvious that the acquisition stage can be identified as a potential high processing load stage, whose performance could be improved using external data provided for instance by inertial sensors. An acquisition aiding strategy has been described and tested in actual conditions for both pedestrian and land vehicle navigation. This strategy mainly relies on the estimation of the velocity and the heading of the user.

The analysis of the conducted trials have shown that in the pedestrian case where the velocity can be modelled within 0.3m/s accuracy, the information provided by MEMS sensors decreases tremendously the user's Doppler uncertainty to ±6Hz. The frequency search time is

consequently reduced by at most 95% compared to the frequency search time assuming a user's Doppler uncertainty of ±250Hz. The availability of the Doppler prediction is furthermore 100%.

In the land vehicle case, the prediction performs as well by reducing the user's Doppler uncertainty down to ±25Hz. However, the Doppler prediction can only be done once two satellites are acquired since the velocity provided by the sensors assembly is not enough reliable. Moreover, the user's Doppler prediction availability is degraded and depends on the geometry of the satellites with respect to the user's heading.

Chapter 6: GPS/IMU Hybridisation for Personal Navigation

This chapter is dedicated to the study of the position solution availability and accuracy improvement in urban and indoor environments. More specifically, it focuses on the analysis of the hybridisation performance of either a HSGPS or an AGPS with a low-cost Inertial Measurement Unit in two different use cases: the land vehicle navigation and the pedestrian navigation. A brief summary of the hybridisation schemes is first given. Then the two navigation methods are discussed separately. The land vehicle is addressed within the scope of a tight integration scheme in the perspective of using very few measurements as it is likely the case in urban environments. The pedestrian navigation is detailed through a simpler loose coupling architecture and the developed real time pedestrian navigation system software is detailed.

6.1 Integration Strategies & Architectures

There are several ways of integrating a GPS receiver together with an INS. They all depend on what measurements are available at the GPS level. If the GPS position and velocity information are available, both systems can be integrated according to the so-called loose coupling architecture. If the raw GPS measurements are available (i.e. Doppler and pseudorange measurements), a tight integration scheme can be used. Finally, if one has access to the processing core of the GPS receiver and especially the tracking loops, the integration can be done at such a very high level. We talk then about ultra-tight coupling. The integration strategies depend on the type of application aimed by the integrated navigation system, the environment the system is likely to operate in as well as the acceptable system complexity. In all the aforementioned integration strategies, the combination of the different information is done through Kalman filtering (see for instance appendix C or [45]).

Two implementations are possible regarding each integration strategy. The integrated navigation system can indeed operate in an open-loop or in a closed-loop mode. The first one involves the correction of the INS output errors (i.e. position, velocity and attitude) using GPS measurements, whatever their type. In such an implementation, the INS mechanisation operates independently without being aware of the existence of an error estimator. The Kalman filter estimates the errors that are used to correct the output of the INS. The INS error model implemented in the Kalman filter is obtained through linearisation of the inertial differential equations, as detailed in chapter 3, in which the second order (and higher) terms are neglected. Without feedback, the mechanisation error grows rapidly, which can make the neglected terms significant, and thus can introduce large errors into the integrated system. In a closed loop integration scheme, a feedback loop is used to correct the raw sensor output and other mechanisation parameters using the error estimates obtained from the Kalman filter. In this way, the mechanisation propagates small errors thus maintaining the small error assumptions used to get the inertial error model linear. The error states in that case must be reset to zero after every filter update.

6.1.1 Loose Coupling

The loose integration scheme fuses GPS with INS at the lowest level. It uses GPS position and velocity to correct the INS errors. This integration method is suboptimal because the GPS position and velocity are computed in a separate filter using the estimated pseudoranges of the satellites that are tracked. If one of these measurements is affected by a non-negligible error, it will consequently impact the accuracy of the GPS position and the hybridisation performance will be degraded accordingly. The tracking of four satellites at least is required to enable such an integration principle, which limits its operational environments, especially if the GPS receiver used is not capable of tracking weak signals. However, with the increase of the position solution availability brought by AGPS and HSGPS in urban environments, such an integration scheme can be very attractive. It furthermore can give a great deal of performance for a minimal software integration complexity.

Figure 6.1 illustrates the open-loop loose coupling architecture. The GPS receiver processes independently the pseudoranges of the satellites that are tracked, and provides the position and the velocity of the receiver's antenna. The motion experienced by the IMU is measured by the sensors and all the measurements are processed to get the position, velocity and attitude of the IMU. Data from both navigation systems are then combined and fed into the Kalman filter as measurements.

The filter estimates the INS errors according to the models implemented, and the corrections are added to the output of the inertial navigation algorithm. In such an integration scheme, the measurement noise matrix for the Kalman filter is often constructed based on the position/velocity covariance matrix from the GPS filter.

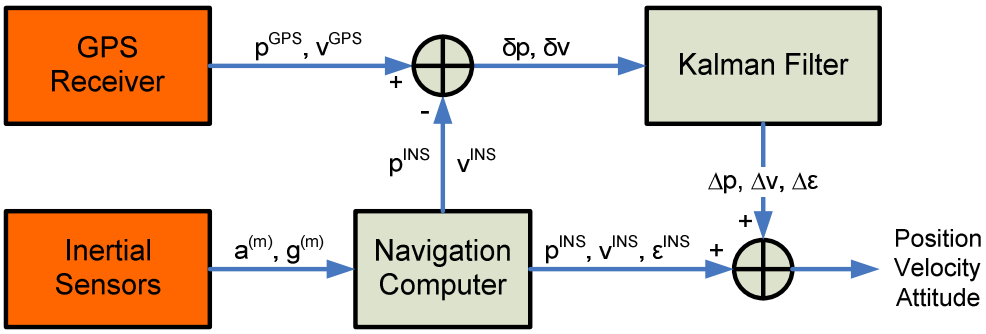

Figure 6.1: Loose coupling integration scheme. Open-loop architecture.

Figure 6.2 illustrates the typical closed-loop architecture of a loose-coupling integration scheme. Opposite to the previous architecture of Figure 6.1, the error estimates as provided by the Kalman filter are not used to correct the outputs of the navigation computer but rather the inertial sensors errors (mainly biases) and the position, velocity and attitude used as inputs in the navigation mechanisation. This has the advantage of keeping the error estimates small, which is more coherent to the approximations made when derivating the INS error model.

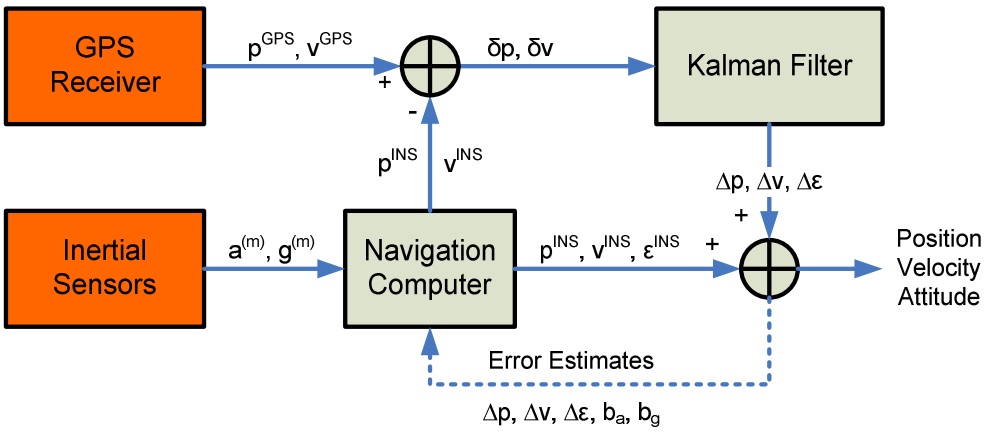

Figure 6.2: Loose coupling integration scheme. Closed-loop architecture

6.1.2 Tight Coupling

The tight integration combines the INS outputs with the raw GPS measurements made of pseudoranges and pseudorange rates (Doppler), even carrier phases (not in the scope of this study). This coupling method is more optimal than the previous one since each GPS measurement is combined independently with the INS outputs. Outliers are more likely to be detected and removed using appropriate fault detection and exclusion algorithms based on the combination of the two different navigation systems. There is furthermore no need to track at least four satellites to enable the correction of the INS errors, which makes such a hybridisation strategy very attractive, especially in urban canyon or indoor environments. However, there are much more non-linear equations in the Kalman filter design to fuse all the measurements, so that this integration scheme is

more complex to implement as compared to the previous one.

Figure 6.3 illustrates the tight coupling integration scheme according to the open-loop architecture. The GPS receiver provides pseudorange and pseudorange rate or Doppler measurements, as well as the ephemeris of each satellite that is tracked. These ephemeris data are used to form estimates of the pseudorange and pseudorange rate measurements from the INS measurements, which requires a good synchronisation between the two navigation systems in order to correctly form the error measurements. A small time offset may indeed introduce a non negligible bias in the INS pseudorange and Doppler estimates due to the high velocity of the satellites. The Kalman filter estimates the INS errors and the corrections are done directly on the outputs of the INS navigation computer.

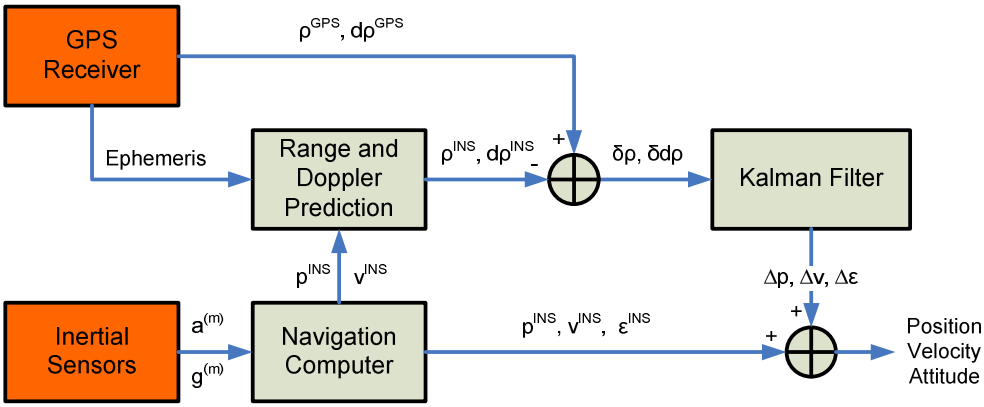

Figure 6.3: Tight coupling integration scheme. Open-loop architecture.

The closed-loop architecture is shown in Figure 6.4. As discussed above, the corrections are rather done at the sensors and navigation computer level, which maintains the small error assumption especially if low-cost sensors are used.

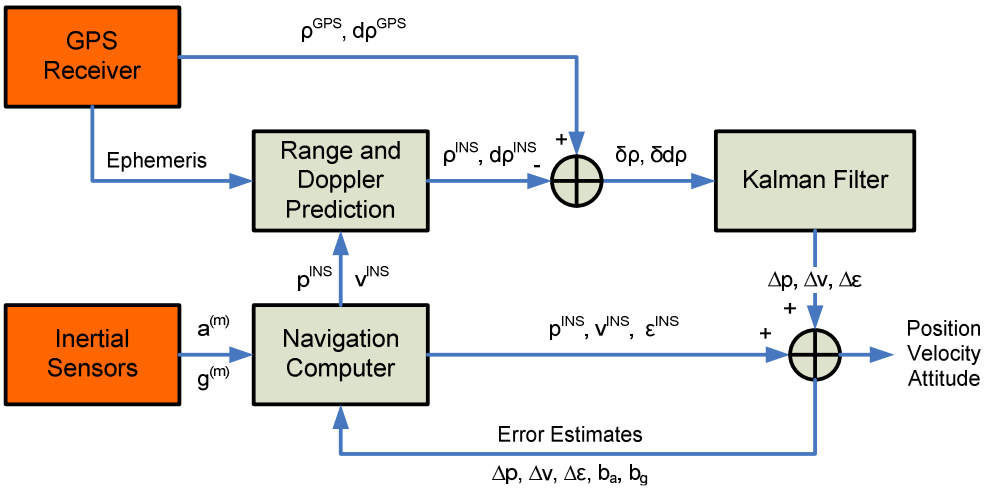

Figure 6.4: Tight coupling integration scheme. Closed-loop architecture.

6.1.3 Sensors Augmentation

Other sensors than GPS can be used to provide extra information in order to estimate the inertial errors, and consequently improve the integrated navigation system performance especially

during GPS outages. Chapter 4 discussed the possible aids using the sensors presented in the frame of the thesis. In all cases, the addition of external information impacts the measurement equations and consequently the measurement matrix complexity. Figure 6.5 shows how such external measurements are fed in the Kalman filter. The loose coupling is here shown as an example, but the integration principle is the same whatever the architecture.

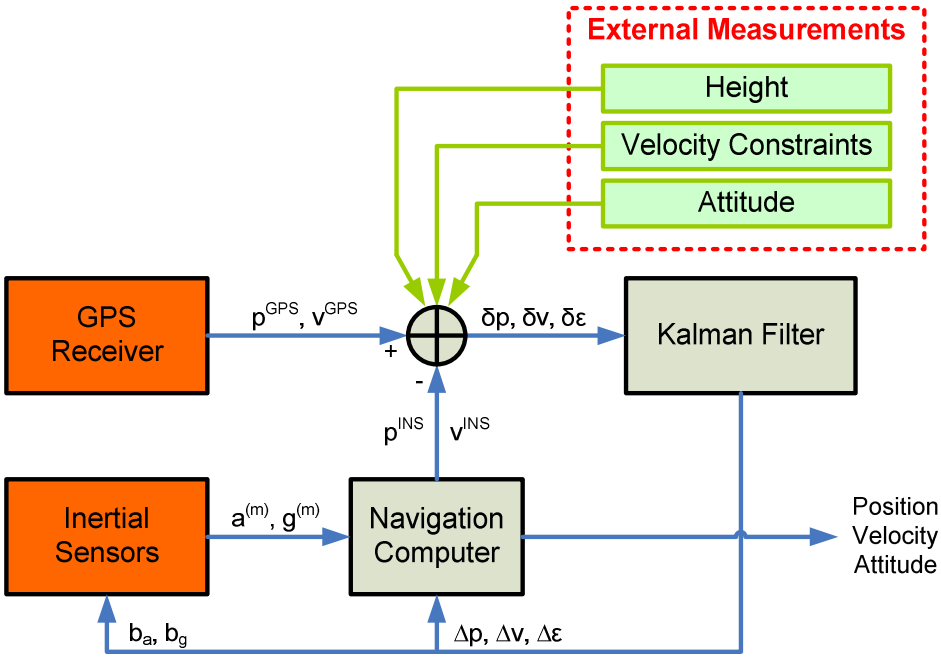

Figure 6.5: Hybridisation architecture using external measurements for correction purposes.

6.1.4 Practical Use Cases

The following of this chapter focuses on the hybridisation of either a HSGPS or an AGPS with a low-cost Inertial Measurement Unit in two different cases: the land vehicle navigation and the pedestrian navigation. As discussed previously in chapter 3, both navigation methods involve different mechanisations. As a consequence, the need for corrections is different in the two cases. It has been shown for instance that the pedestrian mechanisation allows more accurate standalone navigation, so that a tight architecture that takes benefit of very view GPS measurements may be not mandatory in order to increase the integrated system reliability and accuracy. Opposite, the traditional inertial mechanisation involved in the land vehicle navigation requires corrections as often as possible and therefore rather suits such a tight coupling architecture. For these reasons, the two navigation methods are discussed separately in the following. The land vehicle is addressed within the scope of a tight integration scheme, whereas the pedestrian navigation is detailed through a simpler loose coupling architecture.

6.2 Land Vehicle Navigation Case

6.2.1 Introduction

When a vehicle navigates in urban environments and more specifically in city centres, its location becomes very challenging because of the buildings that are very likely to fade and bloke

the GPS signals and to introduce large multipath. Pure non Line-of-Sight signals may also be integrated in the position computation stage. As a consequence, the positioning system relying on the processing of GPS signals may experience long unavailability and large inaccuracy.

A hybridised system made of a GPS receiver and an INS could handle such issues by taking advantage of the two navigation systems. Numerous studies have already been conducted on this topic, as for example [39], [40] or [41]. In this section, the feasibility of using very few GPS measurements to estimate IMU errors and thus provide a smoothed and accurate position solution is more specifically studied. As discussed and justified in [41], the augmentation of the GPS receiver needs to be small and cheap for LBS perspectives. The hybridisation with the low-cost IMU presented in chapter 3 is therefore addressed hereafter.

The typical environment the hybridised system will operate in is the urban area. Consequently, numerous outages and signal re-acquisitions may increase the computation load of the GPS receiver core, whose position solution availability may furthermore be degraded. In such conditions, the tight coupling integration of both navigation systems is obvious. This choice is furthermore motivated by the use of a low-cost IMU, whose measurements are very likely to be of bad accuracy, requiring corrections from an external sensor as often as possible. However, as discussed above, this implies an increase of the filter complexity.

In the tight integration scheme, the equations involved at both state transition and measurement level are indeed highly non-linear. As all the INS errors must be estimated in order to improve the performance of the integrated navigation system, they are included in the state vector of the Extended Kalman Filter (EKF) used to fuse the two navigation systems. Equation (6.1) recalls the error model as defined in [9] in the navigation frame. It is basically composed of 15 states that consequently is the minimum dimension of the state transition and covariance matrices.

$$\begin{bmatrix} \delta\dot{p} \\ \delta\dot{v} \\ \delta\dot{\rho} \\ \delta\dot{\varepsilon}_a \\ \delta\dot{\varepsilon}_g \end{bmatrix} = \begin{bmatrix} Fpp & Fpv & F_{p\rho} & 0 & 0 \\ Fvp & Fvv & Fv\rho & F_{v\varepsilon_a} & 0 \\ F\rho p & F\rho v & F\rho\rho & 0 & F_{\rho\varepsilon_g} \\ 0 & 0 & 0 & F_{\varepsilon_a\varepsilon_a} & 0 \\ 0 & 0 & 0 & 0 & F_{\varepsilon_g\varepsilon_g} \end{bmatrix} \cdot \begin{bmatrix} \delta p \\ \delta v \\ \delta\rho \\ \delta\varepsilon_a \\ \delta\varepsilon_g \end{bmatrix} + \begin{bmatrix} n_p \\ n_v + n_{\varepsilon_a} \\ n_\rho + n_{\varepsilon_g} \\ n_{\varepsilon_a} \\ n_{\varepsilon_g} \end{bmatrix} \tag{6.1}$$

where:
- δp is the position error in the navigation frame.
- δv is the velocity error in the navigation frame.
- δρ is the attitude error.
- $\delta\varepsilon_a$ is the accelerometers errors (bias and/or scale factor).
- $\delta\varepsilon_g$ is the gyroscopes errors (bias and/or scale factor).

At the measurements level, the complexity is rather due to the use of the pseudorange rates measurements (equivalent to Doppler by a multiplicative constant) of the GPS receiver. As a reminder, the typical pseudorange and pseudorange rate measurement equations as given in chapter 2 are recalled below in equations (6.2) and (6.3) where all the error terms are grouped together in the single noise term N for more simplicity.

$$\rho = \sqrt{\left(x_u^{(e)} - x_s^{(e)}\right)^2 + \left(y_u^{(e)} - y_s^{(e)}\right)^2 + \left(z_u^{(e)} - z_s^{(e)}\right)^2} + c \cdot \Delta t + N_\rho \tag{6.2}$$

where:
- $x_u^{(e)}$, $y_u^{(e)}$, $z_u^{(e)}$ are the user's position coordinates expressed in the ECEF frame.
- $x_s^{(e)}$, $y_s^{(e)}$, $z_s^{(e)}$ are the satellite's position coordinates expressed in the ECEF frame.
- Δt is the GPS receiver clock bias.
- N_ρ accounts for all errors affecting the pseudorange measurement.

$$\dot{\rho} = \frac{\left(x_u^{(e)} - x_s^{(e)}\right)\left(\dot{x}_u^{(e)} - \dot{x}_s^{(e)}\right) + \left(y_u^{(e)} - y_s^{(e)}\right)\left(\dot{y}_u^{(e)} - \dot{y}_s^{(e)}\right) + \left(z_u^{(e)} - z_s^{(e)}\right)\left(\dot{z}_u^{(e)} - \dot{z}_s^{(e)}\right)}{\sqrt{\left(x_u^{(e)} - x_s^{(e)}\right)^2 + \left(y_u^{(e)} - y_s^{(e)}\right)^2 + \left(z_u^{(e)} - z_s^{(e)}\right)^2}} + c \cdot \frac{d(\Delta t)}{dt} + N_{\dot{\rho}} \tag{6.3}$$

where:
- $\dot{x}_u^{(e)}$, $\dot{y}_u^{(e)}$, $\dot{z}_u^{(e)}$ are the user's velocity coordinates expressed in the ECEF frame.
- $\dot{x}_s^{(e)}$, $\dot{y}_s^{(e)}$, $\dot{z}_s^{(e)}$ are the satellite's velocity coordinates expressed in the ECEF frame.
- $d\Delta t/dt$ is the GPS receiver clock drift.
- $N_{\dot{\rho}}$ accounts for all errors affecting the pseudorange rate measurement.

Equation (6.3) is highly non-linear and therefore needs to be expanded with Taylor's series in order to be implemented in the Kalman filter. As an example, the measurement sub matrices designed with the user's position, velocity as well as the receiver clock bias and drift as unknowns, are given in equations (6.4) and (6.5) for respectively the pseudorange and pseudorange rate measurements. The measurements matrix H defined in equation (6.6) is the combination of these two sub matrices, whose dimensions depend on the number of available pseudoranges and pseudorange rates.

$$H(\rho) = \begin{bmatrix} \frac{\partial \rho^i}{\partial x_u^{(e)}} & \frac{\partial \rho^i}{\partial y_u^{(e)}} & \frac{\partial \rho^i}{\partial z_u^{(e)}} & 0 & 0 & 0 & 1 & 0 \end{bmatrix}_{N_1 \times 8} \tag{6.4}$$

$$H(\dot{\rho}) = \begin{bmatrix} \frac{\partial \dot{\rho}^i}{\partial x_u^{(e)}} & \frac{\partial \dot{\rho}^i}{\partial y_u^{(e)}} & \frac{\partial \dot{\rho}^i}{\partial z_u^{(e)}} & \frac{\partial \dot{\rho}^i}{\partial \dot{x}_u^{(e)}} & \frac{\partial \dot{\rho}^i}{\partial \dot{y}_u^{(e)}} & \frac{\partial \dot{\rho}^i}{\partial \dot{z}_u^{(e)}} & 0 & 1 \end{bmatrix}_{N_2 \times 8} \tag{6.5}$$

$$H = \begin{bmatrix} H(\rho) \\ H(\dot{\rho}) \end{bmatrix}_{(N_1+N_2) \times 8} \tag{6.6}$$

The aim of the integration filter proposed in the following is to take advantage of the tight coupling properties while using simpler equations. The modification of both the state transition matrix and the measurement equations is investigated. The ability of the filter to provide useful correction as soon as two satellites are tracked is furthermore specifically addressed.

6.2.2 Integrated Navigation System

6.2.2.1 INS Mechanisation

To reduce the complexity of the integration filter and improve its correction capabilities especially when very few GPS measurements are available (i.e. as soon as two satellite

measurements are available) the classical tight coupling architecture has to be modified. It seems obvious that the tight architecture as shown in Figure 6.4 is optimum in the sense it allows a rigorous combination of the GPS and the INS. However as discussed above, the errors of the INS are characterised by non-linear equations that introduce at least 15 unknowns in the state vector. As a consequence, a first improvement would be to use a different INS mechanisation in order to get the state transition matrix simpler with less states to estimate.

To choose a different mechanisation, let's first discuss the use of the positioning system from an operational point of view. The location of one user in the land vehicle navigation requires that the IMU made of low-cost sensors must follow the motion of the vehicle, meaning that it has to be closely attached to the vehicle during the motion. Given this statement, assuming the IMU is oriented such that one of its axis is aligned with the forward direction of the vehicle as shown in Figure 6.6, a simpler mechanisation can be deduced, which is based on the integration of the acceleration sensed along the vehicle displacement direction. The lateral velocity of the vehicle is assumed negligible and not relevant of a typical vehicle motion, as done in [37] or [42] for example. The attitude of the vehicle is likely to be computed using the drift-free attitude filter detailed in chapter 4. Neglecting the roll impact on the restitution of the vehicle trajectory, only heading and pitch angles are used for a complete 3D positioning.

In such a mechanisation, the heading axis of the IMU and the forward direction of the vehicle may not be perfectly aligned. This may introduce an additive bias in the computation of the velocity, and consequently degrade more rapidly the performance of the INS. The estimation of such a heading bias can be done using GPS measurements when the vehicle is detected to move. This initial bias issue is therefore no more considered in the following. The issue arises also with the inclination angle (pitch angle) from the IMU with respect to the vehicle. Assuming the IMU lays on the floor of the vehicle, such an angle error is very small and thus can be neglected as well.

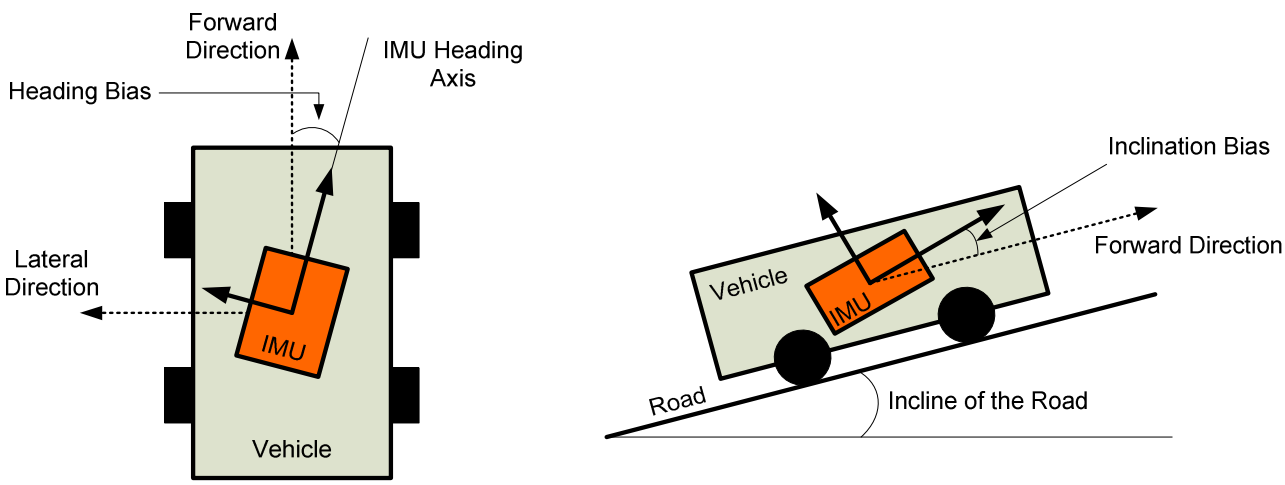

Figure 6.6: IMU placement with respect to the vehicle.

The basic equations characterising the INS mechanisation are given below. Equation (6.7) shows how the along track velocity (i.e. the velocity in the forward direction) is computed. Using the pitch angle as estimated by the processing of the IMU data, the contribution of the gravity vector onto the forward acceleration is removed. The resulting acceleration is then integrated to get the along track velocity.

$$v_{AlongTrack}^{INS}(t) = v_{AlongTrack}^{INS}(t_0) + \int_{u=t_0}^{u=t} \left(a_{AlongTrack}^{INS}(u) - g\sin(\theta(u))\right)du \tag{6.7}$$

where:

- $v_{AlongTrack}^{INS}$ is the along track velocity of the vehicle.
- $a_{AlongTrack}^{INS}$ is the acceleration sensed along the forward axis of the vehicle.
- g is the local gravity vector. In a first approximation, it is assumed perfectly vertical.
- θ is the pitch angle as estimated by the processing of IMU data. It characterises the incline of the road.

The position of the vehicle is obtained by integrating the along track velocity projections onto north, east and down axes according to equations (6.8), (6.9) and (6.10). This integration stage requires both pitch and heading angles.

$$p_n^{INS}(t) = p_n^{INS}(t_0) + \int_{u=t_0}^{u=t} \left(v_{AlongTrack}^{INS}(u) \cdot \cos(\theta(u)) \cos(\psi(u)) \right) du \tag{6.8}$$

$$p_e^{INS}(t) = p_e^{INS}(t_0) + \int_{u=t_0}^{u=t} \left(v_{AlongTrack}^{INS}(u) \cdot \cos(\theta(u)) \sin(\psi(u)) \right) du \tag{6.9}$$

$$p_d^{INS}(t) = p_d^{INS}(t_0) + \int_{u=t_0}^{u=t} \left(v_{AlongTrack}^{INS}(u) \cdot \sin(\theta(u)) \right) du \tag{6.10}$$

where:

- p_n^{INS}, p_e^{INS}, and p_d^{INS} are respectively the north, east and down vehicle position coordinates.
- ψ is the heading of the vehicle.

Figure 6.7 summarises the mechanisation of the Inertial Navigation System according to the simplifications described above. The computation of the attitude of the IMU (and consequently those of the vehicle since the IMU is not moved with respect to it) can be done whether by processing the rotation rate measurements using the standard strapdown algorithm based on the rotation quaternion, as described in chapter 3, or using the attitude filter as detailed in chapter 4. In the latter case and according to the results of chapter 4, the attitude is assumed enough reliable to be considered as external measurements that do not need corrections. This assumption may be somehow wrong since the estimation of the gyroscopes bias in the attitude filter is obviously not perfectly accurate, but it is nevertheless interesting to test it as a first approximation.

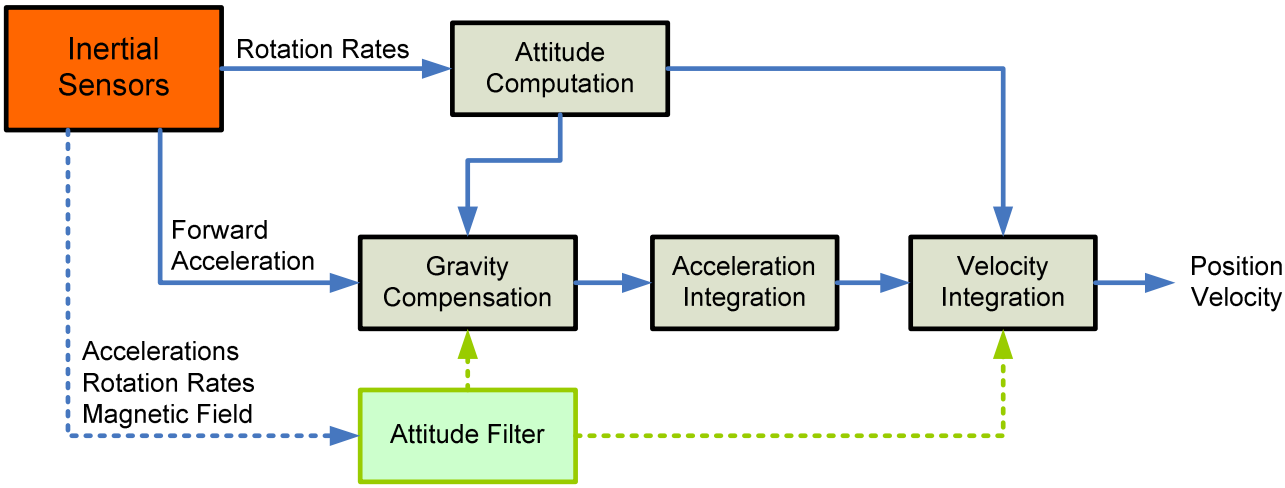

Figure 6.7: Simplified INS mechanisation for land vehicle navigation.

6.2.2.2 Measurement Equations

At the measurement level, a first improvement that would slightly decrease the equations complexity would be to use an INS mechanisation expressed in the ECEF frame rather than in the navigation frame, as for instance it is done in [39]. To have a more drastic simplification of the measurement equations implemented in the Kalman filter, it is better to use the GPS raw measurements from a different point of view.

The pseudorange is very well suited to introduce the position of the integrated navigation system in the filter equations. Its linearisation is quite obvious and consequently its integration into the measurements will not be modified in the following. The pseudorange rates are opposite far more complex to incorporate, as illustrated in equation (6.3). However, they can be equivalently interpreted as Doppler measurements according to the relationship given in chapter 2 and recalled hereafter in equation (6.11).

$$f_d^r = -\frac{L_1}{c}\dot{\rho} \tag{6.11}$$

where:

– $f_d^r = f_d^{user} + f_d^{satellite} + f_d^{LO} + n_f$ is the Doppler affecting the received signal, as defined in chapter 2.

Following the theoretical derivation detailed in chapter 5, the user's Doppler contribution expression is recalled hereafter in equation (5.4). Such an expression is a function of the satellite position with respect to the user through elevation and azimuth angles, but it also depends on the attitude of the vehicle and more specifically on the pitch and heading angles.

$$f_d^{user} = v_{AT}^{true} \cdot \left[\cos(\theta)\cos(E)\cos(\psi - Az) + \sin(\theta)\sin(E)\right] \tag{6.12}$$

where:

– v_{AT}^{true} is the true along track velocity of the vehicle.

If the attitude of the IMU is computed by processing the rotation rates, both pitch and heading angles can not be used as external attitude measurements in order to increase the correction capabilities of the integration filter. The main reason for that is the non negligible impact of the biases that dramatically decreases the accuracy of the gyro-based attitude over time.

Opposite, assuming the attitude is provided by the attitude filter developed and detailed in chapter 4, the number of unknowns to estimate in equation (5.4) can be significantly reduced. Indeed, the results presented in chapter 4 have shown that a good heading restitution of one user is possible by fusing the information of accelerometers, gyroscopes and magnetometers, for both land vehicle and pedestrian navigation. No accurate reference measurements was available to characterise the accuracy of all angles, but as the magnetometers require good tilt compensation to provide accurate heading estimation, it can be inferred that inclination estimation performs quite well too. As a consequence, both pitch and heading angle estimates can be used as reliable known attitude measurements in the Kalman filter. The only unknown remaining in equation (5.4) is then the along track velocity of the user, which dramatically decreases the impact on the filter complexity due to the use of Doppler measurements.

This approach is obviously less rigorous than the approach of the standard tight integration. It indeed directly relies on the accuracy of the estimated pitch and heading angles and also assumes that no bias affects these attitude measurements (which can be wrong in case of long term magnetic interference for instance). It has nevertheless the advantage of simplifying the design of the integrated navigation filter.

6.2.2.3 Coupling Methodology

6.2.2.3.1 Kinematic Model and State Vector

According to the two previous subsections, it is then possible to design a Kalman filter that fuses both navigation systems using the raw GPS outputs to correct the position and the along track velocity as computed by the INS. In the following integration filter, the first variables that are included in the state vector are the true north, east and down components of the user's position, whose kinematic equations are given respectively in equations (6.13), (6.14) and (6.15). Since the position is rigorously the integration of the velocity, no state noise is introduced in these equations.

$$\dot{p}_n^{true}(t) = v_{AT}^{true}(t) \cdot \cos(\theta(t))\cos(\psi(t)) \tag{6.13}$$

$$\dot{p}_e^{true}(t) = v_{AT}^{true}(t) \cdot \cos(\theta(t))\sin(\psi(t)) \tag{6.14}$$

$$\dot{p}_d^{true}(t) = v_{AT}^{true}(t) \cdot \sin(\theta(t)) \tag{6.15}$$

The true along track velocity is modelled as a 1st order Gauss-Markov process tuned according to a Power Spectral Density function, whose parameters namely bandwidth and magnitude are chosen according to the highest dynamic of the motion experienced by the sensors assembly (found by processing the GPS velocity recorded during a typical vehicle trial). The true along track velocity model is given below in equation (4.12). Such an implementation in the Kalman filter also has the advantage of smoothing the velocity solution as corrected by the GPS measurements. In other words, the model allows the prevention of too rapid changes in the velocity magnitude due to GPS outliers used for correction purposes. This is of particular interest since the system will be tested in urban environments.

$$\dot{v}_{AT}^{true}(t) = c_{v_{AT}} \cdot v_{AT}^{true} + w_{v_{AT}} \tag{6.16}$$

where:

- $c_{v_{AT}}$ is the time constant setting the bandwidth of the true along track velocity.
- $w_{v_{AT}}$ is the driving noise, whose variance sets the order of magnitude of the modelled motion.

The velocity as computed by the INS is impacted by the errors of the accelerometer measurements. Since the accelerometer is a low-cost sensor, both bias and scale factor have a non-negligible impact on the accuracy of the computed velocity. As the INS mainly relies on the integration of the forward acceleration, the estimation of all the errors affecting the along track velocity may improve the integrated navigation system performance, especially during GPS outages. Both scale factor and bias are consequently included in the state vector.

Although the turn-on component of the scale factor has been estimated as given in chapter 3, the precise characterisation of its drift has not been done. The scale factor model is empirically chosen as a 1st order Gauss-Markov process with a long correlation time (2 hours), whose driving noise is set according to the specifications provided by the manufacturer. For simplicity, the same model is used for the scale factor of the along track velocity computed by the INS, and whose kinematic model is given below in equation (6.14).

$$\dot{SF}_v(t) = -\beta_v \cdot SF_v(t) + \sqrt{2\beta_v} \cdot w(t) \tag{6.17}$$

where:

- β_v is the inverse of the correlation time of the Gauss-Markov process.
- w is the driving noise.

The bias affecting the acceleration measurements is definitely the contribution of the overall error that has the biggest impact on the performance of the Inertial Navigation System. It is modelled as a 1st Gauss-Markov process, whose characteristics have been found according to autocorrelation identification procedure as described in [47] with long static measurements, even if this method does not provide accurate results, as explained in [47] or [48]. As a consequence, the bias affecting the along track velocity is modelled as an integrated Gauss-Markov process

$$\begin{aligned} \dot{b}_v(t) &= b_{v,2}(t) \\ \dot{b}_{v,2}(t) &= -\beta_x \cdot b_{v,2}(t) + \sqrt{2\beta_x} \cdot w_x(t) \end{aligned} \tag{6.18}$$

where:

- b_v is the integrated Gauss-Markov process used to model the velocity bias.
- β_x is the inverse of the correlation time characterising the integrated Gauss-Markov process.
- w_x is the driving noise.

Finally, the last unknowns included in the state vector are the GPS local oscillator bias and drift, whose kinematic model is chosen as detailed for instance in [44] and recalled hereafter in equation (6.19). The corresponding discrete covariance matrix is defined according to the quality of the local oscillator which is characterised by Allan constants [44]. Its expression is given below in equation (6.20).

$$\ddot{\Delta t} = w_{LO}(t) \tag{6.19}$$

$$Q_{GPS_{LO}} = \begin{bmatrix} q_{11} & q_{12} \\ q_{21} & q_{22} \end{bmatrix} \tag{6.20}$$

where:

- w_{LO} is the noise affecting the clock drift time derivative.
- $q_{11} = \frac{h_0}{2} T_s + 2h_{-1} T_s^2 + \frac{2}{3}\pi^2 h_{-2} T_s^3$
- T_s is the sampling period.

- $q_{22} = \frac{h_0}{2T_s} + 4h_{-1} + \frac{8}{3}\pi^3 h_{-2} T_s$
- $q_{12} = q_{21} = h_{-1}T_s + \pi^2 h_{-2} T_s^2$

Table 6.1 gives typical characteristics of local oscillator as commonly used in GPS receivers

Oscillator Grade	h_0	h_{-1}	h_{-2}
Temperature Compensated Crystal	2.10^{-9}	7.10^{-9}	2.10^{-9}
Ovenized Crystal	8.10^{-9}	2.10^{-9}	4.10^{-9}
Rubidium	2.10^{-9}	7.10^{-9}	4.10^{-9}

Table 6.1: Typical Allan constants for different types of oscillators (units of seconds) [44].

The state vector of the integrated system is thus defined as given in equation (6.21). It involves 9 states which are the 3D position of the vehicle in the navigation frame, the along track velocity scale factor and bias, the true along track velocity and the GPS receiver clock bias and drift.

$$X = \begin{bmatrix} p_n & p_e & p_d & SF_v & v_{AT}^{true} & b_v & \dot{b}_v & \Delta t & \dot{\Delta t} \end{bmatrix}^T \tag{6.21}$$

The kinematic model given below in equation (6.22) is then fully described by the combination of the state transition equations given above.

$$\dot{X}(t) = F(t) \cdot X(t) + G(t) \cdot w(t) \tag{6.22}$$

where:
- $G(t) = diag\left(\begin{bmatrix} 0 & 0 & 0 & 1 & 0 & 1 & 1 & 1 \end{bmatrix}^T\right)$
- w is the state noise vector, whose covariance matrix is $Q(t) = \mathrm{cov}(w(t))$

The continuous definition of the kinematic part of the Kalman filter has no physical meaning but is rather a rigorous implementation methodology. Digital data are provided by the different sensors so that a discrete Kalman filter is more adapted. The discrete form of the model given in equation (6.22) is computed according to the procedure detailed in [44] and recalled in appendix C.

6.2.2.3.2 Measurements Equations

The first measurement equation is provided by the INS. It involves the true along track velocity obtained through the integration of the forward acceleration, and the errors affecting that measurement as given in equation (6.23). It is very easy to get this equation linear.

$$v_{AT}^{INS} = SF_v \cdot v_{AT}^{true} + b_V + n_v \tag{6.23}$$

where:
- n_v is the noise affecting the velocity measurement.

The other measurements are those provided by the GPS receiver modules, which are the pseudorange and Doppler measurements. The pseudorange measurement is given in equation (6.24). The processing of the ephemeris of each satellite allows the estimation of the ionospheric, tropospheric and satellite clock errors. They are removed from the pseudorange so that corrected pseudoranges are actually used as measurements in the Kalman filter. The position of the satellite at time of transmission is computed by processing the ephemeris in the navigation frame to ease the implementation. A first position is thus required to allow such coordinate transformation, which is not a limiting point since the INS also requires a first position to start the dead reckoning navigation.

$$\rho_{corrected}^{GPS} = \sqrt{\left(p_n - p_n^{satellite}\right)^2 + \left(p_e - p_e^{satellite}\right)^2 + \left(p_d - p_d^{satellite}\right)^2} + c \cdot \Delta t + n_\rho \tag{6.24}$$

where:

– n_ρ is the noise affecting the pseudorange measurement.

Because the vehicle is aimed at going in urban / deep urban canyons, multipaths are very likely to affect the pseudorange measurements and as a consequence the position solution as well. The receiver Doppler corrected for the satellite contribution (estimated using ephemeris data) is thus used as the second raw GPS measurement in the Kalman filter because it offers more robustness against such perturbations. Its model is as follows:

$$f_{d,corrected}^{GPS} = -\frac{L_1}{c}\dot{\Delta t} + v_{AT}^{true} \cdot \alpha_{AT/LOS} + n_{f_d} \tag{6.25}$$

where:

– $\alpha_{AT/LOS}$ is the projection coefficient of the along track velocity onto the user to satellite LoS.

– n_{f_d} is the noise affecting the Doppler measurement.

Another improvement tested within the proposed tight integration architecture is the use of a low-cost pressure sensor. In that case, the pressure measurements once calibrated and converted into altitude (height) measurements are used to directly correct the vertical position as estimated in the Extended Kalman Filter.

6.2.2.3.3 Mechanisation

Figure 6.8 summarises the principle of the integrated navigation system. The GPS receiver provides raw measurements that are used as measurement inputs of the Kalman filter. Ephemeris data are used to compute the satellites position and Doppler contributions. They also are combined with the attitude estimates as provided by the attitude filter detailed in chapter 4 to compute the projection coefficient from the user to satellite Line-of-Sight, as defined in equation (6.25).

This coupling methodology is somehow not optimum but it allows the reduction of the number of unknowns in the state vector and it furthermore enhances the capability of the filter to provide corrections as soon as two satellites are available. A closed-loop architecture is proposed here, in which the Kalman filter estimates the position and velocity errors (including bias and scale factor) that are fed back into the INS to keep the INS errors as small as possible.

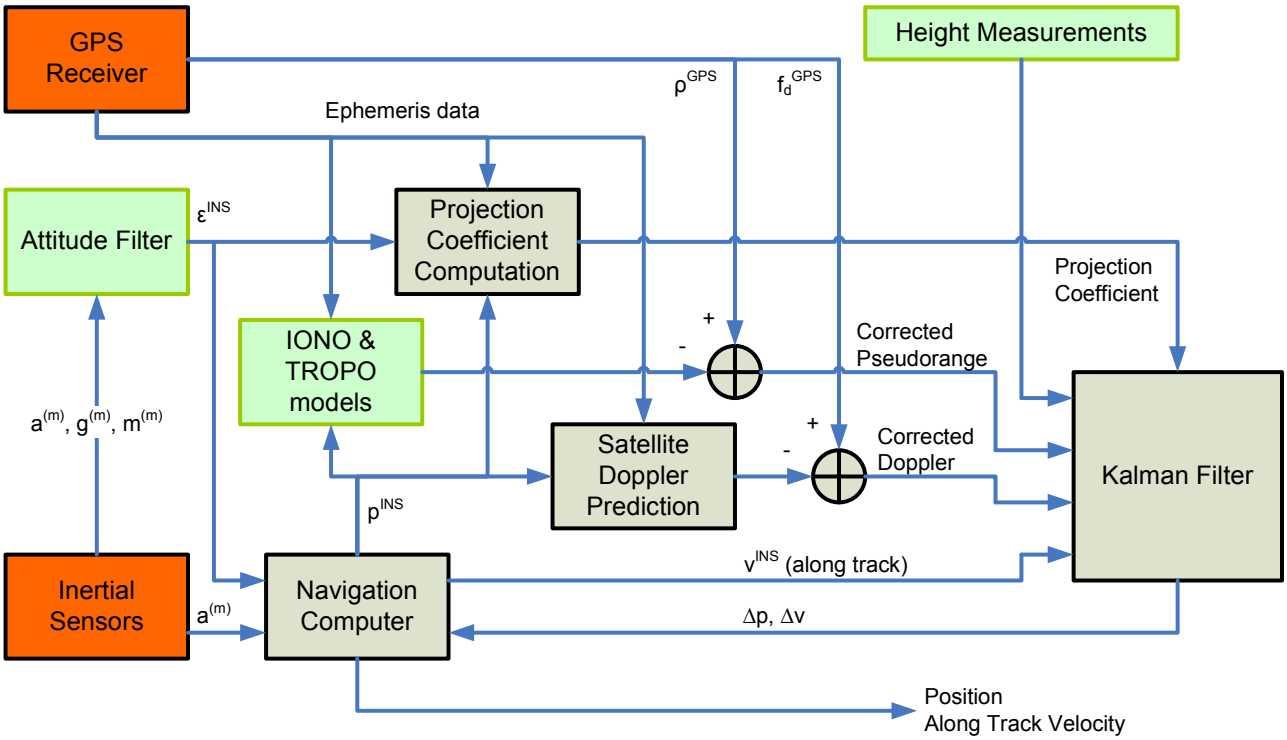

Figure 6.8: Integrated Navigation System mechanisation as designed for land vehicle navigation. Closed-loop architecture.

6.2.3 Test Results

This section presents the results of the tests conducted with the system described above. The capability of the integrated navigation system to provide a position solution in challenging urban canyon conditions is more specifically addressed. When the tests were performed, no HSGPS or AGPS receiver capable of providing raw GPS measurements was available. Consequently, the trial detailed in the following has been done using a geodetic grade OEM4 GPS receiver from Novatel. As a result, the GPS position solution availability can be expected to be quite low. This is not an issue regarding the performance analysis the subsection is aimed at since one of the objective is to evaluate the capability of the integrated navigation system to correct INS errors using very few GPS measurements. The use of such a geodetic grade receiver nevertheless increases the quality of the raw measurements available for hybridisation due to particular processing techniques that are implemented to mitigate errors such as multipath, as compared to what HSGPS and AGPS can do (indeed, their aim is not primarily to deal with signals of good quality but rather to have the highest possible availability).

The data provided by the Motion Tracker from Xsens are recorded at 25Hz, whereas GPS data are recorded at 1Hz. The IMU was lying on the ground of the vehicle and not moved during all the trial. The calibration of the magnetometers is also done before the test starts and a first GPS position is computed to initialise all the algorithms.

The urban reference trajectory is plotted in Figure 6.9 as the red path. The travelled distance in the exercised vehicle trial is about 4.5 km for 15 minutes of pure urban navigation. The position solution given by the OEM4 GPS receiver is plotted in blue as an illustration of its urban performance. The corresponding tracking statistics are given below in Table 6.2.

	OEM4 Tracking Status			
Nb of satellites	0-1	2	3	≥4
% of time	7.2%	12.3%	14%	66.5%

Table 6.2: OEM4 tracking performance in urban environment.

As illustrated in Figure 6.9, the position solution availability is medium (66,5 %), which does not allow a full urban navigation. The receiver tracked at least 2 satellites about 93% of the time, which makes the trial suitable for testing the proposed tight integration. During the trial, GPS measurements experienced large errors probably due to multipath, as shown by the position solutions inside the green circles.

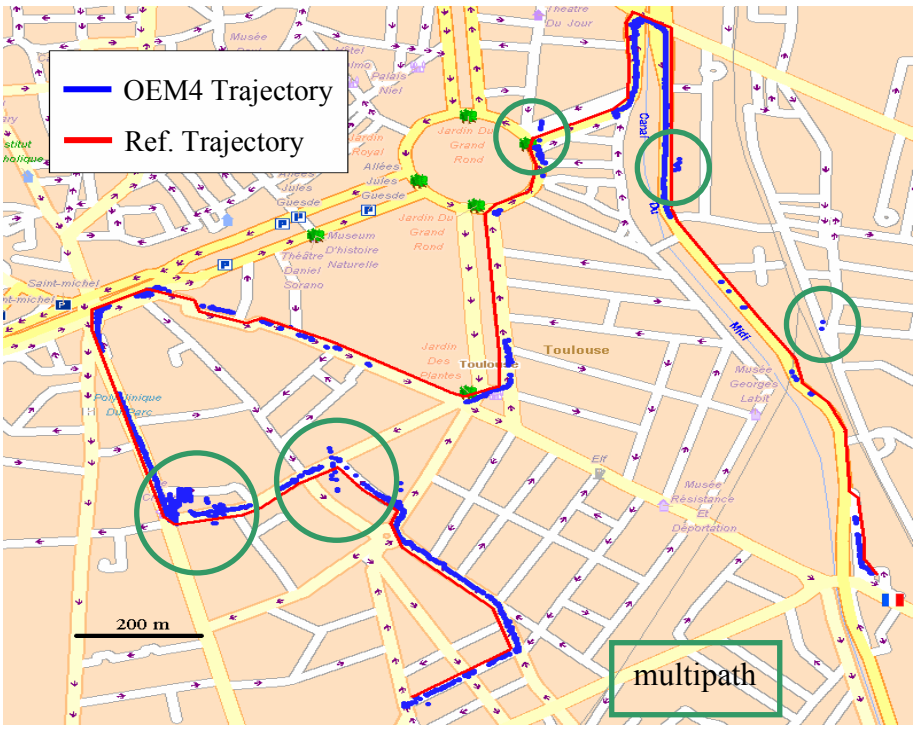

Figure 6.9: Reference trajectory (red) and OEM4 position solution (blue). Urban trial.

In the following, the measurements of the two latest satellites that are acquired and tracked will be used as inputs in the integrated navigation system in order to process data from many satellite configurations (i.e. combination of two GPS measurements) and thus simulate real conditions where only two GPS measurements are available. In the exercised trial, the satellite configuration changes approximately every 8 seconds.

As an illustration of the performance of the attitude filter during the trial, Figure 6.10 presents the headings computed with different algorithms. The GPS-based heading is plotted as well as the gyroscope-based heading, the magnetometer-based heading and the heading estimated by the attitude filter. The upper part shows the drift of the gyro-based heading (dashed red plot) with respect to the magnetometer-based one (green plot). The GPS derived heading assesses the long term reliability and accuracy of the magnetic heading. The lower part of Figure 6.10 is a close-up of the upper part that illustrates the magnetic interference mitigation. As expected, interferences occurred during the test conducted in the city centre. This close-up shows a 15-second magnetic perturbation disturbing the heading restitution during which the attitude filter succeeded in mitigating the perturbation.

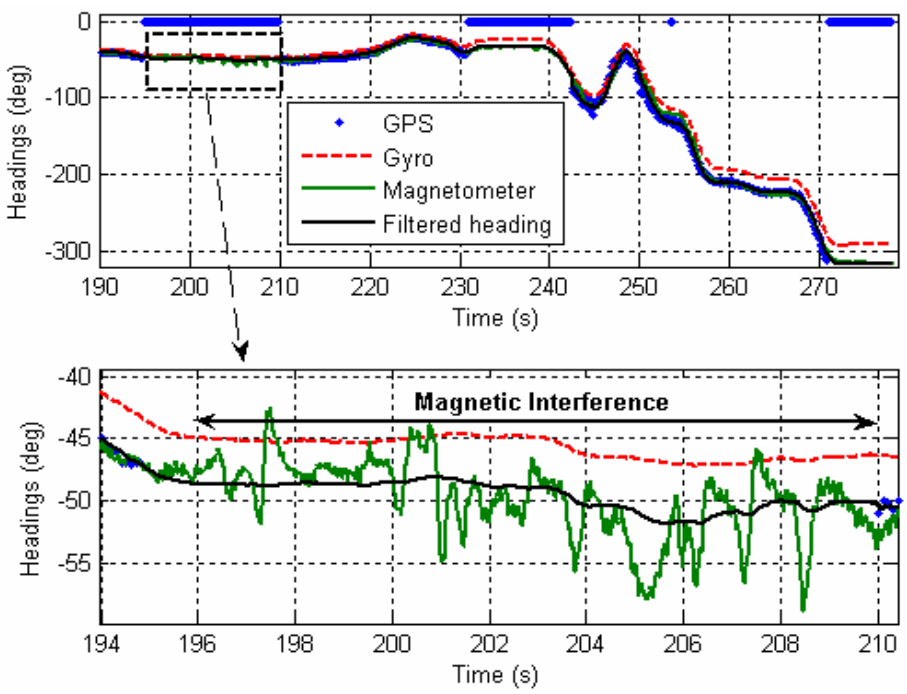

Figure 6.10: Different heading estimates as computed during the urban trial.

As a comparison of both GPS and INS intrinsic performance, the trajectory as computed by the standalone INS is plotted in Figure 6.11. The OEM4-based trajectory is also plotted in blue. The INS initial position and velocity is given by GPS measurements, whereas the heading is initialised using the magnetometers and the declination correction at the test location, as explained in chapter 4. The heading initialisation is then checked by the first GPS velocity measurements. As recalled above, the magnetometers have been calibrated before the trial, so that the magnetic heading is not affected by interference due to the vehicle itself.

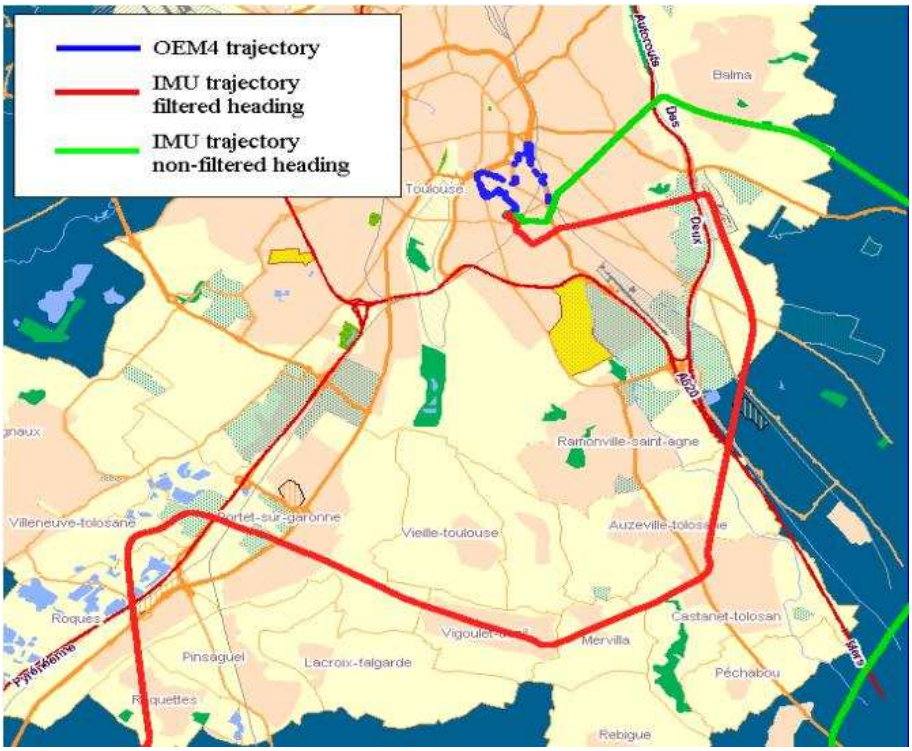

Figure 6.11: Standalone Inertial Navigation System position solutions using different heading sources.

Two trajectories have been computed using different heading sources. The first one is based on the processing of the gyroscopes measurements and is illustrated in Figure 6.11 as the green plot. The second one uses the attitude measurements provided by the attitude filter detailed in chapter 4. The corresponding trajectory is plotted in red. As it can be seen in the figure, both trajectories are rapidly drifting as compared to the GPS reference path plotted in blue. This illustrates the non-negligible impact of the accelerometer bias that varies during the trial and significantly degrades the accuracy of the computed velocity and position (it is indeed never estimated). The trajectory using the filtered heading provides however the best position solution.

In order to test the ability of the integrated navigation system to provide a reliable position solution using very few GPS measurements and also the accuracy of the heading provided by the sensors assembly, a first hybridisation is performed using only two Doppler measurements. Results are illustrated below in Figure 6.12.

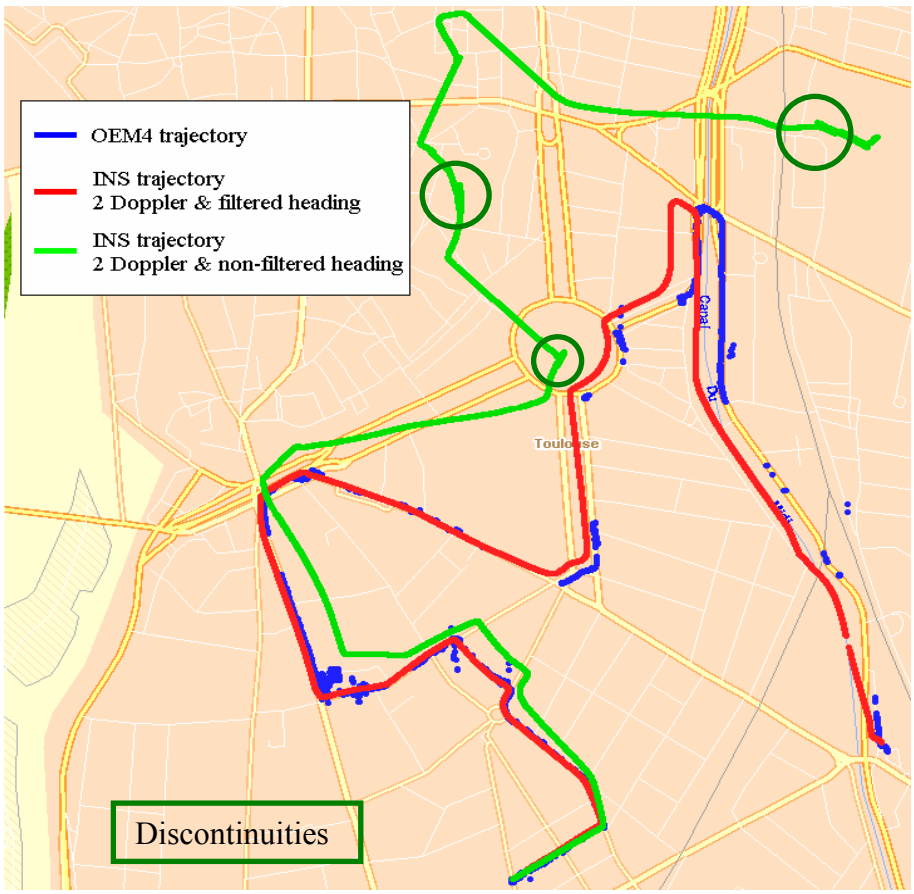

Figure 6.12: INS/GPS position solution using filtered and non-filtered heading. Two Doppler measurements used for hybridisation when available.

As it was expected, the trajectory using these two Doppler measurements and the gyroscope-based heading is drifting. The gyroscopes drift affects the heading but also the estimation of the along track velocity, as shown by the green circles. Opposite, the position solution using the filtered heading and the two Doppler measurements is far more accurate. The trajectory shape is clearly recognisable and follows the true path quite well, with a horizontal error bounded by 70 metres after 15 minutes of navigation. Even if two Doppler measurements are used in that test case, the error of the trajectory computed by the integrated navigation system was clearly predictable since no external position measurement is used to correct the position errors and no estimation of the heading error is done using GPS measurements. However, in such conditions, the performance of

the system seems very good. The attitude as provided by the attitude filter is quite accurate. No precise quantification of the attitude filter contribution onto the overall horizontal error has been done, but regarding the trajectory of Figure 6.12, it can reasonably account for almost all the error (i.e. 70 metres after 15 minutes of navigation with only two Doppler measurements), which is an interesting result using such low-cost sensors. Because the INS provides a position solution in a Dead Reckoning mode by integrating the debiased velocity, error accumulates so that the position is getting unreliable and consequently prevent from any long term positioning. It can also be noticed that the trajectory as computed by the integrated navigation system and the two Doppler measurements is robust to multipath opposite to the GPS-based position solution. This is mainly due to the fact that Doppler measurements are less sensitive to multipath than pseudoranges.

This first hybridisation scheme shows that the use of only Doppler measurements does not allow the computation of a reliable position with an error bounded in time. As a consequence, pseudorange measurements seem necessary in the integration process. They can be used to correct the position drift as soon as they are available, or according to the performance of the navigation system as presented above, only when they are detected no to be affected by large multipath. Another hybridisation including to the former Doppler measurements the two corresponding pseudorange measurements is therefore processed. The resulting trajectory provided by the integrated navigation system using the attitude filter outputs as well as two Doppler and two pseudoranges measurments is plotted in Figure 6.13 in red. As a comparison, the GPS trajectory is also plotted in blue.

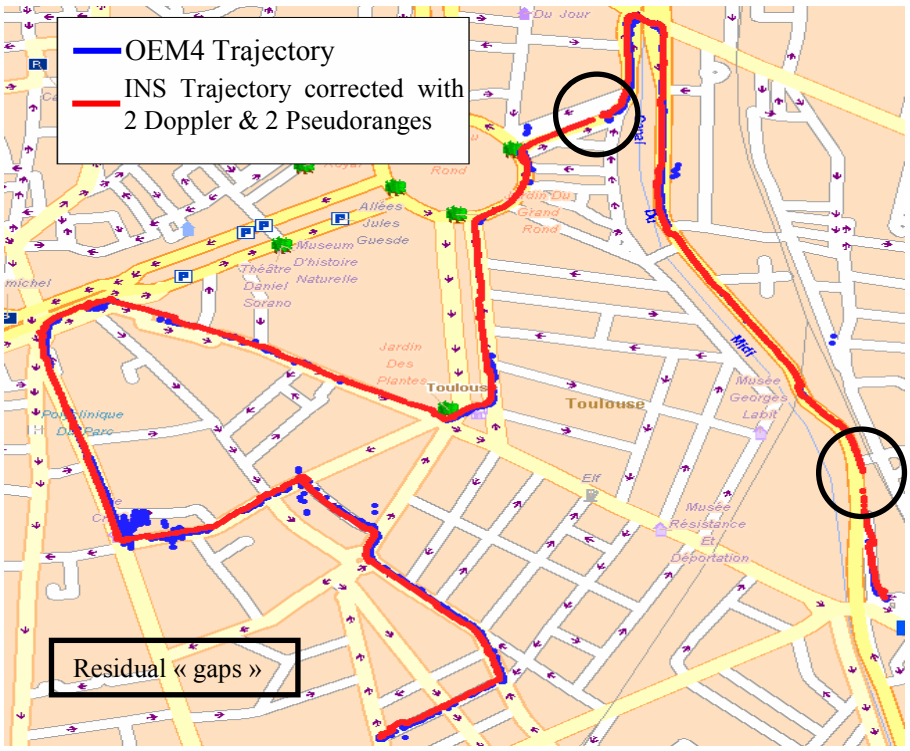

Figure 6.13: Integrated Navigation System trajectory. 2 Doppler and 2 pseudorange measurements used when available.

The overall accuracy is tremendously increased with the use of pseudorange measurements. The horizontal error stays indeed within 40 metres from the reference trajectory during all the trial. Even if pseudoranges are used, the trajectory computed with the hybridised system is again resistant to multipath affecting the GPS measurements because of the high confidence in the Doppler measurement model and the position computation strategy implemented in the Kalman filter.

The along track velocity profile of the vehicle computed using two Doppler and two pseudorange measurements is plotted in Figure 6.14 in blue. The velocity of the integrated navigation system is well debiased compared to the one provided by the integration of the forward direction corrected for the incline of the road. However, the along track velocity profile experiences sudden variations that affect the position solution. Some holes appear in the computed path, which sometimes may be very large, as shown with the black circles in Figure 6.13. Two velocity profile close-ups are plotted in Figure 6.15 that both clearly show the discontinuities that sometimes appear. In these two examples, discontinuities clearly occur around samples 6750 and 39600. They can be due to two events.

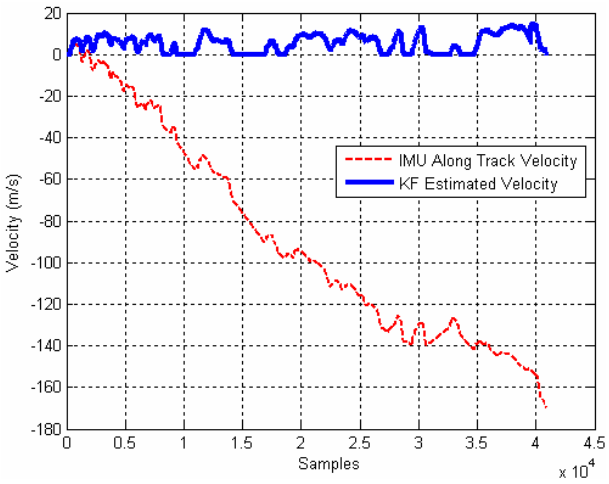

Figure 6.14: Biased (red) and unbiased (blue) along track velocity profile.

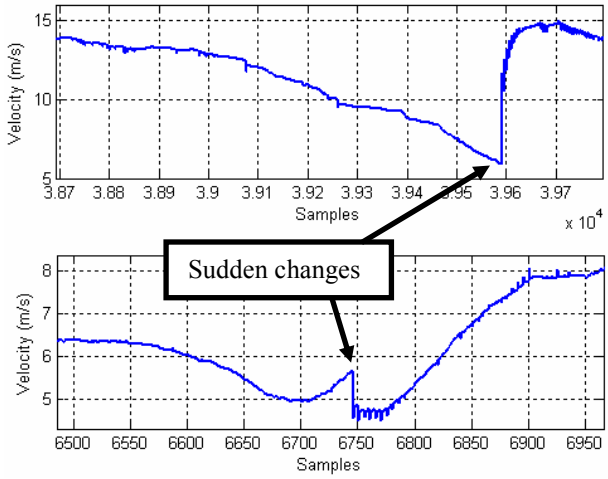

Figure 6.15: Two particular velocity profile discontinuities.

The first one occurs when the hybridised solution relies exclusively on IMU data, thus accumulates errors, and then is corrected by GPS data. The second one occurs when low quality GPS data are used to correct the velocity and the position provided by the IMU. Since in our case, discontinuities appear when GPS measurements are combined with IMU data, the hybridisation methodology can be considered responsible for these issues.

Figure 6.16 presents three different plots that explain the reasons of this bad velocity estimation when GPS and IMU data are tightly integrated. The middle plot gives the PRNs used in the Kalman filter, the right hand side plot the velocity computed using these different PRNs and the left hand side plot the satellite geometry and user heading at time of data combination. At the beginning, PRN 14 and 6 are used for hybridisation. Based on these two PRNs, the user's velocity along the track followed by the vehicle has been computed and plotted. It corresponds to the green dots in the right hand side plot. This velocity has got a large variance. The position of PRN 14 when it is used in the Kalman filter is plotted on the left as the blue dots, whereas the position of PRN 6 is plotted as the red dots. The heading of the user is also referenced as the black dots.

Given this satellites configuration with respect to the user's heading, the estimation of the user's Doppler contribution from the two Doppler measurements is obviously very difficult, even not possible. This explains why the GPS-based user's velocity is very noisy. The Kalman filter uses then PRNs 14 and 5 to estimate the along track velocity. The configuration of the satellite's position with respect to the user's heading is far better, as it can be seen in the left plot. This also explains why the user's velocity is computed with much accuracy, as shown with the red curve in the upper right plot. It can thus be stated that the satellite geometry is of tremendous importance to estimate the velocity of the vehicle, as the DOP is for GPS positioning accuracy.

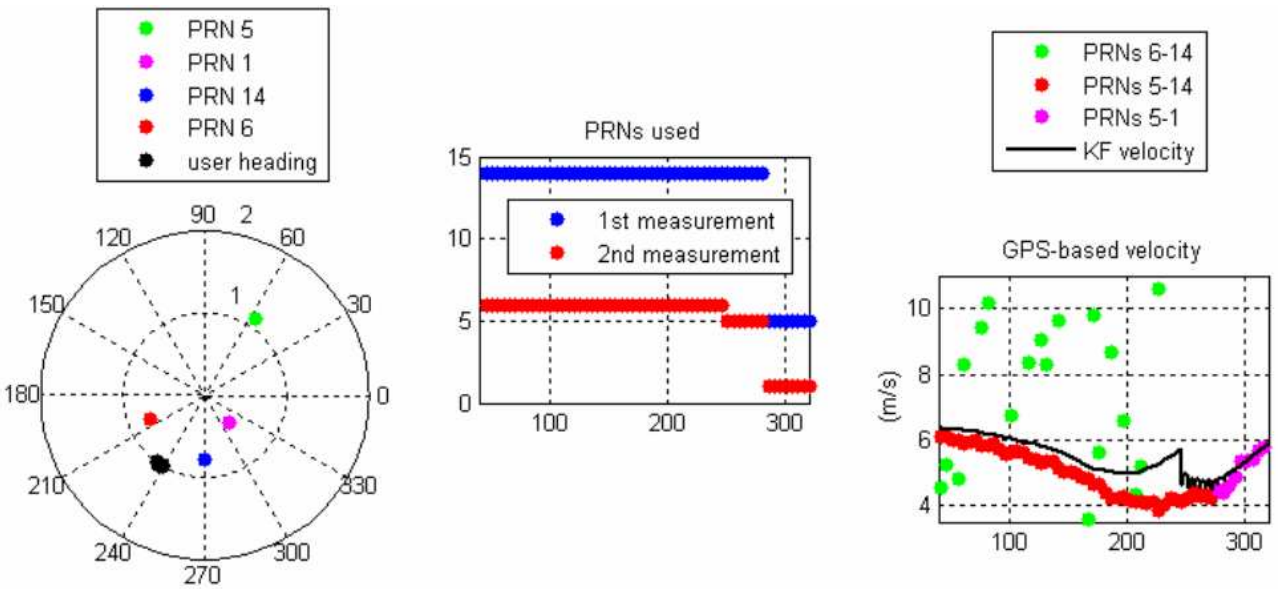

Figure 6.16: Satellite geometry issue.

The bad satellite geometery impacts the efficiency of the proposed tight coupling architecture. To avoid this discontinuity issue, a protection criterion based on the geometry of the satellites used for hybridisation is implemented according to the previous statements. When bad geometry configurations are detected, GPS measurements are no more taken into account and the integrated navigation system relies exclusively on the processing of IMU data. In such a case, the accuracy of the navigation system relies on the quality of the inertial sensors that are used.

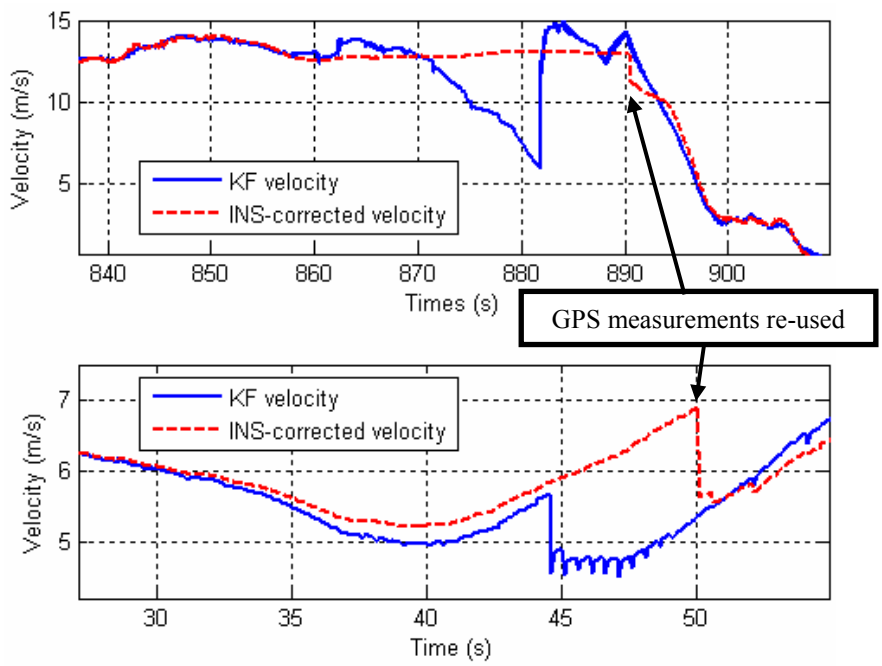

Figure 6.17: Along track velocity profile corrected by the Inertial Navigation System when bad satellites configurations are detected.

The results of the along track velocity estimation taking into account the aforementioned protection principle is plotted above in Figure 6.17 using only two Doppler measurements to avoid the pseudoranges to interfere in the velocity and the position computation stages. The improvement

is not obvious. The upper part of Figure 6.17 shows one case where the correction improves the accuracy. Opposite, the lower part shows an example where the velocity estimated by the Inertial Navigation System is less accurate than the velocity computed using the integration Kalman filter. Sudden variations are still observable, but in that case, they are due to the re-use of new good GPS measurements. The performance of the INS without GPS updates directly depends on the quality of the INS sensors that are used.

The impact of the use of pure INS velocity estimates during the detected bad satellite configurations is shown in Figure 6.18 as the green plot (for comparison, the uncorrected trajectory is plotted in red). Even if the horizontal accuracy stays within 100 metres from the reference trajectory, the final error is worst than without IMU-based corrections.

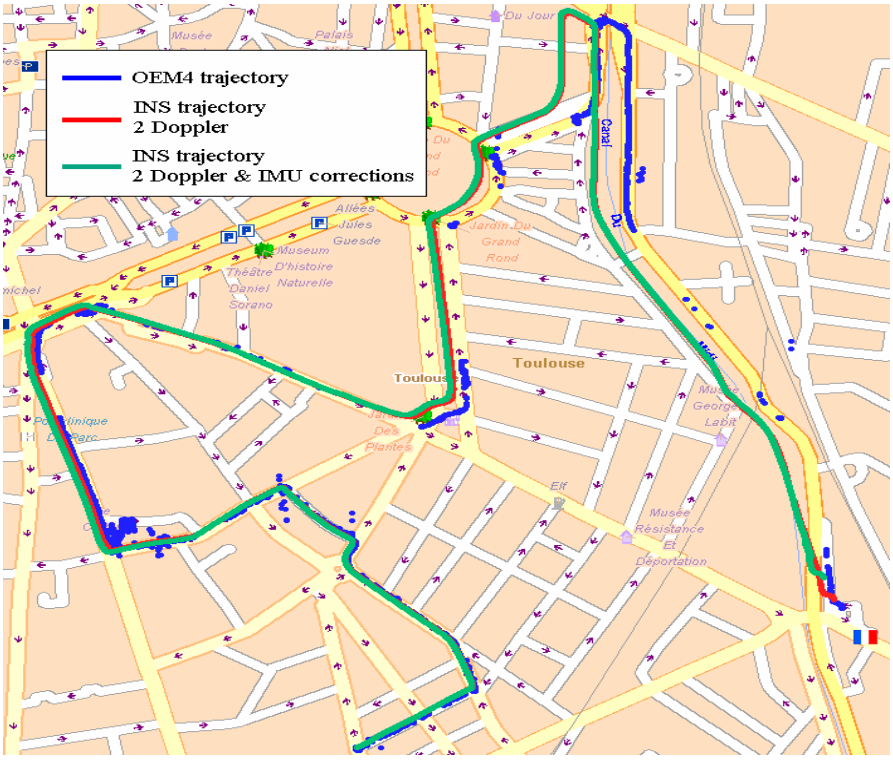

Figure 6.18: Corrected and non-corrected Integrated Navigation System trajectories. 2 Doppler measurements used for hybridisation when available.

In the previous test, position estimations with and without height-aiding were performed. However, the horizontal position solution does not vary very much from each integration scheme that is why only the non height-aided solution is plotted in Figure 6.13. Figure 6.19 shows the vertical performance of the hybridised system using only two Doppler and two pseudorange measurements. The upper part of the figure gives the vertical accuracy, with respect to the pressure sensor measurements.

As it can be seen in the figure, the vertical error reaches about 30 metres without height-aiding, whereas it stays below 5 metres when the altitude from the pressure sensor is used in the Kalman filter. The path followed during the test was however quite flat as shown in the lower part of the figure. Thus, the capability of the filter to bound the vertical error when height-aiding is performed has to be considered with care. The vertical accuracy should be assessed with a hillier path.

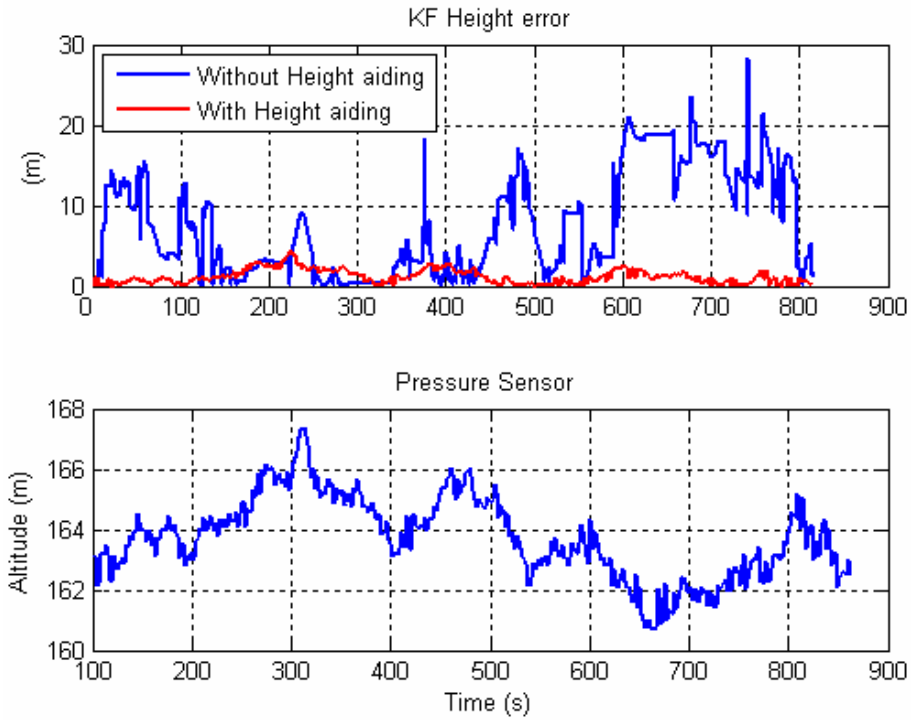

Figure 6.19: Vertical performance of the Integrated Navigation System (upper plot). Vertical profile of the exercised trial (lower plot).

6.2.4 Conclusion

According to the trials detailed above, the proposed hybridisation architecture allows the estimation of the errors affecting the along track velocity provided by a low-cost MEMS-based IMU using only two Doppler and two pseudorange measurements. The use of only two Doppler measurements shows that the accuracy of the heading provided by the IMU was reliable enough to provide a good short term position solution (<5 min). Long term (>15min) positioning is rather difficult since the trajectory is slowly accumulating errors due to the residual attitude errors of the filter detailed in chapter 4. These errors permanently affect the computed trajectory because of the dead reckoning algorithm memory effect, so that the integrated system may be unreliable if used without any pseudorange measurements during a long navigation period. However, and according to the conducted tests, it has been shown that a horizontal error within 70 metres is achievable for 15 min of navigation with only two Doppler measurements.

The adjunction of two pseudorange measurements tremendously improves the position accuracy. A horizontal error within 40 meters of the reference trajectory can indeed be achieved using only two Doppler and two pseudorange measurements. No more shift is noticeable in the integrated navigation system position solution. However, it increases the multipath sensitivity of the system so that their use shall be done with care. The tight coupling architecture allows accurate short term navigation, so that it is possible to choose good epochs where pseudoranges shall be integrated in the filter for position correction.

Height aiding improves the vertical accuracy. In the test conducted, the vertical error is reduced from 30 metres to 5 metres with the adjunction of pressure sensor measurements in the Kalman filter. The trial exercised here is however quite flat, so hilly tests should be performed to assess this vertical improvement.

However, the performance of the proposed tight coupling architecture is closely dependent on the geometry of the satellites used for hybridisation, especially if only two measurements are used. Bad satellites configurations with respect to the user's heading yield erroneous velocity updates. A protection criterion has thus been implemented to prevent these configurations from biasing both the velocity and the position of the vehicle. During these periods, the performance of the integrated navigation system relies exclusively on the quality of the sensors used in the IMU, which can lead to rapid drift of the position solution in our case.

As the hybridisation was tested with a geodetic grade receiver, the measurements used may be of good quality. A future work would be to assess the performance of such hybridisation architecture in the case where only two HSGPS or AGPS measurements are available.

The proposed tight coupling architecture gives good results according to the trial exercised. Although the proposed integration of all the sensors seems less optimised than the standard tight integration (because of the residual biases that affect the attitude measurements), it nevertheless shows what performance can be achieved with low-cost sensors. Such a performance should be compared to what would have been obtained with a standard tight integration scheme aided with drift-free attitude measurements and velocity constraints, and involving the standard INS mechanisation. This also remains to be done in a future work.

6.3 Pedestrian Navigation Case

6.3.1 Introduction

Another application that is expected to tremendously grow is the location of a pedestrian. As demonstrated in chapter two, even the powerful HSGPS and AGPS receivers can not fulfil such a requirement especially indoors and in deep urban canyon where not enough satellite can be tracked in order to compute a position solution. In some cases, they are likely to compute the position of the user using only pure multipath replicas which as a consequence decreases the accuracy of the positioning system.

As discussed in chapter 3, the Pedestrian Navigation System mechanisation is very likely to tremendously improve the accuracy of the sensor-based navigation system even if low-cost sensors are used. When proper initialisation and calibration is done, the accelerometer bias impact onto the performance of the navigation system can be well reduced. The use of an attitude filter capable of estimating the gyroscopes bias may also tremendously improve the system accuracy and also availability.

In order to assess the performance of the PNS in actual conditions, the first following subsection discusses the use of the different inertial navigation algorithms as detailed in chapter 3. The focus is more specifically put on the performance of the systems in actual conditions once they properly have been initialised and calibrated. The second part rather deals with the hybridisation of GPS modules with the chosen pedestrian navigation system. The selection of the sensor fusion algorithm is discussed and detailed. Its performance is assessed trough real test in actual urban and indoor conditions using a real time demonstrator developed for that purpose. The issue of GPS measurements quality is also addressed.

6.3.2 PNS Mechanisation Performance

As a first assessment of the Pedestrian Navigation System (PNS) performance, this section analyses the position accuracy that can be achieved with such a particular mechanisation. The classical Inertial Navigation System algorithm is also tested to show the improvement brought by the PNS. Whatever the navigation algorithm, the attitude filter that fuses accelerometers, gyroscopes and magnetometers information (detailed in chapter 4) is used to provide the attitude estimates.

As discussed in chapter 3, there are mainly two use cases in which the azimuth of displacement has to be estimated. It depends on the motion of the sensors assembly relative to the user, whether it follows the movement of the pedestrian or not. In the first case called constrained navigation, the sensors unit is fixed anywhere onto the user, or simply put in a pocket of the user. The computed heading is thus the displacement azimuth that is biased by an additive constant because of the non alignment of the sensors unit heading axis and the true direction of walk. In the second case called unconstrained navigation, the true azimuth of displacement is not the heading provided by the sensors assembly since it has its own movement relative to the pedestrian.

The two navigation modes are tested in the following. As discussed in chapter 3, the unconstrained navigation issue lies in the computation of the true displacement direction. The method used to get such an estimated heading is based on the projection of the pedestrian velocity of displacement along the north and east axes of the navigation frame. The attitude filter detailed in chapter 4 is used for that purpose.

In the tests presented hereafter, the pedestrian velocity model is calibrated using GPS measurements. A step counting algorithm is developed to detect the motion of the pedestrian and the distance travelled between two consecutive steps is estimated by integrating the estimated velocity. The true displacement direction is computed based on attitude filter outputs. GPS heading measurements are used at the beginning of the trials to estimate the constant bias that affects the heading as provided by the attitude filter.

Experiments are conducted in three phases. First, the static behaviour of the algorithms detailed in chapter 3 and augmented with the developed attitude filter is tested. The performance of the constrained navigation algorithm is analysed in second and the unconstrained navigation in third. In all the trials exercised, GPS data are processed differentially to get accurate position solutions that will be used as reference trajectories.

6.3.2.1 Static Performance

In this test, the sensors assembly is laying at rest in a pocket of the user for 60 seconds with a random attitude. Three algorithms used in the frame of pedestrian navigation are compared: the Classic Inertial Navigation System (C-INS) which uses attitude estimates provided by the processing of gyroscope measurements, the Enhanced Inertial Navigation System (E-INS) which uses attitude estimates provided by the attitude filter and the Pedestrian Navigation System (PNS) based on step counting using the attitude filter. Results are plotted in Figure 6.20. As it could be expected, The PNS clearly outperforms the two other algorithms. The error is indeed 0 metre at the end of the trial since no motion has been detected. Although it still remains some residual error mainly due to the integration of the accelerometer biases, the Enhanced INS gives good results

compared to the Classic INS. After 60 seconds of navigation, the error is indeed reduced by 95% by the use of non-drifting attitude estimates (570 metres for the C-INS algorithm versus 25 metres for the E-INS algorithm). The improvement provided by the attitude filter is assessed and very effective.

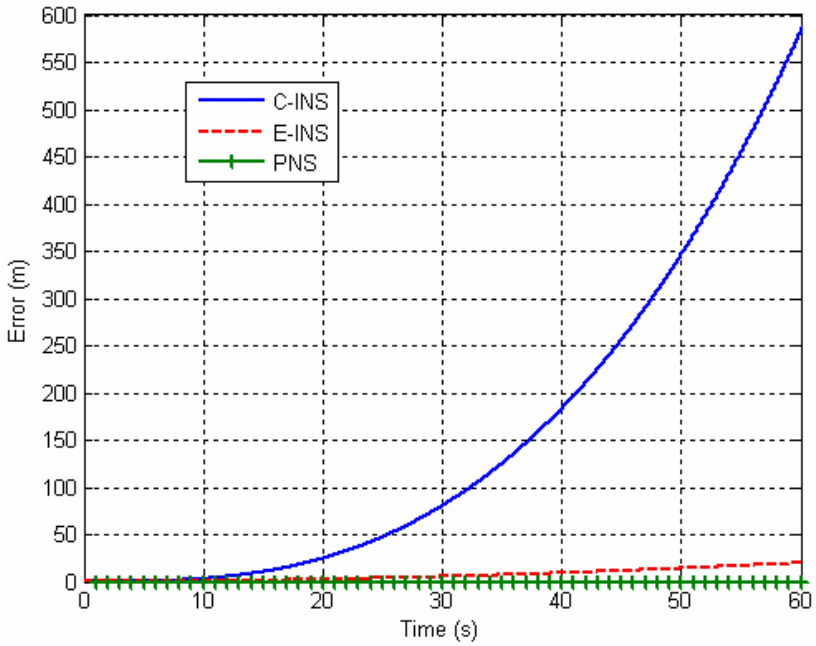

Figure 6.20: Static errors of three different inertial navigation algorithms using low-cost sensors.

6.3.2.2 Constrained Navigation

To compare the behaviour of the three inertial navigation algorithms in dynamic conditions, a short trial is exercised which lasts slightly more than 1 minute. Only the constrained pedestrian navigation is addressed through this test, meaning that the sensors assembly is put on a pocket of the user with a random attitude and is no more moved until the end of the test. The velocity model is calibrated using the GPS measurements (post-processing calibration). In all cases, the initial heading offset is found and removed by processing GPS heading measurements.

Figure 6.21 shows the different trajectories as computed by the three navigation algorithms. The PNS solution, which is plotted in dashed red, is the most accurate. The final horizontal RMS error is about 5 metres. No major drift either in attitude or in position is noticeable on this short duration. Opposite, the solutions based on the traditional inertial mechanisation perform worst. The green dotted plot illustrates the E-INS position solution. In that case, the final horizontal error is about 90 metres. At the beginning of the test, the pedestrian was standing for 3 seconds. No drift is remarkable on the green trajectory. This is however not the case at the end of the run identified as the black asterisk, which clearly illustrates the position drift while the pedestrian is stopped for another 3 seconds. The attitude of the pedestrian matches quite well the reference attitude plotted in blue and obtained with DGPS data. It can thus be stated that the attitude provided by the attitude filter is reliable. The attitude filter is efficient in removing gyro drifts, but it experiences difficulties in removing the acceleration biases affecting the measurements, leading to a drifting position solution. Nevertheless, the E-INS clearly outperforms the C-INS, whose position solution is represented by the black dash-dotted plot. The improvement is of about 90% since the corresponding C-INS final horizontal error is 950 metres (The whole trajectory is not plotted here

for visual convenience).

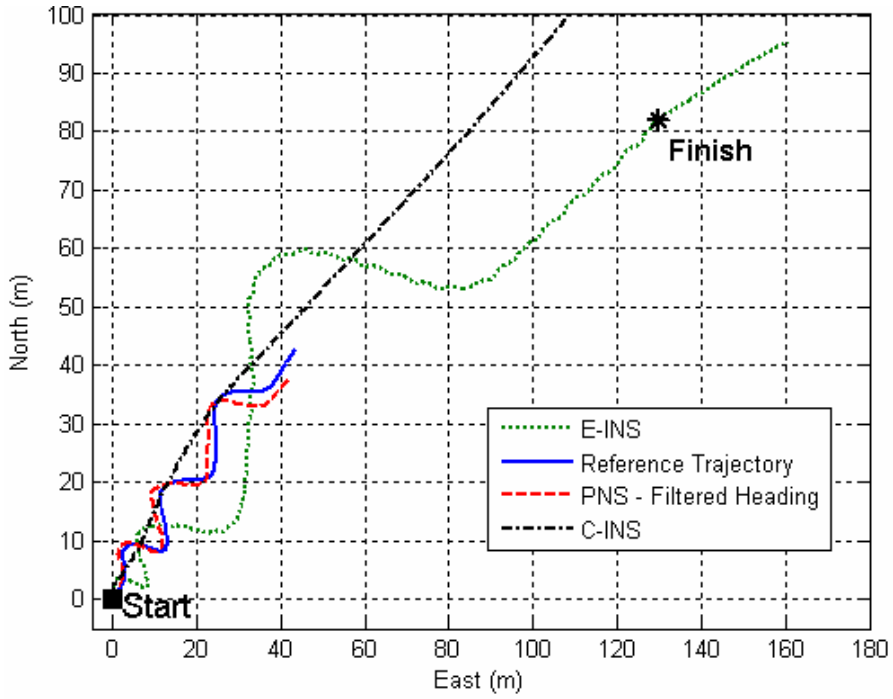

Figure 6.21: Position solutions as provided by three different navigation systems. Short dynamic test.

To assess the complementary nature of the attitude filter and the PNS, another dynamic test is conducted over a longer period. In this trial, the pedestrian walks about 1 km in 13 minutes with the sensors assembly being in a pocket with a random attitude. The sensors assembly is still not moved compared to the user's body during the trial. The resulting trajectory using 100% of GPS data for velocity model calibration is plotted in Figure 6.22.

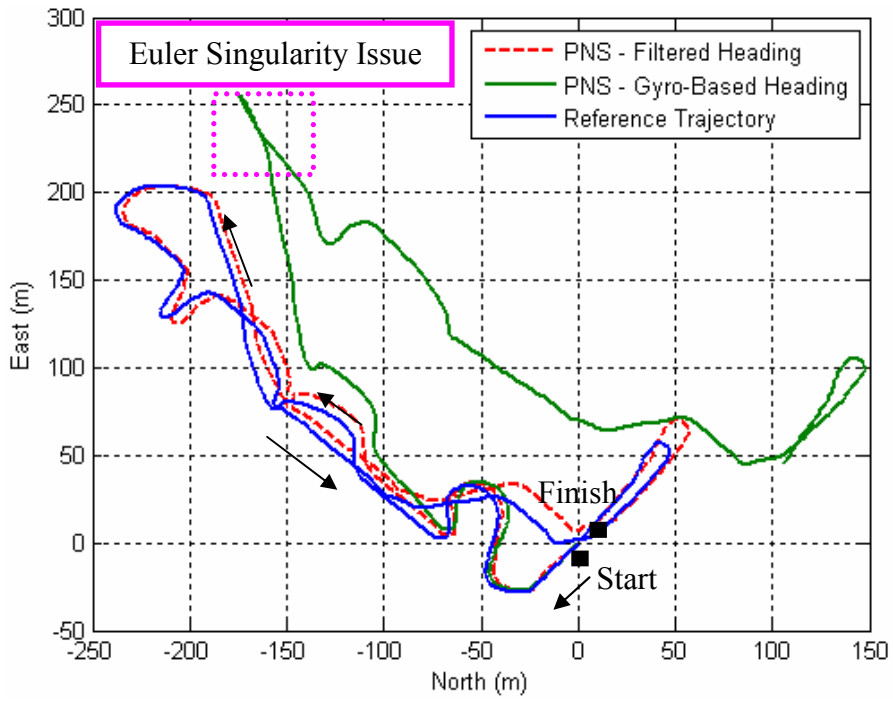

Figure 6.22: PNS position solutions using 100% of GPS data for velocity model calibration. Long dynamic test.

As a comparison, the trajectory computed with the PNS mechanisation using the gyroscope-based heading is plotted in green. The position solution is obviously drifting, which demonstrates the very interesting improvement brought by the magnetometers in terms of position solution accuracy over time. The PNS position solution using the filtered heading is accurate to within 20 meters over the whole test period, with a final horizontal RMS error of 16 meters. Opposite, the solution using the gyroscope-based heading is continuously drifting as shown below in Figure 6.23. The error reaches up to 110 meters after 13 minutes of navigation.

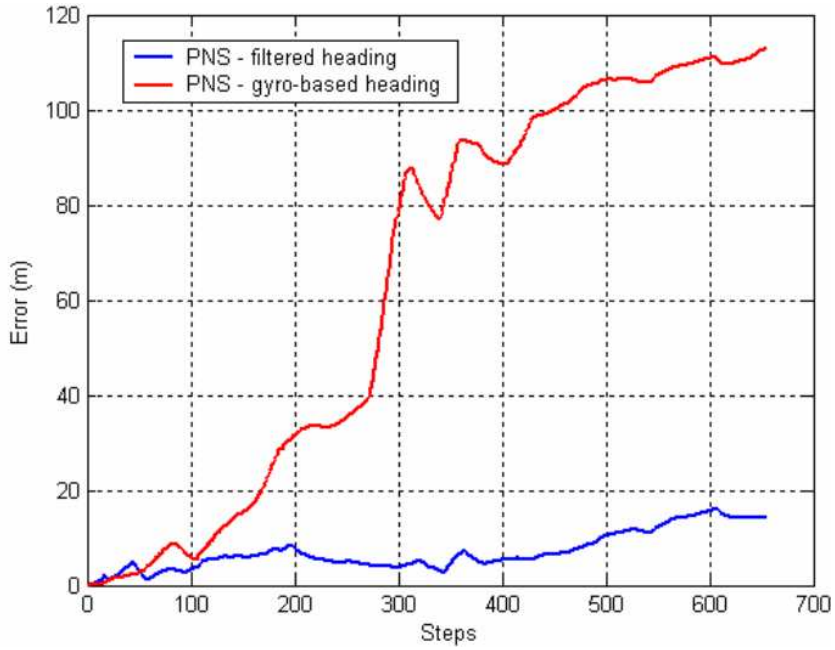

Figure 6.23: PNS horizontal RMS error. Long dynamic test.

Based on the same trial, the trajectory using only the first 10% of GPS data for velocity model calibration is computed and illustrated in Figure 6.24

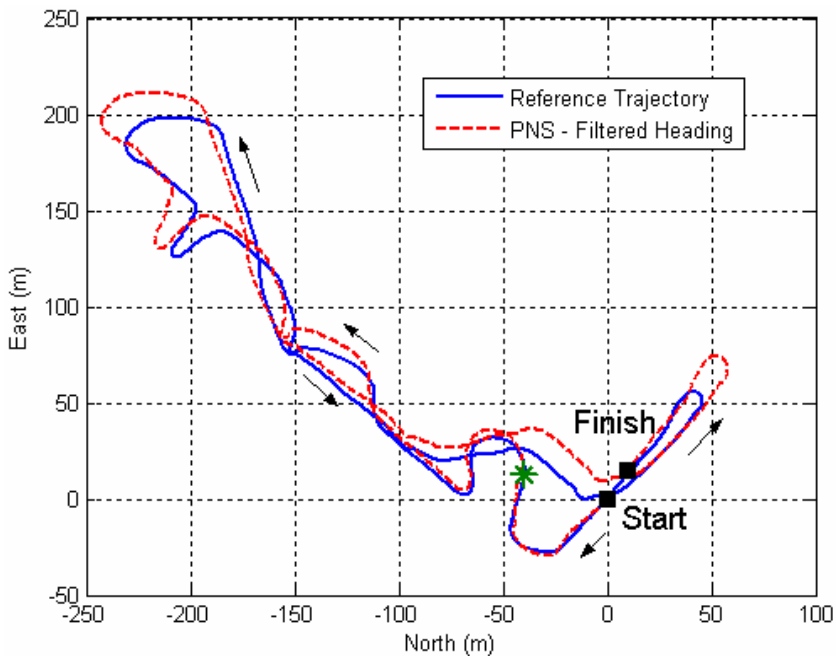

Figure 6.24: PNS position solutions using the first 10% of GPS data for velocity model calibration. Long dynamic test.

These 10% of data are collected between the beginning of the walk and the green asterisk, as shown in Figure 6.24, which represents approximately 1 minute. The accuracy of the PNS position solution stays within 25 metres from the reference trajectory during the whole path. This corresponds to 12 minutes of navigation without any GPS data. The final horizontal RMS error is 18 metres.

Even with a little part of data for calibration, the velocity model provides good estimates of the curvilinear travelled distance. Accuracy stays within acceptable limits that are suitable for LBS applications during GPS outages. Moreover, trajectories reconstructed using the heading provided by the attitude filter and illustrated in Figure 6.21 and in Figure 6.22 are not affected by Euler's angles singularities, opposite to the gyroscope-based solution of Figure 6.22. According to the attitude computation algorithm, the position solution can then be provided regardless of the orientation of the sensors assembly.

6.3.2.3 Unconstrained Navigation

The position solution accuracy is very likely to be affected by the movement of the sensors assembly with respect to the user's body, especially if the latter is contained in a handheld device such as a cell phone or a PDA. To assess the capability of the PNS to provide a reliable position solution while the sensors unit is moved during the walk, another dynamic test is performed.

In this test, a pedestrian follows an athletic track of 250 metres for 4 minutes. At the beginning of the test, the sensors assembly is in the pocket of the pedestrian, with a random attitude. While walking, he pulls randomly the sensors unit out of his pocket and moves it as if he was looking at his cell phone. Then he replaces it inside his pocket. The movements of the unit with respect to the pedestrian are not stressed but rather reflect typical low motions cell phones may experience. The resulting trajectories are given in Figure 6.25.

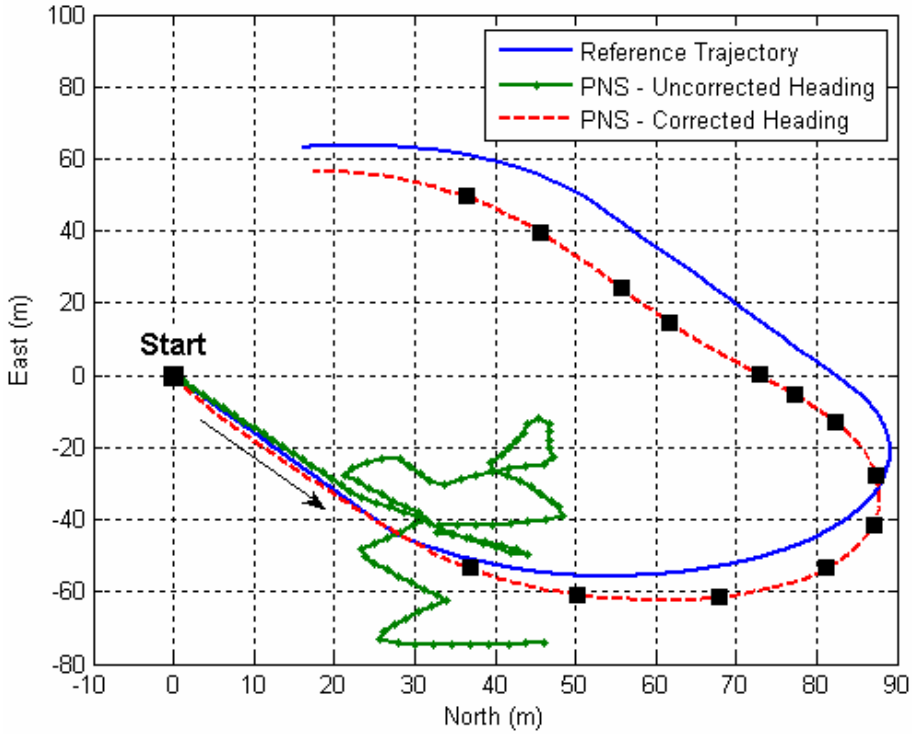

Figure 6.25: Unconstrained navigation solutions.

The sensors unit is moved 13 times during the trial as indicated by the black squares (excepting the first one indicating the start position). The PNS trajectory as computed above is represented by the green plot. The trajectory is clearly not relevant of the true path. Opposite, the PNS position solution whose heading is estimated by processing both north and east projections of the pedestrian velocity as detailed in chapter 3 is far more accurate. The performance is degraded as compared to the constrained navigation, but the corrected trajectory nevertheless matches quite well the true trajectory.

Both travelled distance and displacement direction are coherent with the actual ones. There is no noticeable drift in the curvilinear travelled distance. The velocity model once calibrated is thus robust to such sensors assembly movements during the walk. For visual convenience, the trajectory provided by the modified E-INS, (i.e. the E-INS algorithm modified to estimate both North and East velocities) is not plotted here for comparison. The acceleration biases yield a drifting position that goes quickly out of the figure.

Figure 6.26 illustrates the headings estimated with the two different PNS algorithms. The GPS solution plotted in blue is shown here as a reference. The processing of both north and east velocities tends to prove the efficiency of the displacement direction detection algorithm discussed above and detailed in chapter 3. However, it still is sensitive to the dynamic experienced by the sensors assembly which shall not be too high as compared to those of the pedestrian.

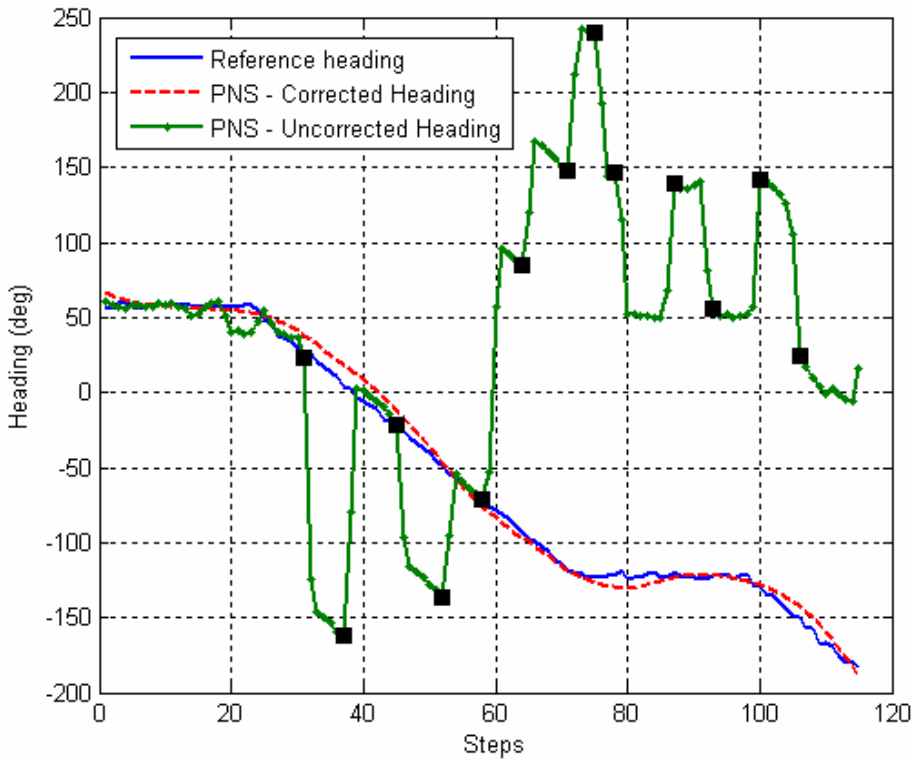

Figure 6.26: Displacement direction detection result.

6.3.2.4 Conclusion

The aim of this subsection was to analyse the performance of two different inertial navigation algorithms used as an alternative positioning system during GPS outages. Both were tested with low-cost sensors for the so-called constrained navigation. The classic inertial navigation

algorithm has been found to give the worst performance, whether the drift-free attitude filter is used or not. Its integration with the C-INS has indeed led to the implementation of the E-INS, whose performance is improved by more than 90% compared to what can be achieved with the C-INS using the same low-cost sensors. However, even if the navigation solution drift is well reduced because of the attitude filter, this is not enough to be used as an alternative positioning system for pedestrians. Indeed, accelerometer biases are badly estimated and consequently are responsible for the residual errors. The position is drifting so that this algorithm can only be used for short term positioning for both constrained and unconstrained navigation.

To cope with this issue, the PNS mechanisation has been implemented and tested on the same trials. Coupled with the attitude filter and properly calibrated and initialised, this algorithm provides reliable position solutions over time, with a horizontal RMS error within 25 metres for 12 minutes of constrained navigation without GPS assistance for velocity model calibration.

The unconstrained navigation mode was also studied and tested with the PNS algorithm modified to enable the estimation of the true pedestrian displacement direction. In this mode, the sensors assembly has got its own motion relative to those of the pedestrian. Assuming a low dynamic with respect to pedestrian motion, it was shown that the true displacement direction could be estimated with an acceptable accuracy (25 metres for 4 minutes of navigation). Even if the horizontal error is higher than in the constrained navigation mode, the modified algorithm makes the system robust to low motion of the sensors assembly. However, it obviously does not reflect the all day life behaviour of a handheld positioning device, and therefore does not allow the total generalisation of the pedestrian mechanisation concept.

According to these first conclusions, only the PNS mechanisation within the frame of the constrained navigation will be considered in the following. In this context, a real time integrated system is developed to assess the performance that can be achieved with the use of low-cost sensors to supply GPS during outages and improve the accuracy of the position computed by the navigation system. This real time software is based on the attitude filter detailed in chapter 4 and the pedestrian mechanisation discussed in chapter 3 and recalled above. Details and performance assessment are given in the next subsection.

6.3.3 Integrated Navigation System

6.3.3.1 Introduction

The hybridisation of the GPS modules with other sensors is a good mean to improve the availability and the accuracy of the navigation system. As discussed in the beginning of this chapter, several integration schemes are possible (loose and tight coupling). Considering the use of low-cost inertial sensors of MEMS type, the approach can be the same as in the land vehicle case. The tight integration would be very well suited in this typical navigation use case since the pedestrian is very likely to go inside buildings where only few GPS measurements are available. However, ENAC lab did not own any HSGPS or AGPS receiver capable of providing raw measurements (i.e. pseudoranges and pseudorange rates) at the time the study was conducted, which would have allowed a tight coupling implementation. Since HSGPS and AGPS modules capable of providing processed measurements (i.e. position and velocity) were nevertheless available, the following will address the loose coupling of such GPS-based modules with the low-cost sensors assembly described in chapter 3. A real time C/C++ implementation is described hereafter that also

includes as an important feature the attitude filter described in chapter 4. This real time software is then used to assess the performance of the system in typical pedestrian environments.

One important issue that must be handled when dealing with hybridisation in urban area is the detection of outliers and bad GPS measurements since they are used to correct the inertial navigation system errors. Such an issue is all the more important since raw measurements are not available in our hybridisation case. No particular RAIM or integrity monitoring algorithm have been used. GPS processed measurements are rather used in the software when signals are strong enough to reasonably assume that no major degradation in the position accuracy may happen. This will certainly decrease the amount of GPS data used for correction purposes, but as shown above, the PNS mechanisation provides good performance up to about 15 minutes without any update, assuming a proper initialisation of the navigation algorithm.

The PNS mechanisation is used in the following as the primary navigation system that provides the position of the user. The GPS modules are used to correct the position and attitude errors when the measurements are declared reliable. An Extended Kalman Filter is used to fuse both navigation systems. The PNS mechanisation is based on the estimation of the velocity of the pedestrian, whose model has been detailed in chapter 3 and is recalled hereafter in equation (6.26).

$$v^{pedestrian}(t) = A(t) \cdot Mean + B(t) \cdot Freq + C(t) \cdot Std \tag{6.26}$$

In the developed software, no step detection algorithm is implemented. The reason for that is first to get a more robust travelled distance estimation procedure with respect to miss and fault step detections that may occur, and second to ease the integration of data in the EKF. In the proposed implementation, the parameters MEAN, FREQ and STD are computing over a time window of 2 seconds every sampling period. The variance of the acceleration magnitude is checked to declare whether the user is walking or not according to a predetermined threshold. This methodology also has the advantage of rendering the synchronisation of the GPS modules with the sensors easier.

The following describes in details the Kalman filter designed to fuse the two navigation systems according to a loose coupling architecture.

6.3.3.2 Coupling Methodology

6.3.3.2.1 Kinematic Model and State Vector

As a result of the motivations detailed above, the integration of the different navigation systems is done through a Kalman filter according to a loose coupling architecture. The filter is naturally designed to estimate 8 error states, which basically are the 2D position error, the errors affecting the heading provided by the PNS and the error made on the regression coefficients used to model the pedestrian velocity. The corresponding state vector is given in equation (6.27).

$$\delta X = \begin{bmatrix} \delta N & \delta E & b_{\psi,ir} & \dot{b}_{\psi,ir} & b_{\psi,al} & \delta A & \delta B & \delta C \end{bmatrix} \tag{6.27}$$

where:
- δX is the state vector.
- δN, δE are respectively the error made on the north and east component of the user's position.
- $b_{\psi,ir}$ is the in run bias affecting the PNS heading.

- $b_{\psi,al}$ is the initial offset between the GPS heading and the PNS heading.
- δA is the regression coefficient error for the MEAN parameter.
- δB is the regression coefficient error for the FREQ parameter.
- δC is the regression coefficient error for the STD parameter.

The general model of the errors included in the Kalman filter is given in equation (6.28). It is defined as the difference between the value provided by the PNS and the GPS. The "x" in equation (6.28) is a general variable that could stand for the north, east, velocity and heading or regression coefficients error.

$$\delta x(t) = x^{PNS}(t) - x^{GPS}(t) \tag{6.28}$$

The stochastic part of the state transition matrix is composed of the biases affecting the heading of the PNS and the error made on the regression parameters used to model the velocity magnitude of the pedestrian. The heading used in the PNS mechanisation can be based either on gyroscope measurements or on the attitude filter. As the pedestrian is very likely to go inside buildings where magnetic interferences may occur, the error affecting the PNS heading can not be a priori characterised.

The worst case that may degrade the performance of the PNS is a long term magnetic interference that would degrade the efficieny of the heading drift correction by processing magnetometer measurements. However, it is difficult to estimate the probability of occurrence of such a use case. Therefore, in order to take into account that worst case in the design of the Kalman filter, the error affecting the PNS heading is assumed to follow an integrated random walk as described in equation (6.29), whose driving noise is a function of the magnetic interference magnitude.

$$\ddot{b}_{\psi,ir} = w_{b,ir}(t) \tag{6.29}$$

The second part of the bias affecting the PNS heading is the offset that is introduced by the position of the sensors assembly onto the user's body. It indeed introduces an offset between the true azimuth of displacement given by the GPS and the heading provided by the assembly. This bias is modelled as a constant random process, as described by equation (6.30).

$$\dot{b}_{\psi,al} = 0 \tag{6.30}$$

Once GPS measurements are available, it is possible to compute the regression coefficient A, B and C as given in equation (6.26) in order to get a model of the pedestrian velocity. In this EKF, the regression coefficients errors are modelled as random walk processes. The corresponding equations are given below from equation (6.31) to (6.33). The stochastic models are chosen empirically with low driving noise variances ($2 \cdot 10^{-3}$) according to what has been observed during several trials.

$$\dot{\delta A}(t) = w_{\delta A}(t) \tag{6.31}$$

$$\dot{\delta B}(t) = w_{\delta B}(t) \tag{6.32}$$

$$\dot{\delta C}(t) = w_{\delta C}(t) \tag{6.33}$$

According to the Pedestrian Navigation System mechanisation, the position along the north axis is the integration result of the pedestrian velocity projection. Both PNS and GPS north position estimates are given below. The initial position is assumed known. The same

$$N^{PNS}(t) = N^{PNS}(0) + \int_0^t v^{PNS}(u) \cdot \cos\left(\psi^{PNS}(u)\right) \cdot du$$

$$N^{GPS}(t) = N^{GPS}(0) + \int_0^t v^{GPS}(u) \cdot \cos\left(\psi^{GPS}(u)\right) \cdot du$$

The estimation of the PNS errors is only possible when GPS measurements are considered reliable. The north position error as defined in equation (6.28) is obviously not linear with respect to the pedestrian heading and velocity errors. It should be linear with respect to the errors included in the state vector in order to ease the design of the Kalman filter. Assuming ψ^{PNS} the linearisation point and neglecting as a first approximation the second order derivation terms, the position error along the north axis δN as defined in equation (6.28) can be written as follows:

$$\delta N(t) = \delta N(0) + \int_0^t \left[\delta v(u) \cdot \cos\left(\psi^{PNS}(u)\right) - v^{PNS}(u) \cdot \sin\left(\psi^{PNS}(u)\right) \cdot \delta\psi(u)\right] \cdot du \tag{6.34}$$

It is then straightforward to get the time derivative of the north position error as expressed in equation (6.34). It is given below in equation (6.35), which stands for the first state transition function needed to build the kinematic part.

$$\dot{\delta N}(t) = \cos\left(\psi^{PNS}(t)\right) \cdot \delta v(t) - v^{PNS}(t) \cdot \sin\left(\psi^{PNS}(t)\right) \cdot \delta\psi(t) \tag{6.35}$$

Following the same methodology, the time derivative of the east position error is as given in equation (6.36).

$$\dot{\delta E}(t) = \sin\left(\psi^{PNS}(t)\right) \cdot \delta v(t) + v^{PNS}(t) \cdot \cos\left(\psi^{PNS}(t)\right) \cdot \delta\psi(t) \tag{6.36}$$

It is straightforward to get the velocity error model as a function of the stochastic errors. Based on the velocity model used in the frame of this subsection, Equation (6.37) gives the time derivative of the velocity error as a function of the regression coefficient errors.

$$\dot{\delta v}(t) = \dot{\delta A}(t) \cdot Mean + \dot{\delta B}(t) \cdot Freq + \dot{\delta C}(t) \cdot Std \tag{6.37}$$

The kinematic model given below in equation (6.38) is then fully described by the combination of the equations (6.29), (6.30), (6.31), (6.32), (6.33), (6.35), (6.36) and (6.37). The continuous state transition matrix F is obvious to compute. Hereafter is recalled the continuous covariance matrix Q.

$$\dot{\delta X}(t) = F(t) \cdot \delta X(t) + G(t) \cdot w(t) \tag{6.38}$$

where:

- $G(t) = diag\left(\begin{bmatrix}0 & 0 & 0 & 1 & 0 & 1 & 1 & 1\end{bmatrix}^T\right)$
- w is the state noise vector, whose covariance matrix is $Q(t) = \mathrm{cov}\left(w(t)\right)$

As the hybridisation is done with navigation systems capable of providing digital data, the continuous definition of the kinematic part of the Kalman filter has no physical meaning but is rather a rigorous implementation methodology. The discrete form of the model given in equation (6.38) is done according to the procedure detailed in [44] and recalled in appendix C.

6.3.3.2.2 Measurements Equations

In the integrated pedestrian navigation system developed within section 6.3, the GPS receiver is assumed to be the reference sensor (i.e. the sensor that provides non biased information). The number of external measurements used to correct the PNS errors at each hybridisation epoch (position, velocity, heading…) mainly depends on the quality of the GPS data as well as the dynamic of the user.

As discussed in chapter 2, the different GPS-based positioning modules are designed to increase the availability of the position solution. As a consequence, even if weak signals are tracked, the modules are likely to compute the location of the user. However, such measurements (namely position and velocity) are very noisy and affected by multipath in harsh environments. In such conditions, the initialisation and the calibration of the pedestrian navigation algorithm may be unreliable, which consequently will degrade the positioning performance of the integrated navigation system during outages. RAIM techniques could have been implemented to detect and exclude bad GPS measurements as discussed for example in [49] and [50], but the integration level chosen here does not allow such measurement quality monitoring (we only have to deal with position and velocity measurements). Furthermore, such quality monitoring techniques do not provide reliable results in harsh environments due to the limited amount of data that are not affected by errors (multipath, cross-correlation, noise…) as compared to the data set used for analysis purposes [50]. In the following, the GPS measurement reliability assessment is rather based on a practical approach. The C/N_0 of the satellites that are used to compute the position solution is permanently checked, together with the current Horizontal Dilution of Precision (HDOP) figure of merit. According to several tests that have been conducted in different urban environments, it has been found that in most of the cases when the HDOP was below 2.5 and the C/N0 of the 4th worst satellite used to compute the position of the user was higher than 25 dBHz, the measurements were enough reliable to allow the calibration of the velocity model and correct the position error. Otherwise, the integrated navigation system relies exclusively on the data provided by the IMU. Such a decision algorithm has then been implemented in the real time positioning software.

The choice of the external measurements is basically illustrated in Figure 6.27. The first use case occurs when GPS processed data are declared reliable. In that case, the velocity as estimated by the receiver is checked to detect whether the user is moving or not. A cross-check is also performed with the simple motion detection algorithm discussed in chapter 5 and based on the processing of the acceleration magnitude of the sensors unit. If a motion is detected, GPS positions, velocities and headings are used as measurements. If not, the heading is provided by the attitude filter if no magnetic interference is detected, and no measurements are used for heading correction if interferences are detected. When GPS measurements are declared not reliable, the only external measurement than can be used to correct the PNS errors is the heading provided by the attitude filter, assuming no magnetic interference.

The measurements errors are computed as defined below in equation (6.39). The index ‘i’ stands for the possible measurements that can be used for correction purposes, as discussed above and illustrated in Figure 6.27. The observation matrix H_k at epoch k is then straightforward to compute. The general observation model is given in equation (6.40).

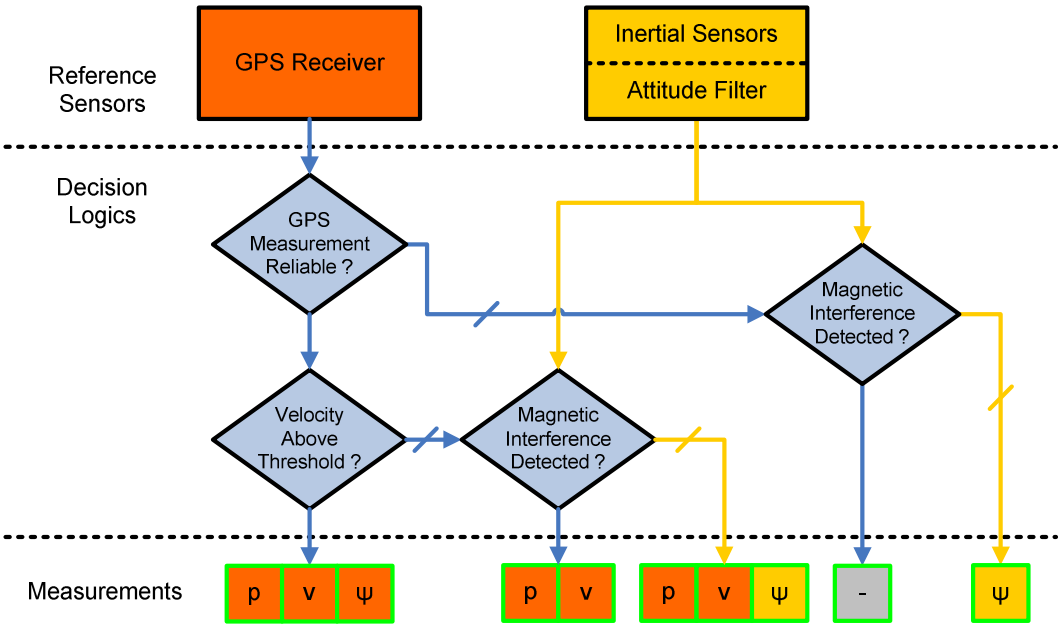

Figure 6.27: Possible measurement configurations.

$$\delta z_i = z_i^{GPS} - z_i^{PNS} \tag{6.39}$$

$$\delta z_k = H_k \cdot \delta X_k + v_k \tag{6.40}$$

6.3.3.2.3 Mechanisation and System Configuration

Figure 6.28 summarises the hybrid system architecture, as implemented in the real time positioning software. A closed-loop loose coupling methodology is used. The GPS module (which can be either a HSGPS or an AGPS) provides position, velocity and heading measurements. The attitude filter provides an estimate of the pedestrian heading. The measurement data set is chosen according to the decision logic described in the previous subsection.

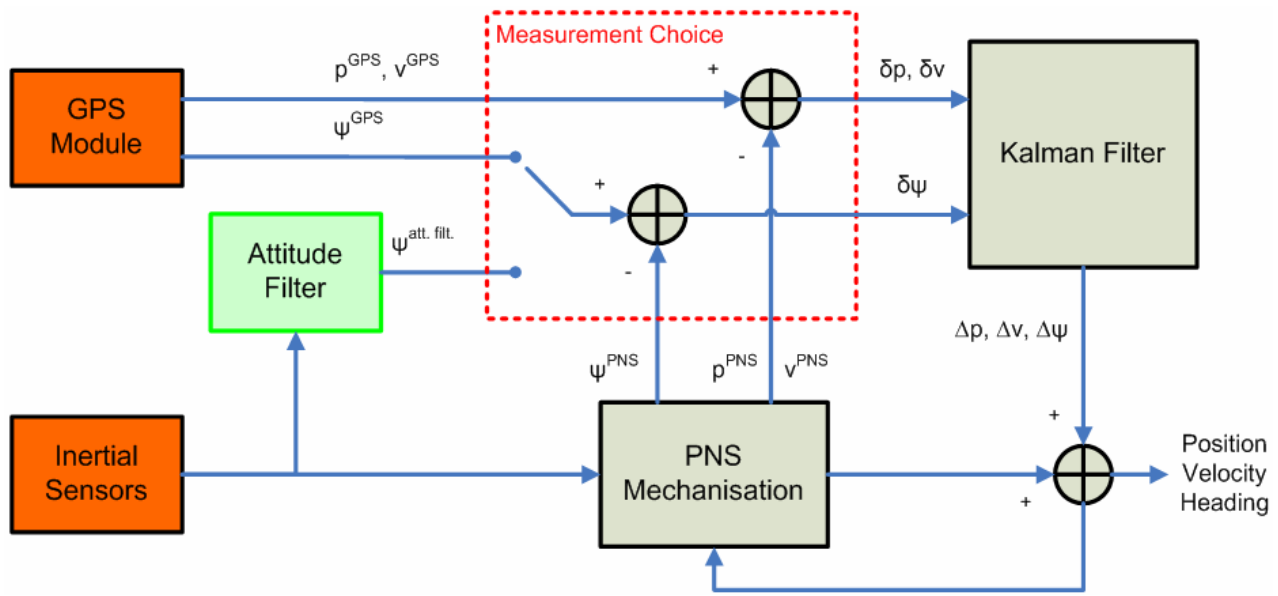

Figure 6.28: Real time sensor fusion architecture (closed-loop loose coupling architecture).

All the filters described above as well as the pedestrian mechanisation are implemented in C/C++ in order the integrated navigation system to be able to provide a position solution in real time. As part of the functionalities of the software, raw data from all sensors can be stored while operating the navigation system for post-processing analysis.

The synchronisation of the data is done prior to the hybridisation. The sampling rate of the data provided by the Xsens MTi is 50Hz whereas the GPS modules are configured to output measurements at 1Hz. Both are not synchronised to each other using a specific hardware so that an offset is likely to affect the time stamping of the data. The left hand part of Figure 6.29 illustrates such an issue. As the sampling rate of the MTi is 50Hz, this shift is at most equal to 10ms, which is considered negligible with no major impact on the further processing of the measurements.

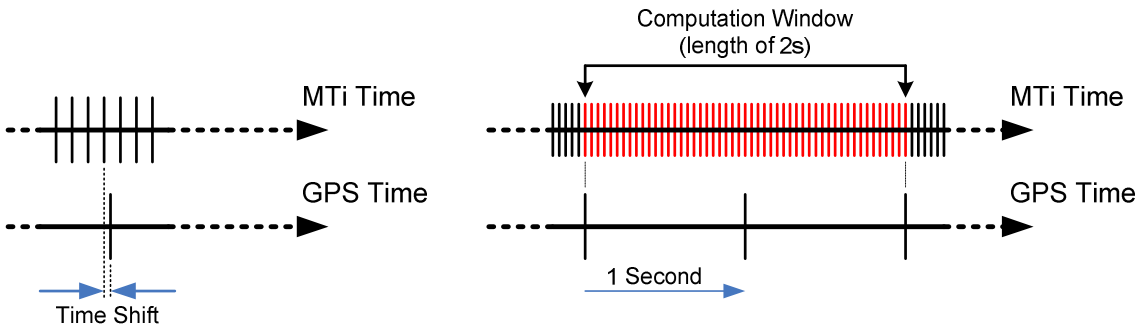

Figure 6.29: Data synchronisation principle.

Once the data have been collected, they are synchronised in order for the time window used to compute the pedestrian velocity model parameters to match the GPS measurements occurrences, as illustrated in the right hand part of Figure 6.29 (parameters are computed at the MTi sampling rate). As a result, the synchronisation method introduces a time lag of one second in the position solution computed by the integrated navigation system, which remains acceptable.

Figure 6.30 illustrates the integrated pedestrian navigation system developed within the scope of this study. The off-the-shelf MTi is connected via the USB port to the processing unit (Dialogue FlyBook) and provides accelerations, rotation rates and magnetic field measurements. The GPS module we used is Bluetooth capable and can be configured either in a high sensitivity or assisted mode. Data are provided through NMEA frames to the processing unit. The Thales Alenia Space assistance server processes the GPS signals to elaborate the assistance data that are transmitted to the processing unit on the demand of the user through a wireless connection (in the test conducted, the wireless connection is the GPRS, which is supported on the GSM cellular network). The data are then uploaded into the assisted GPS chipset for further processing. The processing unit computes and displays the position of the user on a map that can be whether on its screen or a distant one.

The interface of the real time pedestrian navigation software is shown in Figure 6.31. It is basically composed of a local map where are displayed the HSGPS or AGPS position solutions as well as the hybrid position solution. The interface also allows the user to see in real time the current navigation mode (i.e. GPS, MEMS standalone or hybrid mode). As raw data can be collected while the software computes the position of the pedestrian, it offers some post-processing capabilities using for instance Matlab, in order to adjust some algorithms and emphasizes typical pedestrian navigation issues.

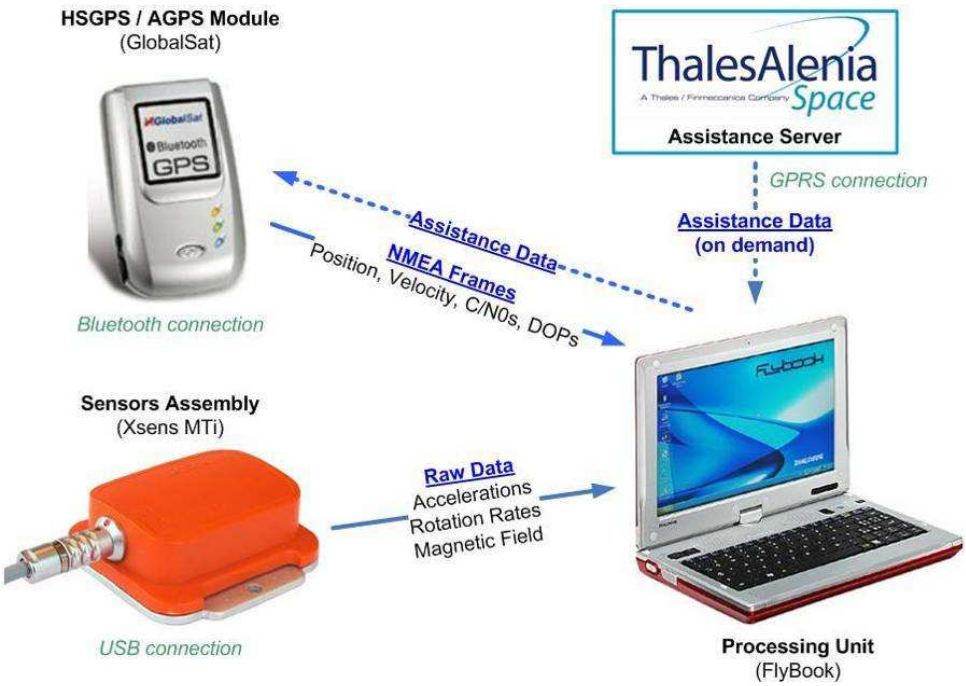

Figure 6.30: Integrated Pedestrian Navigation System.

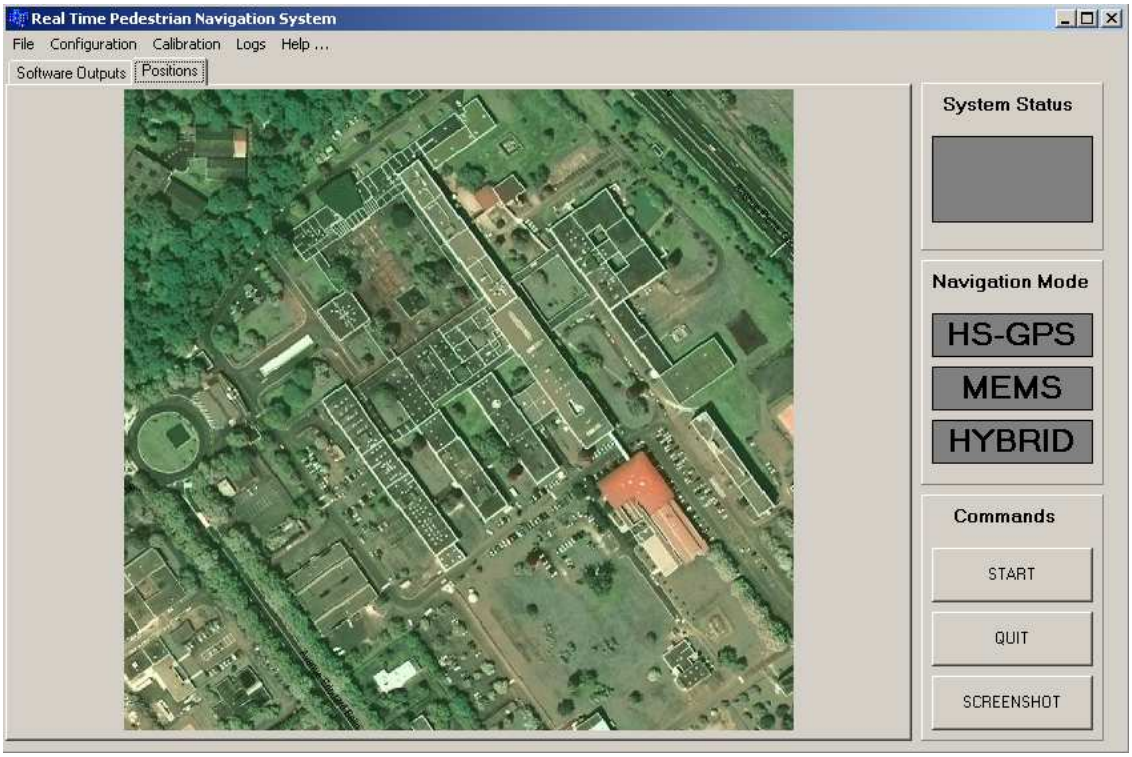

Figure 6.31: Real time Pedestrian Navigation System interface [53].

6.3.3.3 Test Results

The integrated pedestrian navigation system described in the previous section has been tested in actual conditions [53]. Test results are presented in this section. As a first assessment of the hybridisation algorithm described above, the two HSGPS and AGPS outdoor/indoor trials

presented in chapter 2 are used as short-term test cases. The two paths as computed by the two GPS modules are plotted hereafter in blue as a reminder in Figure 6.32 and in Figure 6.33. As focused by the green rectangles, outages occur when the pedestrian walks inside the buildings.

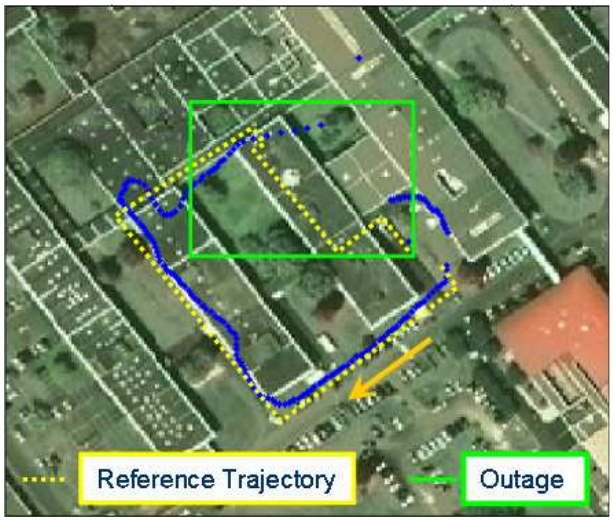

Figure 6.32: HSGPS tracking performance in urban and indoor environments.

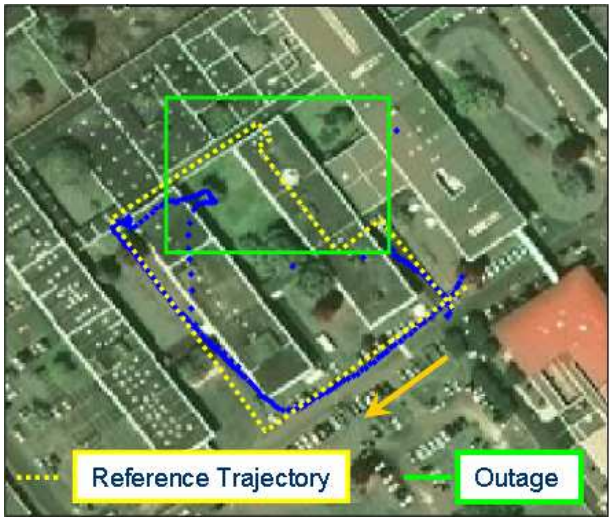

Figure 6.33: AGPS tracking performance in urban and indoor environments.

The result of the hybridisation of the HSGPS module with the low-cost IMU is shown in Figure 6.34. In the figure, the output of the integrated navigation system using both information of the PNS and the HSGPS module is plotted in green. This trajectory illustrates the output of the PNS that has been corrected using HGSPS measurements. Since no measurement quality monitoring algorithm is applied on GPS measurements, the hybrid solution may sometimes be affected by errors as for instance multipath, as shown within the magenta circle in Figure 6.34. This is clearly a drawback of the loose coupling architecture used here to fuse the two navigation systems. In red is plotted the position solution of the integrated navigation system relying exclusively on the MTi data. In that case, the GPS measurements are whether declared not reliable according to the empiric decision logic added in the sensors fusion filter (HDOP and 4th worst C/N_0 thresholds of respectively 2.5 and 25 dBHz), or simply not available (outage). As it can be seen in Figure 6.34, the hybridisation tremendously improves the position availability and accuracy, especially when the pedestrian is inside the building.

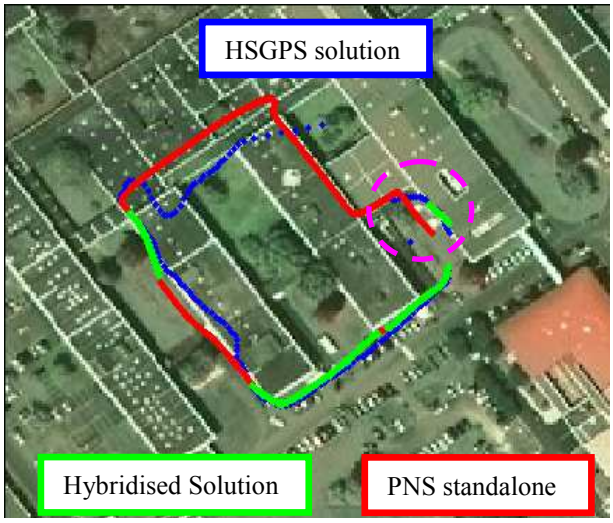

Figure 6.34: HSGPS/IMU hybridisation results.

Figure 6.35: AGPS/IMU hybridisation results.

The same conclusions can almost be drawn in the case of the hybridisation of the low-cost sensors assembly with the AGPS module, as shown in Figure 6.35. The hybrid position solution is nevertheless more accurate than in the previous case, as graphically compared with the reference trajectory followed during the trial.

One interesting point to notice according to the results shown in the two figures is that there are more epochs where the navigation system relies exclusively on the IMU in the HSGPS hybridisation case than in the AGPS hybridisation case. The measurements are indeed less noisy and more reliable according to our empiric decision logic. The position solution is also more accurate thanks to a better dilution of precision due to the availability of the ephemeris of all the satellites that are tracked (as compared to the HSGPS case where each navigation message has to be demodulated for each satellite). This suggests that AGPS is more suited for hybridisation purposes.

In order to assess the medium to long term performance of the integrated system, a longer test using only the AGPS module is conducted. The reference trajectory and the AGPS position solution are plotted below in Figure 6.36. The reference trajectory is plotted in two colours. The yellow dashed part shows the outdoor path followed by the pedestrian while walking and the orange part illustrates the indoor path of the trial. As it can be seen in the figure, two outages in the AGPS single point position solution plotted in blue can be observed (identified as the magenta circles), which makes impossible the tracking of the pedestrian inside the buildings. In these two areas, the integrated navigation system is expected to tremendously increase the tracking of the pedestrian.

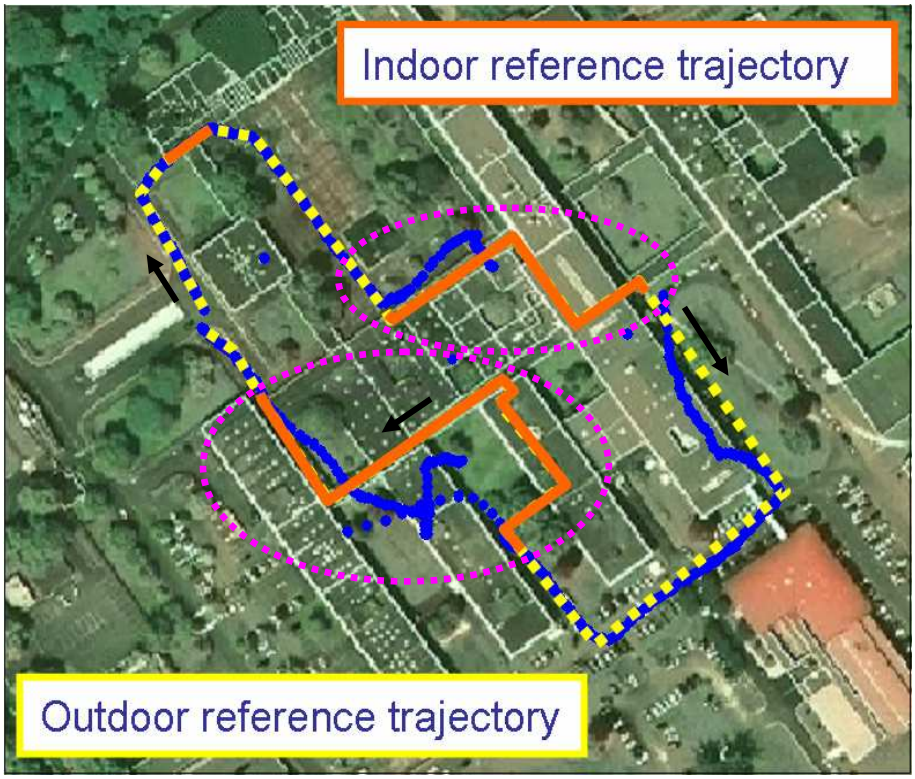

Figure 6.36: Pedestrian trial inside and outside buildings. AGPS single point position solution (blue) and reference trajectory (yellow outdoors, orange indoors).

The performance of the hybrid positioning system is plotted in Figure 6.37 using the same colour legend as in the previous figures (Figure 6.34 and Figure 6.35). The green plot stands for the hybrid solution corrected with GPS measurements, whereas the red plot is the pure PNS trajectory. The hybrid position solution is far more relevant of the true trajectory followed during the trial, as it

was expected. There are two main periods where the integrated navigation system relies exclusively on the IMU data, which corresponds approximately to the outages experienced by the AGPS receiver. This tends to prove the reliability of the AGPS measurements. The estimation of the heading is quite good, but the travelled distance is sometimes very badly estimated, as for example during the first outage (identified by the magenta circle in Figure 6.37). In that case, the travelled distance is under-estimated.

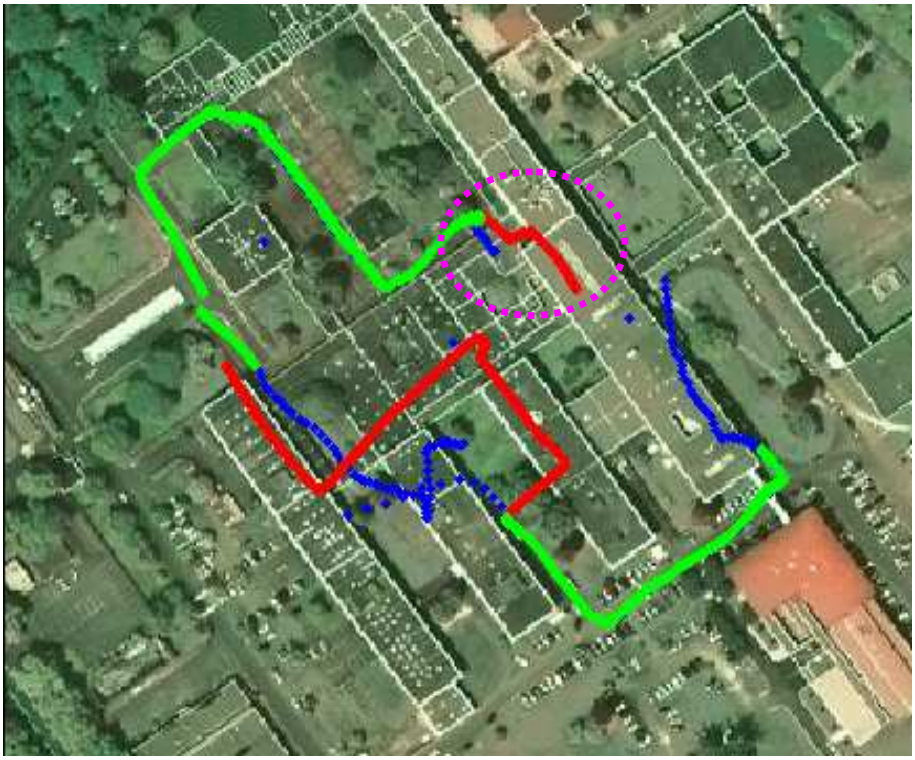

Figure 6.37: AGPS/IMU hybridisation. Long test.

This bad travelled distance estimation is directly the consequence of a bad pedestrian velocity modelling, which in turn is closely related to the quality of the GPS measurements used for calibration purposes. To analyse the reason of this bad travelled distance estimation, Figure 6.38 presents the regression coefficients as corrected by the Kalman filter, as well as the availability of the GPS measurements (including the epochs where GPS measurements are declared unreliable).

Just before the first outage (around time 2min), the regression coefficients experience very large variations due to very noisy GPS measurements that have not been excluded according to the decision logic implemented in the sensors fusion filter (i.e. the 4th satellite used to compute the position solution is higher than 25 dBHz). Outliers or large multipath may have affected the measurements used for correction, which consequently are responsible for this large variation, clearly not relevant of what physically should have been observed.

When the first GPS outage occurs, the inaccurate regression coefficients are kept constant leading to a bad estimation of the travelled distance. In the case presented hereafter, the coefficients are lower than their value estimated with good GPS measurements, which explains why the estimated travelled distance is under-estimated. The first decision logic is therefore not enough efficient to prevent bad GPS measurements from degrading the initialisation of the PNS for further standalone navigation.

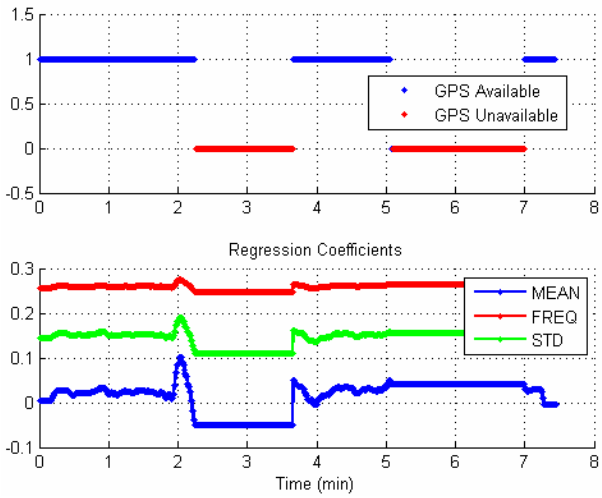

Figure 6.38: GPS measurements availability and regression coefficients (unitless) without variability detection (real time results).

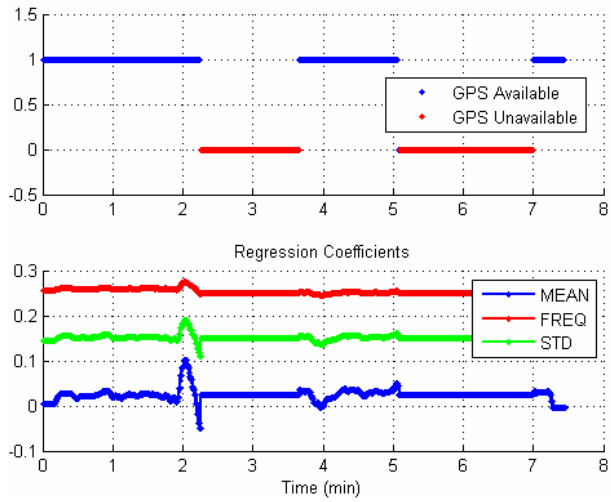

Figure 6.39: GPS measurements availability and corrected regression coefficients (unitless) after variability detection (post processing results).

In order to enhance the monitoring of the quality of the GPS measurements and get the integrated navigation system more robust, another condition is added to the sensors fusion filter according to the conclusions that have just been drawn. If a strong variability in the regression coefficients is detected (which obviously does not reflect a real change in the pace of the pedestrian), then the GPS measurements are assumed unreliable. The regression coefficients are furthermore corrected by their mean value over the previous minute, which is an approximation of their actual values (it is important to say here that another option would have been to check the innovation of the EKF in order to detect strong difference between measurements and predictions, meaning that GPS measurements may be unreliable).

The effect of the correction brought to the regression coefficients is illustrated in Figure 6.39. These results are obtained using the raw data collected during the trial with the real time software. The proposed correction method is clearly efficient as compared to the previous estimation, even if in that case it requires some time to detect bad GPS measurements. Such a quality test on the estimated regression coefficients has been found enough reliable to remove the first decision logic based on the C/N0 of the 4th satellite used in the computation of the user's position. As it can be seen in Figure 6.39, the regression coefficients have a smoother shape with is consistent with the typical pace of a pedestrian, whatever its velocity.

The impact of correction method onto the accuracy of the position solution as provided by the integrated pedestrian navigation system is illustrated in Figure 6.40. The travelled distance accuracy is tremendously increased during the first GPS outage and the position solution is clearly relevant of the true path followed inside the building. The 2D horizontal accuracy stays within 10m from the true trajectory for the whole test, even during the two outages which both last about 2min.

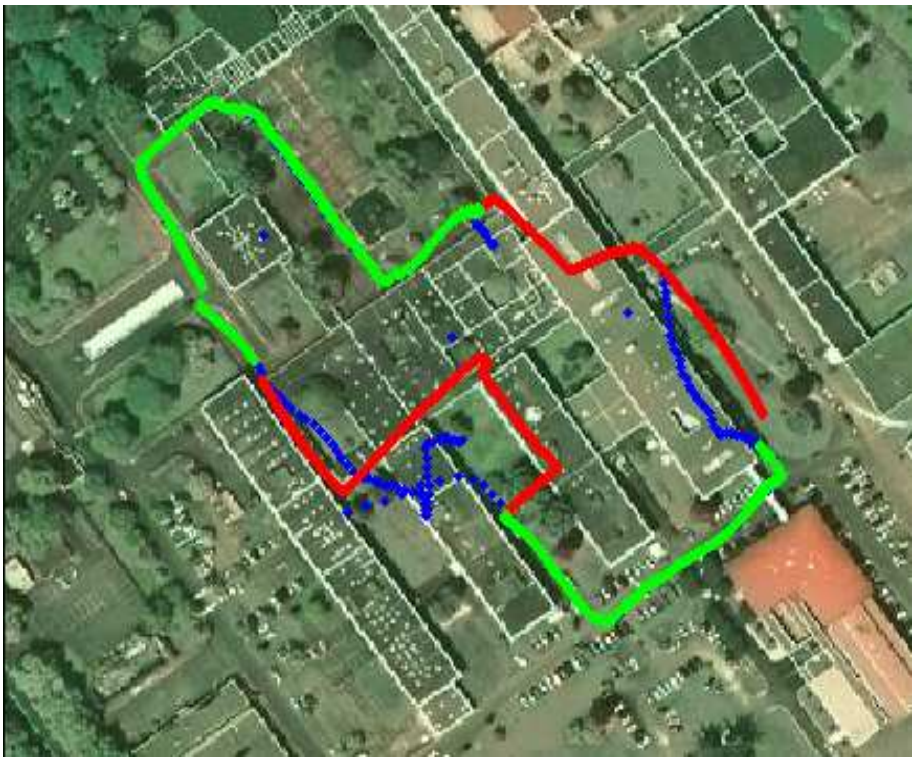

Figure 6.40: AGPS/IMU hybridisation results. Long test with corrected regression coefficients (post processing results).

6.3.4 Conclusion

A real time pedestrian navigation system has been developed based on the combination of different GPS modules (HSGPS and AGPS) with a low-cost IMU made of accelerometers, gyroscopes and magnetometers. The purpose of this integration was twofold: first, to face typical GPS outages that occur inside buildings and second to increase the position solution availability (and somehow accuracy as well) whatever the location of the pedestrian. An optimised pedestrian mechanisation has been used to limit the impact of both accelerometers and gyroscopes bias and consequently improve in the same time the performance of the navigation system during outages. Both integrations with HSGPS and AGPS have been tested.

The results of the conducted trials have shown that AGPS provides measurements less noisy than HSGPS does, which makes it more suited to hybridisation purposes. Because there is no need to demodulate the ephemeris of the satellite in visibility, the AGPS receiver produces measurements of better quality which is of tremendous importance since no RAIM or no GPS measurement quality monitoring algorithm has been implemented as part of the integration navigation system. However, a method aimed at detecting unreliable AGPS measurements through the dynamic of the estimated regression coefficients has been developed. Its implementation and test on real data collected with the developed software during the different trials has demonstrated its efficiency.

The accuracy of the developed integrated pedestrian navigation system stays within 10 metres (horizontal position error) from the true trajectory according to the trial exercised, which makes such an integrated pedestrian navigation system very promising for indoor applications.

6.4 Conclusion

In this chapter, the enhancement of the availability and the accuracy of a positioning system based on GPS have been discussed. The hybridisation of a receiver with low-cost sensors of MEMS type was more specifically addressed. In a first time, a non-conventional tight coupling architecture build around the attitude filter developed in chapter 4 and a simplified INS mechanisation was detailed. It was shown that such a coupling methodology involving more linear equations than the standard tight hybridisation can give quite accurate position solutions using very few GPS measurements (at least 2). Indeed, the hybridised system was found to be accurate within 70 metres for 15 minutes of navigation using only 2 Doppler measurements (horizontal error). To prevent the position error from cumulating because of the memory effect of the dead reckoning algorithm, pseudorange measurements were found necessary to be integrated as measurements. Due to the good performance of the Doppler-based navigation system, their use is not mandatory, which makes possible the accurate navigation (2D error below 70 metres) in environments very affected by multipath.

The pedestrian navigation was also addressed through the pedestrian mechanisation. The integration with both HSGPS and AGPS was tested. Assuming the sensors unit attached to the body, it was shown that the combination of AGPS, the attitude filter detailed in chapter 4 and the pedestrian mechanisation can give position solutions with interesting an interesting accuracy, as compared to what is currently achievable with HSGPS and AGPS receivers. The real time pedestrian navigation system has indeed shown a 2D error of 10 metres from the reference trajectory, even during complete GPS outages of about 2 min, according to the trials exercised.

Chapter 7: Conclusions and Future Work

This chapter recalls the main objectives set up at the beginning of the thesis and discusses the achievements of the contributions that have been detailed throughout the report. A discussion of the technical points that would be interesting to further investigate is also provided.

7.1 Conclusions

As discussed in the introduction, the purpose of this Ph.D thesis was to analyse the benefit that can be brought to GPS-based positioning techniques (namely HSGPS and AGPS) with the use of low cost sensors. In **chapter 1**, the performance of the new processing techniques such as AGPS and HSGPS have been analysed and detailed. Given the low performance of the systems in harsh environments, inertial navigation algorithms based on gyroscopes, accelerometers, magnetometers as well as a pressure sensor have been studied for both pedestrian and land vehicle cases. Weak points relative to the inertial algorithms and sensors quality have been stressed, motivating the study of augmentations based on low cost sensors. Several techniques were proposed to enhance the performance of the standalone inertial navigation systems. Some of them can be used to reduce AGPS/HSGPS acquisition stage complexity; the others can rather be used in GPS/low cost sensors hybridisation schemes.

In **chapter 2**, the new GPS architectures designed to face urban and indoor issues such as HSGPS and AGPS were presented, and their performance were analysed theoretically and practically in terms of time to acquire, time to fix, as well as position accuracy. It was shown that AGPS clearly outperforms HSGPS in terms of time to first fix. Even if such a result was predictable, it was also shown that AGPS produces measurements of better quality than HSGPS probably due to ephemeris data transmitted to the handset. It indeed relieves the GPS chipset from decoding the navigation message of the tracked signal in order to compute the position of the user. This navigation data demodulation can be very difficult in urban areas as soon as the C/N_0 of the satellite goes below 25 dBHz. However, it finally was demonstrated that these AGPS techniques were somehow inefficient in very harsh environments such as inside buildings or in deep urban areas.

Chapter 3 was dedicated to the analysis of inertial navigation algorithms performance. Mechanisations for land vehicle and pedestrian navigation were analysed in great details and their respective weakest points were discussed. In the particular case of pedestrian navigation (PNS), a relationship between the frequency, the standard deviation and the mean of the acceleration magnitude and the pedestrian velocity was established in order to compensate for accelerometer biases. Theoretical simulations showed that it was possible to stay below 150 metres from the reference trajectory for 10 minutes of autonomous navigation, clearly outperforming the classical INS mechanisation. However, such a comparison may be somehow unfair as such a comparison involves a non-optimised classical INS, including improvements comparable to those of the PNS. As the unit containing the sensors may be packed in handheld devices, the singularity issue that may affect the Euler's angles and so the heading was analysed. An algorithm dedicated to avoid such singularities was proposed and successfully tested on real data collected during pedestrian walks. The problem of estimating the true pedestrian heading that arises when sensors are

embedded in handheld devices was also addressed. A heading estimation technique was proposed and results demonstrated the effectiveness of the methodology especially for low to medium motions of the unit with respect to the user. However, typical cell phone movements render the true heading measurement inaccurate.

As the two independent navigation systems were characterised, **chapter 4** discussed the improvement of the inertial navigation algorithms performance in order to increase the accuracy of the data that seemed to be useful in further integration. Algorithms based on the processing of sensors data were set up to reduce the impact of the biases that dramatically decrease the accuracy of the inertial position solution and attitude angles. In particular, an attitude filter was developed to limit the impact of gyroscope biases on the heading accuracy. The accuracy of the filter was tested on actual land vehicle and pedestrian trials. It was found that 1-degree accuracy was achievable in the pedestrian navigation case, according to the tests that were conducted. However, such accuracy is very dependent on the duration of magnetic interferences that may occur. The land vehicle trial demonstrated that in such navigation type, magnetometer data were often unreliable. The use of a pressure sensor as a barometer was studied as well. The vertical velocity was found very noisy making mandatory a low-pass filtering of the measurements. Different integration techniques have been studied. The integration of the altitude measurements as an additive pseudorange measurement was found to give the best improvements in terms of 3D position accuracy. In the perspective of an integrated GPS / inertial sensors system, height constraint seems however more adapted to give a great deal of performance for a minimal increase of algorithm complexity.

Chapter 5 discussed the integration of the low-cost sensors and augmentation algorithms studied in chapter 4 with AGPS / HSGPS receivers in order to decrease the complexity of the acquisition stage by reducing the number of frequency bins to search in. Results have shown that in the pedestrian case where the velocity can be modelled within ±0.3m/s accuracy, the information provided by MEMS sensors decreases the user's Doppler uncertainty to ±6Hz. The user's contribution on the overall frequency search time is consequently reduced up to 95% compared to the frequency search time assuming a user's Doppler uncertainty of ±250Hz. The availability of the Doppler prediction is furthermore 100%. In the land vehicle case, the prediction performs as well by reducing the user's Doppler uncertainty down to ±25Hz. However, the Doppler prediction can only be done once two satellites are acquired since the velocity provided by the sensors assembly is not enough reliable in that case. Moreover, the user's Doppler prediction availability is degraded and depends on the geometry of the satellites with respect to the user's heading.

Finally, **chapter 6** discussed the hybridisation of the low cost sensors with AGPS and HSGPS. A non-conventional tight coupling architecture built around the attitude filter developed in chapter 4 and a simplified INS mechanisation was found to be accurate within 70 metres for 15 minutes of navigation using only 2 Doppler measurements (horizontal error). To prevent the position error from cumulating because of the memory effect of the Dead Reckoning algorithm, pseudorange measurements were found necessary to be integrated as measurements. Due to the good performance of the Doppler-based navigation system, their use is not mandatory, which makes possible the accurate navigation (2D error below 70 metres) in environments very affected by multipath. The pedestrian navigation was addressed assuming the sensors unit attached to the body. The real time pedestrian navigation prototype system developed to assess the performance of such a navigation method has demonstrated a promising accuracy with respect to the trials exercised (2D error of 10 metres, even during complete GPS outage of approximately 2 minutes).

7.2 Future Work

Although the integration of low cost sensors together with hardware-based or software-based GPS receiver in handheld devices is being more and more obvious, the possible motion of the sensors with respect to the user is a big issue. It is very difficult to keep track of the user's heading as the handset may have its own attitude, which consequently limits the use of the pedestrian mechanisation. Opposite, if sensors are attached to the user's body, a good accuracy can be achieved and the performance of an integrated pedestrian navigation system can be significantly increased.

As a consequence, the opinion of the author would be to focus further researches on the processing improvement of AGPS and HSGPS cores. In particular, algorithms using a motion/static status of one user (thanks to accelerometers) as well as attitude measurements of the receiver's antenna (thanks to an attitude filter or simply gyroscopes) may be further investigated from both standalone and differential positioning point of view. A more sophisticated motion recognition algorithm should be developed in order to precisely detect the type of motion experienced by the handset containing the sensors, including states such as idling pedestrian with a moving sensors unit, walking pedestrian with moving sensors assembly…

The attitude filter proposed in this thesis may also be improved by estimating magnetic interferences rather than relying exclusively on gyroscope data. This would certainly increase the complexity of the filter but would in turn decrease the sensitivity to magnetic perturbations.

Another interesting point to focus on would be the use of sensors information in order to improve the acquisition of GPS signals. With the modernisation of the GNSS signals, the combination of MEMS sensors with the GPS acquisition stage can indeed by fruitful for acquiring pilot tones, especially when the receiver is moving and the signal to acquire exhibit a low power.

Improving the land vehicle navigation with a set of low-cost sensors is difficult to achieve due to large biases that affect the acceleration measurements. Even if the heading accuracy can be improved with an attitude filter as the one developed in this thesis, the travelled distance estimation is still an issue. One interesting point would be to analyse the benefit brought by wheel speed and steering sensors, whose information is accessible through the vehicle local area network. In that perspective, the performance of the proposed hybridisation scheme could be studied. The use of AGPS or HSGPS receivers may also be of great interest.

Appendix A: Doppler Effect

Definition

The Doppler effect is the variation of communication signal frequencies caused by the relative motion of the transmitter with respect to the receiver. In GPS transmissions, this effect can be decomposed into a first effect due to satellite motion with respect to the Earth and a second effect caused by user's motion with respect to the Earth (the effect of the receiver local oscillator is here neglected). Assuming time synchronisation, the received phase of the GPS signal carrier from satellite i at epoch t is equal to:

$$\varphi^i(t) = 2\pi L_1\left(t - \tau^i(t)\right) - \theta_0^i = 2\pi f t - \theta_0^i$$

where:

- L_1 stands for the L1 carrier frequency.
- τ^i is the propagation delay affecting the signal from satellite i.
- f is the instantaneous frequency of the received signal.
- θ_0^i is the initial phase offset affecting the received signal.
- φ^i is the phase of the received signal.

The geometric distance between satellite i and the user depends on both movements of the GPS emitter satellite on its orbit with respect to an Earth-Centred Earth-Fixed (ECEF) reference frame, and the user (or more precisely receiver's antenna) on the Earth. The instantaneous frequency of the received signal is given by :

$$f(t) = \frac{1}{2\pi}\frac{d\varphi^i(t)}{dt} = L_1 - L_1\frac{d\tau^i(t)}{dt} = L_1 - \frac{L_1}{c}\frac{dD^i(t)}{dt} = L_1 - \frac{L_1}{c}v_d^i(t) = L_1 + f_d^i(t)$$

where:

- $D^i(t) = c \cdot \tau(t)$ is the satellite-to-user geometric distance.
- v_d^i is the Doppler velocity (i.e. the rate of change of the satellite-to-user geometric distance)
- $f_d^i(t) = -\frac{L_1}{c}v_d^i(t)$ is the Doppler frequency affecting the received signal.

Given the above notations, and assuming f_d^i constant over a short time interval, the phase of the received signal can be written as given below. In that case, it is then fully described by the L_1 carrier frequency, the initial phase and the Doppler affecting the carrier.

$$\varphi^i(t) = 2\pi L_1 t + 2\pi f_d^i(t)t - \theta_0^i$$

Doppler Frequency for Typical Use Cases

Let's assume a configuration with one satellite in motion and a user on ground, as illustrated in the figure below. The projection of the satellite velocity onto the user's Line of Sight is equal to

v_{ds} [5]. It can be written as a function of the satellite velocity according to the following equation:

$$v_{ds} = v_s \sin(\beta)$$

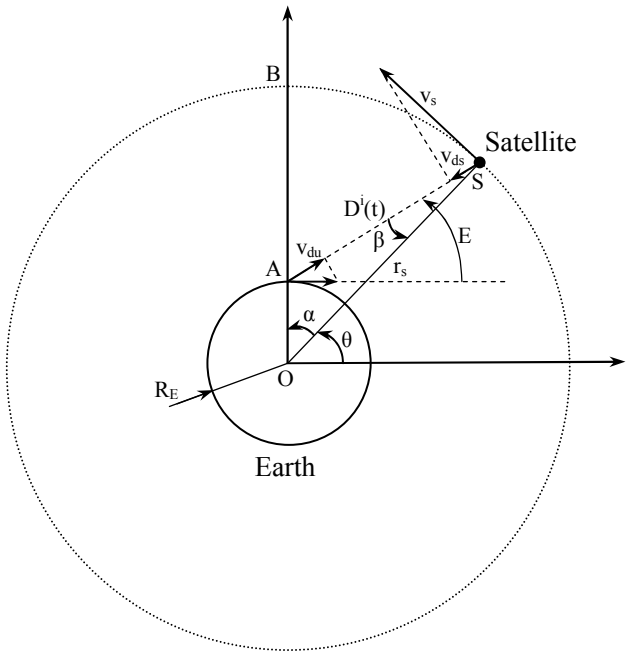

Given the basic relationships that characterises the OAS triangle, it is straightforward to express the projected satellite velocity as a function of the θ angle:

OAS relationships: $\dfrac{\sin(\beta)}{OA} = \dfrac{\sin(\alpha)}{D^i}$ and $r_s^2 = OA^2 + D^{i2} - 2 \cdot OA \cdot D^i \cdot \cos(\theta)$

$$v_{ds} = \frac{v_s R_E \cos\theta}{AS} = \frac{v_s R_E \cos\theta}{\sqrt{R_E^2 + r_s^2 - 2R_E r_s \sin(\theta)}}$$

The period of an orbit in seconds of solar time is given by $T = 2\pi\sqrt{a^3/\mu}$. The period of the GPS satellite is 12 sidereal hours, that is 11h 58min and 2.045s solar time. Sidereal time is slightly shorter than solar time. One sidereal day is equal to 86164.1 seconds of mean solar time [5]. Thus, assuming the orbit of GPS satellites a circle with a mean radius of $a = 26560\ km$, the velocity v_s of a GPS satellite with respect to an ECEF reference frame is then:

$$v_s = \frac{2\pi \cdot a}{T_{solar_time}} = \frac{4\pi \cdot 26560 \cdot 10^3}{86164.09054} \approx 3873.5\ m.s^{-1}$$

The maximum satellite Doppler velocity is obtained when the θ-derivative of v_{ds} is equal to zero, or equivalently when $\theta = \theta_{d\max}$. This occurs when the satellite is at the horizontal of the user. In such a case, $v_{ds_{\max}} = v_s\ R_E / r_s \approx 929\ m.s^{-1}$ which gives a maximum Doppler shift due to satellite motion of about $f_{ds_{\max}} \approx 4.9\ kHz$.

Following the same methodology, the effect of the user's motion on the overall Doppler will be maximum for a null elevation E. Assuming the user is walking, his maximum velocity is about 10 km/h (2,8 m/s), which introduces a maximum Doppler shift on the received GPS L_1 carrier frequency of about $f_{du_{\max}} = L_1 v_u \cos(E_{\min}) / c = L_1 v_{du_{\max}} / c \approx 14.6\ Hz$. Assuming the maximum velocity of a user in a vehicle of about 150 km/h (41.7 m/s), the maximum Doppler shift introduced by the user's motion is equal to $f_{du_{\max}} \approx 219\ Hz$.

The overall Doppler affecting the received signal at the user's antenna is then the combination of the two contributions described above plus an extra contribution due to the receiver local oscillator drift. That contribution, for a 1 ppm local oscillator is around $1.5 \cdot 10^9 \times 10^{-6} = 1.5 kHz$.

Appendix B: Quaternion-Based Attitude Computation

Edward's Algorithm

This section describes the Edouard's algorithm that is used to compute the attitude of a mobile based on gyroscopes measurements [20], [21]. Assume a triad of gyroscopes mounted on the mobile. The measured values are the rotation rates of the mobile with respect to the inertial frame ***(I)***, expressed in the mobile frame ***(m)***. Using the quaternion-based attitude determination, the differential equation to solve for is equation 3.9. This equation involves the rotation rate of ***(m)*** with respect to ***(n)***, which can be decomposed as follows:

$$\omega_{m/n}^{(m)} = \omega_{m/I}^{(m)} - \omega_{n/I}^{(m)}$$

where:

- $\omega_{m/I}^{(m)}$ is the sensed values coming from the gyros output.
- $\omega_{n/I}^{(m)}$ can be decomposed into the sum of:
  $\omega_{n/e}^{(m)}$, which is the rotation rate of the navigation frame ***(n)*** with respect to the ECEF-frame ***(e)***
  $\omega_{e/I}^{(m)}$, which is the rotation rate of ***(e)*** with respect to ***(I)***.
- $\omega_{n/e}^{(m)} = R_{m2n}^{-1} \cdot \left[v_E / (R_\Phi + h) \quad -v_N / (R_\lambda + h) \quad -v_E \tan(\lambda) / (R_\Phi + h) \right]^T$
- $\omega_{e/I}^{(m)} = R_{m2n}^{-1} \cdot \left[\omega_{ei} \cos(\lambda) \quad 0 \quad -\omega_{ei} \sin(\lambda) \right]^T$
- v_N, v_E are the North and East velocity components of the mobile.
- λ is the current latitude of the mobile.
- ω_{ei} is the actual rotation rate of the Earth with respect to the inertial frame.
- R_Φ is the transverse radius of curvature (See section 3.3.2 for details).
- R_λ is the radius of curvature in a meridian (See section 3.3.2 for details).
- h is the current altitude of the mobile.

a) Initialisation of the Rotation Quaternion

The computation of the rotation quaternion is mainly composed of three steps. The first step is the initialisation of the rotation quaternion Q. It is usually done with initial values of roll ϕ_0, pitch θ_0 and heading ψ_0 according to the following equations:

$$q_0 = \cos\left(\frac{\phi_0}{2}\right) \cdot \cos\left(\frac{\theta_0}{2}\right) \cdot \cos\left(\frac{\psi_0}{2}\right) + \sin\left(\frac{\phi_0}{2}\right) \cdot \sin\left(\frac{\theta_0}{2}\right) \cdot \sin\left(\frac{\psi_0}{2}\right)$$

$$q_1 = \sin\left(\frac{\phi_0}{2}\right) \cdot \cos\left(\frac{\theta_0}{2}\right) \cdot \cos\left(\frac{\psi_0}{2}\right) - \cos\left(\frac{\phi_0}{2}\right) \cdot \sin\left(\frac{\theta_0}{2}\right) \cdot \sin\left(\frac{\psi_0}{2}\right)$$

$$q_2 = \sin\left(\frac{\phi_0}{2}\right) \cdot \cos\left(\frac{\theta_0}{2}\right) \cdot \sin\left(\frac{\psi_0}{2}\right) + \cos\left(\frac{\phi_0}{2}\right) \cdot \sin\left(\frac{\theta_0}{2}\right) \cdot \cos\left(\frac{\psi_0}{2}\right)$$

$$q_3 = \cos\left(\frac{\phi_0}{2}\right) \cdot \cos\left(\frac{\theta_0}{2}\right) \cdot \sin\left(\frac{\psi_0}{2}\right) - \sin\left(\frac{\phi_0}{2}\right) \cdot \sin\left(\frac{\theta_0}{2}\right) \cdot \cos\left(\frac{\psi_0}{2}\right)$$

Consequently, the rotation quaternion Q at first epoch is given by:

$$Q_0 = q_0 + q_1 \cdot \vec{i} + q_2 \cdot \vec{j} + q_3 \cdot \vec{k}$$

b) Initialisation of Angular Increments

Angular increments are intermediate variables needed all along the Edward's computation process. They are used to store angular increment information experienced by the sensors assembly between two consecutive epochs. Edward introduced two areas before and after the instant at which the quaternion associated to the rotation is computed, as described below.

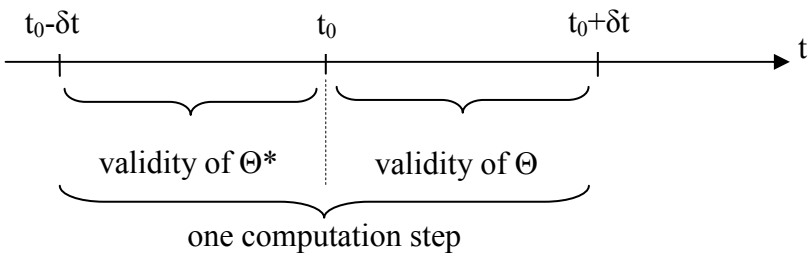

$$\Theta = \int_{t_0}^{t_0+\delta t} \omega_{m/n}^{(m)}(t) \cdot dt = \omega_{m/n}^{(m)}(t_0) \cdot \delta t + \frac{\dot{\omega}_{m/n}^{(m)}(t_0)}{2} \cdot \delta t^2 + \frac{\ddot{\omega}_{m/n}^{(m)}(t_0)}{6} \cdot \delta t^3 + \frac{\dddot{\omega}_{m/n}^{(m)}(t_0)}{24} \cdot \delta t^4$$

$$\Theta^* = \int_{t_0-\delta t}^{t_0} \omega_{m/n}^{(m)}(t) \cdot dt = \omega_{m/n}^{(m)}(t_0) \cdot \delta t - \frac{\dot{\omega}_{m/n}^{(m)}(t_0)}{2} \cdot \delta t^2 + \frac{\ddot{\omega}_{m/n}^{(m)}(t_0)}{6} \cdot \delta t^3 - \frac{\dddot{\omega}_{m/n}^{(m)}(t_0)}{24} \cdot \delta t^4$$

- Θ is the last angular increment. $\Theta = 0 + \Theta_i \cdot \vec{i} + \Theta_j \cdot \vec{j} + \Theta_k \cdot \vec{k}$.
- Θ^* is the next to last angular increment. $\Theta^* = 0 + \Theta_i^* \cdot \vec{i} + \Theta_j^* \cdot \vec{j} + \Theta_k^* \cdot \vec{k}$.

The current angular increment Θ is initialised to zero: $(\Theta_i)_0 = (\Theta_j)_0 = (\Theta_k)_0 = 0$.

c) Update of the Rotation Quaternion

The third step is the update of the quaternion Q. The angular increment Θ is computed from the values of $\omega_{m/n}^{(m)} = \omega_{m/I}^{(m)} + \omega_{e/n}^{(m)} - \omega_{e/I}^{(m)}$ as described above. The next to last increment is first updated ($\Theta^* = \Theta$), and then the current increment angle is computed ($\Theta \approx \omega_{m/n}^{(m)}(t_0) \cdot \delta t$). The quaternion Q is updated according to the following equation [20], [21]:

$$\begin{bmatrix} q_0 \\ q_1 \\ q_2 \\ q_3 \end{bmatrix}(t_0 + \delta t) = \begin{bmatrix} q_0 & -q_1 & -q_2 & -q_3 \\ q_1 & q_0 & -q_3 & q_2 \\ q_2 & q_3 & q_0 & -q_1 \\ q_3 & -q_2 & q_1 & q_0 \end{bmatrix}(t_0) \cdot \begin{bmatrix} 1 - \frac{1}{8}\|\Theta\|^2 \\ \left(\frac{1}{2} - \frac{1}{48}\|\Theta\|^2\right) \cdot \Theta_i + \frac{1}{24}\left(\Theta_j^* \cdot \Theta_k - \Theta_k^* \cdot \Theta_j\right) \\ \left(\frac{1}{2} - \frac{1}{48}\|\Theta\|^2\right) \cdot \Theta_j + \frac{1}{24}\left(\Theta_k^* \cdot \Theta_i - \Theta_k^* \cdot \Theta_i\right) \\ \left(\frac{1}{2} - \frac{1}{48}\|\Theta\|^2\right) \cdot \Theta_k + \frac{1}{24}\left(\Theta_i^* \cdot \Theta_j - \Theta_j^* \cdot \Theta_i\right) \end{bmatrix}$$

with $\|\Theta\| = \sqrt{\Theta_i^2 + \Theta_j^2 + \Theta_k^2}$

Quaternion Q is then normalised since a rotation quaternion must be unitary:

$$Q = \frac{Q}{\|Q\|} = \frac{Q}{\sqrt{q_0^2 + q_1^2 + q_2^2 + q_3^2}}$$

Once the computation process is done, it is straightforward to get the rotation matrix from ***(m)*** to ***(n)***, or the attitude angles pitch, roll and heading.

Rotation matrix from ***(m)*** to ***(n)***:

$$R_{m2n} = \begin{bmatrix} q_0^2 + q_1^2 - q_2^2 - q_3^2 & 2(q_1q_2 - q_0q_3) & 2(q_1q_3 + q_0q_2) \\ 2(q_1q_2 + q_0q_3) & q_0^2 + q_2^2 - q_3^2 - q_1^2 & 2(q_3q_2 - q_0q_1) \\ 2(q_1q_3 - q_0q_2) & 2(q_2q_3 + q_0q_1) & q_0^2 + q_3^2 - q_1^2 - q_2^2 \end{bmatrix}$$

Attitude angles:

$$\text{Roll: } \theta = \arcsin(-2(q_1q_3 + q_0q_2))$$

$$\text{Pitch: } \phi = \arctan\left(\frac{2(q_3q_2 - q_0q_1)}{-1 + 2(q_0^2 + q_1^2)}\right)$$

$$\text{Heading: } \psi = \arctan\left(\frac{2(q_1q_2 - q_0q_3)}{-1 + 2(q_0^2 + q_3^2)}\right)$$

Appendix C: Least Squares and Kalman Filtering

The purpose of this appendix is not to set up Least Squares and Kalman Filtering theories and algorithms, but it rather aims at simply describing their respective basic principles and fundamental implementation steps as they are widely used in GPS and INS/GPS integration. For more details, see for instance [44], [45] or [51].

Least Squares

a) Least Squares Solutions

Least Squares aim at fitting measurements provided by an external source to a mathematical model depending on several parameters to estimate. Ideally, the system shall be linear in order to implement the algorithm. But in most of cases it is not so that the system must be linearised prior to use the algorithm under its iterative form.

In the linear case, let's assume the mathematical model of the system as follows:

$$Y(t) = H \cdot X(t) + B(t)$$

where :

- Y is the vector of external measurements.
- X is the vector of the parameter to estimate. It is a deterministic vector.
- H is the measurement matrix.
- B is the noise affecting the measurements. It is assumed stationary with the following properties: $E[B] = 0$ and $Cov(B) = R$.

It can be shown [45] that the LS solution $\hat{X}$ of the system previously described is given by:

$$\hat{X} = \left[H^T \cdot H\right]^{-1} \cdot H^T \cdot Y$$

An optimal estimator is obtained if we have information about the noise affecting the measurements. In such a case, the addition of the inverse of the noise covariance matrix allows to weight each of the measurements according to the power and the correlation of the noise affecting those measurements. The optimal LS solution is thus as follows:

$$\hat{X} = \left[H^T \cdot W \cdot H\right]^{-1} \cdot H^T \cdot W \cdot Y \text{, with } W = R^{-1}$$

b) Iterative Least Squares Algorithm

In the usual case of non-linear system, the mathematical model can be written as follows. Same notations are reused here with h standing for the non-linear measurement function.

$$Y(t) = h\big(X(t)\big) + B(t)$$

In such a non-linear case, the parameters are estimated iteratively once the model has become linear. Let's note $\hat{X}$ an estimation of X at epoch t. The first step is to get h linear. With ΔX defined as the difference between the actual parameters and their respective estimation (i.e. $\Delta X(t) = X(t) - \hat{X}(t)$) h can be written as follows:

$$h(X(t)) = h(\hat{X}(t)) + \Delta X(t) \cdot \frac{\partial h}{\partial X}(\hat{X}(t))$$

The non-linear system can then be rewritten as:

$$\Delta Y(t) = H \cdot \Delta X(t) + B(t)$$

where:

- $\Delta Y(t) = Y(t) - h(\hat{X}(t))$
- $H = \frac{\partial h}{\partial X}(\hat{X}(t)) = \begin{bmatrix} \frac{\partial h_1}{\partial x_1}(\hat{X}(t)) & \cdots & \frac{\partial h_1}{\partial x_n}(\hat{X}(t)) \\ \vdots & & \vdots \\ \frac{\partial h_N}{\partial x_1}(\hat{X}(t)) & \cdots & \frac{\partial h_N}{\partial x_n}(\hat{X}(t)) \end{bmatrix}$

The new system is linear. Therefore the error vector ΔX can be computed through the classical Least Square estimation method for a given epoch t. However, since approximations have been made when getting the model linear, the vector ΔX of unknown parameters will contain errors. Therefore, to ensure a good result to the Least Square estimation computation, an iterative process has to be implemented for each epoch. At epoch t and according to Least Square theory, the estimation of the unknown parameters contained in ΔX are thus given by:

$$\Delta \hat{X} = [H^T \cdot H]^{-1} \cdot H^T \cdot \Delta Y$$

The iterative process for epoch ends when the error vector $\Delta \hat{X}$ has a norm below a predefined threshold, or when the difference between the observed measures and the noiseless predicted ones ΔY is small enough. As a summary, the Iterative Least Square algorithm is given below.

Steps	Operations	Comments
1	$\hat{X}(t) = \hat{X}_0(t)$	Set initial value of estimates for iteration 0
2	$H_i = \frac{\partial h}{\partial X}(\hat{X}_i)$ $\Delta Y_i = Y(t) - h(\hat{X}_i(t))$ $\Delta \hat{X}_i(t) = [H_i^t H_i]^{-1} H_i^t \times \Delta Y_i(t)$	Iteration i: do Least Square estimation
3	$\hat{X}_{i+1} = \hat{X}_i + \Delta \hat{X}_i$	Update estimates
4	$\lVert \Delta Y_i \rVert < Threshold$, or $\lVert \Delta \hat{X}_i \rVert < Threshold$	If ΔY_i or $\Delta \hat{X}_i$ has significant low norm, stop iterative process, otherwise return to step 2

Kalman Filtering

Kalman filtering is a recursive technique that allows the estimation of a state vector characterising a system. It differs from the Least Squares in the sense it uses a mathematical model that gives the relationship between the state vector and the system, and also observations (or measurements) collected from that system. For a given epoch k, the estimation of the sate vector is done by combining its previous value at epoch k-1 with observations collected from that epoch. Usually, the system is described in its continuous form and then as to get discretised in order to adapt its use on real use cases that only involve sampled data.

a) State Model

The general model of a system is as follows:

$$\dot{x}(t) = f\big(x(t)\big) + w(t)$$
$$y(t) = h\big(x(t)\big) + v(t)$$

where:
- f is the sate transition function.
- h is the observation (or measurement) function.
- x is the state vector.
- w is the state noise.
- y are the observations (measurements).
- v is the measurement noise.

This model is composed of two parts. The first one is the stochastic part that involves the time derivative of the state vector. The second one involves the measurements obtained from the system. These two equations fully describe the system.

b) Discretisation Process

The Kalman equations as given above shall be used on a discreet system. As the system may be described in its continuous form, one has first to get it discreet. The discretisation procedure is based on Taylor series. Equations are given below for each matrix involved in the algorithm.

State Transition Matrix:

$$F_k = \exp\big(F(t)\cdot T_s\big) = I + F(t)\cdot T_s + \frac{\big(F(t)\cdot T_s\big)^2}{2!} + o\big(T_s^2\big)$$

State Covariance Matrix:

$$Q_k = Q(t)\cdot T_s + \big(F(t)\cdot Q(t) + Q(t)\cdot F(t)^T\big)\cdot\frac{T_s^{\,2}}{2} + o\big(T_s^2\big)$$

Measurement Matrix:

$$Y_k = Y(t = k)$$

Measurement Covariance Matrix:

$$R_k = R(t = k)$$

One important thing to notice is that discretisation of the continuous state transition matrix F is valid if and only if it can be considered constant during the discretisation time T_s. It is generally not the case in GNSS/INS integration, which is therefore usually processed on subdivisions of T_s [20].

c) Kalman Filter Equations

The equations of the discrete Kalman filter are deduced from the above system model. There are 5 equations that must be sequentially computed as follows:

1	*Prediction*	$\hat{X}_{k+1\|k} = f(\hat{X}_{k\|k})$
2	*Covariance Prediction*	$\Sigma_{k+1\|k} = F_k \Sigma_{k\|k} F_k^T + Q_k$
3	*Kalman Gain*	$K_{k+1} = \Sigma_{k+1\|k} H_{k+1}^T (H_{k+1} \Sigma_{k+1\|k} H_{k+1}^T + R_{k+1})^{-1}$
4	*State Vector Update*	$\hat{X}_{k+1\|k+1} = \hat{X}_{k+1\|k} + K_{k+1}[Y_{k+1} - h(\hat{X}_{k+1\|k})]$
5	*Covariance Update*	$\Sigma_{k+1\|k+1} = \Sigma_{k+1\|k} - K_{k+1} H_{k+1} \Sigma_{k+1\|k}$

where:

- $F_k = \frac{\partial f}{\partial X}\left(\hat{X}_{k|k}\right)$ and $H_{k+1} = \frac{\partial h}{\partial X}\left(\hat{X}_{k+1|k}\right)$.
- Q_k is the state noise covariance matrix at epoch k.
- R_k is the measurement noise covariance matrix at epoch k.
- Y_k is the measurement vector at epoch k.

Appendix D: Frequency Estimation Techniques

This appendix assesses the performance of four methods dedicated to the estimation of the step frequency characterising a pedestrian acceleration signal. These methods are compared using real data recorded during typical pedestrian walks. The focus is put in the frequency estimation using very few samples. Details about these techniques are given below in the table.

Description of the Techniques

Technique Number	Principle of the Frequency Estimation Technique
1	The first method is to detect step occurrences in the total acceleration signal, as defined in equation 3.34. Occurrences are time tagged and the step frequency is then deduced. As the frequency estimation is performed at each step; this technique is a step-based frequency determination
2	The second technique uses the well-known periodogram as a tool to estimate the frequency. This technique is applied on a signal that contains at least two step impacts in order to detect a periodicity. The frequency estimation accuracy depends on the number of samples available to compute the periodogram. One solution to get rid off this lack of resolution is to increase the number of samples used in the computation process, even if it reduces the capability of detecting rapid frequency variations.
3	To cope with the resolution issue of technique n°2, the use of High Resolution techniques is investigated. Several High Resolution methods exist, namely the correlation technique using the Levinson-Durbin algorithm, the modified covariance and the Prony techniques. Details about their principles and properties can be found in [58]. All the three methods are implemented and tested.
4	The last technique used to estimate the frequency characterising the pedestrian walk is based on filtering the acceleration signal through a Kalman filter. Two filters are tested, one able to track one sinus-like signal, the other one able to track a combination of two sinus-like signals. Observation models are given below, as well as the common state vector composed of the amplitude, the frequency, the mean and the phase of the acceleration signal. Observation model: $a_k = M + A\sin(2\pi \cdot F \cdot t + \Phi)$ State Vector $X = [M \quad A \quad F \quad \Phi]^T$ or Observation model: $a_k = M + A_1 \sin(2\pi \cdot F_1 \cdot t + \Phi_1) + A_2 \sin(2\pi \cdot F_2 \cdot t + \Phi_2)$ State Vector: $X = [M \quad A_1 \quad A_2 \quad F_1 \quad F_2 \quad \Phi_1 \quad \Phi_2]^T$

The comparison of the four techniques is done with both time-tagged and step-tagged systems. The signal used to assess the accuracy of technique 1 to 4 is recorded during a walk on a

flat surface. The acceleration magnitude a_k as defined in equation 3.34 is shown below.

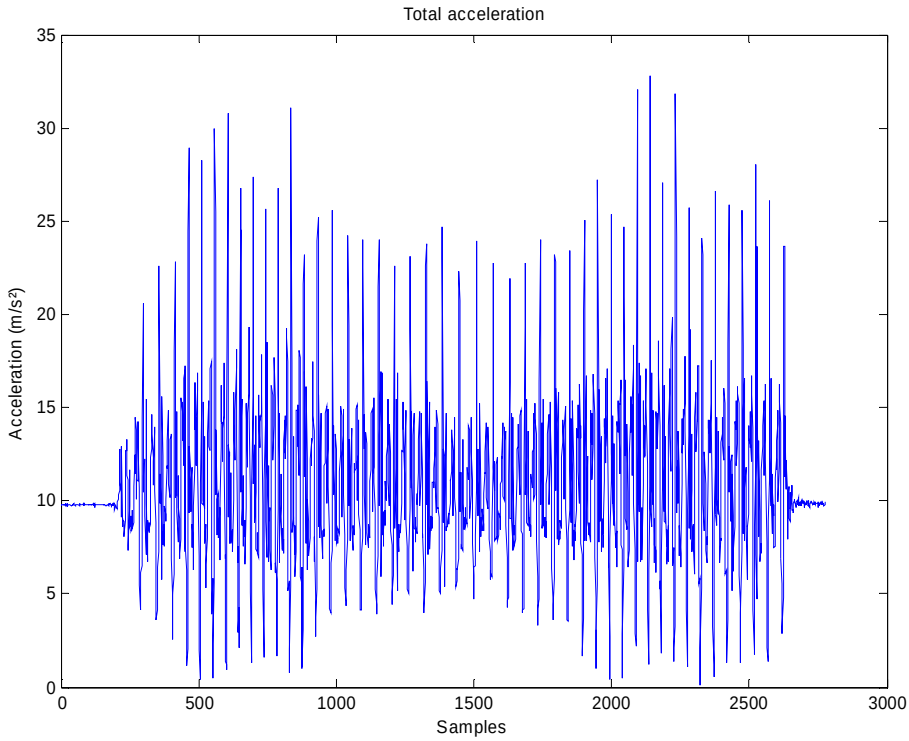

Performance Assessment

a) Step-tagged Frequency Estimation

The first technique was tested using a step detection algorithm in order to get step occurrences from the acceleration magnitude. As the other techniques requires more than exactly a period of data in order to estimate the step frequency, half a second of signal was added before and after the two consecutive step occurrences. That new short signal was then used as an input for techniques n°2, n°3 and n°4. Tests were conducted to find the best order needed compute the Prony, correlation and modified covariance High Resolution models. The best order was empirically found to be 14 (usual order estimation methods such as AIC, CAT or FPE [58] did not provide any relevant information).

Results of frequency estimation over 1 and 2 steps are shown below. In both figures, the cyan plot is the mean GPS velocity averaged over 1 and 2 steps. From both figures, it is obvious that the frequency parameter has the same behaviour as the GPS velocity, thus shall be included in the velocity model. As it could have been expected, the step-based technique produces noisy step frequency estimates. Opposite, techniques n°2, n°3 and n°4 give smoother frequency estimations. Results from technique n°4 based on Kalman filtering are not presented here. Although the implementation works well on synthetic data, the convergence of the filter processing real data was found very difficult to achieve. The main reason for that is that variables carried by the state vector (i.e. mean, amplitude, frequency and phase) compensate each other for individual variations, and the real acceleration signal is not stationary.

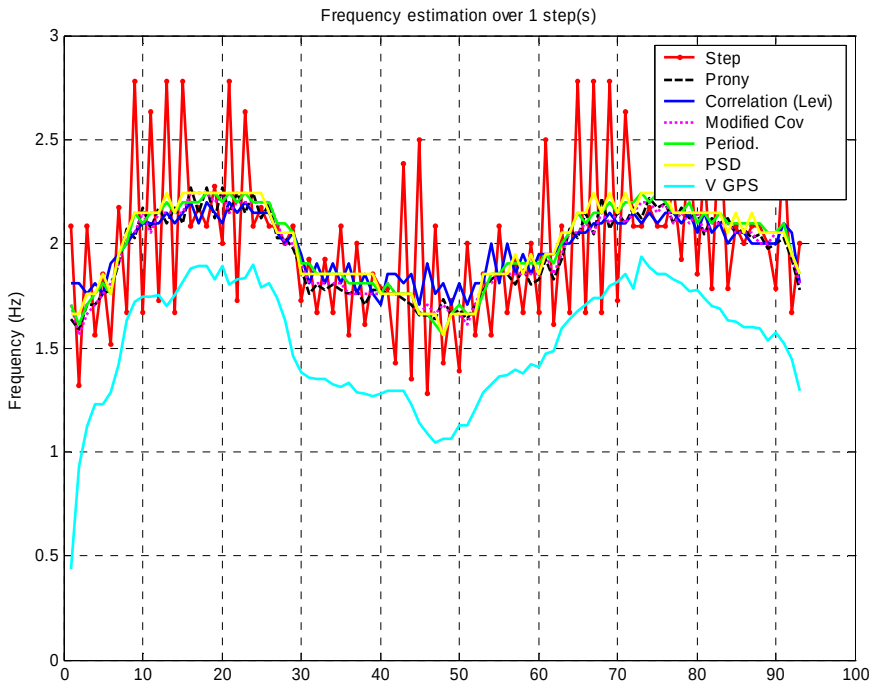

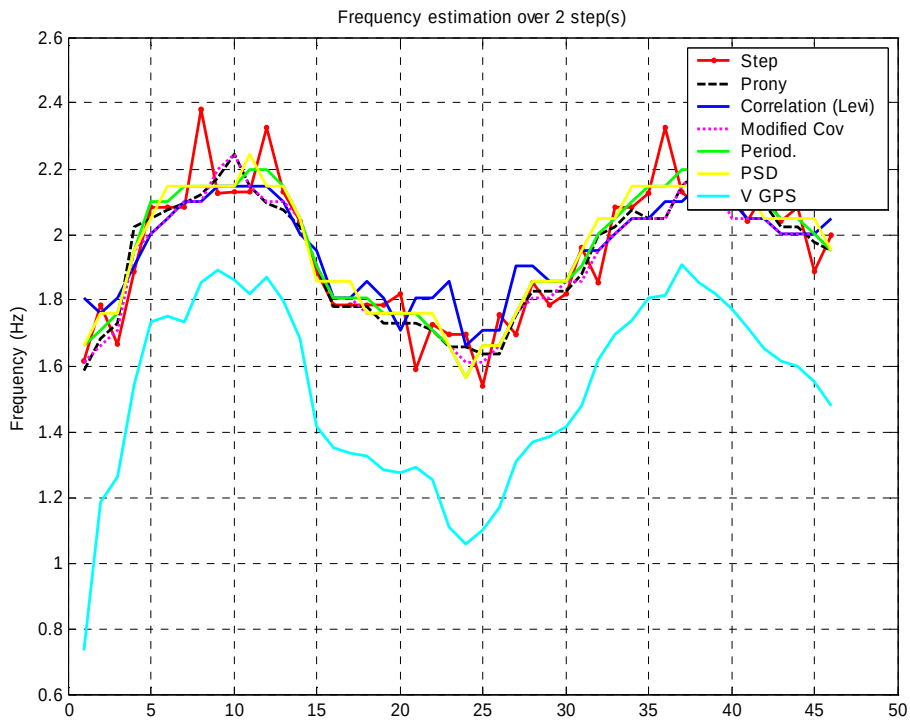

The table below gives the correlation computed between the mean GPS velocity and the different estimated frequency. Whatever the computation span (i.e. 1 or 2 steps), the periodogram and PSD methods are the best ones.

Methods	Step	Prony	Levi	Mod. Cov.	Periodogram	PSD
Correlation for freq. estimated over 1 step	0,440	0,941	0,888	0,943	0,944	0,944
Correlation for freq. estimated over 2 steps	0,908	0,966	0,912	0,964	0,967	0,967

b) Time-tagged Frequency Estimation

As a comparison, results of step frequency estimation by processing data at each sampling period over a time widows of 1 and 2 seconds are shown below.

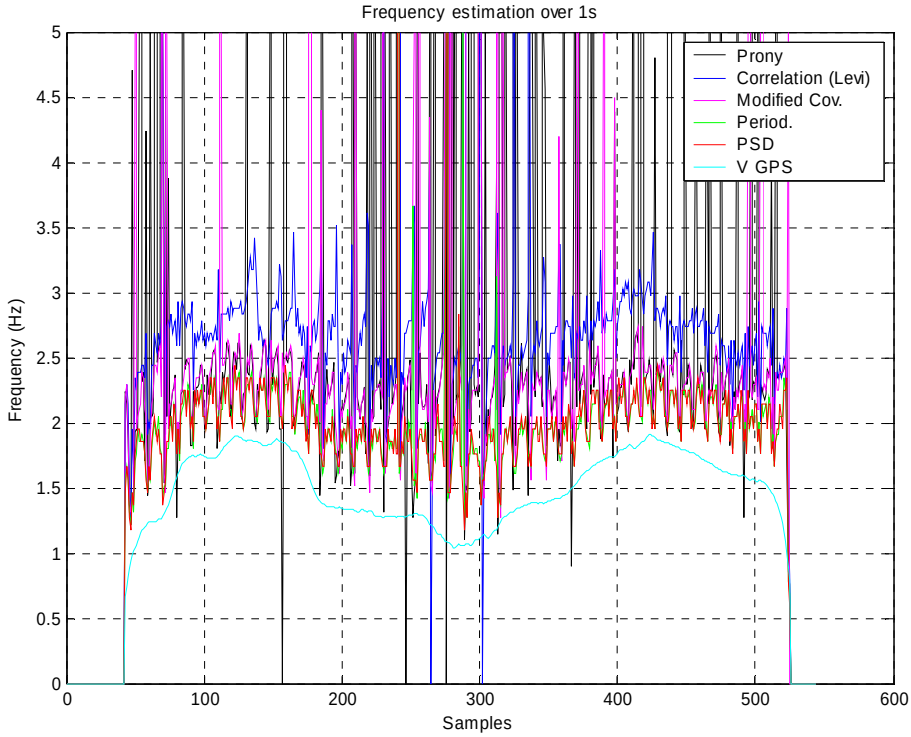

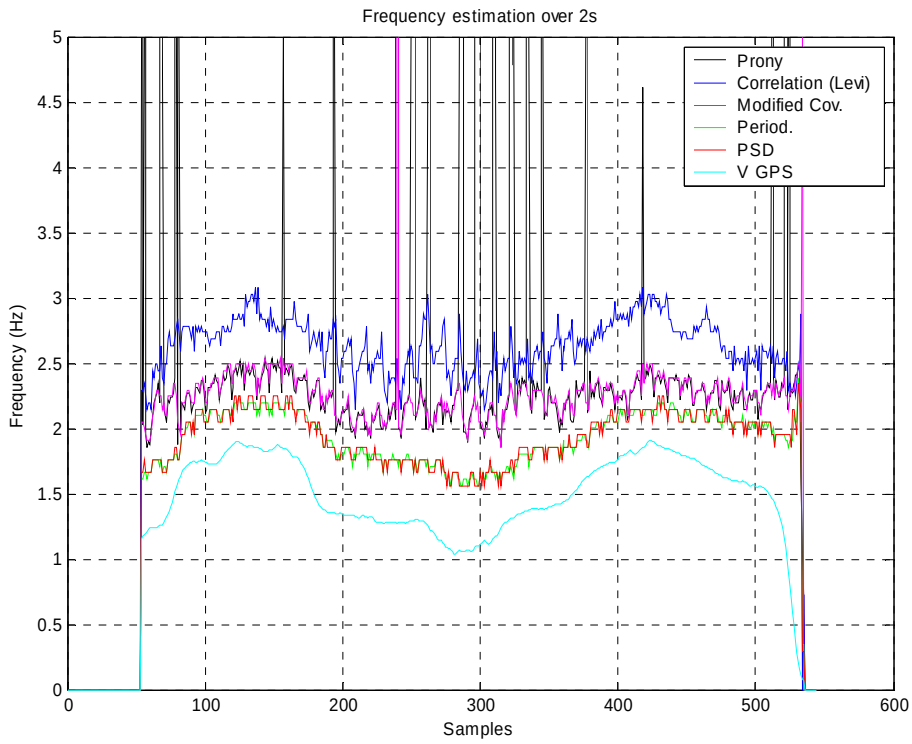

High Resolution techniques fail to estimate the frequency in many cases. This explains the poor correlations between frequency estimations and the mean GPS velocity, as presented in the table below. This is mainly due to bad order of the model used in the respective high resolution

algorithms (usual methods that estimate this order such as AIC, CAT or FPE did not provide relevant information), as well as the non stationary property of the signal to analyse.

Methods	Prony	Levi	Mod. Cov.	Periodogram	PSD
Correlation for freq. estimated over 1 second	0,314	0,661	0,402	0,765	0,834
Correlation for freq. estimated over 2 seconds	0,375	0,920	0,796	0,931	0,931

As a conclusion, according to correlation performance presented in both tables, the techniques that give the best performance are the periodogram and PSD estimation. The periodogram technique is used throughout this thesis.

Bibliography

[1] GPS ICD 200C. http://www.navcen.uscg.gov/pubs/gps/icd200/default.htm.

[2] B. W. Parkinson, J. J. Spilker. *The Global Positioning System: Theory and Applications*. American Institute of Aeronautics and Astronautics, 1996.

[3] C. Macabiau. *GPS* internal course notes, ENAC, 2002.

[4] J.K. Holmes. *Coherent Spread Spectrum Systems*. R. E. Krieger Publishing Company, 1990.

[5] J. Bao, Y. Tsui. *Fundamentals of Global Positioning System Receivers - A Software Approach*. Wiley Interscience.

[6] C Macabiau, AC Escher. *GNSS* master internal course notes, ENAC, 2002.

[7] C Macabiau. *Analysis of the Feasability of Using GPS Carrier Phase Ambiguity Resolution Techniques for Precision Approach*. Ph.D. Thesis Report, September 29, 1997.

[8] P. Misra, P. Enge. *Global Positioning System- Signals, Measurements, and Performance*. Ganga Jamuna Press, 2001.

[9] J. A. Farrell, M. Barth. *The Global Positioning System and Inertial Navigation*. Mc Graw Hill, 1999.

[10] G. Macgougan. *High Sensitivity GPS Performance Analysis in Degraded Signal Environments,* MSc Thesis, University of Calgary Geomatics Engineering, 2003.

[11] A.J. van Dierendonck, P. Fenton, T. Ford. *Theory and Performance of Narrow Correlator Spacing in a GPS receiver*. Journal of The Institute of Navigation, vol. 39, no.3, pp. 265-283, 1992.

[12] D. Kubrak, C. Macabiau, M. Monnerat. *Vehicular Navigation using a Tight Integration of Aided-GPS and Low-Cost MEMS Sensors*. Proceedings of the ION NTM 2006.

[13] B. Peterson, D. Bruckner, and S. Heye. *Measuring GPS Signals Indoors*. ION GPS 1997.

[14] F. van Diggelen. *Global Locate Indoor GPS Chipset & Services*, Proceedings of the ION GPS 2001.

[15] F. van Diggelen, C. Abraham. *Indoor GPS Technology*. Global Locate inc. CTIA Wireless-Agenda, Dallas 2001.

[16] D. Kubrak, C. Macabiau, M. Monnerat. *Analysis of a software-based A-GPS acquisition performance using statistical processes*. Proceedings of the ION NTM 2005.

[17] V. Garbi, S. Corazza. *Field trial: Assisted GPS (A835, A1000, HP6515) and autonomous GPS (BT-338)*. Alcatel Alenia Space, internal report, 2006.

[18] M.S. Grewal, L.R. Weill, A.P. Andrews. *Global Positioning Systems, Inertial Navigation, and Integration*. John Wiley & Sons Inc, 2001.

[19] M. Kayton, W. Fried. *Avionics Navigation Systems*, second edition. John Wiley & Sons Inc.

[20] A.C. Escher. *Study of the contribution of GNSS/INS Hybridisation to GNSS Integrity Monitoring for Civil Aviation Applications*. Ph.D. Thesis Report, INP Toulouse, 2003.

[21] J. C. Radix. *Systèmes inertiels à composants liés STRAP-DOWN*. Cépaduès-éditions, 1991.

[22] US National Geophysical Data Centre web site (http://www.ngdc.noaa.gov).

[23] Nemerix NJ2020 datasheet (downloaded from Nemerix website, 2006).

[24] SiRFstarIII™ GPS Single Chip datasheet (downloaded from SiRF website, 2006).

[25] Philips Application Note AN00022. *Electronic Compass Design using KMZ51 and KMZ52* (downloaded from Philips website, 2005).

[26] Analog Devices ADXRS300 data sheet (downloaded from Analog Devices website, 2005).

[27] Analog Devices ADXL203 data sheet (downloaded from Analog Devices website, 2005).

[28] Analog Devices ADXL202E data sheet (downloaded from Analog Devices website, 2005).

[29] Q. Ladetto. *On foot navigation: continuous step calibration using both complementary recursive prediction and adaptive Kalman filtering*. Proceedings of the ION GNSS 2000.

[30] V. Gabaglio. Ph.D. Thesis Report, EPFL website, 2003.

[31] Intersema MS5534 Datasheet (downloaded from Intersema website, 2005).

[32] J. Stephen, G. Lachapelle. *Development of a GNSS-Based Multi-Sensor Vehicle Navigation System*. Proceedings of the ION NTM 2000.

[33] G.J. Olson et al. *Non-gimbaled Solid-State Compass*. Solid-State Sensor and Actuator Workshop, June 1994.

[34] M.J. Caruso, L.S Withanawasam. *Vehicle detection and compass applications using AMR Magnetic Sensors*. Honeywell website.

[35] E.R. Bachmann, X. Yun, R.B. McGhee, *Sourceless Tracking of Human Posture Using Small Inertial/Magnetic Sensors*, IEEE Computational Intelligence in Robotics and Automation Symposium, 2003.

[36] D. Kubrak, C. Macabiau, M. Monnerat. *Performance Analysis of MEMS based Pedestrian Navigation Systems*. Proceedings of the ION GNSS 2005.

[37] S. Sukkarieh. *Low Cost, High Integrity, Aided Inertial Navigation Systems for Autonomous Land Vehicles*, PhD Thesis, Department of Mechanical and Mechatronic Engineering,

University of Sydney, Australia, 2000.

[38] D. Brzezinska, C. Toth, Y. Yi. *Bridging GPS Gaps in Urban Canyons: Can ZUPT Really Help?* Proceedings of the ION GPS 2001.

[39] S. Godha et al. *Performance Analysis of MEMS / IMU / HSGPS / Magnetic Sensor Integrated System in Urban Canyons*. Proceedings of the ION GNSS 2005.

[40] S. Godha and M. E. Cannon. *Integration of DGPS with a Low Cost MEMS – Based Inertial Measurement Unit (IMU) for Land Vehicle Navigation Application*. Proceedings of the ION GNSS 2005.

[41] Collin J., J. Kappi, and K. Saarinen. *Unaided MEMS-Based INS Application in a Vehicular Environment*. Proceedings of the ION GNSS 2001.

[42] G. Dissanayake, S. Sukkarieh, E. Nebot, H. Durrant-Whyte. *The Aiding of a Low-Cost Strapdown Inertial Measurement Unit Using Vehicle Model Constraints for Land Vehicle Applications*. IEEE Transactions on Robotics and Automation, vol. 17, n°5, October 2001.

[43] M. S. Grewal, A. P. Andrews. *Kalman filtering – Theory and practice*. Prentice Hall, 1993.

[44] R. G. Brown, P. Y. C. Hwang. *Introduction to Random Signals and Applied Kalman Filtering*. Wiley, 3rd Edition, 1994.

[45] C. Macabiau. *Kalman Filtering* internal course notes, ENAC, 2003.

[46] J. Collin, H. Kuusniemi, O. Mezentsev, G. MacGougan, G. Lachapelle. *HSGPS under Heavy Signal Masking – Accuracy and Availability Analysis*. Proceedings of 6th Nordic Radio Navigation Conference and Exhibition "NORNA 03", Stockholm-Helsinki.

[47] H. Hou. *Modeling Inertial Sensors Errors Using Allan Variance*. Msc Thesis. UCGE Reports Number 20201. September 2004.

[48] S. Nassar. *Improving the Inertial Navigation System (INS) Error Model for INS and INS/DGPS Applications*. Ph.D. Thesis Report. UCGE Reports Number 20183. November 2003.

[49] O. Mezentsev. *Sensor Aiding of HSGPS Pedestrian Navigation*. Ph.D. Thesis Report, University of Calgary website (PLAN group), 2005.

[50] H. Kuusniemi. *User-Level Reliability and Quality Monitoring in Satellite-Based Personal Navigation*. Ph.D. Thesis Report, University of Calgary website (PLAN group), 2005.

[51] C. Macabiau. *Least Squares* internal course notes, ENAC, 2003.

[52] D.Kubrak, C.Macabiau, M.Monnerat. *Low-Cost MEMS Sensors for Aided-GNSS Processing Enhancement*. Proceedings of the 13th Saint Petersburg International Conference on Integrated Navigation Systems. 2006.

[53] D.Kubrak, C.Macabiau, M.Monnerat. *Real Time Pedestrian Navigation System*. Proceedings of the ION GNSS 2006.

[54] Wicht Technologie Consulting. *Think small !* issue 2, volume 1, May 2006.

[55] InvenSense IDG-1000 Integrated Dual Axis Gyroscope datasheet (from Invensense website, 2006).

[56] Analog Devices ADXL330 data sheet (from Analog Devices website, 2006).

[57] AKM 8970N 3D magnetic compass datasheet (from AKM website, 2006).

[58] C. Lambert-Nebout. *Parametric and Non Parametric Estimation Techniques* internal course notes, ENAC, 2003.

[59] H.S. Hopfield. *Two-Quadratic Tropospheric Refractivity Profile for Correction Satellite Data. Journal of Geophysical Research*, 74(18), 4487 – 4499. 1969.

[60] S. Alban, D. Akos, S. Rock & D. Gebre-Egziobher. *Performance Analysis and Architectures for INS-Aided GPS tracking loops*. Proceedings of the ION NTM 2003.

[61] D. Li, J. Wang. *Performance Analysis of the Ultra-Tight GPS/INS Integration Based on an Improved Kalman Filter Design for Tracking Loops*. International Global Navigation Satellite Systems Society. IGNSS Symposium 2006.